SIGNAL PROCESSING FOR RADAR WITH ARRAY ANTENNAS AND FOR RADAR WITH MICRO-DOPPLER MEASUREMENTS

Svante Björklund

Blekinge Institute of Technology
Doctoral Dissertation Series No. 2017:02

Department of Mathematics and Natural Sciences

Signal Processing for Radar with Array Antennas and for Radar with Micro-Doppler Measurements

Svante Björklund

Blekinge Institute of Technology doctoral dissertation series
No 2017:02

Signal Processing for Radar with Array Antennas and for Radar with Micro-Doppler Measurements

Svante Björklund

Doctoral Dissertation in
Applied Signal Processing

Department of Mathematics and Natural Sciences
Blekinge Institute of Technology
SWEDEN

Department of Mathematics and Natural Sciences
Publisher: Blekinge Institute of Technology
SE-371 79 Karlskrona, Sweden
Printed by Exakta Group, Sweden, 2017
ISBN: 978-91-7295-335-2
ISSN:1653-2090
urn:nbn:se:bth-13639

Till min mamma

Abstract

Radar (RAdio Detection And Ranging) uses radio waves to detect the presence of a target and measure its position and other properties. This sensor has found many civilian and military applications due to advantages such as possible large surveillance areas and operation day and night and in all weather. The contributions of this thesis are within applied signal processing for radar in two somewhat separate research areas: 1) radar with array antennas and 2) radar with micro-Doppler measurements.

Radar with array antennas: An array antenna consists of several small antennas in the same space as a single large antenna. Compared to a traditional single-antenna radar, an array antenna radar gives higher flexibility, higher capacity, several radar functions simultaneously and increased reliability, and makes new types of signal processing possible which give new functions and higher performance.

The contributions on array antenna radar in this thesis are in three different problem areas. The first is High Resolution DOA (Direction Of Arrival) Estimation (HRDE) as applied to radar and using real measurement data. HRDE is useful in several applications, including radar applications, to give new functions and improve the performance. The second problem area is suppression of interference (clutter, direct path jamming and scattered jamming) which often is necessary in order to detect and localize the target. The thesis presents various results on interference signal properties, antenna geometry and subarray design, and on interference suppression methods. The third problem area is measurement techniques for which the thesis suggests two measurement designs, one for radar-like measurements and one for scattered signal measurements.

Radar with micro-Doppler measurements: There is an increasing interest and need for safety, security and military surveillance at short distances. Tasks include detecting targets, such as humans, animals, cars, boats, small aircraft and consumer drones; classifying the target type and target activity; distinguishing between target individuals; and also predicting target intention. An approach is to employ micro-Doppler radar to perform these tasks. Micro-Doppler is

created by the movement of internal parts of the target, like arms and legs of humans and animals, wheels of cars and rotors of drones.

Using micro-Doppler, this thesis presents results on feature extraction for classification; on classification of targets types (humans, animals and man-made objects) and human gaits; and on information in micro-Doppler signatures for re-identification of the same human individual. It also demonstrates the ability to use different kinds of radars for micro-Doppler measurements. The main conclusion about micro-Doppler radar is that it should be possible to use for safety, security and military surveillance applications.

Preface

The contributions of this thesis are within applied signal processing for radar in two somewhat separate research areas: 1) radar with array antennas and 2) radar with micro-Doppler measurements. The thesis consists of two parts:

I An introduction to the areas addressed and publications included in this thesis:.

1 Motivation and overview.

2 Radar basics.

3 Radar with array antennas.

4 Radar with micro-Doppler measurements.

5 Contributions of the included publications.

II Included publications within the two areas:

A Radar with array antennas.

B Radar with micro-Doppler.

Acknowledgments

My path to a Ph.D. degree has been a long and tortuous one. In 1993 I was employed at the FOA (Defence Research Establishment) in Linköping, Sweden, and started to work with Hans Ottersten, Anders Nelander, Per Grahn and Anders Alm. Thank you for letting me be part of your group and discover the beautiful world of radar. I have been working with radar with array antennas since 1993 and with radar with micro-Doppler measurements since 2008. I have also worked with other areas within the radar field which are not part of this thesis. One of the first things I did at FOA was to read the Ph.D. thesis by an Ulrich Nickel [1] and implement his DOA (Direction Of Arrival) estimation method PTMF (Parametric Target Model Fitting) in Matlab.

During the years I have been working with many persons at FOA/FOI, too many to mention them all, but I give thanks to them here. (In 2001 FOA changed name to FOI [Swedish Defence Research Agency]). Especially I would like to mention Anders Nelander. Thank you for all cooperation and help during the years. Your door has always been open for discussions about all aspects of radar, including complicated theoretic reasoning. Per Grahn, thank you for all cooperation in radar work and thank you for all help with computers. Lars Pettersson, thank you for help with antennas and signal processing. Tomas Boman and David Rejdemyhr, thank you for successful cooperation on radar with array antennas. Thanks to Henrik Petersson, Gustaf Hendeby and Tommy Johansson for invaluable contributions to our micro-Doppler work. Thanks to the Arken radar group for important micro-Doppler measurements.

Thank you all colleagues which I during the years have worked together with at companies and organizations within the scientific areas of this thesis: Saab AB (Gothenburg, Sweden), Saab AB (Järfälla, Sweden), Thales Systèmes Aéroportés (Paris, France), Selex SI (Rome, Italy), TNO (The Hague, Netherlands), Thales Nederland (Delft, Netherlands), IMST (Kamp-Lintfort, Germany) and others. Even if most of the results of those cooperation are not published, I have learned and gained understanding. Especially, I would like to thank for the cooperation with professor Mats Viberg and his Signals and Systems group at Chalmers Institute of Technology (Gothenburg, Sweden) and professor Fredrik

Gustafsson and his Sensor Informatics group at Linköping University.

In 1999 I was offered a postgraduate student position in the Signals, Sensors and Systems group at KTH (Royal Institute of Technology) in Stockholm. Due to some reasons I turned it down. Thank you for the opportunity I did not take. However, I accepted an offer and in 2001 I started as a postgraduate student at the Automatic Control group at Linköping University. I completed a Licentiate of Engineering degree in the system identification field with professor Lennart Ljung as supervisor [2]. (A Licentiate degree is between a M.Sc. degree and a Ph.D. degree). Thank you for teaching me about how research should be done and giving me insight into a very successful research group.

In 2004 I came back to FOI and continued to work in the radar field. Mats Pettersson, who had moved from FOI to BTH (Blekinge Institute of Technology) encouraged me to continue with postgraduate studies to a Ph.D. degree at BTH. Professor Ingvar Claesson thank you for accepting me as a postgraduate student in 2007 and also being my supervisor. Since then I have worked on this thesis in part time besides my work at FOI. My main supervisor Mats, now professor, has helped and encouraged me along the way. Thank you, Mats; without you I would not have been where I am today. I also would like to thank Thomas Sjögren and Viet Thuy Vu for being friends and, for a while, co-students at BTH. I would like to thank David Lindgren at FOI for supporting me on my path to this thesis. Also thanks to David and to Christina Grönwall, FOI, for reviewing parts of the manuscript and giving valuable comments.

I would like to thank the co-authors of the publications included in this thesis for a good work together: Per Grahn, Lars Pettersson, Amir Heydarkhan, Anders Nelander, Mats Pettersson, Tomas Boman, Henrik Petersson, Gustaf Hendeby and Tommy Johansson.

I have struggled with the editors and anonymous reviewers of conferences and journals who have handled and reviewed our manuscripts. Thank you for your time and commitment which you have given me. I have myself been reviewer of papers for conferences and journals. It has given me experiences and the feeling that I am part of the scientific community. Thank you editors for that opportunity.

Last but not least I would like to give my deepest gratitude to my beloved mother, who has always been there for me and has let me do what I want.

Svante Björklund
Linköping, January 2017

Publication list

Publications included in this thesis

Radar with array antennas

1. Svante Björklund, Per Grahn, Lars Pettersson: "Radar-Like Measurements with an Experimental Digital Beamforming Array Antenna", Proceedings of the International Radar Symposium (IRS) 98, Munich, Germany, 15-17 September 1998, pp. 993-1002 [3].

2. Svante Björklund, Amir Heydarkhan: "High Resolution Direction of Arrival Estimation Methods Applied to Measurements from a Digital Array Antenna", Proceedings of the First IEEE Sensor Array and Multichannel Signal Processing Workshop (SAM) 2000, 16-17 March 2000, Cambridge, Massachusetts, USA, pp. 464-468 [4].

3. Svante Björklund, Anders Nelander, Mats I. Pettersson: "Auxiliary Beam Terrain-Scattered Interference Suppression: Reflection System and Radar Performance", IET Radar, Sonar & Navigation, Volume 7, Issue 8, October 2013 [5].

4. Svante Björklund, Per Grahn, Anders Nelander, Mats I. Pettersson: "Measurement of Rank and Other Properties of Direct and Scattered Signals", International Journal of Antennas and Propagation, 2016 [6].

5. Svante Björklund, Tomas Boman, Anders Nelander: "Clutter Properties for STAP with Smooth and Faceted Cylindrical Conformal Antennas", The 2010 IEEE International Radar Conference, Washington DC, USA, May 10-14, 2010 [7].

6. Svante Björklund: "Clutter Properties for a Side-Looking Radar with Planar Regular and Irregular Subarrays", International Radar Symposium (IRS) 2015, Dresden, Germany, June 24-26, 2015 [8].

7. Svante Björklund: "Three-Dimensional DPCA with Rotating Antenna for Clutter Cancellation", The 2015 IEEE International Radar Conference, Arlington, Virginia, USA, May 11-15, 2015 [9].

Radar with micro-Doppler measurements

8. Svante Björklund, Henrik Petersson, Gustaf Hendeby: "Features for Micro-Doppler Based Activity Classification", IET Radar, Sonar & Navigation, Special Issue: Micro-Doppler, Volume 9, Number 9, December 2015 [10].

9. Svante Björklund, Tommy Johansson, Henrik Petersson: "Target Classification in Perimeter Protection with a Micro-Doppler Radar", International Radar Symposium (IRS) 2016, 10-12 May 2016, Kraków, Poland [11].

10. Svante Björklund, Henrik Petersson, Gustaf Hendeby: "On Distinguishing between Human Individuals in Micro-Doppler Signatures", International Radar Symposium (IRS) 2013, Dresden, Germany, June 19-21, 2013 [12].

Some publications not included in this thesis

- Svante Björklund, Anders Nelander, Mats I. Pettersson, "Fast-Time and Slow-Time Space Time Adaptive Processing for Bistatic Radar Interference Suppression", The 2015 IEEE International Radar Conference, 10-15 May 2015, Arlington, Virginia, USA [13].
- Svante Björklund , Mats I. Pettersson: "A Three-Dimensional Displaced Phase Center Antenna Condition for Clutter Cancellation", The Eighth IEEE Sensor Array and Multichannel Signal Processing Workshop (SAM) 2014, A Coruña, Spain, June 22-25, 2014 [14].
- Svante Björklund: "The Design, Development and Use of a Matlab Toolbox for Radar Modeling, Simulation and Signal Processing", International Radar Symposium (IRS) 2013, Dresden, Germany, June 19-21, 2013 [15].
- Svante Björklund, Tommy Johansson, Henrik Petersson: "Evaluation of a Micro-Doppler Classification Method on mm-Wave Data", IEEE Radar Conference 2012, May 7 - 11, 2012, Atlanta, Georgia, USA [16].

- Svante Björklund, Henrik Petersson, Amer Nezirovic, Mehmet B. Guldogan, Fredrik Gustafsson: "Millimeter-Wave Radar Micro-Doppler Signatures of Human Motion", International Radar Symposium (IRS) 2011, Leipzig, Germany, September 7 - 9, 2011 [17].

- Mehmet B. Guldogan, Fredrik Gustafsson, Umut Orguner, Svante Björklund, Henrik Petersson, Amer Nezirovic: "Human Gait Parameter Estimation Based on Micro-Doppler Signatures Using Particle Filters", IEEE ICASSP (International Conference on Acoustics, Speech and Signal Processing) 2011, Prague, Czech Republic, May 22-27, 2011 [18].

- Svante Björklund, Tomas Boman, Anders Nelander: "UAVs (Unmanned Aerial Vehicles) for surveillance and information acquisition about ground targets", Back cover figures and text in IEEE Aerospace and Electronic Systems Magazine, Vol 26, No. 3, March 2011 [19].

- Svante Björklund, Lennart Ljung, "An Improved Phase Method for Time-Delay Estimation", Automatica (a journal of IFAC, the International Federation of Automatic Control), Volume 45, Issue 10, October 2009 [20].

- Svante Björklund, Anders Nelander: "Fast-Time STAP for Clutter Suppression between Transmitter and Receiver in Bistatic Radar", International Radar Conference RADAR 2009, Bordeaux, France, 12-16 October 2009 [21].

- Svante Björklund: "Space-Time Adaptive Processing with a Half-Cylinder Faceted Conformal Antenna", International Radar Conference RADAR 2009, Bordeaux, France, 12-16 October 2009 [22].

- Henrik Petersson, Svante Björklund, Mikael Karlsson, Andris Lauberts: "Towards surveillance using micro-Doppler radar", International Radar Symposium (IRS) 2009, 9-11 September 2009, Hamburg, Germany [23].

- Svante Björklund, Tomas Boman: "Virtual Antennas for Clutter Suppression in Forward-Looking Airborne Radar", Proceedings of RVK 2005 (RadioVetenskap och Kommunikation 2005), Linköping, Sweden, 14-16 June, 2005 [24].

- Svante Björklund, Anders Nelander: "Theoretical aspects on a method for terrain scattered interference mitigation in radar", IEEE International Radar Conference 2005, 9-12 May 2005, Washington DC, USA [25].

- Svante Björklund, Lennart Ljung: "A review of time-delay estimation techniques", Proceedings of 42nd IEEE Conference on Decision and Control, 9-12 December 2003, Hawaii, USA [26].

- Svante Björklund: "A Survey and Comparison of Time-Delay Estimation Methods in Linear Systems", Licentiate thesis no. 1061, Department of Electrical Engineering, Linköping University, Sweden, 2003 [2].

- Svante Björklund, Per Grahn, Anders Nelander: "Analysis of Array Antenna Measurements with a Rough Surface Reflector", Proceedings of 34th Asilomar Conference on Signals, Systems, and Computers, October 29 - November 1, 2000, Pacific Grove, California, USA [27].

- Per Grahn, Svante Björklund: "Short Range Radar Measurements with an Experimental Digital Array Antenna", Proceedings of the IEEE International Radar Conference RADAR 2000, May 7-12, 2000, Alexandria, Virginia, USA, pp. 178-182 [28].

- Svante Björklund, Per Grahn, Anders Nelander: "Measurement and Analysis of Multipath by a Rough Surface Reflector using a Digital Array Antenna", Proceedings of ISSPA '99 (IEEE Fifth International Symposium on Signal Processing and its Applications), August 22-25, 1999, Brisbane, Australia, p. 859-862 [29].

- Svante Björklund: "Implementierung einer Schrittweitensteuerung für eine Freisprecheinrichtung" (Implementation of a stepsize control for an acoustic echo canceler), Diplomarbeit (Master of Science thesis) D85, Technische Hochschule Darmstadt, Germany, 1993, in German language [30].

Contents

Part I

Introduction

1 Motivation and overview

A *radar* (RAdio Detection And Ranging) is a measurement device, by which radio waves are transmitted, then reflected back from an object, called the *target*, and again received and processed by the radar. By this, the radar can detect the presence of a target and measure its position and other properties.

The radar was invented at the beginning of the 20th century but it was not employed in large scale before the Second World War. There was an intense development of radar systems just before and during the war [31, 32]. The targets were mostly aircraft, but also ships.

The reason for developing and using radar sensors from the beginning was that they have some unique and desired properties: Radar can have a large measurement capacity. This means that a radar can cover a large surveillance area or volume, thanks to the possible large field-of-view and to the possibility to measure at long distances. Moreover, radar can operate at day and night and in all types of weather. Later, additional advantages of radar have been utilized and many new applications for radar measurements have been developed.

This thesis deals with radar in two research areas, first, radar with array antennas and, then, radar with micro-Doppler measurements. This chapter tries to summarize the research problems and challenges and also the results and conclusions of the work by FOI (Swedish Defence Research Agency) in these two research areas. Since the author of this thesis has been a part of FOI's work, he has had the same research problems and challenges. This chapter thus contains a motivation for the research of the author of this thesis and also an overview of the research work done by FOI. Chapter 5, which describes the publications included in the theses, is confined to publications where the author of the thesis has contributed.

A radar uses an antenna for transmission of the radio signal and another or the same antenna for the reception of the back-reflected signal. If a single large antenna is replaced by several smaller antennas in the same space an *array*

antenna is created. Some important advantages with replacing a single large antenna by an array antenna are: By higher flexibility and higher capacity an array antenna radar can replace several single antenna radars. An array antenna radar has the possibility to handle several radar functions at the same time, e.g. search for new targets, track several already detected targets and perform target recognition or classification. Moreover, an array antenna radar makes new types of processing possible, e.g. interference (clutter, direct path jamming and TSI [see below]) suppression by STAP (Space Time Adaptive Processing) and high resolution DOA (Direction of Arrival) estimation, giving new radar functions and higher performance. Array antenna radars also provide increased reliability. The main drawback with array antenna radars is the high cost and added complexity of hardware and large data volumes. See Section 3.1 for some applications of radar with array antennas. (TSI [Terrain Scattered Interference] are jammer signals scattered in ground or sea. Explanations of clutter, direct path jamming and TSI can be found in Section 2.1). Several aspects of incorporating signal processing for array antennas in radar are addressed in [33].

At FOI, the main research problems with array antenna radars from 1993 until now have been: designing and building radars with array antennas; calibration of array antenna radars; how using array antennas in radar; performing DOA estimation on real measured data; incorporating DOA estimation in monostatic and bistatic radar; estimation of the number of targets; detection performance of moving targets in interference (clutter, direct path jamming and TSI) in monostatic and bistatic radar; suppression of interference in monostatic and bistatic radar with and without hardware imperfections; modeling and simulation of radar signals; learning properties of internal signals (noise) and external signals (targets and interference); how to choose antenna geometry and design subarrays in array antennas in order to minimize the clutter problem; and using MIMO radar techniques for achieving a large antenna by sparsity. (*Monostatic radar* has the transmitter antenna and receiver antenna at the same place while *bistatic radar* have the antennas geographically separated. Almost all radars operating today are monostatic. *MIMO* [*Multiple Input Multiple Output*] radar can select the transmitted signal in all small transmitter antennas individually.)

FOI has achieved results and conclusions for all the above mentioned research problems. To obtain the results, theoretic derivations, simulations and real measured data from experimental array antenna radars have been used. The summarizing conclusion is that it is possible to design and use array antennas in radar. This knowledge and experience can be used for many civilian and

military applications.

We now turn to the second research area of this thesis. By using micro-Doppler measurements a radar can see how internal parts of a target move. The goal of FOI's work is to use radar with such measurements for safety, security and military surveillance at short distances (up to a few hundred meters) with tasks such as detecting targets, classifying target type and target activity and distinguishing between target individuals, see Section 4.1.

Important advantages with a micro-Doppler radar for such surveillance are: the possibility to classify target type and activity by the internal movements of the target; the possibility to operate in very varied environments and under severe conditions, which is a general radar property; large surveillance area, also thanks to a general radar property; and privacy preserving because the human eye cannot see the identity of individual persons from micro-Doppler measurements.

At FOI, the research problems with micro-Doppler radar from 2008 until now have been: classification of target type; classification of target activity; extended target tracking of both target position and internal micro-Doppler parameters; detection of carried objects by humans; re-identification of the same human; coping with target variations and different environments; and being able to use different kinds of radars.

The main results of FOI's micro-Doppler research are: classification of target types (humans, animal and man-made objects) and of human gaits (walking, running, etc.); suggestion of two types of features for classification and two types of classifiers; the insight that detection of carried objects is very difficult; the likely existence of information in the micro-Doppler signatures for re-identification of the same human individual; the understanding that there is no use to track both target position and internal micro-Doppler parameters in the same filter [34], and the ability to use different kinds of radars for micro-Doppler measurements. FOI have conducted measurements with four different real radars, some of which together with Saab AB, and also used data from a fifth radar. The radars operate at different frequencies (9-16, 10, 24 and 77 GHz) and have different properties. Also a small test with simulated data has been made. See the report [34] for a summary, including scientific conclusions, of two main projects about micro-Doppler at FOI.

The conclusion of FOI's micro-Doppler radar results is that this radar type should be possible to use for safety, security and military surveillance at short distances.

The first part of this thesis is an introduction to the research areas addressed in it. Since the contributions of this thesis are within the two separate areas: 1) Radar with array antennas and 2) micro-Doppler radar, there will be introductions to these areas in Section 3 and 4, respectively. However, first there will be a general introduction to the basics of radar in Section 2. Section 5 is a summary of the publications included in the thesis. The second part of this thesis contains the included publications within the two areas.

2 Radar basics

2.1 Radar principles

As already said, *radar*, or *radar sensor*, is a technique for detecting objects and measuring their distance, direction, velocity and other properties with radio waves at a distance. Radio waves are electromagnetic waves, with wavelengths for radar usually between 100 m and 3 mm, corresponding to frequencies between 3 MHz and 100 GHz. The radar system emits a radio wave by a *transmitter antenna*. The wave is reflected (or "scattered") at a *radar target*, i.e. the object, and then received by the radar *receiver antenna*. Often the transmitter and receiver antennas are the same antenna. The principle is depicted in Figure 1. If a strong enough returning wave is observed, a target is considered to be *detected*. The radio wave is often called *radar signal* or just *signal*.

The distance (usually called *range* in radar), R, to the target is measured by the time delay between transmitted and received wave

$$R = \frac{c\tau}{2}, \tag{1}$$

where c is the velocity of light and τ is the time delay. SI units are used throughout this thesis. The radial velocity of the radar target can be measured

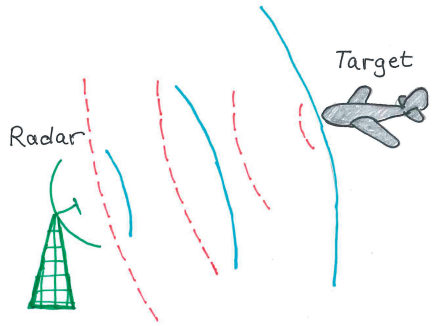

Figure 1: Principles of radar. A radio, i.e. electromagnetic, wave is scattered back from a target. The phase fronts of the outgoing wave are the solid (cyan) lines. The phase fronts of the back-scattered wave are the dashed (red) lines.

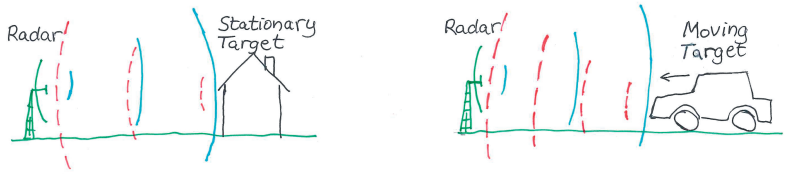

Figure 2: Principles of velocity measurement by the Doppler effect: Left: A stationary target. Right: A moving target. The moving target causes the wavelength of the reflected wave to decrease, and therefore the frequency to increase, giving a positive Doppler shift. The phase fronts of the outgoing wave are the solid (cyan) lines. The phase fronts of the back-scattered wave are the dashed (red) lines. The distance between the phase fronts of the back-scattered wave is smaller for the moving target due to the Doppler effect.

by the Doppler effect, which means that the wavelength, or equivalently the frequency, of the returned wave is changed when reflected at a target moving radially relative the radar. For example, the wavelength will become shorter, and the frequency higher, when the target is approaching the radar. Figure 2 illustrates this. The relation between the *Doppler frequency* f_d, which is the frequency deviation for the received wave from the transmitted wave, and the radial velocity is

$$f_d = \frac{2v_r}{\lambda}, \tag{2}$$

where v_r is the relative radial velocity between radar and target, with positive sign when they are approaching each other, and λ is the radar wavelength. Equation (2) is valid for low velocities ($v_r \ll c$). The non-radial target velocity can be measured by tracking the target in direction for some time.

The direction to, or *DOA* (*Direction of Arrival*) of, the radar target is measured by utilizing a direction dependent antenna. The antenna has different amplification, or *gain*, in different directions. It is *directive*. Usually it has a *main beam* with the largest gain and *sidelobes* and *backlobes* with much lower gain (Figure 3). Figure 4 illustrates the DOA measurement of a radar. Another common task for the radar is to determine the target type or identity, also called *target classification* or *target recognition*.

Besides the desired radar signal, i.e. the target reflection, the radar receiver senses undesired signals. All objects in the universe with a temperature above zero Kelvin will radiate random electromagnetic waves, called *thermal noise*.

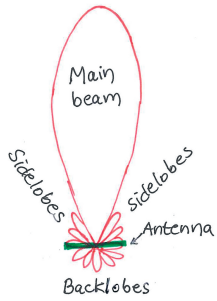

Figure 3: Illustration of the antenna gain in different directions with antenna main beam, sidelobes and backlobes.

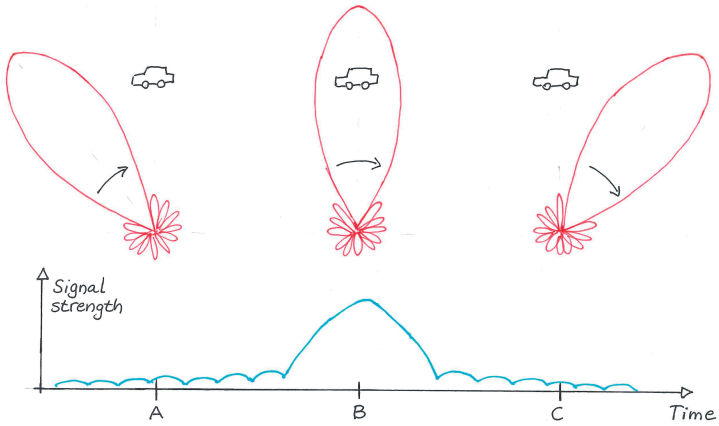

Figure 4: Principles of DOA (direction) measurement by a directive antenna. The antenna, which has the antenna gain in Figure 3, is rotating clockwise. The antenna beam is shown at three time instants A, B and C. Below the illustrations of the beam the received signal strength is shown as a function of time. The DOA of the target is estimated as the direction with the maximum signal strength, here at time B.

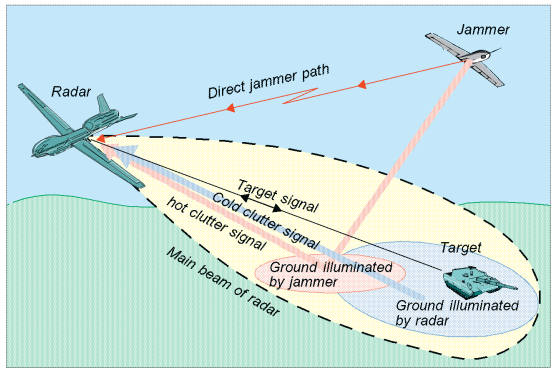

Figure 5: Radar target and interference scenario with UAVs and a ground vehicle.

The *receiver noise* is mainly internally generated thermal noise at the used radar frequencies. *External noise*, which is caused by external sources, such as the sun, the atmosphere and man-made equipment like computers and cars, is received by the radar antenna and can be a problem for some radar types. *Clutter* is disturbing reflected radar signals from ground or other uninteresting objects. What is clutter depends on the application. For example, when looking for aircraft with an air surveillance radar, the ground is clutter, but when looking for properties of the ground from a satellite-borne remote sensing radar, the ground is the "target". Another type of undesired signal is *jamming*, which are signals intentionally transmitted by an adversely to disturb the radar. Jamming can be *direct path jamming* or *scattered jamming*. The latter is often called *TSI* (*terrain scattered interference*), *terrain scattered jamming* or *hot clutter*. Also, non-intentional interference, such as broadcasting radio and TV signals, can disturb the radar. In this thesis all types of undesired signals, except the receiver noise, is called *interference*. See Figure 5 for an example scenario for a radar with different kinds of signals, both target signal and interference signals.

2.2 Radar applications

Radar has very diverse utility with many applications within civil, scientific, security and military areas. Some examples are:

- Surveillance of air, sea and ground traffic.

- Anti-collision warning for aircraft and ships.
- Navigation of ships.
- Automobile radar: driving aid and collision prevention and mitigation.
- Speed limit enforcement in road traffic.
- Weather radar.
- Distance (range) measurements, e.g. levels in tanks, altitude of aircraft, and industrial length measurements [35].
- Security surveillance within short distances.
- Remote sensing from aircraft or satellite from long distances to collect information about the earth surface for agriculture, forestry, environmental protection, humanitarian, scientific, military and other uses. Also remote sensing of other planets or moons like the Magellan mission to Venus [36].
- Military uses in fighter aircraft radars, missile radar seekers, fire control radars, etc.

2.3 Advantages and drawbacks with radar

Radar sensors have several advantages compared to electro-optical (EO) sensors, such as video and IR (infra-red) cameras. Here some advantages are listed. Radar:

- Can operate at day and night and in all weather. A radar can be much less affected by the weather than EO sensors.
- Can operate in dusty, dirty, hot, foggy and wet environments [35, 37].
- Can measure radial velocity very accurately.
- Can measure distance (range) directly. Can measure short distances (down to millimeters for industrial measurement radar [35]) or long distances (up to 4000 km for skywave OTH [Over-The-Horizon] radar [38] or even longer for space radar).
- Can have a large capacity: Can have a large surveillance area or volume capability. Can have a large field-of-view combined with seeing targets at long ranges.

- Is less vulnerable to combating in military and security applications, thanks to the long-range capability.
- Can be installed concealed behind a covering surface.
- Is less affected by human clothing choices and is human privacy preserving in security applications.

Radar sensors also have some drawbacks. Radar:

- Often has low cross range (perpendicular to line-of-sight) resolution compared to EO sensors. An exception is satellite based radar for remote sensing of the earth surface, where Synthetic Aperture Radar (SAR) and EO sensors have comparable resolution.
- Has not in general yet reached so far as EO sensors in reducing size, weight, power consumption and cost. For some types of EO sensors this reduction has been possible thanks to a large civil employment. However, the civil employment of radar sensors is increasing. Another reason for this reduction for EO sensors is the shorter wavelength in EO sensors which gives a high resolution for free, while radar sensors need to utilize the signal to the outermost.
- Delivers output which looks different than what the human eye is accustomed to. This can be an impediment to humans.

2.4 Radar signal processing

2.4.1 Structure of transmitted and received signals

The transmitted radar signal is usually pulsed with a certain *PRF* (*Pulse Repetition Frequency*), see Figure 6, left. The time between the pulses is called the *PRI* (*Pulse Repetition Interval*). PRI can also be a synonym to the term "radar pulse", see Figure 6. The pulses have some kind of *pulse modulation*, which can be amplitude, frequency and phase modulation. The received radar signal (Figure 6, right) is sampled in time. The samples in the interval between the start of two pulses, i.e. within the same PRI, correspond to different time delays of the transmitted pulse and therefore to different target ranges. These samples are also called *range bins* and the sampling is called *range-bin-to-range-bin* sampling. Since this sampling is the fastest time sampling, it is

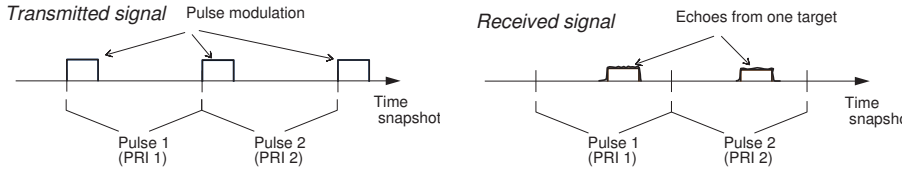

Figure 6: Left: Transmitted radar pulses. Right: Received radar pulses.

also called *fast-time* sampling. The same time-sample within the PRIs but for different pulses or PRIs are called different *radar pulses* (or PRIs). Since this sampling is slower than range-bin-to-range-bin sampling, it is called called *slow-time* sampling.

If a single antenna is replaced by several smaller antennas, called *antenna elements*, an *array antenna* is obtained. The antenna elements themselves may be directive but by summing the received signals from the elements the array antenna will become more directive than the elements. The summing, called *beamforming*, can be done before or after the ADC (Analog to Digital Converter) giving an *analog* or *digital array antenna*. It is also possible to perform part of the summation before the ADC and part after the ADC by analogously summing groups of antenna element, called (analog) *subarrays*, then digitize the sum signals, and finally sum the digital signals. The digital signals from the antenna elements, if all antenna element signals are digitized, or the digital signals from analog subarrays are called *antenna channels*.

The antenna elements of an array antenna can be positioned in different ways. They can be placed on a line, giving a *linear antenna*. A *ULA* (*Uniform Linear Array*) is a common special case where the identical elements are placed equidistantly on a line. A *planar antenna* is an array antenna with all elements on a plane. A *conformal antenna* is an array antenna with its elements on a bent surface, often the outer surface of the radar platform. An array antenna can be seen as sampling the receiving radio wave at different positions in space. This is also called *space* sampling. Some examples of array antennas are shown in Figure 9 (planar and linear array), 11 (linear array), 12 (planar array) and 13 (linear array). Figure 16 shows two conformal antennas, which have been designed and built by FOI.

The samples in fast-time, slow-time and space can be arranged in a *radar data cube* with samples from each of the three types of sampling in a separate

Figure 7: Left: The radar data cube. Right: space-slow-time and space-fast-time 2D snapshots as slices of the radar data cube.

dimension. See Figure 7, left. We then also talk about the fast-time, slow-time and space dimensions of the received radar signal.

2.4.2 Processing of the received signals

The traditional processing of the received radar signal can be divided in a linear processing part and a non-linear processing part, see Figure 8. The task for the linear processing is to change to a more revealing signal domain and to enhance the target signal while suppressing interference. While suppressing noise and interference, there are two ratios: the *Signal to Noise Ratio* (*SNR*), if there is no interference except receiver noise, or the *Signal to Interference plus Noise Ratio* (*SINR*), if both receiver noise and external interference is present. If SNR or SINR is increased, it will facilitate the target detection and parameter estimation in the non-linear processing. The change of signal domain is usually from fast-time samples (time in the same PRI) to range bins, by linear filtering called *pulse compression*; from slow-time samples (radar pulses) to Doppler channels, by *Doppler filtering*; and from antenna channels to antenna beams or DOAs, by beamforming. See Figure 7, left and Figure 8. This filtering can be performed in one of the mentioned dimensions at a time or in two or all three dimensions simultaneously. Then 1D, 2D or 3D snapshots are extracted from the radar data cube and used in the processing, see Figure 7, right. The three new signal domains (range, Doppler and antenna beam/DOA) are better suited for the target detection and the target parameter estimation. In the linear processing, the order of the processing can be changed and processing of the same type can be cascaded, which is indicated by the possible loop in Figure 8.

The traditional non-linear processing (Figure 8) has several tasks. First, the target must be detected. A more developed form of detection is to estimate the number of targets or signal sources. Then, target parameters should be

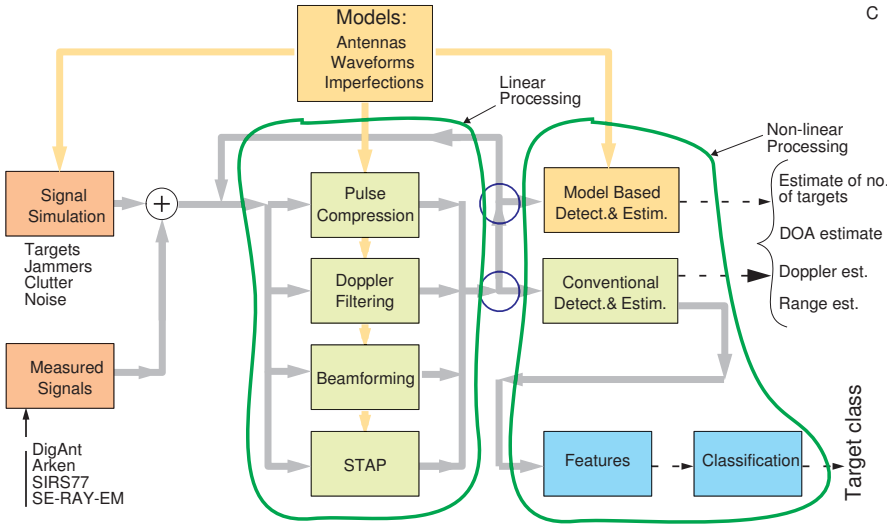

Figure 8: Block diagram of traditional radar signal processing.
One radar data cube is processed at a time. The gray wide solid lines show where the data cube can travel in the diagram. At a fork symbol  , where the line branches out in two lines, the data cube will proceed in exactly one direction. This means that the data cube only goes through one of the linear processing blocks at a time. With the copy symbol  the data cube can either proceed in one of the branches or a copy of the same data cube can proceed in each of the branches. In the summation symbol ⊕, two data cubes can be added together, e.g. measured target signal added to simulated noise. Before the "Features" and "Classification" blocks, a suitable part of the data cube is cut out in the "Conventional Detect. & Estim" block. Compare with Figure 28. The models consist of steering vectors, covariance matrices, covariance matrix tapers [39] and parameter structures.

estimated, of which the basic parameters are range, DOA and radial velocity. A more higher-level parameter is the target type or identity which is the task of the target classification. The estimated parameters is then usually fed to a *target tracker* which creates target tracks. The *target tracking* and subsequent processing in radar is traditionally called *data processing* and is not shown in Figure 8. (Non-linear means as usual that an operation $\mathcal{H}$ does not fulfill the linearity condition: $\mathcal{H}(\alpha\mathbf{x}+\beta\mathbf{y}) = \alpha\mathcal{H}(\mathbf{x})+\beta\mathcal{H}(\mathbf{y})$, where α and β are arbitrary scalars and $\mathbf{x}$ and $\mathbf{y}$ are arbitrary input signals).

There is another, non-traditional, approach to detection and tracking, called *Track Before Detect* (TkBD or TBD), which is still not used much in radar. TkBD means merging the detection, estimation and tracking into a single operation. Then the tracker works on the whole, non-detected, radar signal and tracks both the target parameters and the presence of the target. The main advantage is the possible detection and tracking at lower SNR. The main drawback is the high computation complexity. See [40, 41, 42] for more on this approach.

A Matlab [43] and Octave [44] software toolbox, called DBT and mainly developed by the author of this thesis, contains linear and nonlinear signal processing according to Figure 8 and also signal simulation, import of measured signals, and modeling of radar antennas & waveforms and of imperfections [15, 45]. A limited version of DBT is available for download at Blekinge Institute of Technology [46].

3 Radar with array antennas

We will now concentrate on radar with array antennas, the first research area of this thesis.

3.1 Some applications

Here we give some examples of applications of radar with array antennas. Figure 9 shows the dutch frigate Tromp of the De Zeven Provinciën class, which possesses two main array antenna radars. The large fore radar, called APAR (Active Phased Array Radar), has four fixed planar antenna arrays. It is a multifunction radar with array beamforming horizontally and vertically (probably) and the following capabilities: air and sea target tracking, horizon search, limited volume search, surface naval gunfire support, guidance of semi-active radar homing missiles and Electronic Counter-Countermeasures (ECCM) [47]. The large aft radar, called SMART-L (Signaal Multibeam Acquisition Radar for Tracking, L band) is a long range volume search radar and has a vertical linear array antenna. The antenna has array beamforming vertically and is rotating horizontally. Figure 10 is an illustration of a multifunction naval radar using the simulation software SADM [48] and the visualization software SIMDIS [49].

The Swedish AEW&C (Airborne Early Warning & Control) radar PS-890 on top a Saab 340 AEW&C aircraft is shown in Figure 11. An AEW&C system has the task to search for and detect aircraft and ships at long distances (ranges) and direct fighter and attack aircraft [51]. The PS-890 is operating at 3 GHz and has a 192 element linear array antenna with horizontal array beamforming [52].

In Figure 12, a mock-up of the antenna of the radar EuroRADAR CAPTOR-E for the fighter aircraft Eurofighter Typhoon is depicted. CAPTOR-E is under development and is a radar with a planar array antenna with 1300 to 1500 antenna elements. It will enhance the older version of the Eurofighter radar and perform task such as detection, tracking and recognition/classification of air targets, also with clutter and jamming background; detection and locating slow moving ground targets; imaging of the earth surface with automatic target detection and classification; and noise jamming [54] .

Radar with array antennas is also increasingly finding civilian applications. For example, such radars are used as weather radar for “early warning detection of severe impending weather” [56], simultaneous air traffic control and weather

Figure 9: Left: The frigate HNLMS Tromp (F803) of the Royal Netherlands Navy with the APAR and the SMART-L radars. Middle: The APAR Naval radar with two of the four fixed planar antenna apertures visible. Right: The SMART-L radar. The rotating antenna is the dark rectangle. It is a vertically steerable array. All three photos: Royal Netherlands Navy / Koninklijke Marine [50].

tracking [56], security surveillance of "critical infrastructures" and "integrity sensitive areas" [57], "obstacle detection and collision avoidance systems in mobile industrial, farming and forestry equipment" [57] and automotive driver assistance systems [58].

For research purposes a horizontal linear digital array with 12 digital channels, called DigAnt, was designed and built by FOA (today FOI) and Ericsson Microwave Systems (today Saab Electronic Defence Systems) during the 1990s [59, 60]. See Figure 13 and 14. It has been used at FOI for research on antennas, microwave electronics, calibration, DOA estimation, direct jammer suppression, scattered jamming, radar processing and bistatic radar. Several of the publications in this thesis use measured data from the DigAnt.

At FOI we have the last years concentrated our radar antenna and microwave electronics research to radars on small airborne radar platforms, such as small UAVs (Unmanned Aerial Vehicles, Figure 15), with conformal antennas (Figure 16), among other because these give a difficult radar design problem. The requirements on space, weight and power consumption are higher than for, for example, naval radar and ground based radar, and this necessitates new hardware technologies, such as RF-MEMS (Radio Frequency MicroElectroMe-

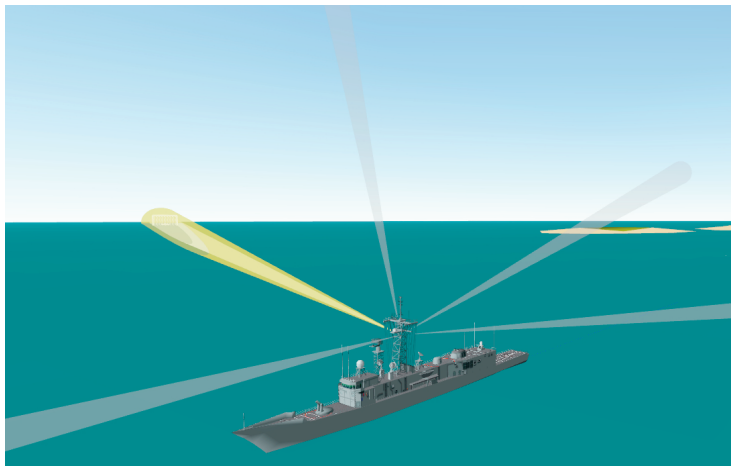

Figure 10: Multifunction radar on a naval ship. Five simultaneous beams are shown, one yellow (direction 10 o'clock) and four gray. The gray beams are search beams searching for different types of target and at different elevations and ranges. The yellow beam is tracking a target. Simulation by SADM [48] and visualization by SIMDIS [49].

chanical Systems) [65]. A moving radar, such as an airborne radar, also gives larger problems with interference than a stationary radar, because the clutter has a wider Doppler bandwidth and TSI appears as a larger number of jammers.

The work on array antenna radar which is covered by this thesis is described in Section 5.

3.2 Radar signal model

In this section we will show a standard mathematical model of the received radar signal from different kinds of sources, valid for both targets and interference. This model is commonly used in the signal processing of these signals. We denote scalar quantities with italic non-bold font, vectors with lower-case upright bold font (not upright for Greek letters) and matrices with upper-case upright bold font.

The radar array signal processing in this thesis emanates from the following standard signal model. The received space (antenna channels), slow-time

Figure 11: The Swedish Airborne Early Warning radar PS-890 with the array antenna on top of the aircraft fuselage at the Swedish Armed Forces' Airshow 2010. The linear array antenna is the box on the back of the aircraft. Photo by "Gnolam" [53].

Figure 12: Left: Mock-up of the array antenna of the fighter radar CAPTOR-E of a Eurofighter Typhoon without nose. Right: Close up on the array antenna, which is a planar array. Photo by "Bin im Garten". Modified by "MagentaGreen". Source: [55].

Figure 13: The FOI DigAnt receiving array antenna [59, 60] in an anechoic chamber. The digital array is linear in the horizontal direction with 12 digital channels. It was designed and built by FOA (FOI) and Ericsson Microwave Systems (Saab Electronic Defence Systems). This antenna is used in Publication 1 (reference [3]), 2 (reference [4]) and 4 (reference [6]) and in [27, 28, 29, 59, 60, 61, 62, 63, 64]. Photo by FOI.

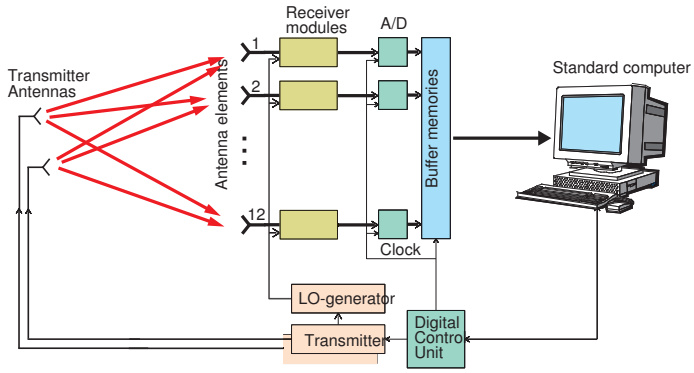

Figure 14: Block diagram of the FOI DigAnt receiving array antenna in Figure 13. Image by Lars Pettersson, Per Grahn and Svante Björklund.

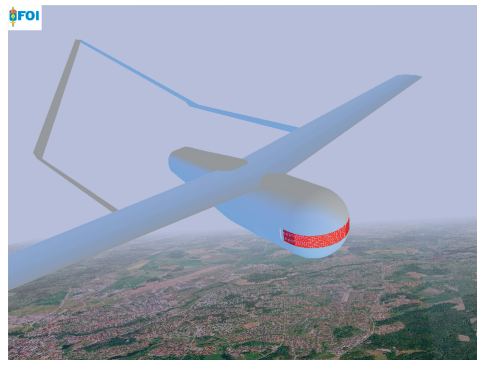

Figure 15: The FOI experimental conformal array antenna mounted on a UAV. Image from [66], also present in in [7, 19]. Image by Roland Erickson.

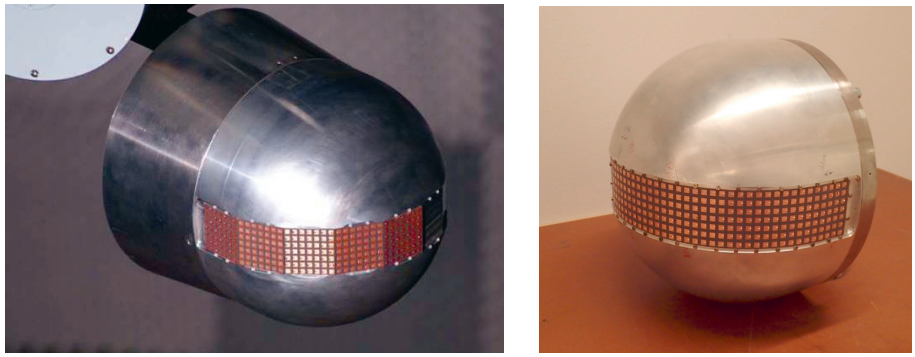

Figure 16: Experimental conformal antennas on a half-cylinder (diameter 30 cm) for 16-18 GHz, designed and built by FOI. Both antennas have 35 x 7 antenna elements. Left: Planar facets. Photo from [66]. Also present in [7, 19]. Right: Smoothly bent aperture. Photo Svante Björklund.

(radar pulses) and fast-time (target range) signal $\mathbf{x}_\mathrm{s}$ from K_s point sources, which is a complex baseband signal, can be written

$$\mathbf{x}_\mathrm{s} = \sum_{k=1}^{K_\mathrm{s}} \alpha_k \mathbf{v}(\boldsymbol{\theta}_k, f_{dk}, \bar{r}_k), \tag{3}$$

where α_k is the amplitude of the k^{th} point source, and $\boldsymbol{\theta}_k$ is the DOA (Direction Of Arrival), f_{dk} is the Doppler frequency and $\bar{r}_k$ is the range to this point source. The DOA $\boldsymbol{\theta}_k$ can be either a single angle or a vector of two angles, e.g. azimuth and elevation angles. The received signal is the signal after the antenna elements, analog antenna subarrays (if any), analog receiving electronics such as amplifiers, filters and mixers and after analog to digital conversion (ADC). The inevitable receiver noise is not included in the model $\mathbf{x}_\mathrm{s}$ in (3). A *point source* can be a point target, one of a collection of scattering points of a composite target, a direct path jammer, scattering points of scattered jamming, scattering points of clutter; or some other interference source. See also Section 2.1 about different kinds of interference. The complex amplitude α_k of the source can be either deterministic or random. The number of "independent" point sources is called the *signal rank*. The vector $\mathbf{v}(\boldsymbol{\theta}_k, f_{dk}, \bar{r}_k)$ is the *steering vector*, which is a model of the received radar signal from a point source at a certain DOA, Doppler frequency and range. Remember, DOA (direction), Doppler frequency and range are the three dimensions of the radar data cube (Figure 7).

If the three dimensions of the data cube are independent of each other, which is a common assumption, the steering vector can be separated into

$$\mathbf{v}(\boldsymbol{\theta}, f_d, \bar{r}) = \mathbf{c}(\bar{r}) \otimes \mathbf{b}(f_d) \otimes \mathbf{a}(\boldsymbol{\theta}), \tag{4}$$

where $\mathbf{a}(\boldsymbol{\theta})$ is the spatial (antenna channels/DOA) steering vector, $\mathbf{b}(f_d)$ slow-time (radar pulses/Doppler) steering vector, $\mathbf{c}(\bar{r})$ is the fast-time (range) steering vector and $\otimes$ denotes the Kronecker product [67].

Depending on the type of interference to handle and what processing to perform, one or two of the three signal dimensions in (3) and (4) can be omitted. Compare with the 1D, 2D and 3D snapshots in Figure 7 and in Section 2.4.2 and see later in Section 3.3.2 - 3.3.4 for examples.

Now, we give examples of some steering vectors. A fast-time steering vector $\mathbf{c}(\bar{r})$ has the same number of elements as the number of (fast-time) samples within a PRI and contains the pulse modulation, time delayed to the range of

the point source. A standard slow-time steering vector for regular sampling in slow-time is

$$\mathbf{b}(f_d) = [e^{j2\pi f_d T_R \cdot 0}, \ldots, e^{j2\pi f_d T_R \cdot (M-1)}]^T, \tag{5}$$

where f_d is the Doppler frequency, $T_R = 1/\text{PRF}$ is the PRI, M is the number of radar pulses. $\mathbf{A}^T$ denotes the transpose of a matrix (or vector) $\mathbf{A}$.

The spatial steering vector for a ULA with isotropic (see below) antenna elements is

$$\mathbf{a}(\theta) = [e^{-j\frac{2\pi}{\lambda}d \cdot 0 \cdot \sin\theta}, \ldots, e^{-j\frac{2\pi}{\lambda}d \cdot (N-1) \cdot \sin\theta}]^T, \tag{6}$$

where θ is the single-angle DOA (Figure 17), d is the inter-element distance, λ is the radar wavelength and N is the number of antenna elements. An *isotropic* antenna element has the same radiation in all directions, which is not physically possible but an often used model. Equation (6) can be understood by studying Figure 17. Narrowband signals and far-field conditions are assumed. *Narrowband* means that the bandwidth of the pulse modulation is much smaller than the carrier frequency. For us, this has the implication that the different propagation times of the radio wave to the antenna elements can be treated as phase shifts. For us, *far-field* means that a point source is so far away from the antenna that the radio wave from the source is a plane wave over the antenna.

The steering vector for a more general antenna (arbitrary antenna element positions and arbitrary antenna element patterns) can be expressed as

$$\mathbf{a}(\mathbf{k}) = [g_0(\mathbf{k})e^{j\mathbf{k}^T\mathbf{r}_1}, \ldots, g_{N-1}(\mathbf{k})e^{j\mathbf{k}^T\mathbf{r}_N}]^T \tag{7}$$

with $\mathbf{k} = \frac{2\pi}{\lambda}\hat{\mathbf{k}}$, and where $g_n(\mathbf{k}) = g_n(\hat{\mathbf{k}})$ is the antenna pattern for the n^{th} antenna element and $\mathbf{r}_n$ is the position of the same element, and $\hat{\mathbf{k}} = \hat{\mathbf{k}}(\boldsymbol{\theta})$ is the direction vector of the impinging wave. Still, narrowband signals and far-field conditions are assumed. The "direction of an impinging wave" is a vector in the 3D space and the corresponding DOA $\boldsymbol{\theta}$ is a parametrization of this direction with one or two angles. See Figure 17 for an example.

The steering vector $\mathbf{a}(\boldsymbol{\theta})$ can include the effects of subarrays. Signal processing for radar with subarrays are addressed in [33, 68].

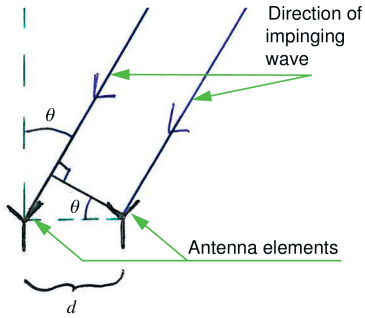

Figure 17: Antenna geometry for a ULA. The angle θ is the DOA. The antenna element separation is d. The two arrows from the upper right corner of the illustration towards the lower left corner is the direction of the impinging radio wave.

The total received radar signal $\mathbf{x}$ from a target (a point target or a collection of scattering points), interference and noise is

$$\mathbf{x} = \mathbf{x}_{\mathrm{t}} + \mathbf{x}_{\mathrm{c}} + \mathbf{x}_{\mathrm{j}} + \mathbf{x}_{\mathrm{tsi}} + \mathbf{n}, \tag{8}$$

where $\mathbf{x}_{\mathrm{t}}$, $\mathbf{x}_{\mathrm{c}}$, $\mathbf{x}_{\mathrm{j}}$ and $\mathbf{x}_{\mathrm{tsi}}$ are the received radar signals from the radar target, from clutter, direct path jamming and TSI, respectively, and $\mathbf{n}$ is the receiver noise. Each of the signals $\mathbf{x}_{\mathrm{t}}$, $\mathbf{x}_{\mathrm{c}}$, $\mathbf{x}_{\mathrm{j}}$ and $\mathbf{x}_{\mathrm{tsi}}$ can be modeled by (3). The receiver noise is often modeled as white Gaussian noise in the used radar dimensions. See Section 3.3.2 - 3.3.4 for more on different kinds of interference.

3.3 Detection of moving targets in interference

Target detection and interference suppression is a compound problem. In order to detect the target, the interference must be suppressed sufficiently. In Section 3.3.1 we show the basic interference suppression filter. In Section 3.3.2 - 3.3.4 we describe frequent interference, namely direct path jamming, clutter and TSI.

3.3.1 Interference suppression and target detection

Suppression of interference in radar is usually performed with linear *FIR* (*Finite Impulse Response*) filters. The FIR filter is

$$y = \mathbf{w}^H \mathbf{x}, \tag{9}$$

where $\mathbf{x}$ is a snapshot of the received radar signal. The number of coefficients (minus one) in the weight vector $\mathbf{w}$ we call the *DoF* (*Degrees of Freedom*). Usually, the filter weights are computed as [69, 70, 71, 72]

$$\mathbf{w}_{\text{opt}} = \eta \mathbf{R}_i^{-1} \mathbf{w}_0, \tag{10}$$

where η is a scalar, but not necessarily a constant, which can be chosen in different ways [one example is given by (21)], $\mathbf{R}_i = \mathrm{E}\{\mathbf{x}_i \mathbf{x}_i^H\}$ is the covariance matrix of the interference plus noise $\mathbf{x}_i$ and $\mathbf{w}_0$ is a vector which depends on the DOA, Doppler frequency and/or range to investigate, often an adjusted version of the steering vector $\mathbf{v}(\boldsymbol{\theta}, f_d, \bar{r})$.

The filter (9) - (10) is optimal under several criteria, namely Maximum Likelihood, Maximum SNR (or SINR) and Linearly constrained minimum noise power for some usual assumptions [72].

The filter (9) - (10) is commonly called "adaptive beamforming" for space-only snapshots (see Section 3.3.2) and *STAP* (*Space Time Adaptive Processing*) for space-time snapshots (see Section 3.3.3). We call (9) - (10) with known covariance matrix the *optimal* filter and we say *optimal beamforming* and *optimal STAP*.

The same filter structure is employed for suppression of direct path jamming, clutter and TSI but with different choices of which radar signal dimensions (space, slow-time and fast-time) to include in the filter. For example, for suppression of direct path jamming, usually the filter (9) - (10) with space-only signals is suggested [73, 74].

An early form of surface clutter suppression in moving radar was to try total cancellation of the clutter signal with no thought of the target signal [75]. This objective led to *DPCA* (*Displaced Phase Center Antenna*) [69, 70, 75, 76, 77]. DPCA is a special case of the interference suppression filter (9) - (10) but it can only be used for suppression of clutter, not other interference. Another objective is maximizing the Signal to Interference plus Noise Ratio (SINR) [69, 70]. This led to Space-Time Adaptive Processing (STAP) (fully adaptive, reduced dimension and reduced rank [69, 78]), which resulted in the filter (9) - (10) with the scalar η an constant. Finally, by maximizing detection probability while holding a constant probability of false detection

[79, 80], CFAR (Constant False Alarm Ratio) detection filters like Kelly's [81] and AMF (Adaptive Matched Filter) [82] were the result. These are also the filter (9) - (10) but with the scalar η not constant and chosen in certain ways.

Normally $\mathbf{R}_i$ is unknown and must be estimated. A common estimate is [70, 83]

$$\hat{\mathbf{R}}_i = \frac{1}{L}\sum_{l=1}^{L} \mathbf{x}_{i_l}\mathbf{x}_{i_l}^H, \tag{11}$$

where $\mathbf{x}_{i_l}$ is a received interference plus noise snapshot. The number of training snapshots is L. The estimation of $\hat{\mathbf{R}}_i$ is the main problem for STAP in radar. The reason for this is that the, usually many, elements in the received radar signal vector $\mathbf{x}$ require many training snapshots $\mathbf{x}_{i_l}$ of good quality for a good estimate of $\hat{\mathbf{R}}_i$ and the number of good training snapshots usually is very limited. We call (9) - (10) with estimated covariance matrix the *adaptive* filter and we say *adaptive beamforming* and *adaptive STAP*.

For effective interference suppression the DoFs of the filter (9) - (10) must be larger than the interference (signal) rank and the number of training snapshots for estimation of $\hat{\mathbf{R}}_i$ must be sufficiently large compared to the rank and the DoF. For this reason the rank must be known or estimated. This is in principle the same problem as estimation of the number signal sources in DOA estimation (Section 3.4).

The target detection is performed by comparing the output y of filter (9) - (10) with a threshold. If y is larger than the threshold, the detection of a supposed target is declared. Before the supposed target is regarded as a confirmed target, usually several supposed target detections are required.

3.3.2 Direct path jamming

Direct path jamming is performed via the line-of-sight radio wave from a jammer to the radar. It is concentrated to a single DOA, the same DOA for all radar pulses (PRIs) and range bins of the radar. The jammer waveform can be either random noise or a deterministic waveform. The objective of the jammer is either to drown the radar with disturbance so that the target detection and parameter estimation fails, or to deceive the radar regarding the target parameters, e.g. the target position and velocity. For suppression of direct path

jamming, usually space-only adaptive filtering is used, i.e. adaptive beamforming. The signal model of the received signal from of K_s point sources in space-only, which is a special case of (3), is

$$\mathbf{x}_{\mathrm{s}_{pr}} = \sum_{k=1}^{K_\mathrm{s}} \alpha_{kpr} \mathbf{v}(\boldsymbol{\theta}_{kpr}), \tag{12}$$

where p is the index for radar pulse/slow-time, r is the index for range bin/fast-time, α_{kpr} is an either deterministic or random scalar and $\mathbf{v}(\boldsymbol{\theta}_{kpr}) = \mathbf{a}(\boldsymbol{\theta}_{kpr})$ is the spatial steering vector for the k^{th} point source, the p^{th} radar pulse and the r^{th} range bin. Both the target signal $\mathbf{x}_\mathrm{t}$ and the jammer signal $\mathbf{x}_\mathrm{j}$ use this model, with different choices of α_{kpr}, $\boldsymbol{\theta}_{kpr}$ and K_s. The subscript "s" of $\mathbf{x}_{\mathrm{s}_{pr}}$ in (12) can be replaced by the subscripts "t" and "j" to give the signal models for the target and the jammer, respectively.

3.3.3 Clutter

Clutter are undesired reflected signals from the radar transmission, as mentioned in Section 2.1. Clutter is also called *cold clutter* to distinguish it from hot clutter (Section 3.3.4). The clutter we are concerned with are reflections on the ground or sea, i.e. the earth's surface. When the target is moving and the radar is not, there is the possibility to distinguish the target from the ground by different Doppler frequencies, hence by Doppler filtering, which is a 1D filtering. However, if the radar is also moving, this is not sufficient, since the radar movement and the sidelobes and backlobes of the radar antenna can generate clutter signals within a wide Doppler region. There is a relation between the DOA and the Doppler frequency of the clutter:

$$f_d = \frac{2v_\mathrm{p}}{\lambda} \cos\alpha. \tag{13}$$

See Figure 18 for v_p and α and compare with (2). In the DOA-Doppler dimensions, the clutter will be confined to narrow ridges, see Figure 19 for an example. This figure shows that space-only processing, i.e. adaptive beamforming, would suppress both the clutter and the target since the target appears in the clutter main beam. It also shows that a weak target will be hidden by Doppler sidelobes. Therefore slow-time-only processing, i.e. Doppler filtering, or space-only processing, i.e. beamforming, would be ineffective. However, it can be seen that if the filtering (9) - (10) can be conducted simultaneously in

the space and slow-time dimensions, the target is free from clutter. This is an effective way to suppress clutter in moving radar. It can be noted that direct path jamming can also be suppressed with the same filter.

For the clutter suppression problem the following signal model is appropriate. The signal model of a received space (antenna channels) and slow-time (radar pulses) signal $\mathbf{x}_{\mathrm{s}_r}$, from K_{s} point sources for a single range bin r, is

$$\mathbf{x}_{\mathrm{s}_r} = \sum_{k=1}^{K_{\mathrm{s}}} \alpha_{kr} \mathbf{v}(\boldsymbol{\theta}_{kr}, f_{dkr}), \tag{14}$$

where $\boldsymbol{\theta}_{kr}$ is the DOA, f_{dkr} is the Doppler frequency and α_{kr} is the amplitude of the k^{th} point source at the r^{th} range bin. Both the target signal $\mathbf{x}_{\mathrm{t}}$ and the clutter signal $\mathbf{x}_{\mathrm{c}}$ use this model, with different choices of α_{kr}, $\boldsymbol{\theta}_{kr}$, $f_{dkr}$and K_{s}. The subscript "s" of $\mathbf{x}_{\mathrm{s}_r}$ in (14) can be replaced by the subscripts "t" and "c" to give the signal models for the target and the clutter, respectively. The space slow-time steering vector is $\mathbf{v}(\boldsymbol{\theta}, f_d) = \mathbf{b}(f_d) \otimes \mathbf{a}(\boldsymbol{\theta})$. The model (14) is also a special case of the general model (3).

There exist very much research literature about STAP for suppression of clutter. Introductions to the subject are given by [69, 70, 72, 85, 86].

3.3.4 Terrain scattered interference

In Section (2.1) it was mentioned about TSI, also called *terrain scattered jamming* or *hot clutter*. TSI is the disturbing signals from a jammer which are arriving at a radar after being reflected on the ground or sea. The reflected waves which are impinging on the radar receiver antenna have different DOAs and different time-delays of the jammer waveform. See Figure 20 for an illustration of this and Figure 21 for measured TSI signals with the FOI DigAnt antenna (Figure 13). The relation between the space and fast-time dimensions makes it natural to try suppression of the TSI in these dimensions.

The signal model for point sources in space and fast-time, a special case of (3), is

$$\mathbf{x}_{\mathrm{s}_p} = \sum_{k=1}^{K_{\mathrm{s}}} \alpha_{kp} \mathbf{v}(\boldsymbol{\theta}_{kp}, \bar{r}_{kp}). \tag{15}$$

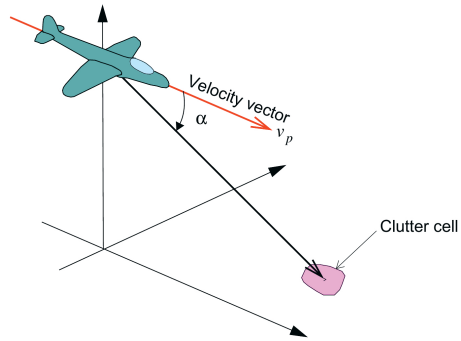

Figure 18: Geometry of airborne radar and surface clutter. The angle α is the angle between the radar platform velocity vector $\mathbf{v}_p$ and the direction to a ground patch. The platform velocity is $v_p = |\mathbf{v}_p|$. Modified figure from [84].

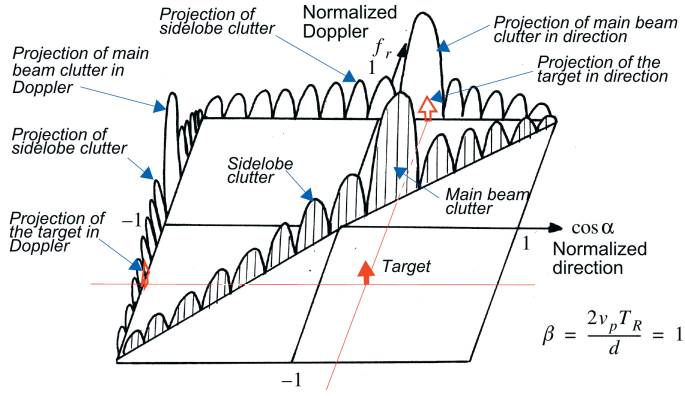

Figure 19: DOA Doppler clutter spectrum with clutter ridge for side-looking, i.e. antenna line parallel to the radar platform velocity vector, ULA. A target is present. The DOA α is defined in Figure 18. The normalized Doppler frequency is $f_r = 2f_d/f_{\mathrm{PRF}}$, where f_{PRF} is the PRF. The platform velocity is $v_p = |\mathbf{v}_p|$ (Figure 18). Modified figure from [84].

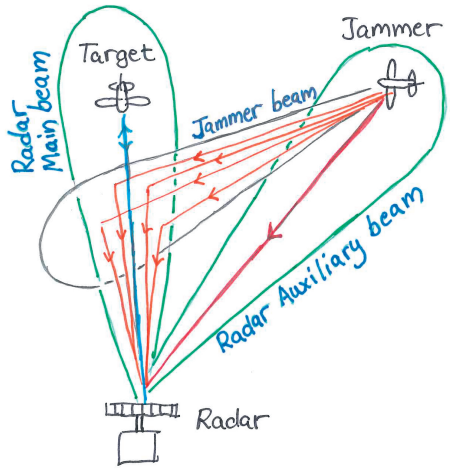

Figure 20: Illustration of TSI. The (red) cracked and bent lines from jammer to radar are the TSI. The (red) single-arrow line from jammer to radar is direct path jamming and the (blue) line with a double arrow between the target and the radar is the target signal.

The space fast-time steering vector is $\mathbf{v}(\boldsymbol{\theta}_{kp}, \bar{r}_{kp}) = \mathbf{c}(\bar{r}) \otimes \mathbf{b}(f_d)$. Both the target signal $\mathbf{x}_{\mathrm{t}}$ and the TSI signal $\mathbf{x}_{\mathrm{tsi}}$ use this model, with different choices of α_{kp}, $\boldsymbol{\theta}_{kp}$, $\bar{r}_{kp}$and K_{s}, when suppressing the TSI in the space-fast-time dimensions. The subscript "s" of $\mathbf{x}_{\mathrm{s}_p}$ in (15) can be replaced by the subscripts "t" and "tsi" to give the signal models for the target and the TSI, respectively.

There is very little written about TSI in the open literature.

3.4 High resolution direction of arrival estimation

We now turn to a different problem than target detection and interference suppression, namely estimation of the direction to, or DOA (Direction Of Arrival) of, the target. We will call it High Resolution DOA Estimation (HRDE) because the methods can achieve a higher resolution than (conventional) beamforming (Section 2.4.1). HRDE especially for radar has been treated in [33].

The signal model for K_{s} point sources is the same as (12) for direct path jamming. We change the term p (index for the radar pulse) to t (time index), omit the index r for the range, skip the subscript "s" and include the receiver

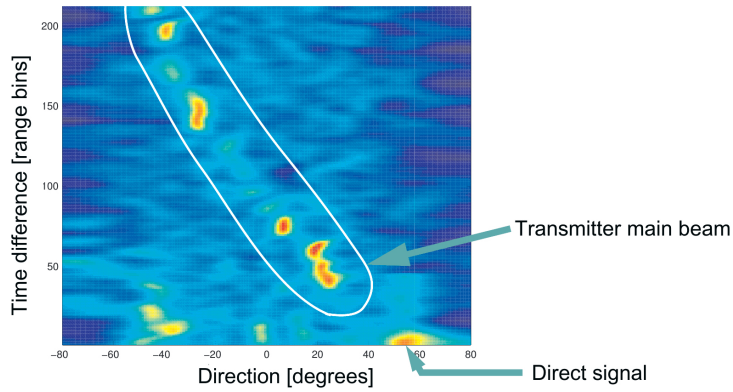

Figure 21: Measured TSI, i.e. bistatic ground reflections in a time-difference–direction coordinate system. Horizontal axis is DOA in degrees. Vertical axis is the time-difference between the direct path signal and the TSI, expressed as number of range bins of the radar. The airborne transmitter was located at a distance of 50-60 km and at an altitude of 4000 m. The receiver was the FOI DigAnt (Figure 13). The diagonal stripe of reflections are created by the transmitter main beam. Image originally by Per Grahn in [87]; then annotated by Svante Björklund.

noise in the model. Then the used model of the received antenna signals for the r^{th} range bin is the common one in the DOA estimation literature:

$$\mathbf{x}(t) = \sum_{k=1}^{K_\text{s}} \alpha_k(t)\mathbf{a}(\boldsymbol{\theta}_k) + \mathbf{n}(t) = \mathbf{A}(\boldsymbol{\theta})\mathbf{s}(t) + \mathbf{n}(t) \tag{16}$$

where $\mathbf{A}(\boldsymbol{\theta}) = [\mathbf{a}(\boldsymbol{\theta}_1), \ldots, \mathbf{a}(\boldsymbol{\theta}_{K_s})]$ is called the *steering matrix*, $\mathbf{s}(t) = [\alpha_1(t), \ldots, \alpha_{K_s}(t)]^T$ are the source signals and $\mathbf{n}(t) = [n_1(t), \ldots, n_N(t)]$ is the receiver noise. The number of antenna channels is N. This signal model is thus a special case of the general model (3) [and (8) including the noise] for space-only signals with $\mathbf{x}_\text{c} = 0$, $\mathbf{x}_\text{j} = 0$, $\mathbf{x}_\text{tsi} = 0$.

DOA estimation methods can be divided into two different types: spectral methods and parametric methods. *Spectral DOA estimation* methods primarily deliver a real and scalar valued function $P(\boldsymbol{\theta})$, a *DOA spectrum*, of one or two variables, which are the angles which define the DOA $\boldsymbol{\theta}$. This spectrum should have peaks at the DOAs of the sources and is often plotted, see for

example Figure 12 and 16-17 in Publication 1 and Figure 10a in Publication 4 (included later in this thesis). The DOAs are then found by an 1D or 2D search for the peaks. The most well-known spectral method is *MUSIC* (MUltiple SIgnal Classification)[88, 89]. Figure 15-17 in Publication 1 and Figure 5 in Publication 2 use MUSIC. *Parametric DOA estimation* methods directly deliver the estimated DOAs and other parameters of the sources as a finite number of parameters. These parameters are often found by a multidimensional optimization. Examples of parametric methods are maximum likelihood methods and WSF (Weighted Subspace Fitting) [89]. All parametric methods and most spectral methods utilize a parametrized signal model. For this the number of signal sources need to be known. Estimation of the number of signal sources is an important research problem, e.g. see [33, 89]. In principle this is the same problem as estimating the interference (signal) rank in radar interference suppression (see Section 3.3.1).

Here we show one spectral DOA estimation method which is called *Capon's beamformer* [89, 90]. It is of special interest to us because it is related to the interference suppression filter (9) - (10) and it is also used in several of the publications included in this thesis. As with (9) a FIR filter is used to obtain a filter output signal

$$y(t) = \mathbf{w}^H \mathbf{x}(t), \tag{17}$$

where $\mathbf{w} = \mathbf{w}(\boldsymbol{\theta})$ is the filter vector for a look direction $\boldsymbol{\theta}$. Assuming that the source signals $\mathbf{s}(t)$ are stochastic, the DOA spectrum is

$$P(\boldsymbol{\theta}) = P(\mathbf{w}(\boldsymbol{\theta})) = P(\mathbf{w}) = \mathrm{E}\{|y(t)|^2\} = \mathbf{w}^H \mathbf{R} \mathbf{w}, \tag{18}$$

where $\mathbf{R} = \mathrm{E}\{\mathbf{x}(t)\mathbf{x}^H(t)\}$ is the covariance matrix of the received signals. The Capon beamformer solves the optimization problem

$$\begin{aligned} \mathbf{w}_{\mathrm{cap}} &= \arg\min_{\mathbf{w}} P(\mathbf{w}) \\ \text{subject to} \quad & \mathbf{w}^H \mathbf{a}(\boldsymbol{\theta}) = 1 \end{aligned} \tag{19}$$

The solution is

$$\mathbf{w}_{\mathrm{cap}} = \frac{\mathbf{R}^{-1}\mathbf{a}(\boldsymbol{\theta})}{\mathbf{a}^H(\boldsymbol{\theta})\mathbf{R}^{-1}\mathbf{a}(\boldsymbol{\theta})} \tag{20}$$

Note, this is the interference suppression filter (9) - (10) with $\mathbf{w}_{\text{opt}} = \mathbf{w}_{\text{cap}}$, $\mathbf{R}_i = \mathbf{R}$, $\mathbf{w}_0 = \mathbf{a}(\boldsymbol{\theta})$ and

$$\eta = \frac{1}{\mathbf{a}^H(\boldsymbol{\theta})\mathbf{R}^{-1}\mathbf{a}(\boldsymbol{\theta})}. \tag{21}$$

The DOA spectrum is now

$$P_{\text{cap}}(\boldsymbol{\theta}) = P_{\text{cap}}(\mathbf{w}(\boldsymbol{\theta})) = \mathrm{E}\{|y(t)|^2\} = \frac{1}{\mathbf{a}^H(\boldsymbol{\theta})\mathbf{R}^{-1}\mathbf{a}(\boldsymbol{\theta})} \tag{22}$$

The DOAs are found by searching $P_{\text{cap}}(\boldsymbol{\theta})$ for maxima.

The DOA spectrum of Capon is also an estimation of the power impinging on the antenna. Other spectral methods, such as MUSIC, delivers a pseudo-spectrum, which do not estimate the power. Several of the publications included in this thesis employ the Capon method: for DOA estimation in Figure 4 in Publication 2; for estimation of the impinging power in Figure 7 - 12 in Publication 5, Figure 3 in Publication 6 and Figure 2, 7, 8a - 14a in Publication 4 and also Figure 21 in this thesis.

Most DOA estimation methods, like the Capon method in (22), utilize the received antenna signals $\mathbf{x}(t)$ in the form of their covariance matrix $\mathbf{R}$. These methods assume that $\mathbf{R}$ is known but in reality it is unknown. Traditionally $\mathbf{R}$ has been estimated by the *SCM* (*Sample Covariance Matrix*):

$$\hat{\mathbf{R}} = \frac{1}{L}\sum_{l=1}^{L}\mathbf{x}_l\mathbf{x}_l^H, \tag{23}$$

where $\mathbf{x}_l$ is a received training signal snapshot. The number of snapshots is L. This is the same estimation method as for the estimate (11) of the interference covariance matrix $\mathbf{R}_i$ in interference suppression and target detection in Section 3.3.1. This estimate of $\mathbf{R}$ is good if the number of snapshots L is large ($L \to \infty$). However, there is often a shortage of training snapshots in radar, especially if high resolution estimation is performed simultaneously in more than one of the dimensions in the radar data cube (see below). This is the same problem as for interference suppression (Section 3.3.1).

An alternative approach for coping with a limited number of training snapshots is to derive methods which are good if the number of snapshots L and the number of sensors N are both of the same order of magnitude and both are

large ($L,\ N \to \infty$ such that $(L/N) \to c > 0$ in [91, 92, 93]). The idea is that the estimation performance then should be good also for few snapshots, in the order of the number of sensors [91, 93]. Using this approach, in [93] an improved DOA estimator for random source signals and in [91] a DOA estimator for unknown deterministic source signals were derived.

The same techniques as for high resolution DOA estimation can be used for the other dimensions of the radar data cube (Figure 7), namely Doppler and range, and even for two or all three of the dimensions DOA, Doppler and range at the same time. Figure 7- 12 in Publication 5 and Figure 3 in Publication 6 show Capon spectra in the DOA-Doppler dimensions.

4 Radar with micro-Doppler measurements

We will now turn to the other research area of this thesis, namely radar with micro-Doppler measurements.

4.1 Introduction

In safety, security and military applications there is a need at short distances (up to a few hundred meters) to detect targets, such as humans, animals, cars, boats, small aircraft and consumer drones; further to classify the target type and activity; to distinguish between target individuals; and also to foresee target intent in order to obtain situational awareness now and anticipate what will happen in the future. See Figure 22 for examples of some radar targets. Safety applications can be, for example, situation consciousness and search & rescue at catastrophes or patient and elderly monitoring in health and welfare. Security applications can be surveillance of protected zones around, e.g., airports, power plants and political summits, or law enforcement operations. Military applications can be situation awareness in combat situations and surveillance around checkpoints and camps. Figure 23 illustrates a security scenario.

Radar measuring micro-Doppler could be employed to perform the above tasks.

Figure 22: Examples of targets for a micro–Doppler radar for security surveillance. Top right: a consumer drone, a quadrocopter. These targets were used in Publication 9 (reference [11]). Photo by FOI.

Figure 23: An illustration of a micro–Doppler radar scenario for security surveillance. Illustration by Henrik Pettersson.

Micro-Doppler is created by the movement of internal parts of the target, such as arms and legs of humans and animals, wheels of cars and rotors of drones. See Figure 24 for an example of a micro-Doppler signature of a walking human. It is possible to discern the trajectories of different body parts as the figure indicates. Figure 25, 26 and 27 show some radars which have been used for micro-Doppler measurements by FOI.

4.2 Research on micro-Doppler in radar

Research on micro-Doppler in radar is a relatively new research area. Classification of human activities has been conducted in [94, 95, 96] and separation of humans and vehicles in [97, 98]. Birds and different kinds of consumer drones are classified in [99, 100]. Only a few research results on automatic separation of humans from animals has been reported [11, 101, 102]. Only a few books, dedicated entirely to radar micro-Doppler, have been published [103, 104]. The literature about micro-Doppler is not at all so extensive as the literature about signal processing for array antennas. One reason is that the radar micro-Doppler field of research is much younger.

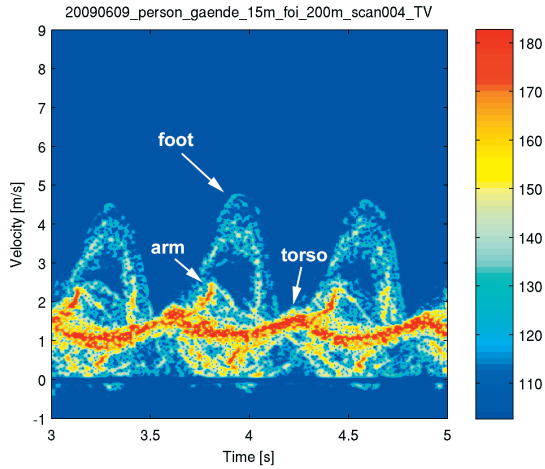

Figure 24: Micro-Doppler signature of a walking human. Image from [17]. Reproduced with permission from DGON (German Institute of Navigation).

The Swedish Defence Research Agency (FOI) has earlier analyzed micro-Doppler of humans at mm-wave (77 GHz) [17] and of vehicles (wheeled and tracked) at X and Ku band [105]; performed detailed electromagnetic simulations of micro-Doppler of humans and animals [106]; classified different human gaits using micro-Doppler at Ku band (15 GHz) [23] and mm-wave (77GHz) [10, 16]; classified humans, animals and man-made objects [11]; simultaneously estimated and tracked micro-Doppler and position parameters [18]; and done work on distinguishing human individuals using micro-Doppler signatures [107]. FOI has also worked on detection of humans around corners and behind walls [108, 109, 110]. The work on micro-Doppler which is covered by this thesis is described in Section 5.

4.3 Signal processing for micro-Doppler radar

4.3.1 Structure of transmitted and received signals

Transmitted signal Two kinds of transmitted signals are common in micro-Doppler radar:

Figure 25: The FOI Arken radar [111]. The left antenna is used for transmission and the right for reception. The middle antenna is used for special purposes. The radar is pulsed and can operate in 6-18 GHz for both horizontal and vertical polarization. This radar is used in [23, 105]. Photo by FOI.

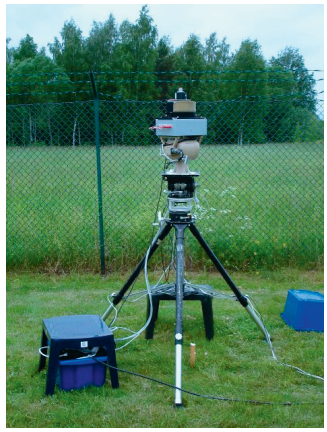

Figure 26: The Saab SIRS 77 radar. It is a single-channel pulsed FMCW (Frequency Modulated Continuous Wave) radar operating at 77 GHz with horizontal polarization. It has a resolution in range of 1 m and in azimuth of 1°. The radar antenna, RF electronics and a turn table are mounted on top of the tripod. This radar was used in Publication 8 (reference [10]) and in [12, 16, 18, 112, 113]. Photographer: Svante Björklund. Photo from [17]. Reproduced with permission from DGON (German Institute of Navigation).

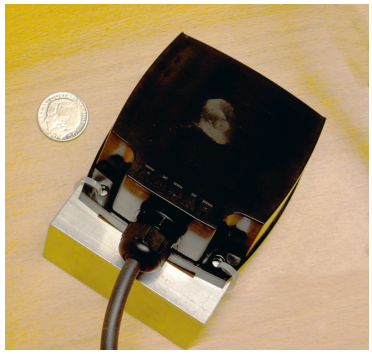

Figure 27: Left: The IMST radar and a radar target. In the micro-Doppler mode the radar is a pure-carrier radar with frequency 24 GHz and vertical polarization. The radar antenna and RF electronics, which are manufactured by the German company IMST, are mounted on top of the tripod. The box on the ground contains the control computer. Photo by Karl-Göran Stenborg. Modified by Svante Björklund. Right: Close-up of the IMST radar antenna and RF electronics module. Photo by Svante Björklund. This radar is used in Publication 9 (reference [11]).

- Pulsed signal. The pulse modulation can either occupy a part of the PRI or fill the whole PRI. The latter case, which has no gap between the pulse modulations, is a *CW* (*Continuous Wave*) signal. A common pulse modulation is linear *FM* (*Frequency Modulation*). An *FMCW* signal is thus a repeated, i.e. pulsed, frequency modulation without gaps. Therefore a FMCW signal is also a pulsed signal. With a pulsed transmitted signal it is possible to measure the range to the target. The bandwidth of the signal determines the range resolution, with higher bandwidth giving better resolution.

- Pure carrier. This is a sinusoid without modulation. This signal is also a CW signal. With this transmitted signal it is possible to measure Doppler and micro-Doppler but not target range (distance).

Received signal We will mention three important aspects of the received signal, namely observation interval, sampling frequency and structure of the received signal.

The *observation interval* is the time interval in which the radar is staring at the target and is collecting data. In order to discern the movements of the internal parts of the target, the observation interval should cover some cycles of these movements, e.g. leg movements of humans and animals or wheel rotations of a car. Thus, the suitable observation interval depends on the target type. A suitable observation interval for a walking or running human target is 2-3 s.

The *sampling frequency* of the received signal must be sufficiently high to measure the highest velocity unambiguously. It is well-known that an analog signal must be sampled sufficiently fast relative the bandwidth of the signal in order to avoid aliasing. The highest target velocity depends on the target type, e.g. about 10 m/s for a human walking or running. The required sampling frequency also depends on the carrier frequency, or alternatively the carrier wavelength, according to (2). For example, the walking or running human requires a sampling frequency $f_s \geq 3.2$ kHz at a carrier frequency of 24 GHz.

The *structure of the received signal* is somewhat different for the two kinds of transmitted signals above:

- Pulsed signal. For the pulsed transmitted signal the received signal can be organized in a radar data cube (Section 2.4.1 and Figure 7). For this case the Doppler shift is measured by the phase shift between pulses. Thus, the Doppler filtering is performed in the pulse/slow-time dimension, as in Section 2.4.2. The sampling frequency is equal to the PRF. The range to the target can also be measured.

- Pure carrier. There is only a single time dimension. It can be interpreted as the pulse/slow-time dimension. The PRI only contains a single range bin. By this choice the radar signal from all ranges will be folded into this single range bin. The result is that objects and targets from all ranges will be visible, if they give a sufficiently strong reflected radar signal. The sampling frequency is also now equal to the PRF and the Doppler filtering is performed also now in the "pulse/slow-time" dimension.

4.3.2 Processing of the received signals

The processing of the received radar signal in a micro-Doppler radar can be divided into the steps in Figure 28. In the block **Radar receiver** the signal is down-converted to base-band and analog-to-digital-converted. The digital processing starts with beamforming, if the antenna is a digital array antenna,

and pulse compression in order to localize a target in DOA and range. This is performed in the block **Beamform. Pulse comp**. Then the signal passes the velocity compensation (the block **Velocity comp.**), this the first time without any compensation. Since the radar is supposed to be stationary, clutter suppression in the Doppler domain now follows in the block **Clutter filter**. After that, if an object is detected by its signal strength in the block **Detect**, its position and (radial) base velocity will be estimated by the block **Estimate pos & vel**. The (radial) base velocity is the (radial) velocity of the main body of the target. This velocity is measured with normal Doppler filtering. The position and velocity information is fed back to the velocity compensation in order to counteract against the object migrating between range bins during the observation interval, and possibly set the base velocity to zero. The received signal is once again put through the velocity compensation, this time with active compensation, and the clutter filter and then directed to the **Select** block. This block cuts out the correct part of the received signal for classification analysis. The block **Transform** possibly transforms to a new signal domain which is better suited for the following feature extraction. A common transform is to convert to the combined time and velocity domain by a short-time Fourier transform. This transform uses an *integration interval* for each (short) Fourier transform. The integration time should be long in order to give high velocity resolution but it should also be short so that the internal target parts do not change velocity during the interval. (This is dependent on target type). Therefore the integration interval is a compromise.

The micro-Doppler classification problem can be decomposed in the two stages *feature extraction* (blocks **Transform** and **Feature extract**) and *classification* (block **Classify**). In Figure 8 the transform is included in the "Features" block. There is a large variation in the proposed approaches in the literature for both of these stages, especially for the feature extraction. The choice of feature extraction is partly directed by the radar type, the environment and the type of radar targets. Some feature extraction methods first transforms to the combined time and velocity domain [94, 95, 96, 98, 114], which is possible to interpret manually, while others extract their features directly from the received radar signal [97, 115, 116, 117], often inspired by speech signal processing. The classification consists of two sub-stages, first building (training) a model of different classes from training data, and second a decision rule for comparing the model with the data to classify. Two common classifiers are SVM (Support Vector Machine) [118] and k-Nearest Neighbor [119].

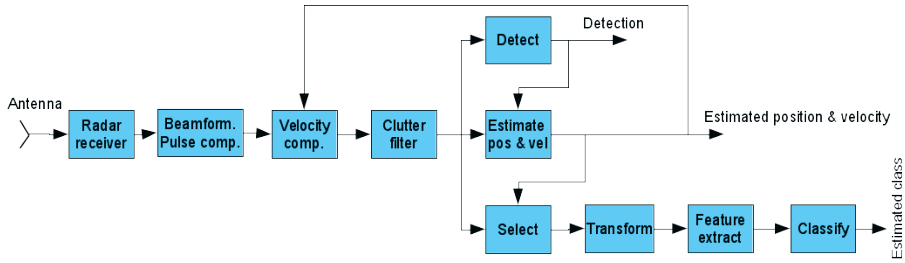

Figure 28: Block diagram of signal processing in a micro-Doppler radar for security surveillance in real operation. See the text in Section 4.3.2 for an explanation of the blocks. Compare with Figure 8.

What we have described is the processing in a real operation. The needs for the processing in research and development are different. In this latter case, tools for storing and managing measured and simulated data, tools for selecting and annotating data, tools for training classifiers and tools for analysis are also needed.

5 Contributions of the included publications

This chapter summarizes the contributions of the selected and included publications in this thesis. The contributions are also listed in Section "Publication list" at the beginning of the thesis.

Publication 1: Radar-Like Measurements with an Experimental Digital Beamforming Array Antenna, 1998 [3]

This publication addresses High Resolution DOA Estimation (HRDE) in radar. "When required, HRDE in radar could be applied as a special radar function for the resolution of target groups, estimation of jammer DOAs, detection & estimation in jamming environments, handling of multipath etc." [3]. HRDE could also be used to resolve target scattering points as an aid for target recognition/classification. The main results of this publication are two: 1) demonstration of incorporating HRDE into a radar system and 2) the design of "radar-like" measurements, which means using emulated radar targets via measurements of direct path signals from transmitter(s) to receiver in an anechoic chamber. The advantage of these measurements is the good control of the influencing factors. The measurement design and the radar DOA estimation are verified by real measurements in this publication.

The work was later continued in [28] in which radar and HRDE are combined in monostatic measurements outdoors and in [63] in bistatic measurements outdoors. The report [87] contains more results on the combination of radar and HRDE using outdoor measurements. The report [120] investigates, with the aid of simulations, how to incorporate HRDE in a radar application example.

Publication 2: High Resolution Direction of Arrival Estimation Methods Applied to Measurements from a Digital Array Antenna, 2000 [4]

High resolution DOA estimation can be useful for several applications, including radar applications, to give new functions and improve the performance. This publication shows a test of DOA estimation methods on measured data, and also compares ten DOA estimation methods, both spectral ones and parametric ones, on the data. The conclusions of the work are: 1) High-resolution methods work on measured data. At ideal conditions the resolution can be improved considerable compared to conventional beamforming. 2) Some conclusions about properties of some specific DOA estimation methods are given.

Complementary work to Publication 1 and 2 was published in [63], where the influence of calibration and broadband signals on HRDE is investigated.

Publication 3: Auxiliary Beam Terrain-Scattered Interference Suppression: Reflection System and Radar Performance, 2013 [5]

Terrain-scattered interference (TSI), i.e. jammer signals reflected on the surface of the earth, can deny military radar the detection and localization of targets. The TSI must therefore be suppressed. TSI signals are usually more difficult for the radar to handle than direct-path jamming. This publication presents results on the structure of auxiliary beam TSI suppression (one of several possible TSI suppression methods), on the estimation of the reflection system (which describes the scattering on the earth surface) and on the quality of the estimate. Further, it derives theoretical expressions for the signal-to-interference plus noise ratio (SINR) and the remaining TSI power for a single auxiliary beam. Since the SINR is directly connected to the radar performance, these expressions show what factors affect the performance and how. A precursor of this publication was the conference paper [25].

Publication 4: Measurement of Rank and Other Properties of Direct and Scattered Signals, 2016 [6]

The interference in radar must be suppressed in order for the radar to detect and localize the targets. The interference can be clutter, direct path jamming or TSI (terrain scattered interference/jamming). The interference rank is important to know. The rank determines the required size of the suppression filter and also the number data needed to estimate the interference properties which are used in the filter.

The results of this publication are two: 1) Design of a low-cost experiment with good control of influencing factors for measuring rank and other properties of direct and scattered electromagnetic signals. This design, which takes several important aspects into account, can be an aid for designing future experiments and measurements. 2) Signal rank and other properties of direct and scattered signals. A verification of these measured properties is carried out with properties described in the literature, there acquired from theory and simulations.

The measurements in this publication are performed in an anechoic chamber with transmitters, a receiving digital array antenna [60] and a moving reflector. A first experimental design was used in [29] and then improved in [27].

Publication 4 contains more details and a significantly deeper analysis than [27].

Publication 5: Clutter Properties for STAP with Smooth and Faceted Cylindrical Conformal Antennas, 2010 [7]

The application in mind in this publication is an airborne radar used to detect and localize slowly moving targets in a ground clutter environment. In order to achieve this, the clutter must be suppressed. The investigated problem in the publication is how to choose the geometry and the subarrays of the radar antenna in order to suppress the clutter effectively, or more specifically, investigation of how severe the clutter is for some antenna geometries and some subarray designs. The employed geometries are three: 1) a faceted and 2) a smoothly bent vertical half cylinder, pointing forward, and 3) a planar forward-looking aperture. See Figure 15 and 16 in this thesis for similar antennas. The two half-cylinder antennas are conformal because their apertures are bent and adapted to the outer surface of the radar platform. Advantages with conformal antennas are reduced space and weight, larger field of view and aerodynamic design. The employed subarray designs consist of subarrays of different sizes. The results are created by simulations. Conclusions of the publication are: "the faceted and smooth half-cylinder antennas have no significant differences in clutter suppression performance. The plane antenna has poorer performance. The subarray division is more important than the antenna geometry. The number of antenna channels is related to the clutter rank and the clutter fraction of the signal space" [7]. Also, some new analysis tools are proposed.

Figure 1 and 2 and part of the introduction of Publication 5 were also published in the IEEE Aerospace and Electronic Systems Magazine [19].

Publication 6: Clutter Properties for a Side-Looking Radar with Planar Regular and Irregular Subarrays, 2015 [8]

Publication 6 is similar to Publication 5 but it uses side-looking antennas instead of forward-looking. Further, it employs a different antenna geometry and uses different subarray designs. Only a single antenna geometry is used, namely a (side-looking) planar aperture. Four different subarray designs are investigated. A conclusion is that irregular subarrays and large subarrays are advantageous according to different performance measures. Another conclusion is that none of the subarray designs is the best for all used performance

measures in the studied case. It is also noted that "the properties of the clutter received by a radar depend on the radar design" [8].

Publication 7: Three-Dimensional DPCA with Rotating Antenna for Clutter Cancellation, 2015 [9]

For a radar on a moving platform the clutter from the earth's surface must be suppressed in order to detect and localize targets. In this publication an extension of the well-known clutter cancellation method DPCA (Displaced Phase Center Antenna) to other antenna element positions than on a line parallel with the velocity vector of the radar platform is made. Together with the previous paper [14], a new mathematical condition for total cancellation of the clutter is derived, a condition that do not require that all antenna element positions are on a single line parallel with the velocity vector. The antenna can even be rotating. Further, an optimization problem is formulated for maximizing the target signal with the clutter cancellation as a constraint. An extra discussion about the new clutter cancellation method, the target signal, the relation to the traditional DPCA and about model errors is found in paper [14].

Publication 8: Features for Micro-Doppler Based Activity Classification, 2015 [10]

There is an increasing need in safety, security and military surveillance at short distances to detect targets; to classify the target type and target activity; to distinguish between target individuals; and also to foresee target intention. An approach is to employ radars measuring micro-Doppler to perform these tasks.

Together with [23] and [16] this publication suggests a new feature extraction method, in which the components with most energy in the Cadence Velocity Diagram (CVD) are utilized in the feature vector, which then is used in a classifier. The CVD is created by the Fourier transform along the time dimension in the Time Velocity Diagram (TVD). This publication also in practice applies a feature extraction method from the literature, a method that delivers physical features, such as target base velocity, cycle frequency (limb frequency for humans and animals) and Doppler bandwidth [94]. This publication uses measurements on moving humans conducted with a 77 GHz radar (see Figure (26)) which were made by FOI together with Saab AB. Micro-Doppler signatures of moving humans using this radar are shown in [17]. Further, this publication classifies the gait of a moving human with good results. Since no significant difference in classification result between the two feature extraction methods is

found, the publication suggests and also demonstrates that only two properties, namely the base velocity and the cycle frequency, are sufficient to distinguish between the activities at hand. These two properties are explicitly or implicitly present in the feature vectors of the two methods.

Publication 9: Target Classification in Perimeter Protection with a Micro-Doppler Radar, 2016 [11]

In security surveillance at the perimeter of vital infrastructure, such as airports and power plants, it is important to detect and classify approaching objects. Especially important is to distinguish between humans, animals and vehicles. It is also desirable that the sensor equipment is sufficiently cost-effective to facilitate a large area deployment.

This publication uses measurements from a low-complexity and cost-effective 24 GHz radar (see Figure 27) on moving humans, a moving dog, a moving horse and various man-made objects. The measurements were conducted by FOI. In principle, the same physical feature extraction method as in Publication 8 is used in this publication. The classification result of separating humans, animals and man-made objects is good. Especially interesting is the good ability to separate humans and the animals at hand. The publication also shows that it is possible to choose to have limitations in the radar, and thereby make the surveillance system more affordable, and still solve the classification task.

This publication also demonstrates together with Publication 8 and [23] the ability to use different kinds of radars for micro-Doppler measurements and classifications. In these three documents, three different radars of different types and frequency bands have been used.

The main conclusion from Publication 8 and 9 about micro-Doppler radar is that this type of radar should be feasible for safety, security and military surveillance applications.

Publication 10: On Distinguishing between Human Individuals in Micro-Doppler Signatures, 2013 [12]

This publication also concerns security applications, as with Publication 8 and 9. The research problem is now to distinguishing between human individuals from micro-Doppler signatures (MDS). “By distinguishing between human individuals we mean to recognize the same individual in a short time frame but not to establish the identity of the individual” [12]. This ability could be used

to improve multiple target tracking, which in its turn could enhance the classification of target type and activity and perhaps also make it easier to predict the intent of the target.

This publication is investigating whether there is information in MDSs to distinguishing between human individuals. If there is, this information could be utilized by a machine to perform the task. The investigation was conducted by letting six test persons put MDSs, measured by an 77 GHz radar by FOI together with Saab AB (see Figure 26), from three humans into three groups. The idea was that if the test persons separated the individuals better than random, there should be information about the individuals in the MDSs. A statistical hypothesis test concludes that the test persons did this better than random. The conclusion of the publication is that "micro-Doppler signatures of walking humans likely contain information to distinguish between different human individuals" [12]. The publication also discusses features in the MDSs which could be used for this.

This research methodology to use test persons to see if information is present which also could be utilized by a machine is unusual in electrical engineering and signal processing.

Bibliography

[1] Ulrich Nickel. *Winkelauflösung eng benachbarter Ziele mit Gruppenantennen*. PhD thesis, Technische Hochschule Aachen, 1982.

[2] Svante Björklund. *A Survey and Comparison of Time-Delay Estimation Methods in Linear Systems*. Licentiate thesis no. 1061, Department of Electrical Engineering, Linköping University, SE-581 83 Linköping, Sweden, December 2003. ISBN 91-7373-870-0.

[3] Svante Björklund, Per Grahn, and Lars Pettersson. Radar-like measurements with an experimental digital beamforming array antenna. In *Proceedings of the International Radar Symposium IRS 98*, pages 993–1002, München, Germany, 15-17 September 1998.

[4] Svante Björklund and Amir Heydarkhan. High resolution direction of arrival estimation methods applied to measurements from a digital array antenna. In *Proc. of IEEE SAM 2000 (First IEEE Sensor Array and Multichannel Signal Processing Workshop)*, Cambridge, MA, USA, 16-17 March 2000.

[5] Svante Björklund, Anders Nelander, and Mats I. Pettersson. Auxiliary beam terrain-scattered interference suppression: Reflection system and radar performance. *IET Radar, Sonar & Navigation*, 7(8):836 –847, oct 2013.

[6] Svante Björklund, Per Grahn, Anders Nelander, and Mats I. Pettersson. Measurement of rank and other properties of direct and scattered signals. *International Journal of Antennas and Propagation*, 2016. `http://www.hindawi.com/journals/ijap/2016/5483547`.

[7] Svante Björklund, Tomas Boman, and Anders Nelander. Clutter properties for STAP with smooth and faceted cylindrical conformal antennas. In *2010 IEEE International Radar Conference*, Washington DC, USA, May 10-14 2010.

[8] Svante Björklund. Clutter properties for a side-looking radar with planar regular and irregular subarrays. In *International Radar Symposium (IRS) 2015*, Dresden, Germany, June 24-26 2015.

[9] Svante Björklund. Three-dimensional DPCA with rotating antenna for clutter cancellation. In *The 2015 IEEE International Radar Conference*, Arlington, Virginia, USA, 11-15 May 2015.

[10] Svante Björklund, Henrik Petersson, and Gustaf Hendeby. Features for micro-doppler based activity classification. *IET Radar, Sonar & Navigation*, 9(9):1181–1187, dec 2015.

[11] Svante Björklund, Tommy Johansson, and Henrik Petersson. Target classification in perimeter protection with a micro-doppler radar. In *International Radar Symposium (IRS) 2016*, Kraków, Poland, 10-12 May 2016.

[12] Svante Björklund, Henrik Petersson, and Gustaf Hendeby. On distinguishing between human individuals in micro-doppler signatures. In *International Radar Symposium (IRS-2013)*, Dresden, Germany, June 19-21 2013.

[13] Svante Björklund, Anders Nelander, and Mats I. Pettersson. Fast-time and slow-time space time adaptive processing for bistatic radar interference suppression. In *2015 IEEE International Radar Conference*, Arlington, VA, USA, May 10-15 2015.

[14] Svante Björklund and Mats I. Pettersson. A three-dimensional displaced phase center antenna condition for clutter cancellation. In *The Eighth IEEE Sensor Array and Multichannel Signal Processing Workshop (SAM 2014)*, A Coruña, Spain, June 22-25 2014.

[15] Svante Björklund. The design, development and use of a Matlab toolbox for radar modeling, simulation and signal processing. In *International Radar Symposium (IRS-2013)*, Dresden, Germany, June 19-21 2013.

[16] Svante Björklund, Tommy Johansson, and Henrik Petersson. Evaluation of a micro-doppler classification method on mm-wave data. In *IEEE Radar Conference 2012*, Atlanta, USA, May 7-11 2012.

[17] Svante Björklund, Henrik Petersson, Amer Nezirovic, Mehmet Burak Guldogan, and Fredrik Gustafsson. Millimeter-wave radar micro-doppler signatures of human motion. In *International Radar Symposium 2011*, Leipzig, Germany, September 7-9 2011. Available from IEEE Xplore.

[18] Mehmet Burak Guldogan, Fredrik Gustafsson, Umut Orguner, Svante Björklund, Henrik Petersson, and Amer Nezirovic. Human gait parameter estimation based on micro-doppler signatures using particle filters. In *ICASSP 2011 (International Conference on Acoustics, Speech and Signal Processing)*, Prague, Czech Republic, May 22-27 2011.

[19] Svante Björklund, Tomas Boman, and Anders Nelander. UAVs (unmanned aerial vehicle) for surveillance and information acquisition about ground targets. Back cover figures and text in IEEE Aerospace and Electronic Systems Magazine, Vol 26, No. 3, March 2011.

[20] Svante Björklund and Lennart Ljung. An improved phase method for time-delay estimation. *Automatica*, 45(10), October 2009.

[21] Svante Björklund and Anders Nelander. Fast-time STAP for clutter suppression between transmitter and receiver in bistatic radar. In *International Radar Conference RADAR 2009*, Bordeaux, France, 12-16 October 2009.

[22] Svante Björklund. Space-time adaptive processing with a half-cylinder faceted conformal antenna. In *International Radar Conference RADAR 2009*, Bordeaux, France, October 12-16 2009.

[23] Henrik Petersson, Svante Björklund, Mikael Karlsson, and Andris Lauberts. Towards surveillance using micro-doppler radar. In *IRS (International Radar Symposium) 2009*, Hamburg, Germany, September 9-11 2009.

[24] Svante Björklund and Tomas Boman. Virtual antennas for clutter suppression in forward-looking airborne radar. In *Proceedings of RVK 2005 (RadioVetenskap och Kommunikation 2005)*, Linköping, June 14-16 2005.

[25] Svante Björklund and Anders Nelander. Theoretical aspects on a method for terrain scattered interference mitigation in radar. In *IEEE International Radar Conference 2005*, pages 663–668, Washington DC, USA, 9-12 May 2005.

[26] Svante Björklund and Lennart Ljung. A review of time-delay estimation techniques. In *Proceedings of 42nd IEEE Conference on Decision and Control*, Hawaii, USA, 9-12 December 2003.

[27] Svante Björklund, Per Grahn, and Anders Nelander. Analysis of array antenna measurements with a rough surface reflector. In *Signals, Systems and Computers, 2000. Conference Record of the Thirty-Fourth Asilomar Conference on*, volume 2, pages 1135–1139 vol.2, Oct 2000.

[28] Per Grahn and Svante Björklund. Short range radar measurements with an experimental digital array antenna. In *IEEE International Radar Conference RADAR 2000*, Alexandria, VA, USA, 2000.

[29] Svante Björklund, Per Grahn, and Anders Nelander. Measurement and analysis of multipath by a rough surface reflector using a digital array antenna. In *ISSPA '99 (IEEE Fifth International Symposium on Signal Processing and its Applications)*, pages 859–862, Brisbane, Australia, 22-25 August 1999.

[30] Svante Björklund. Implementierung einer Schrittweitensteuerung für eine Freisprecheinrichtung" (Implementation of a stepsize control for an acoustic echo canceler). Diplomarbeit (Master of science thesis) D85, Technische Hochschule Darmstadt, Germany, 5 February 1993. In German language.

[31] Wikipedia. Radar. `https://en.wikipedia.org/wiki/Radar`, 4 December 2016.

[32] Wikipedia. Radar. `https://de.wikipedia.org/wiki/Radar`, 11 October 2016.

[33] Ulrich Nickel. Array processing for radar: Achievements and challenges. *International Journal of Antennas and Propagation*, 2013, 2013.

[34] Hans Frennberg, Svante Björklund, and Niclas Wadströmer. FOI Centre for advanced sensors, multisensors and sensor networks, FOCUS - SSF ProInstitute Annual Report 2013. Technical Report FOI Memo 4882, FOI, March 2014.

[35] Christian Rusch, Tobias Klein, Stefan Beer, and Thomas Zwick. A short distance CW-radar sensor at 77 GHz in LTCC for industrial applications. *Journal of Infrared, Millimeter, and Terahertz Waves*, 34(12):856–865, 2013.

[36] Wikipedia. Magellan (spacecraft). `https://en.wikipedia.org/wiki/Magellan_(spacecraft)`, 29 January 2017.

[37] Fraunhofer Institute for High Frequency Physics and Radar Techniques FHR. High-precision radar for the steel industry. research news, 2 March 2015. Press Release.

[38] Simon Kingsley and Shaun Quegan. *Understanding Radar Systems*. Scitech Publishing, 1999. ISBN:1-891121-05-7.

[39] J. R. Guerci and J. S. Bergin. Principal components, covariance matrix tapers, and the subspace leakage problem. *IEEE Transactions on Aerospace and Electronic Systems*, 38(1):152–162, Jan 2002.

[40] Samuel J Davey, Mark G Rutten, and Brian Cheung. A comparison of detection performance for several track-before-detect algorithms. *EURASIP Journal on Advances in Signal Processing*, 2008, 2008.

[41] Samuel J. Davey, Mark G. Rutten, and Neil J. Gordon. *Integrated Tracking, Classification, and Sensor Management, Theory and Applications*, chapter Chapter 8 Track-Before-Detect Techniques, pages 311–361. Wiley, 2013. ISBN 978-0-470-63905-4.

[42] Branko Ristic, Sanjeev Arulampalam, and Niel Gordon. *Beyond the Kalman Filter*, chapter 11, Detection and Tracking of Stealthy Targets, pages 239–259. Artech House, 2004. ISBN 1-58053-631-x.

[43] Mathworks. MATLAB - The language of technical computing. http://mathworks.com/products/matlab/.

[44] GNU Octave, A high-level language, primarily for numerical computations. http://www.octave.org.

[45] Svante Björklund. DBT, a Matlab and Octave toolbox for radar modelling, signal simulation and processing. Release 2.156. Internal report FOI-D–0447–SE, FOI - Swedish Defence Research Agency, March 2011.

[46] Svante Björklund. DBT - A Matlab toolbox for radar modeling, simulation and signal processing. http://www.bth.se/ing/wideband_sar.nsf/pages/dbt, September 2016.

[47] Wikipedia. Active Phased Array Radar (APAR). https://en.wikipedia.org/wiki/Active_Phased_Array_Radar, 24 August 2016.

[48] BAE Systems Australia. SADM, The most versatile model for maritime air defence analysis. https://sadm.au.baesystems.com, September 23 2016.

[49] SIMDIS. https://en.wikipedia.org/wiki/SIMDIS, September 23 2016.

[50] Koninklijke Marine. File:Hr. Ms. Tromp (F803).jpg. https://en.wikipedia.org/wiki/File:Hr._Ms._Tromp_%28F803%29.jpg, 23 September 2016. Photo of the naval ship HNLMS Tromp (F803) at sea.

[51] Wikipedia. Airborne early warning and control. https://en.wikipedia.org/wiki/Airborne_early_warning_and_control, 24 September 2016.

[52] Wikipedia. Erieye. https://en.wikipedia.org/wiki/Erieye, 24 September 2016.

[53] Gnolam. File:S 100B at Malmen 2010-06-13 1.jpg. https://en.wikipedia.org/wiki/File:S_100B_at_Malmen_2010-06-13_1.jpg, 24 September 2016. Photo of S 100 B Argus in flight at the Swedish Armed Forces' Airshow 2010.

[54] Wikipedia. EuroRADAR CAPTOR. https://de.wikipedia.org/wiki/EuroRADAR_CAPTOR, 24 August 2016.

[55] Bin im Garten and MagentaGreen. File:ILA Berlin 2012 PD 193-2.JPG. https://en.wikipedia.org/wiki/File:ILA_Berlin_2012_PD_193-2.JPG, 7 August 2016. Photo of the antenna of the radar EuroRADAR CAPTOR-E. ILA Berlin Air Show 2012.

[56] Glen Fields. Phased array radar at the intersection of military and commercial innovation. *Microwave Journal*, 57(1):42–42,44, January 2014.

[57] Qamcom Research & Technology AB. Qamcom QR77s (radar system). https://www.qamcom.se/radar-systems, January 2017.

[58] smart microwave sensors GmbH. 3DHD - High definition in three dimensions: Range, angle and speed. http://www.smartmicro.de/automotive-radar/products/new-3dhd-technology, January 2017.

[59] Lars Pettersson. An S-band digital beamforming antenna: Design, procedures and performance. FOA Report FOA-R–99-01162-408–SE, FOA, 1999.

[60] Lars Pettersson, Magnus Danestig, and Ulf Sjöström. An experimental s-band digital beamforming antenna. *IEEE Aerospace and Electronics Systems Magazine*, pages 19–26, November 1997.

[61] Svante Björklund, Per Grahn, Staffan Lindström, and Lars Pettersson. Measurement system for an S-band digital beamforming array antenna. In *Proceedings of RVK 96 (RadioVetenskap och Kommunikation 1996)*, pages 250–254, Luleaa och Kiruna, 3-6 June 1996.

[62] Svante Björklund, Per Grahn, and Lars Pettersson. Initial measurements with an experimental radar with a digital array antenna. In *Proceedings of RVK 99 (RadioVetenskap och Kommunikation 1999)*, Karlskrona, Sweden, 14-17 June 1999.

[63] L. Pettersson and P. Grahn. Experiences using DOA methods with a small digital beamforming antenna. In *Phased Array Systems and Technology, 2003. IEEE International Symposium on*, pages 164–169, Oct 2003.

[64] Lars Pettersson. Evaluation of a digital beamforming antenna. In *Antenn 97*, pages 329–338, May 1997.

[65] Wikipedia. Radio frequency microelectromechanical system. `https://en.wikipedia.org/wiki/Radio_frequency_microelectromechanical_system`. Retrieved on 16 August 2016.

[66] Roland Erickson, Torleif Martin, Lars Pettersson, Per Grahn, Tomas Boman, Svante Björklund, Robert Malmqvist, and Anders Nelander. Flexibla mikrovaagssystem - Aarsrapport 2007 (Flexible microwave systems - Annual report 2007). Technical Report FOI Memo 2243, Swedish Defence Research Agency (FOI), 2007. In Swedish.

[67] Dennis S. Bernstein. *Matrix Mathematics. Theory, Facts, and Formulas with Application to Linear Systems Theory*. Princeton University Press, 2005. ISBN 0-691-11802-7.

[68] U. R. O. Nickel. Subarray configurations for digital beamforming with low sidelobes and adaptive interference suppression. In *Radar Conference, 1995., Record of the IEEE 1995 International*, pages 714–719, May 1995.

[69] J. Ward. Space-time adaptive processing for airborne radar. Technical Report 1015, Lincoln Laboratory, 13 December 1994.

[70] J.R. Guerci. *Space-Time Adaptive Processing for Radar*. Artech House, 2003. ISBN 1-58053-377-9.

[71] L. E. Brennan and I. S. Reed. Theory of adaptive radar. *IEEE Trans. Aerospace and Electronic Systems*, AES 9(2):237–252, March 1973.

[72] Richard Klemm. *Principles of space-time adaptive processing*. The Institution of Electrical Engineers, 2002. ISBN 0 85296 172 3.

[73] J. E. Hudson. *Adaptive Array Principles*. Peter Peregrinus Ltd., 1981. ISBN 0 86341 247 5.

[74] Alfonso Farina. *Antenna-Based Signal Processing Techniques for Radar Systems*. Artech House, 1992. ISBN 0-89006-396-6.

[75] P. G. Richardson. Analysis of the adaptive space time processing technique for airborne radar. *IEE Proc. Radar, Sonar, Navigation*, 141(4):187–195, August 1994.

[76] Fred M. Staudaher. *Radar Handbook*, chapter 16. Airborne MTI, pages 16.1–16.31. McGrawHill, 2 edition, 1990. ISBN 0-07-057913-X.

[77] Mark A. Richards. *Fundamentals of Radar Signal Processing*, chapter 5.7 MTI for Moving Platforms: Adaptive Displaced Phase center Antenna Processing, pages 287–293. McGrawHill, 2005. ISBN 0-07-144474-2.

[78] J. R. Guerci, J. S. Goldstein, and L. S. Reed. Optimal and adaptive reduced-rank STAP. *IEEE Transactions on Aerospace and Electronics Systems*, 36(2):647–663, April 2000.

[79] Scott Goldstein and Michael Picciolo. STAP II - Advanced concepts. Tutorial. In *2008 IEEE Radar Conference*, 2008.

[80] Muraldir Rangaswamy. Modern CFAR techniques in heterogeneous radar clutter scenarios. Tutorial. In *2008 IEEE Radar Conference*, 2008.

[81] E.J. Kelly. An adaptive detection algorithm. *IEEE Transactions on Aerospace and Electronic Systems*, AES-22(2):115–127, 1986.

[82] F.C. Robey, D.R. Fuhrmann, E.J Kelly, and R. Nitzberg. A CFAR adaptive matched filter detector. *IEEE Transactions on Aerospace and Electronic Systems*, 28(1):208–216, 1992.

[83] I. S. Reed, J. D. Mallett, and L. E. Brennan. Rapid convergence rate in adaptive arrays. *IEEE Trans. Aerospace and Electronics Systems*, AES-10(6):853–863, November 1974.

[84] Svante Björklund. About spatial and temporal rank of clutter and other interference in radar. Report FOI Memo 1796, FOI, August 2006.

[85] J.R. Guerci. *Space-Time Adaptive Processing for Radar*. Artech House, second edition edition, 2014. ISBN-10 1-60807-820-5.

[86] W.L. Melvin. A STAP overview. *IEEE Aerospace and Electronic Systems Magazine*, 19(1):19–35, Jan 2004.

[87] Per Grahn. Radar- och reflexmätningar under år 2001. DGA - Studie digital gruppantenn (Radar and reflection measurements during year 2001. DGA - Studies of digital array antenna). Technical Report FOI report 02-501, FOI, 2002. In Swedish.

[88] R. Schmidt. Multiple emitter location and signal parameter estimation. *IEEE Transactions on Antennas and Propagation*, 34(3):276–280, Mar 1986.

[89] H. Krim and M. Viberg. Two decades of array signal processing research. *IEEE Signal Processing Magazine*, pages 67–94, July 1996.

[90] J. Capon. High-resolution frequency-wavenumber spectrum analysis. *Proceedings of the IEEE*, 57(8):1408–1418, Aug 1969.

[91] P. Vallet, P. Loubaton, and X. Mestre. Improved subspace estimation for multivariate observations of high dimension: The deterministic signals case. *Information Theory, IEEE Transactions on*, 58(2):1043–1068, Feb 2012.

[92] P. Vallet, X. Mestre, and P. Loubaton. Performance analysis of an improved music doa estimator. *IEEE Transactions on Signal Processing*, 63(23):6407–6422, Dec 2015.

[93] X. Mestre and M.A. Lagunas. Modified subspace algorithms for doa estimation with large arrays. *Signal Processing, IEEE Transactions on*, 56(2):598–614, Feb 2008.

[94] Youngwook Kim and Hao Ling. Human activity classification based on micro-doppler signatures using a support vector machine. *IEEE Transactions on Geoscience and Remote Sensing*, 47(5):1328–1337, May 2009.

[95] Jingli Li, Son Lam Phung, Fok Hing Chi Tivive, and Abdesselam Bouzerdoum. Automatic classification of human motions using doppler radar. In *WCCI 2012 IEEE World Congress on Computational Intelligence*, Brisbane, Australia, June 10-15 2012.

[96] B. Lyonnet, C. Ioana, and M.G. Amin. Human gait classification using microdoppler time-frequency signal representations. In *Radar Conference, 2010 IEEE*, pages 915 –919, may 2010.

[97] Igal Bilik and Peter Khomchuk. Minimum divergence approaches for robust classification of ground moving targets. *IEEE Transactions on Aerospace and Electronic Systems*, 48(1):581–603, January 2012.

[98] Pavlo Molchanov, Jaakko Astola, Karen Egiazarian, and Alexander Totsky. Classification of ground moving radar targets by using joint time-frequency analysis. In *IEEE Radar Conference 2012*, pages 366–371, Atlanta, USA, May 7-11 2012.

[99] Ronny I. A. Harmanny, Jacco J. M. de Wit, and Gilles Premel-Cabic. Radar micro-doppler mini-uav classification using spectrograms and cepstrograms. *International Journal of Microwave and Wireless Technologies*, 7(Special Issue 3-4):469–477, June 2015.

[100] P. Molchanov, K. Egiazarian, J. Astola, R. I. A. Harmanny, and J. J. M. de Wit. Classification of small uavs and birds by micro-doppler signatures. In *EuRad*, pages 172–175, Nuremberg, Germany, 9-11 October 2013.

[101] Youngwook Kim, Sungjae Ha, and Jihoon Kwon. Human detection using doppler radar based on physical characteristics of targets. *Geoscience and Remote Sensing Letters, IEEE*, 12(2):289–293, Feb 2015.

[102] Dave Tahmoush, Jerry Silvious, and John Clark. An UGS radar with micro-doppler capabilities for wide area persistent surveillance. In *Proc. SPIE 7669, Radar Sensor Technology XIV, 766904*, April 26 2010.

[103] Victor C. Chen. *The Micro-Doppler Effect in Radar*. Artech House, 2011. ISBN-10: 1-60807-057-3.

[104] Victor C. Chen, David Tahmoush, and William J. Miceli, editors. *Radar Micro-Doppler Signatures, Processing and Applications*. The Institution of Engineering and Technology, www.theiet.org 2014. ISBN 978-1-84919-716-8.

[105] J. Kjellgren, S. Gadd, N.-U. Jonsson, and J. Gustavsson. Analysis of doppler measurements of ground vehicles. In *IEEE International Radar Conference 2005*, pages 284–289, Washington DC, USA, 2005.

[106] Svante Björklund, Mikael Karlsson, and Henrik Petersson. Measured and simulated radar micro-doppler signatures of human and animal motion. In *Second National Symposium on Technology and Methodology for Security and Crisis Management (TAMSEC 2011)*, Linköping, Sweden, October 19-20 2011.

[107] Svante Björklund, Henrik Petersson, and Gustaf Hendeby. On distinguishing between human individuals in micro-doppler signatures. In *International Radar Symposium (IRS-2013)*, Dresden, Germany, June 19-21 2013.

[108] M. Gustafsson, A Andersson, T. Johansson, S. Nilsson, A. Sume, and A. Örbom. Extraction of human micro-doppler signature in an urban environment using a sensing-behind-the-corner radar. *IEEE Geoscience and Remote Sensing Letters*, 13(2):187–191, Feb 2016.

[109] Tommy Johansson, Jonas Rahm, Jan Gustavsson, Stefan Nilsson, Ain Sume, and Anders Örbom. Through-the-wall detection of human activity. In *SPIE Defence, Security and Sensing*, pages 8022OL–1–7. SPIE, April 2011.

[110] A. Sume, M. Gustafsson, M. Herberthson, A. Jänis, S. Nilsson, J. Rahm, and A Örbom. Radar detection of moving targets behind corners. *IEEE Transactions on Geoscience and Remote Sensing*, 49(6):2259–2267, 2011.

[111] FOI. Mobilt radarmätsystem - Arken (Mobile radar measurement system - Arken). http://www.foi.se/sv/Vara-tjanster/Hyr-labb--och-forskningsresurser/Las-mer-om-FOIs-experimentella-resurser/Arken-mobilt-radarmatsystem. In Swedish. Retrieved on 29 September 2016.

[112] M. B. Guldogan, F. Gustafsson, Umut Orguner, S. Björklund, H. Petersson, and A. Nezirovic. Radar micro-doppler parameter estimation of human motion using particle filters. In *IEEE 19th Conference on Signal Processing and Communications Applications (SIU)*, Antalya, Turkey, 20-22 April 2011.

[113] Amer Nezirovic, Svante Björklund, and Henrik Petersson. Micro-doppler analysis of human motion using 77 GHz radar. In *SPIE Defense, Security, and Sensing*, Orlando, Florida, USA, April 25 - 29 2011. Poster.

[114] Fok Hing Chi Tivive, Abdesselam Bouzerdoum, and Moeness G. Amin. A human gait classification method based on radar doppler spectrograms. *EURASIP Journal on Advances in Signal Processing*, 2010, 2010. Article ID 389716.

[115] J.D. Bryan, J. Kwon, N. Lee, and Y. Kim. Application of ultra-wide band radar for classification of human activities. *Radar, Sonar Navigation, IET*, 6(3):172 –179, march 2012.

[116] Dustin P. Fairchild and Ram M. Narayanan. Classification and modeling of human activities using empirical mode decomposition with S-band and millimeter-wave micro-doppler radars. In *Proc. SPIE 8361, Radar Sensor Technology XV*, pages 83610X–83610X–15, 2012.

[117] I. Bilik and J. Tabrikian. Radar target classification using doppler signatures of human locomotion models. *IEEE Transactions on Aerospace and Electronic Systems*, 43(4), October 2007.

[118] S. Haykin. *Neural Networks: A comprehensive foundation.* Prentice-Hall Inc., 2nd edition, 1999.

[119] Wikipedia. k-nearest neighbors algorithm. https://en.wikipedia.org/wiki/K-nearest_neighbors_algorithm, 28 September 2016.

[120] Svante Björklund and David Rejdemyhr. Värdering av ett tillämpningsexempel för studier av högupplösande riktningsmätning i spaningsradar med digitala gruppantenner (Evaluation of an application example for studies of high resolution direction estimation in surveillance radar with digital beamforming array antennas). Technical Report FOA-R–98-00819-408–SE, FOI, June 1998. In Swedish.

Part II

Publications

Publication 1: Radar-Like Measurements with an Experimental Digital Beamforming Array Antenna

Svante Björklund, Per Grahn, Lars Pettersson: "Radar-Like Measurements with an Experimental Digital Beamforming Array Antenna", Proceedings of the International Radar Symposium IRS 98, Munich, Germany, 15-17 September 1998 [3]. Reproduced with permission from DGON (German Institute of Navigation).

Radar-Like Measurements with an Experimental Digital Beamforming Array Antenna

Svante Björklund, Per Grahn, Lars Pettersson

Department of Sensor Technology
Defence Research Establishment (FOA)
P.O. Box 1165, S-581 11 Linköping, Sweden

Tel: +46 13 37 80 00, Fax: +46 13 37 81 00
E-mail: svabj@lin.foa.se

Abstract

An experimental S-band digital beamforming receiving array antenna has been used in "radar-like" measurements, where radar signals with programmable waveforms are transmitted. The measurements are carried out in an anechoic chamber and the measured signals come from the direct path from transmitter antennas to the receiver antenna. In this way targets are simulated. On the received signals, conventional beamforming, pulse compression, doppler filtering and high resolution direction of arrival estimation are performed. Accurate channel calibration and channel equalization are utilized. This paper first describes the receiving antenna, transmitter control, measurement arrangements, calibration and signal processing. It then presents some measurement results for high resolution direction of arrival estimation and for radar resolution of one and two targets.

1. Introduction

At FOA (Defence Research Establishment of Sweden), an experimental S-band digital beamforming receiving array antenna has been designed and built. By a digital beamforming array antenna (or digital array antenna) we here mean a receiving array antenna where the signals from all the antenna elements are individually digitized and the beamforming is done digitally. In radar, this gives flexibility and new possibilities regarding beam steering, beam shape, multibeam capability, radar energy utilization, jammer and clutter suppression, multidimensional signal processing such as STAP (Space Time Adaptive Processing), model based signal processing (e.g. high resolution direction of arrival estimation), multifunction capability, adaptivity etc. In the future, radar systems with digital array antennas will be of increasing importance to counter the electronic warfare environment.

In our present project, we have used the antenna in "radar-like" measurements, where we transmit a radar signal with a desired PRF (Pulse Repetition Frequency) and waveform. The measurements are, so far, carried out in an anechoic chamber and the measured signals come from the direct path from transmitter antennas to receiver antenna. In this way targets are simulated and hence the term "radar-like". On the received signal, conventional processing (e.g. conventional beamforming, pulse compression, doppler filtering) and model based signal processing for direction of arrival (DOA) estimation are performed.

The purpose of this work at FOA is to gain knowledge and experience of signal processing with digital array antennas and of the use of digital array antennas in radar.

2. The experimental radar system

The experimental receiving antenna

The experimental receiving antenna consists of a horizontal linear array of 12 antenna element subarrays, a calibration network by which a calibration signal can be injected into all channels, and for each of the 12 channels a receiver module, an A/D converter and a buffer memory (figure 1 and 2). A larger number of antenna elements and channels would be desirable. The use of only 12 channels is a matter of cost but still it is possible to draw valuable conclusions.

The antenna elements are stripline dipoles, arranged in the horizontal linear array as vertical linear subarrays with 4 dipoles each. The antenna has an agile frequency band of 2.8-3.3 GHz and an instantaneous bandwidth of 5 MHz. The A/D-conversion is done at IF frequency and the final down conversion is done digitally. The experimental antenna itself has been discussed earlier, e.g. in [1].

From the buffer memories the signals are transferred to an ordinary computer ("Control computer" in figure 2) where the digital signal processing is done in non-real time.

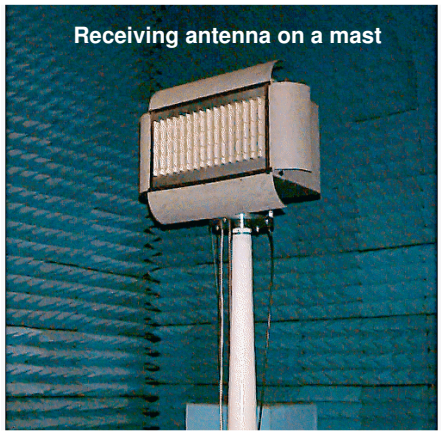

Figure 1: Photo of the receiving antenna in the anechoic chamber.

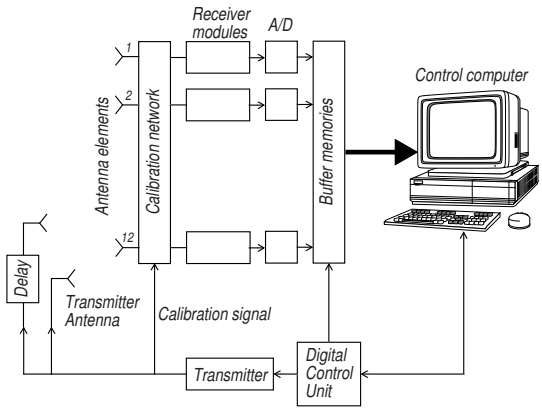

Figure 2: Physical block diagram of the experimental radar system.

Transmitter and waveform control

The digital control unit (figure 2) controls the transmitter and the data acquisition. It generates a programmable analog signal at the start of each radar pulse (figure 3b) that controls the waveform modulation (AM, phase modulation or FM) of the transmitter signal generator. Another programmable signal switches the carrier (RF) on and off (figure 3a). The PRF can be chosen and effects both signals. A commercially available signal generator is used as the transmitter. As transmitter antennas, some (1-3) horn antennas are used.

The digital control unit and the measurement system is described in more detail in reference [2].

Sampling, data acquisition, IQ-conversion and down conversion

At sampling, the signal is located at a IF frequency of 19.35 MHz, which is 3/4 of the sampling frequency 25.8 MHz of the12-bit A/D-converters. The total data acquisition rate for all channels is 464.4 Mbyte/s. The fast buffer memories consists of 1 Mword (12 bit) for each of the 12 channels and this allows for a maximum coherent data acquisition time of about 41 ms.

A prescribed number of data blocks with specified delay time K_{delay} before each block and specified time K_{PRI} between each block (figure 3c) can be collected. This facilitates the collection of radar returns from only a selected portion of range bins (for one or several pulses).

The IQ-conversion, filtering, down conversion and decimation is made in the frequency domain in the ordinary computer. In a real radar, this could be done in the time domain in special hardware, of which one example was given in [1].

The result is a complex base band signal vector $\mathbf{x}_{samp} = \mathbf{A}(t)e^{j\Phi(t)}$ with the sampling rate 6.45 MHz and with one vector element for each antenna channel.

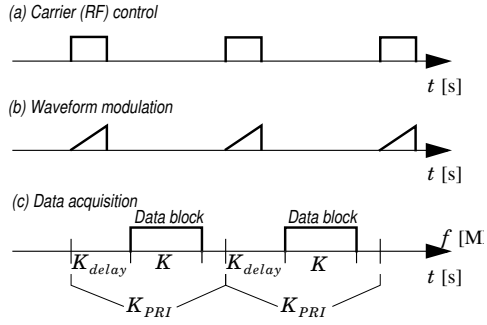

Figure 3: Carrier (RF) (a), waveform modulation (b)and data acquisition (c) control.

Calibration of frequency dependence (equalizing)

For many DOA estimation methods it is important that the frequency response is the same in all channels within the instantaneous bandwidth if high performance should be obtained. With narrow band signals, time delays are equal to phase shifts. Since the time delay to the antenna elements depends on the DOA of the signal source, a way to measure direction is to measure the phase shifts in all elements and then match these phase shifts to a plane wave from a certain direction. If the phases of the frequency responses of all the channels are not the same over the instantaneous bandwidth, the phase differences between the channels will vary with frequency. These phase differences will be interpreted as changes of the time delay to the antenna elements and therefore also as different directions (to the same signal source). In this case the direction estimation will become problematical when trying to find plane waves and the performance of the estimation will be degraded. Also amplitude differences will make the match to plane waves less accurate.

Since each receiver module has relatively narrow band analog anti-aliasing and image rejection filters, there will be differences between the antenna channels in the frequency response within the instantaneous bandwidth. These differences can, however, be reduced by an equalizing filter

in each channel, whose coefficients are based on calibration data (figure 4). By using a 15 tap FIR-filter, the differences can be almost completely eliminated (see [1]).

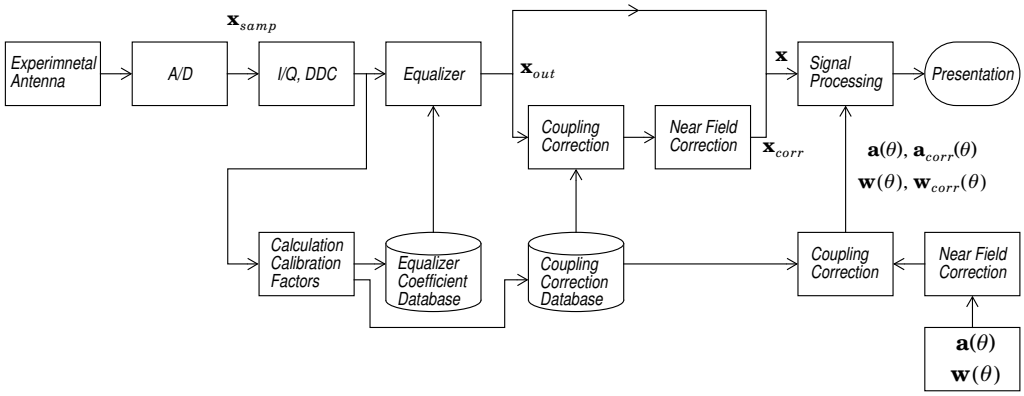

Figure 4: Digital filtering and calibration chain. $\mathbf{x}_{samp}$, $\mathbf{x}_{out}$, $\mathbf{x}_{corr}$ and $\mathbf{x}$ are antenna signal vectors at different places in the chain. Each vector has one vector element for each antenna channel. $\mathbf{a}(\theta)$ are steering vectors. $\mathbf{w}(\theta)$ are coefficient vectors for conventional beamforming. DDC means Digital Down Conversion. See also figure 6.

Calibration of direction dependence (coupling)

If, in the same way as with the frequency dependencies, the direction dependencies of the channels are not the same, the unwanted phase shifts and amplitude variations in the channels will confuse DOA estimation methods and decrease the performance.

By illuminating the antenna with a known incident wave, the amplitude and phase errors of the channels can be corrected. Due essentially to mutual coupling the antenna patterns of the antenna elements differ from each other, in particular for the edge elements, and the array sidelobes becomes higher than the nominal value. The mutual coupling can to a large extent be corrected by using a decoupling matrix, $\mathbf{C}$, calculated via a calibration procedure (see [1]). From the calibration procedure, a table $\mathbf{w}_{ctab}(\theta)$ with amplitude and phase corrections for a number of angles θ can also be obtained.

The correction of direction dependences can either be applied to the received signals $\mathbf{x}_{corr} = \mathbf{C}\mathbf{x}_{out}$, the beamforming weights $\mathbf{w}_{corr} = \mathbf{C}^H\mathbf{w}$ or the steering vectors $\mathbf{a}_{corr}(\theta) = \mathbf{C}^{-1}\mathbf{a}(\theta)$, where $\mathbf{C}^H$ denotes the complex conjugate transpose (Hermitian transpose) of $\mathbf{C}$. These methods will often not be identical, but often essentially equivalent. The steering vector $\mathbf{a}(\theta)$ is a model of the directional properties of the antenna and is used in many high resolution DOA estimation methods.

Radar signal processing

After IQ-conversion, down conversion, equalizing and perhaps coupling correction, the signal is stored in a radar datacube with indices for pulse, time in pulse and antenna channel (figure 5 and 6). For the following radar signal processing, a MATLAB toolbox [3] developed at FOA is used. Mainly methods for the estimation of the number of and the direction to signal sources are implemented but there are also functions for pulse compression, doppler filtering, coupling correction, signal simulation and visualization (figure 6).

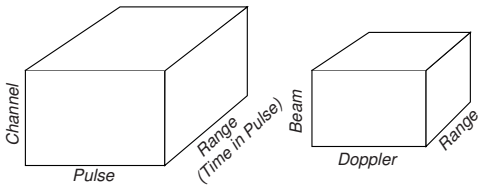

Figure 5: A received radar signal as a radar datacube before (left) and after (right) conventional processing.

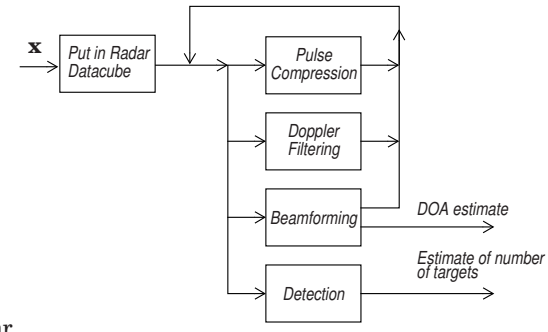

Figure 6: Data flow in the radar signal processing. $\mathbf{x}$ is the antenna signal vector. See also figure 4 and 5.

In this paper, the term “conventional processing” means linear filtering in the form of conventional beamforming (CBF), doppler filtering and pulse compression.

After conventional processing the indices of the radar datacube must be interpreted differently than before. “Pulse” has become “Doppler”. “Time in pulse” has become “Range”. “Channel” has become “Beam” or “Direction”. See figure 5.

Before or after conventional processing, high resolution estimation methods can be used to estimate the number of targets and DOA of targets (see figure 6). For many high resolution methods it is appropriate to correct for direction dependencies on the steering vector $\mathbf{a}(\theta)$ instead of on the signals and to use the table $\mathbf{w}_{ctab}(\theta)$ instead of the decoupling matrix $\mathbf{C}$: $\mathbf{a}_{corr}(\theta) = \mathrm{diag}(\mathbf{w}_{ctab}(\theta))^{-1}\mathbf{a}(\theta)$, where $\mathrm{diag}(\mathbf{w}_{ctab}(\theta))$ means making a diagonal matrix of the vector $\mathbf{w}_{ctab}(\theta)$. In this way corrections can be applied for each test direction separately. This is often more accurate than using the decoupling matrix $\mathbf{C}$ since we then rely on fewer assumptions.

Radar-like measurement arrangements

We have done measurements in an anechoic chamber at FOA. The measured signals came from the direct path from transmitter antennas to receiver antenna (figure 7). The distance

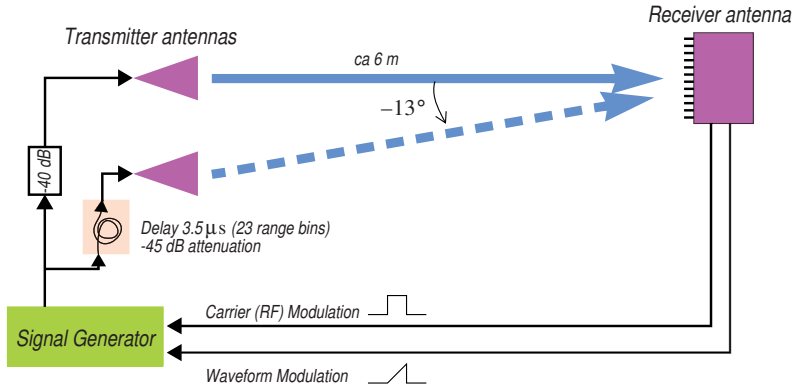

Figure 7: Arrangements for radar-like measurements.

between the transmitter and receiver antennas (6 m) is too short be considered a far field distance. However, the main part of this can be compensated for, either on the signals or on the steering vectors, since the measurement geometry is known and the signal is measured in each channel (figure 4). One signal generator was used as transmitter and one or two transmitter antennas as targets. One of the signals was delayed 3.5 μs (23 range bins) with an optical delay line. In this way two target with different directions of arrival and ranges could be simulated. However, the Doppler frequency of both "targets" were the same.

So far, we have mainly studied direction estimation properties of our "radar" system. In our continued study we will additionally look more at range and Doppler estimation properties. We will also use reflected target signals and bring the whole equipment outdoors and measure on different targets and clutter sources.

3. Conventional processing of a single target

Waveforms of the type Linear Frequency Modulation (linear FM or Chirp) have mostly been used in our measurements. The required bandwidth of the waveform modulation signal for phase modulation is unfortunately to large for our signal generator.

Before processing

Below is an example of the time properties of our system. A single target was present. The waveform modulation was Linear FM of length 64 time samples (range bins), corresponding to 9.9 μs, with a frequency deviation of 0.6 MHz and a PRF of 8.1 KHz. The signal to noise ratio (SNR) was about 44 dB per antenna channel and per time sample. Figure 8 shows the mean value over all

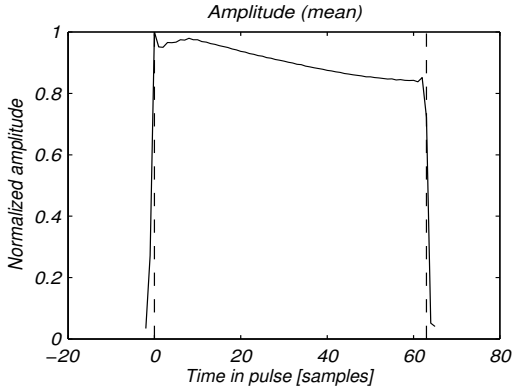

Figure 8: Example of normalized amplitude for linear FM as a function of time in pulse (range). SNR = 44 dB.

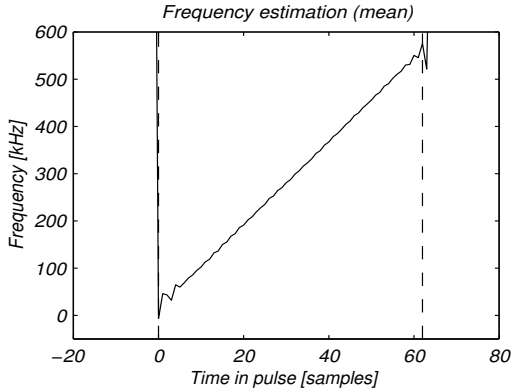

Figure 9: Example of mean value of estimated instantaneous frequency as a function of time in pulse (range). SNR = 44 dB.

128 pulses for the received amplitude as a function of time-in-pulse (range) after the previously described equalizing but before any further radar signal processing. The performed equalization makes the frequency responses the same in all channels but not equal to a constant. This is enough for signal processing in direction but for signal processing in time it is desirable with a constant frequency response. This constant frequency response should apply not only for the receiver antenna but for the whole analog system from D/A- conversion of the waveform modulation signal to A/D-conversion of the received signal. The absence of an equalization to a constant for the system is probably the reason for the time dependence in figure 8. Figure 9 displays the mean value over the 128 pulses of the instantaneous frequency as a function of time-in-pulse.

The standard deviation over the pulses of the instantaneous frequency was about 6 kHz. The performance of our radar system is partly dependent on the used signal generator. We are actually not interested in the properties of this signal generator but nevertheless they influence our measurement results.

After conventional processing

We have taken a measured waveform modulation from one antenna channel (containing its present equalizing filter) and one pulse as the reference waveform, thus including the effects of the whole analog system. This reference has been used for pulse compression of all channels and pulses. With this procedure we have matched the received signal to the right matched filter but we do not exactly get the properties of linear FM. Alternative procedures would be to equalize the system to a constant as discussed above or to optimize the sent waveform modulation given the known (measured) limitations (frequency response) of the whole system.

Figures 10 and 11 show two slices through the radar datacube after pulse compression, doppler filtering and conventional beamforming. No tapering was used in any dimension. The single target is clearly visible. Presently there is unfortunately a doppler offset in the system depending on a phase drift from pulse to pulse, which is probably due to the signal generator.

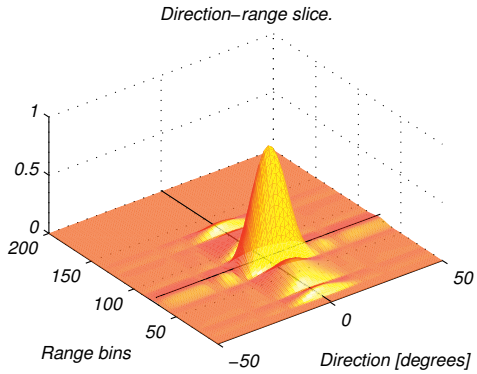

Figure 10: Absolute value for doppler channel 82 (frequency 1.1 kHz) after pulse compression, doppler filtering and CBF. No tapering in any dimension was used. Solid dark lines indicate the real position of the target.

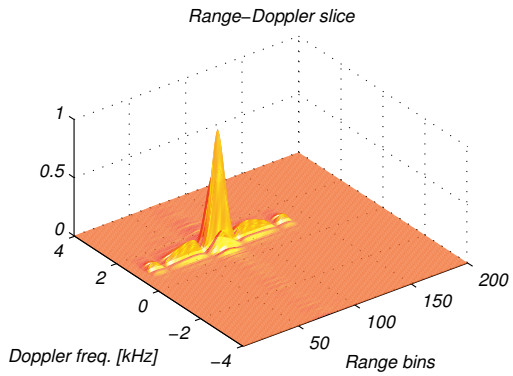

Figure 11: Absolute value for beam 26 (DOA 0°) after pulse compression, doppler filtering and CBF. No tapering in any dimension was used.

4. High resolution direction of arrival estimation

Conventional beamforming versus high resolution direction of arrival estimation

In conventional beamforming (CBF) the received antenna signals are phase shifted to compensate for the different lengths of the propagation paths to the different antenna elements. The signals can also be weighted (tapered) to produce low sidelobes and thereby reduce the influence by other signals sources. A drawback with CBF is that its resolution, i.e. how close in DOA two signal sources can be but still be seen as two sources, is limited by the size of the antenna, no matter how high SNR or how much data are available.

High resolution DOA estimation (here abbreviated “HRDE”) methods use model based signal processing. This means that they try to find a mathematical model that can generate the observed signal. The model contains a limited number of parameters, e.g. directions to targets, which are estimated from the observed signal. HRDE has some promising theoretical properties, among others high angle resolution (better than the conventional beamwidth and not limited by antenna size) and detection & estimation despite jamming. Other common names for HRDE are Sensor Array Signal Processing and DOA Estimation.

HRDE methods can be of two types: spectral and parametric. Parametric methods estimate the parameters (DOA etc.) of the signal sources directly. Especially popular are Maximum Likelihood methods and approximations of them. Spectral methods, MUSIC [5] is probably the best known, generate a directional spectrum, a continuous functions with peaks at signal source DOA:s. See figures 12, 16 and 17 for examples. From these peaks the DOA:s can be found.

For some reasons CBF is suitable to use as the basis method. When required, HRDE can be applied as a special radar function for the resolution of target groups, estimation of jammer directions, detection & estimation in jamming environments, handling of multipath etc. CBF can then be used as a base estimate for HRDE. This makes it unnecessary to engage HRDE on all data. This saves among others computation time.

Results from measurements

In figures 12 and 13, unmodulated continuous wave (CW) signals were used. Figure 12 displays

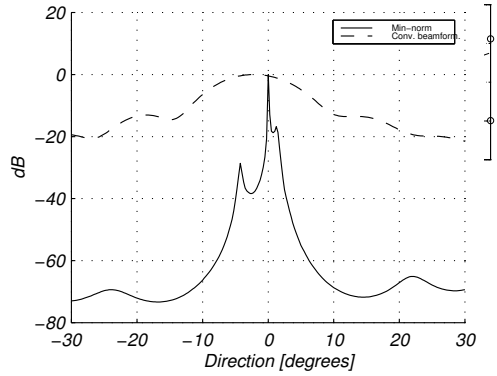

Figure 12: Directional spectra for CBF (no tapering) and the Min-Norm method. Three signals sources are present at angles –4.3° , 0° and 1.55° . SNR = 49 dB, 47 dB and 45 dB respectively.

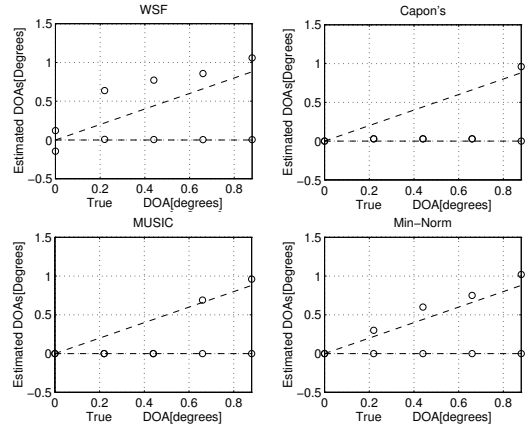

Figure 13: Resolution for the DOA estimation methods WSF, Capon, MUSIC and Min-Norm. The circles are the estimated DOA:s. Two circles at the same true DOA means that the signals could be resolved. The dashed lines are where true and estimated DOA:s are equal. The conventional beamwidth is about 11^o. From [4]. SNR = 50 dB.

directional spectra for CBF and the HRDE method Min-Norm [5]. CBF can not resolve the three signal sources but Min-Norm can just resolve them. In the same measurement the method WSF (Weighted Subspace Fitting [5]) delivered the estimates [-4.35, -0.05, 1.39] degrees for the DOA:s.

Figure 13 shows the result for the four methods WSF, Capon, MUSIC and Min-Norm [5] when two close sources have a varying angle separation from $0°$ to $0.88°$. The SNR was about 50 dB. It is notable that the resolution of some of them is better than 1/20 of the untapered conventional beamwidth that is about $11°$. Of course the resolution and accuracy obtained is dependent on the quality of the calibrations.

5. Resolution of two targets in direction and range

Below is an example of the resolution of two targets. The waveform parameters were same as in the example of the processing of the single target in section 3 but now two targets are present. Target A has the DOA $0°$ and SNR about 37 dB. The range is 11 range bins, which after pulse compression becomes 11+63=74 range bins. Target B has the DOA $-13°$, SNR 31 dB and is delayed 3.5 μs (23 range bins). The delay means that the range is 11+23+63=97 range bins.

Figure 14 shows a slice of the radar datacube after pulse compression, doppler filtering and CBF. The two targets are clearly visible. In figure 15, MUSIC is used instead of CBF. The result is a pseudo spectrum, that is not a measure of signal strength but a measure of the presence of signal sources. The spectrum is really narrow in the direction dimension but there are several peaks in the range dimension. The reason for the peaks in the range dimension is probably that MUSIC is sensible for the range sidelobes. This could maybe be avoided with lower sidelobes. As just said the height of the peaks does not tell us the level of the sidelobes.

It is more interesting to use HRDE methods when the DOA separation is smaller than here. Then HRDE can be used to resolve groups of targets in the same range bin, doppler channel and beam. Conventional processing then points out in which range, doppler and beam to use HRDE. Here, this could be range bin 74 and range bin 97. Figures 16 and 17 shows the MUSIC DOA spectra for range bin 74 respectively 97. In figure 16 we know from the CBF that there can be signal sources around $0°$. The peak at $-13°$ is outside the conventional beamwidth and is therefore probably false. The peak likely depends on the range sidelobes of the other target. In figure 17, for the same reason, the peak at $0°$ is probably false.

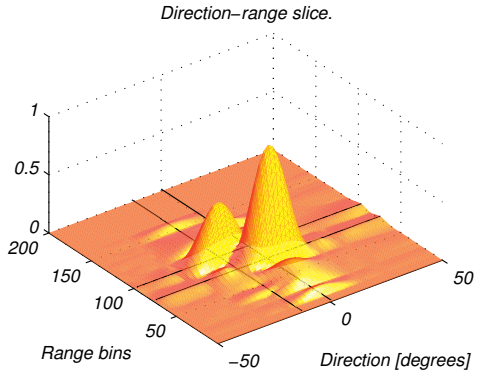

Figure 14: Absolute value for doppler frequency 2.0 kHz after pulse compresion, doppler filtering and CBF. No tapering in any dimension was used. Solid dark lines indicate the real positions of the targets.

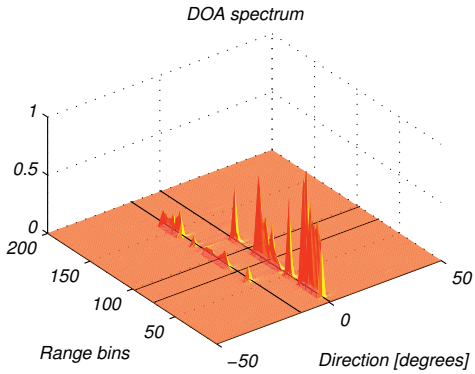

Figure 15: MUSIC DOA pseudo spectrum after pulse compresion and doppler filtering. No tapering in any dimension was used. Solid dark lines indicate the real positions of the targets.

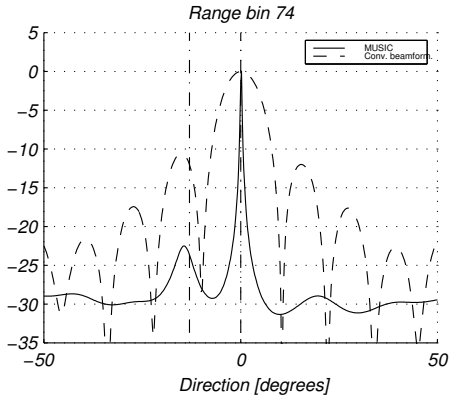

Figure 16: Directional spectra for CBF and MUSIC at range bin 74 and doppler frequency 2.0 kHz. No tapering of CBF. We know that the peak at $-13°$ for MUSIC is probably false because of information from the conventional detection. The vertical dashdotted lines at $-13°$ and $0°$ are the true DOA:s.

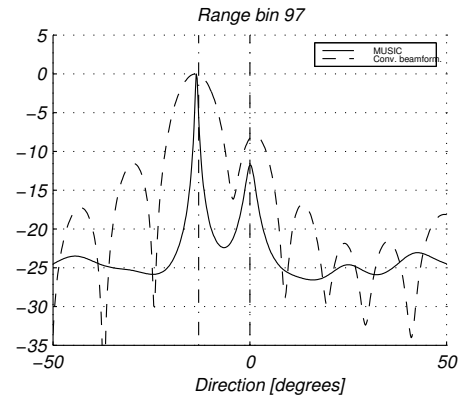

Figure 17: Directional spectra for conventional beamforming and MUSIC at range bin 97 and doppler frequency 2.0 kHz. No tapering of CBF. We know that the peak at $0°$ for MUSIC is probably false because of information from the conventional detection . The vertical dashdotted lines at $-13°$ and $0°$ are the true DOA:s.

6. References

[1] Pettersson L., Danestig M., Sjöström U.: "*An Experimental S-Band Digital Beamforming Antenna*", IEEE Aerospace and Electronics Systems Magazine, Nov. 1997, pp. 19-26.

[2] Björklund S., Grahn P., Lindström S., Pettersson L.: "*Measurement System for an S-Band Digital Beamforming Array Antenna*", Proceedings of the 1996 SNRV (the Swedish National Committee of URSI) and NUTEK Conference on Radio Sciences and Telecommunications (RVK 96), Luleå and Kiruna, Sweden, 3-6 June 1996, pp. 250-254.

[3] Björklund S.:"*A MATLAB Toolbox for Radar Signal Processing*", Proceedings of Nordic MATLAB Conference '97, Stockholm, Sweden, 27-28 October 1997.

[4] Heydarkhan A.:"*Model Based Direction of Arrival Estimation Methods Applied to Experimental Antenna Data*". Scientific Report FOA-R--97-00631-408--SE, FOA Nov. 1997.

[5] Krim H., Viberg M.:"*Two Decades of Array Signal Processing Research*", IEEE Signal Processing Magazine, July 1996, pp. 67-94.

Publication 2: High Resolution Direction of Arrival Estimation Methods Applied to Measurements from a Digital Array Antenna

HIGH RESOLUTION DIRECTION OF ARRIVAL ESTIMATION METHODS APPLIED TO MEASUREMENTS FROM A DIGITAL ARRAY ANTENNA

Svante Björklund[1], Amir Heydarkhan[2]

Defence Research Establishment (FOA), P.O. Box 1165, SE-581 11 Linköping, Sweden,
E-mail: [1]svabj@lin.foa.se, [2]amir_heydarkhan@hotmail.com

ABSTRACT

At the Defence Research Establishment of Sweden (FOA) an experimental S-band receiving digital array antenna for radar applications has been designed and built. It consists of a horizontal uniform linear array (ULA) of 12 antenna elements, whose digitized signals are processed in non-real time in a computer. Accurate calibration is utilized.

We have compared several spectral and parametric direction-of-arrival (DOA) estimation methods for varying DOA separations, number of samples and signal-to-noise ratios (SNR) on measured data from an anechoic chamber.

At ideal conditions the resolution can be improved considerably with model based DOA methods compared to conventional beamforming. We achieved a resolution below $^1/_{10}$ of the resolution of conventional beamforming.

1. INTRODUCTION

At FOA an experimental S-band receiving digital array antenna for radar applications has been designed and built. In an anechoic some measurements have been conducted which have been used for the comparison of some high resolution direction-of-arrival (DOA) estimation methods.

The experimental antenna itself and calibration procedures has been discussed earlier, e.g. in [7, 8]. An early version of the measurement system was presented in [1]. Parts of the signal processing software have been presented in [3] and a free version is available from the Internet [4]. Other measurement results have been published in for example [2, 7]. This paper is in part based on the FOA report [5].

2. THE EXPERIMENTAL ARRAY ANTENNA

The experimental receiving antenna (figure 1) consists of a horizontal linear array of 12 antenna elements (with half a wavelength separation), receiver modules, A/D converters and buffer memories (figure 2). With careful calibration we can model the antenna as a uniform linear array (ULA). The antenna has an agile frequency band of 2.8-3.3 GHz and an instantaneous bandwidth of 5 MHz. The sampling is performed at an IF (intermediate frequency) of 3/4 of the sampling frequency 25.8 MHz of the 12-bit A/D-converters. From the buffer memories the signals are transferred to a standard computer where the IQ-conversion, down conversion, calibration correction and spatial signal processing are performed in non-real time. Accurate channel equalization and spatial channel calibration are utilized. One or more commercially available signal generators and horn antennas are used as the transmitters.

Figure 1: The receiving experimental array antenna in the anechoic chamber.

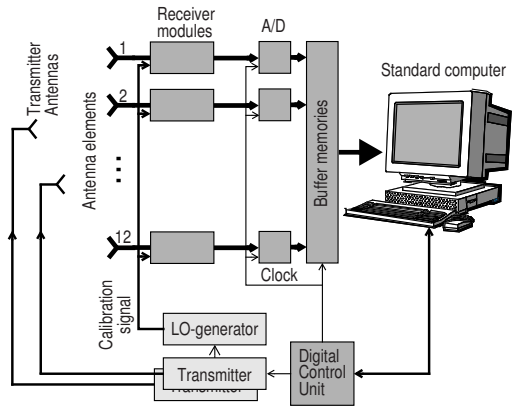

Figure 2: Physical block diagram of the experimental radar system

3. MEASUREMENT ARRANGEMENTS

The measurements have been performed in an anechoic chamber at FOA. The distance between the transmitter and receiver antennas (6 m) is too short be considered a far-field distance and consequently near-field corrections must be applied.

4. METHODS FOR DOA ESTIMATION

We have compared the following methods for DOA estimation [6]:

- Spectral methods: Conventional beamforming (CBF), Capon beamformer, MUSIC and Min-Norm.
- Parametric methods for general arrays: Deterministic Maximum Likelihood (DML), Stochastic Maximum Likelihood (SML), Signal Subspace Fitting (SSF) and Weighted Subspace Fitting (WSF).
- Parametric methods for uniform linear arrays (ULA): ESPRIT and Root-MUSIC.

For model based methods we assume two signal sources, the right number, as a priori knowledge. We find the DOAs of the spectral methods by searching the spectrum. By the used search method, it possible to deliver only one of the two DOAs if there is only one clear peak in the spectrum.

5. DOA ESTIMATION AS A FUNCTION OF DOA SEPARATION

In the following graphs (figure 3-12) there were two equal strong ($\mathrm{SNR} \approx 50\ \mathrm{dB}$) signal sources with constant carriers with a frequency difference of $0.2\ \mathrm{MHz}$ as waveforms. 64 time samples were used in the DOA estimation. The first source had the DOA $0°$ and the DOA of the second source was varied from $0°$ via $0.22°$, $0.44°$ and $0.66°$, $0.88°$ to $1.54°$. As a comparison, the conventional beamwidth is about $10°$, which is also approximately the resolution of conventional beamforming. In the graphs, the mean value and the standard deviation of the estimated DOAs of a set of 88 measurements are plotted for the different DOA separations and different DOA estimation methods. The set consists of all measurements from combining 11 mechanical azimuth angles ($-20°$ to $20°$ in steps of $4°$) of the receiving array antenna with 2 carrier frequencies and 4 replicates. The measurements were not conducted in random order. See figure 6 for how to interpret the graphs.

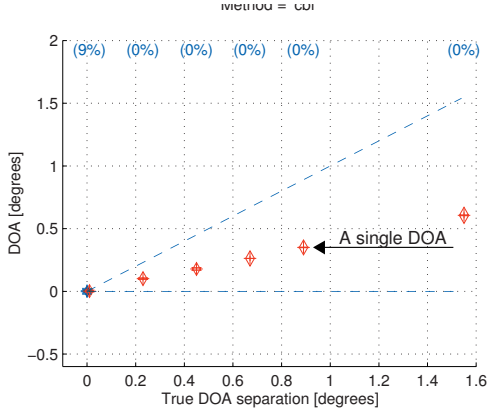

Figure 3: CBF DOA estimation versus DOA separation.

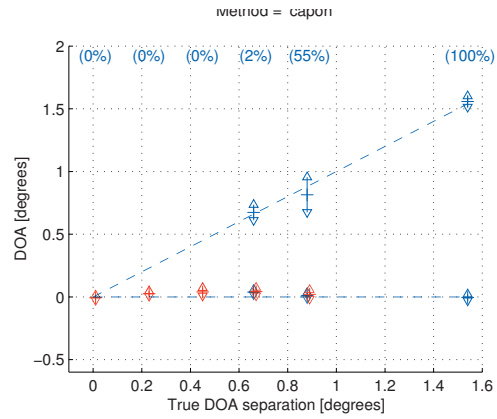

Figure 4: Capon DOA estimation vs. DOA separation.

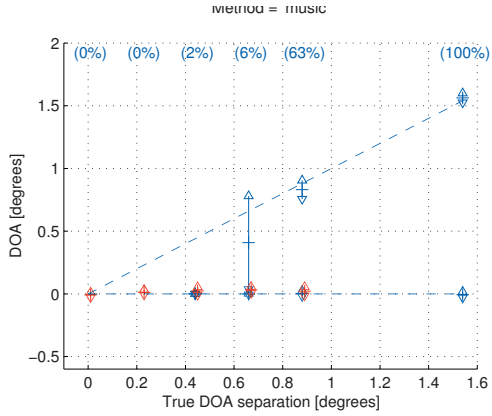

Figure 5: MUSIC DOA estimation vs. DOA separation.

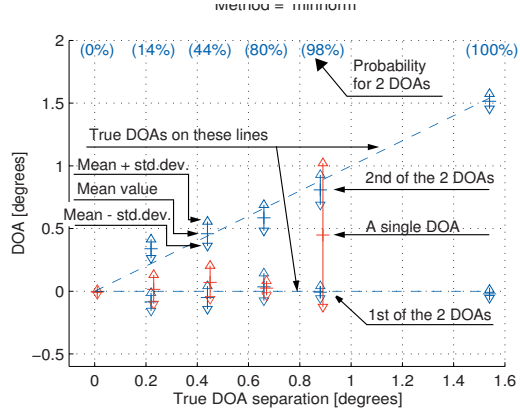

Figure 6: Min-Norm DOA estimation versus DOA separation. The mean values are shown by short horizontal lines. A vertical line is joining the two standard deviation arrows. At the top there are percent numbers telling the probability of resolving the two sources. For the measurements when they are not resolved, a third vertical line with mean value and standard deviation markers for the single estimated DOA is plotted just to the right of the two vertical lines for two resolved DOAs. The true DOAs lie on the dashed lines.

Figure 3 show that only one DOA can be estimated by CBF and it is located nearly half-way between the true DOAs.

The resolution for Capon (figure 4) seems to be slightly poorer than for MUSIC (figure 5) but it is difficult to determine because of the missing measurements with DOA separations between $0.88°$ and $1.54°$.

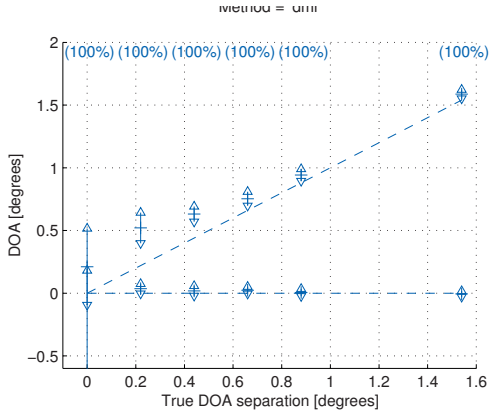

Figure 7: DML DOA estimation vs. DOA separation.

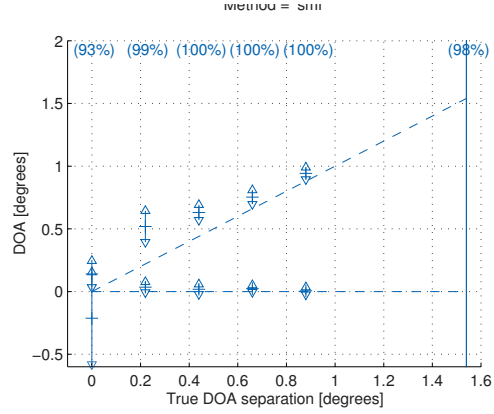

Figure 8: SML DOA estimation versus DOA separation. For some measurements the optimization routine failed, maybe a bug in MATLAB, therefore the resolution probability lower than 100%.

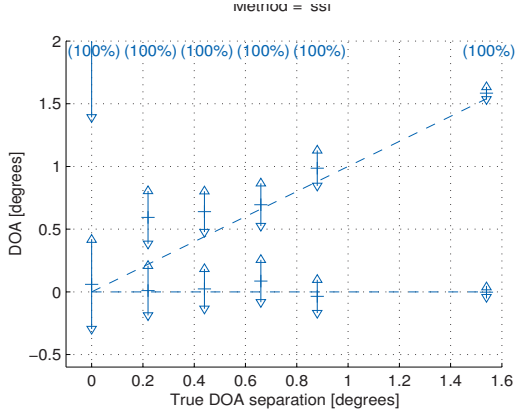

Figure 9: SSF DOA estimation as a function of DOA separation.

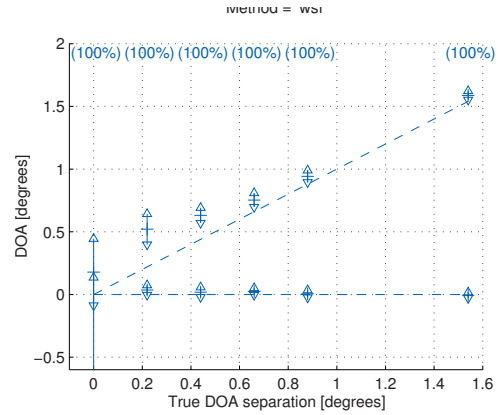

Figure 10: WSF DOA estimation as a function of DOA separation.

The similarity between the two methods can be explained by the fact that Capon and MUSIC are equivalent when $\mathrm{SNR} \to \infty$ and the SNR was very high in our measurements.

Min-Norm (figure 6) exhibits a better resolution than MUSIC (figure 5) but also a larger standard deviation (where the resolution probability is high).

The start values in the optimization of the general parametric DOA methods were $[-0.1^\circ, 0.1^\circ]$. DML, SML and WSF (figure 7, 8 and 10) have similar, and better than SSF (figure 9), performance with the exception that SML failed for some measurements (for unknown reason). All the general parametric methods (DML, SML, SSF and WSF) have a bias for the non-zero DOA which is increased when the DOA separation is decreased. The bias for the zero DOA (0°) is more or less independent of the DOA separation.

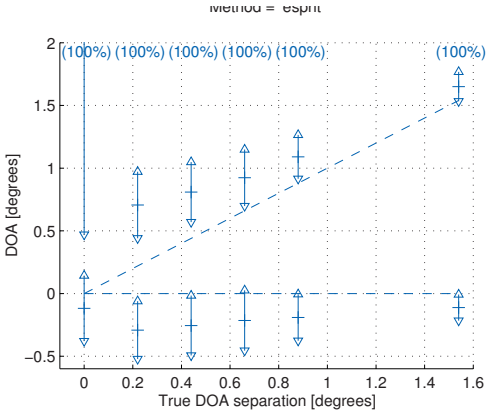

Figure 11: ESPRIT DOA estimation as a function of DOA separation.

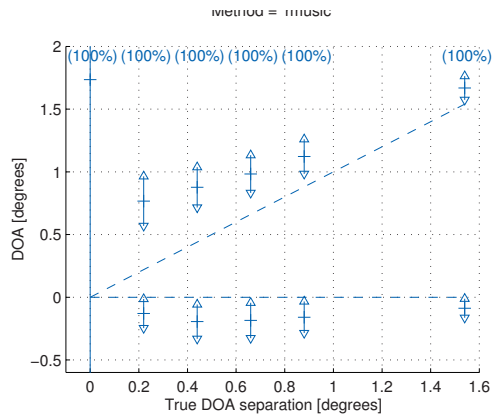

Figure 12: Root MUSIC DOA estimation as a function of DOA separation.

All parametric methods behave poorly at the DOA separation of $0°$ in contrast to the spectral methods which have the desired result of one source at DOA $0°$.

The parametric methods for ULAs, ESPRIT (figure 11) and Root-MUSIC (figure 12), have a larger bias and standard deviation than the general parametric methods. ESPRIT seems to have a larger standard deviation than Root-MUSIC. Both ESPRIT and Root-MUSIC have a significant bias also for the zero DOA and this bias is nearly independent of the DOA separation. The bias for the non-zero DOA is increased when the DOA separation is decreased, as for the general parametric methods.

6. DOA ESTIMATION AS A FUNCTION OF NUMBER OF SAMPLES

We continue with DOA estimations where we have varied the number of time samples used in the estimation from 2 to 100. The two signal sources were equal strong ($\text{SNR} \approx 50$ dB) and had the DOAs $0°$ and $0.66°$ respectively. The waveforms were constant carriers with a frequency difference of 0.2 MHz. The methods MUSIC, Min-Norm, DML, SML, WSF, ESPRIT and Root-MUSIC were studied in a single measurement without statistical analysis. All methods except MUSIC needed less than 25 samples for convergence, although with some bias and variance. The differences in needed samples between these methods seem small. MUSIC needed more than 30 samples. Due to space limitations no graphs are presented here.

7. DOA ESTIMATION VERSUS SNR

In the last measurements the signal sources were located at $0°$ and $1.54°$. The waveform was a constant carrier. 256 time samples were used in the estimation. The sources were equal strong and the SNR was varied from 1.4 dB to 50 dB in six steps. The result from a single measurement without statistical analysis is presented in figures 13-14. MUSIC seems to require a higher SNR than the other tested methods (figures 13-14).

8. FURTHER DISCUSSION

As can be seen in the graphs, the estimation of the DOA $0°$ often works better (can be resolved, lower bias and standard deviation) than the other DOA. The reason for this is that the calibration of the receiv-

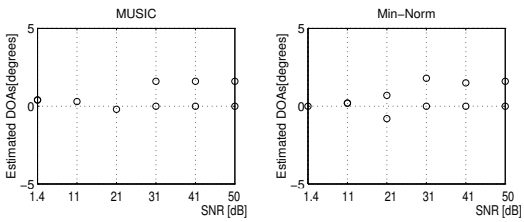

Figure 13: DOA estimation with MUSIC and Min-Norm versus the SNR. The graphs are from [5].

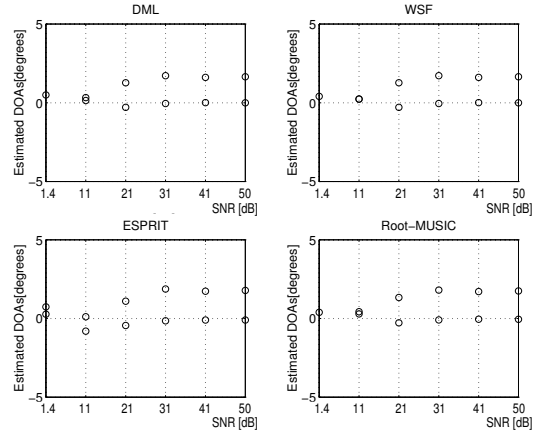

Figure 14: DOA estimation with DML, WSF, ESPRIT and Root-MUSIC vs. the SNR. The graphs are from [5].

ing antenna was conducted with the source with DOA $0°$. However, this improvement applies only for correction table calibration and not decoupling matrix calibration [8]. This is the reason for the high bias and standard deviation of the zero DOA for ESPRIT and Root-MUSIC since these methods only can use the decoupling matrix while the other methods use the correction table.

The standard deviation of the DOA estimates in this paper is partly due to the inaccuracy of the antenna turn table [8].

There could be more factors, like carrier frequency and calibration method, than the ones studied in this paper that affect the result. A more systematic investigation might show which factors and factor interactions that affect the result.

In this paper we have not addressed the important and difficult problem of estimating the number of signal sources. This estimation decides the resolution performance, i.e. the ability to separate two close sources.

9. CONCLUSIONS

It is not obvious how to define DOA resolution but nonetheless we draw the following conclusion. At ideal conditions (accurate calibration, high SNR, no interference, etc.) the resolution can be improved considerable with model based DOA methods compared to conventional beamforming. In our experiments we achieved a resolution below $^1/_{10}$ of the resolution of conventional beamforming.

We also draw the following general conclusions from the result. The parametric methods for ULAs have the largest bias. The methods DML, SML and WSF have the smallest standard deviation.

REFERENCES

[1] S. Björklund, P. Grahn, S. Lindström, L. Pettersson, "Measurement System for an S-Band Digital Beamforming Array Antenna", *Proc. of RVK 96 (Swedish URSI symposium.)*, Luleå, Sweden, 3-6 June 1996, pp. 250-254.

[2] S. Björklund, P. Grahn, L. Pettersson, "Radar-Like Measurements with an Experimental Digital Beamforming Array Antenna", *Proc. of the International Radar Symposium IRS 98*, Munich, Germany, 15-17 Sept. 1998, pp. 993-1002.

[3] S. Björklund, D. Rejdemyhr, "A MATLAB Toolbox for Radar Array Processing", *Proceedings of ISSPA `99 (IEEE Fifth International Symposium on Signal Processing and its Applications)*, August 22-25, 1999, Brisbane, Australia, pp. 547-550.

[4] DBT, A MATLAB Toolbox for Radar Array Processing. A free version is available at <http:// www.s2.chalmers.se/~athley/dbt/>.

[5] A. Heydarkhan, "*Model Based Direction of Arrival Estimation Methods Applied to Experimental Antenna Data*", FOA Report number FOA-R--97-00631-408--SE, 1997.

[6] H. Krim, M. Viberg, "Two Decades of Array Signal Processing Research", *IEEE Signal Processing Magazine*, July 1996, pp. 67-94.

[7] L. Pettersson, M. Danestig, U. Sjöström, "An Experimental S-Band Digital Beamforming Antenna", *IEEE Aerospace and Electronics Systems Magazine*, Nov. 1997, pp. 19-26.

[8] L. Pettersson: "*An S-band Digital Beamforming Antenna: Design, Procedures and Performance*", FOA Report FOA-R--99-01162-408--SE, 1999.

Publication 3: Auxiliary Beam Terrain-Scattered Interference Suppression: Reflection System and Radar Performance

Svante Björklund, Anders Nelander, Mats I. Pettersson: "Auxiliary Beam Terrain-Scattered Interference Suppression: Reflection System and Radar Performance", IET Radar, Sonar & Navigation, Volume 7, Issue 8, October 2013, pp. 836-847. Reproduced with permission from The Institution of Engineering & Technology.

Published in IET Radar, Sonar and Navigation
Received on 22nd December 2011
Revised on 7th September 2012
Accepted on 2nd October 2012
doi: 10.1049/iet-rsn.2011.0407

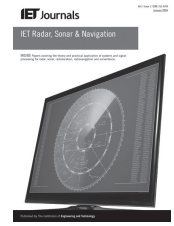

ISSN 1751-8784

Auxiliary beam terrain-scattered interference suppression: reflection system and radar performance

Svante Björklund[1,2], Anders Nelander[1], Mats I. Pettersson[2]

[1]*Swedish Defence Research Agency (FOI), P.O. Box 1165, SE-581 11 Linköping, Sweden*
[2]*Blekinge Institute of Technology, SE-371 79 Karlskrona, Sweden*
E-mail: svabj@foi.se

Abstract: Terrain-scattered interference (TSI), that is, jammer signals reflected on the earth's surface, is a significant problem to military airborne radar. In auxiliary beam TSI suppression, the TSI in the main radar beam is estimated by a single or several auxiliary beams and is subtracted from the main beam channel. The signal to subtract is the auxiliary beam signals fed through an estimate of the 'reflection system', which describes scattering on the surface. The authors first present results on the structure of this TSI suppression, on the estimation of the reflection system and on the quality of the estimate. Then the authors derive theoretical expressions for the signal-to-interference plus noise ratio (SINR) and the remaining TSI power for a single auxiliary beam. Since the SINR is directly connected to the radar performance, it can be seen what factors affect the performance and how. It was noted that when the estimated reflection system is missing one or more delays of the true system, the TSI filter cannot suppress the TSI signal completely. This phenomenon, which is called 'TSI leakage', has a very large impact on the performance. The SINR cannot be kept constant. Instead, an 'SINR improvement' can be defined.

1 Introduction

'Terrain-scattered interference' (TSI) or 'hot clutter' are signals from jammers which are reflected on the ground or sea before they are received by a radar. In the mainbeam an often weak target signal has to compete with TSI. TSI is a significant problem to military airborne radar systems and should be suppressed.

Several approaches to suppress TSI are proposed in the literature. Low sidelobes [1], adaptive beamforming and sidelobe cancellation (SLC) [2] are suggested to be used against TSI in the sidelobes. Fast-time space-time adaptive processing (STAP) [3–7] is proposed to be used against TSI in the mainbeam. Fast-time means range bin to range bin sampling. It does not mean fast execution. In cases where both monostatic (normal) clutter and TSI exist, the monostatic clutter is suggested to be suppressed either separately before [7] or after [4, 7] the TSI suppression or together with the TSI by three-dimensional (3D) STAP [4, 8]. All three approaches have advantages and drawbacks [4, 7]. Some of the literature about TSI suppression is not widely accessible. After the year 2005 we have found nearly nothing published about TSI suppression.

Fast-time TSI suppression methods for TSI in the mainbeam are usually of one of two different architectures [4], either the 'auxiliary beam' architecture (also called 'sidelobe canceller' [4]), where the TSI signal in the main radar channel is subtracted by an estimated TSI signal from a single or multiple auxiliary channels, or the 'fully adaptive array' (also called 2D STAP [13] or 'Direct Form Processor' [8]), where all antenna channels are processed together.

In the auxiliary beam architecture, the TSI signal in the main radar channel is generated by a 'reflection system' with the transmitted jammer signal as input. This system is created by scatterers on the ground or sea with different time delays and directions of arrival. In the fully adaptive array there is no explicit reflection system, since there are no special main and auxiliary channels.

This article consists of two parts. In the first part (Sections 2 and 3) we utilise results from the field of 'system identification' [9] and present a new way to view the auxiliary beam architecture which is centred around the reflection system. We model the reflection system by a linear regression and employ least squares to estimate it, which both are well-known theories. By describing the reflection system as a linear regression we can include both structures of the auxiliary beam architecture, namely 'single auxiliary beam' and 'multiple auxiliary beam', in the same framework and we can choose which time delays and channels to include in the model of the reflection system. By the least squares theory and extensions by us we obtain theoretical expressions for the quality of the estimate of the reflection system. These quality expressions can be interesting by themselves but will become really interesting in the second part (Sections 4–6), where we use them in our derivation of theoretical expressions for the remaining TSI power after suppression and resulting signal-to-interference plus noise ratio (SINR) for a single auxiliary beam when using estimated reflection systems.

We can see what factors affect the SINR and how they do it. It is well-known that the SINR is directly related to radar performance in the form of probability of detection, detection range and estimation accuracy. There the advantages with our new way of viewing the auxiliary beam architecture are realised.

We will see that our use of the reflection system is equivalent to the ubiquitous sample matrix inversion (SMI) method in the STAP and adaptive beamforming literature, which makes our results widely applicable for auxiliary beam TSI suppression.

Some of our results in Sections 2 and 3 are taken from our conference paper [10] but we have extended them with much new material. For instance, paper [10] only treated the single auxiliary beam structure. Some material in [10] is removed here. The results in Sections 4–6 are all new and not published before.

Probably the best survey of TSI suppression methods is article [4]. That article also describes single and multiple auxiliary beam TSI suppression in a general form, by but using the STAP SMI approach, which is different from ours. It does not have any derivations of the suppression methods but the derivations can be found in other literature. Furthermore, it does not model the reflection system and does not contain quality expressions. Gabel *et al.* [4] assume that all delays are used, that is, there are no holes in the delay sequence. Finally, Gabel *et al.* [4] do not consider noise in the auxiliary channels.

In [8], an expression for the optimal SINR in the single auxiliary beam is given but only for a known reflection system. Neither is it stated where the receiver noise enters, which makes a comparison with our results more difficult. A classical result for SINR loss as a function of the number of estimation data and model order for the fully adaptive array when using estimated interference properties is presented in [11]. It cannot be used directly for our problem since the architectures of the suppression methods are different. The result in [11] also assumes the data to have a certain and known probability distribution (Gaussian). Our results are not restricted to that.

In Section 2 we describe the two structures of auxiliary beam TSI suppression, viz. the single auxiliary beam and multiple auxiliary beam structures, and fit both these structures into a general structure. Section 3 treats the estimation of the reflection system, including theoretical expressions for the quality of the estimate. Then in Section 4 we derive the theoretical expressions for TSI power and SINR. We validate that theory with simulations in Section 5. In Section 6 we have a discussion and finally in Section 7 we give some conclusions.

Vectors are denoted by bold lower case letters, matrices by bold upper case letters. Complex conjugate of a quantity b is denoted by b^*, transpose of a matrix $\boldsymbol{B}$ by $\boldsymbol{B}^{\mathrm{T}}$ and complex conjugate transpose by $\boldsymbol{B}^{H}$.

2 Auxiliary beam TSI suppression methods

This section describes the auxiliary beam TSI suppression architecture. Section 2.1 presents a general structure for this architecture, which is then specialised to the single auxiliary beam and multiple auxiliary beam cases in Sections 2.2 and 2.3. By the general structure and the specialisations we will realise that the estimation methods and the properties of the estimated reflection system in Section 3 are valid for both the single and multiple auxiliary beam structures.

2.1 General structure

Auxiliary beam TSI suppression can be depicted by the block diagram in Fig. 1. The principle is to estimate and remove the TSI signal $r(t)$ in the radar main channel signal $m(t)$, where we look for the target. We utilise one or several auxiliary radar beams directed towards the jammer or towards the TSI in other directions than the main beam in order to estimate the TSI signal in the main beam. Since we employ a signal which is both spatial from an array antenna and temporal in fast-time, the suppression method belongs to the fast-time STAP group.

The received radar signal in the main channel is (see Fig. 1)

$$\begin{aligned} m(t) &= \boldsymbol{B}_{\mathrm{M}}(\boldsymbol{r}_{\mathrm{M}}(t) + \boldsymbol{s}_{\mathrm{M}}(t) + \boldsymbol{n}_{\mathrm{M}}(t)) = \boldsymbol{B}_{\mathrm{M}}(\boldsymbol{r}_{\mathrm{M}}(t) + \boldsymbol{e}_{\mathrm{M}}(t)) \\ &= r(t) + e(t) \end{aligned} \tag{1}$$

where $\boldsymbol{r}_{\mathrm{M}}(t)$ are the TSI signals, $\boldsymbol{s}_{\mathrm{M}}(t)$ is the reflected radar signal from targets and (normal) clutter, $\boldsymbol{n}_{\mathrm{M}}(t)$ is the receiver noise in the antenna channels used for the main channel and $\boldsymbol{e}_{\mathrm{M}}(t) = \boldsymbol{s}_{\mathrm{M}}(t) + \boldsymbol{n}_{\mathrm{M}}(t)$. The block $\boldsymbol{B}_{\mathrm{M}}$ is the main channel beamformer. The signals $r(t) = \boldsymbol{B}_{\mathrm{M}}\boldsymbol{r}_{\mathrm{M}}(t)$ and $e(t) = \boldsymbol{B}_{\mathrm{M}}\boldsymbol{e}_{\mathrm{M}}(t)$ are the TSI signal and 'noise' in the main channel. The subscript M is used for the main channel and A for the auxiliary channels.

The block $\boldsymbol{H}_{\mathrm{M}}(q)$ in Fig. 1 is a reflection system from the transmitted jammer signal $\boldsymbol{d}(t)$ to the main channel antenna elements. In the auxiliary channels, $\boldsymbol{H}_{\mathrm{A}}(q)$ and $\boldsymbol{B}_{\mathrm{A}}$ are reflection system and beamformer, respectively, and $\boldsymbol{v}_{\mathrm{A}}(t)$ is receiver noise plus any remaining interference (jammer and radar signal).

The beamformers $\boldsymbol{B}_{\mathrm{M}}$ and $\boldsymbol{B}_{\mathrm{A}}$ are static (i.e. memory-less) linear systems with spatial signals as input and output. These systems can be represented by matrices. Compare with the blocks '$\boldsymbol{s}$' and 'B' in Fig. 3*a* in [8]. The systems $\boldsymbol{H}_{\mathrm{M}}(q)$, $\boldsymbol{H}_{\mathrm{A}}(q)$, $\boldsymbol{H}_{\mathrm{MA}}(q)$ and $\hat{\boldsymbol{H}}_{\mathrm{MA}}(q)$ (see below) are linear dynamic systems in fast-time. The input and output signal vectors are spatial. The beamformers $\boldsymbol{B}_{\mathrm{M}}$ and $\boldsymbol{B}_{\mathrm{A}}$ are chosen by us and are therefore known, while the systems $\boldsymbol{H}_{\mathrm{M}}(q)$ and $\boldsymbol{H}_{\mathrm{A}}(q)$ are unknown.

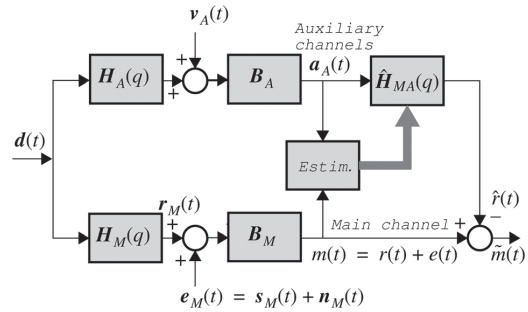

Fig. 1 *Block diagram of auxiliary beam TSI suppression*

$\boldsymbol{d}(t)$ is the transmitted jammer signal. In the auxiliary channels $\boldsymbol{v}_A(t)$ is the receiver noise plus remaining interference (jammer and radar signal), $\boldsymbol{H}_A(q)$ is the reflection system and $\boldsymbol{B}_A$ is the beamformer

In the main channel, $r(t)$ is the reflected jammer signal, $\boldsymbol{H}_{\mathrm{M}}(q)$ and $\boldsymbol{B}_{\mathrm{M}}$ are the reflection system and beamformer, $\boldsymbol{s}_{\mathrm{M}}(t)$ is the reflected radar signal from targets and monostatic clutter and $\boldsymbol{n}_{\mathrm{M}}(q)$ is the receiver noise. $\hat{\boldsymbol{H}}_{\mathrm{MA}}(q)$ is the estimated reflection system in (3)

doi: 10.1049/iet-rsn.2011.0407

The system $\boldsymbol{H}_{\mathrm{MA}}(q)$ such that

$$\boldsymbol{H}_{\mathrm{MA}}(q)\boldsymbol{B}_{\mathrm{A}}\boldsymbol{H}_{\mathrm{A}}(q) = \boldsymbol{B}_{\mathrm{M}}\boldsymbol{H}_{\mathrm{M}}(q) \tag{2}$$

is what we call 'the reflection system'. If we estimate $\hat{\boldsymbol{H}}_{\mathrm{MA}}(q)$ such that

$$\hat{\boldsymbol{H}}_{\mathrm{MA}}(q)\boldsymbol{B}_{\mathrm{A}}\boldsymbol{H}_{\mathrm{A}}(q) = \boldsymbol{B}_{\mathrm{M}}\boldsymbol{H}_{\mathrm{M}}(q) \tag{3}$$

then the TSI in the main channel can be cancelled perfectly.

2.2 Single auxiliary beam

In the 'single beam structure', only a single auxiliary beam is used to estimate the TSI signal. The beam is aimed directly towards the jammer, while placing a null in the main beam direction. We assume that the auxiliary beam can measure the direct jammer signal perfectly, giving $\boldsymbol{B}_{\mathrm{A}}\boldsymbol{H}_{\mathrm{A}}(q) = 1$ (a scalar) and $\boldsymbol{a}_{\mathrm{A}}(t) = a(t) = d(t) + v(t)$. The block diagram in Fig. 1 can be simplified to Fig. 2, where $H(q) = \boldsymbol{B}_{\mathrm{M}}\boldsymbol{H}_{\mathrm{M}}(q)$ and $\hat{H}_{\mathrm{MA}}(q) = \hat{H}(q)$ with an estimate of the reflection system $H(q)$. The signals are $r(t) = \boldsymbol{B}_{\mathrm{M}}\boldsymbol{r}_{\mathrm{M}}(t)$, $s(t) = \boldsymbol{B}_{\mathrm{M}}\boldsymbol{s}_{\mathrm{M}}(t)$, $n(t) = \boldsymbol{B}_{\mathrm{M}}\boldsymbol{n}_{\mathrm{M}}(t)$ and $v(t) = \boldsymbol{B}_{\mathrm{A}}\boldsymbol{v}_{\mathrm{A}}(t)$.

Other names of this TSI mitigation method are 'selected auxiliary TSI mitigation' [4] and 'single beam hot clutter canceller' [5]. The method is also said to be treated in some not widely available literature, like [12–14]. This approach is also commonly used for noise and interference reduction in time [15] and in space [2, 16].

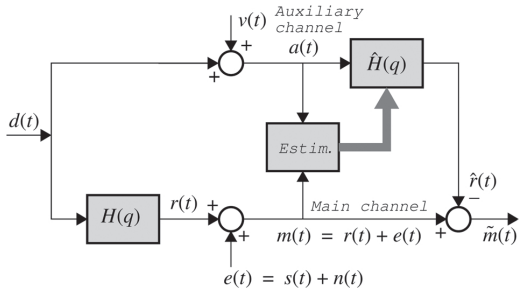

Fig. 2 *Block diagram of single auxiliary beam TSI suppression*

$d(t)$ is the direct jammer signal. $v(t)$ is the receiver noise plus remaining interference in the auxiliary channel. $H(q)$ is the reflection system and $r(t)$ is the TSI (hot clutter), $s(t)$ is the reflected radar signal from targets and (normal) clutter and $n(t)$ is the receiver noise in the main channel

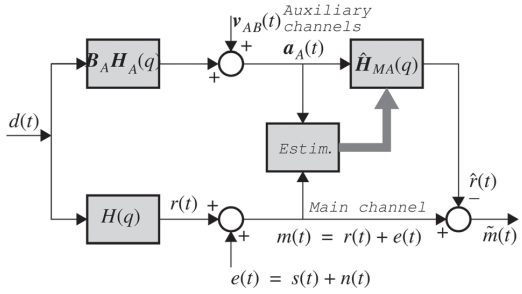

Fig. 3 *Block diagram of multiple auxiliary beam TSI suppression*

$d(t)$ is the direct jammer signal. $\boldsymbol{v}_{AB}(t)$ is the receiver noise plus remaining interference in the auxiliary channels. In the main channel, $H(q)$ is the reflection system, $r(t)$ is the TSI signal, $s(t)$ is the reflected radar signal from targets and monostatic clutter and $n(t)$ is receiver noise

Note that the processing is conducted in two steps:

1. Adaptive processing in space: Estimate (in the auxiliary channel) and suppress (in the main channel) the direct jammer signal. This is done by forming a beam in the auxiliary channel and placing a null in the main channel towards the jammer.
2. Adaptive processing in time: Suppress the TSI signals in the main channel.

Here we assume a single jammer, $\boldsymbol{d}(t) = d(t)$. If there are several jammers, each jammer has to be suppressed separately. We form an auxiliary beam towards the direct signal of each jammer while placing nulls in the antenna pattern towards the direct signal from the other jammers. For this we need sufficiently many spatial degrees of freedom. After the nulling, the remaining jammer signals in the auxiliary beam can be regarded as noise.

Despite the simple structure of single auxiliary beam TSI suppression, it has some advantages over other suppression methods, see [4, 7, 17]. It also has some drawbacks, see [4, 5].

2.3 Multiple auxiliary beams

In the 'multiple beam structure', also called the 'Generalised sidelobe canceller' (GLC) method [4, 5], M beams are formed, one of which is the main beam and the other $M-1$ auxiliary beams must be chosen orthogonal to the main beam to prevent target leakage into the auxiliary channels.

In this structure, Fig. 1 can be simplified to Fig. 3. This block diagram is similar to the one for the single beam structure but with the difference that there are now several spatial channels in the systems and signals in the auxiliary branch. Note that now, $\boldsymbol{B}_{\mathrm{A}}\boldsymbol{H}_{\mathrm{A}}(q) \neq 1$ (not a scalar) and $\boldsymbol{a}_{\mathrm{A}}(t) = \boldsymbol{B}_{\mathrm{A}}\boldsymbol{H}_{\mathrm{A}}(q)d(t) + \boldsymbol{v}_{\mathrm{AB}}(t)$ with $\boldsymbol{v}_{\mathrm{AB}}(t) = \boldsymbol{B}_{\mathrm{A}}\boldsymbol{v}_{\mathrm{A}}(t)$. We again assume a single jammer.

In the multiple beam structure, the reflection system estimate $\hat{\boldsymbol{H}}_{\mathrm{MA}}(q)$ should not be an estimate of $H(q) = \boldsymbol{B}_{\mathrm{M}}\boldsymbol{H}_{\mathrm{M}}(q)$ but of $\boldsymbol{H}_{\mathrm{MA}}(q)$ in (2). We call $\boldsymbol{H}_{\mathrm{MA}}(q)$ the 'generalised reflection system'. The signals $r(t)$, $s(t)$, $n(t)$ are as in Section 2.2.

Also in this structure we have two-step processing as in Section 2.2 but now we have several beams in the auxiliary branch by which to estimate the jammer signal. There are advantages and drawbacks also with the multiple beam structure of auxiliary beam TSI suppression, see [4].

3 Estimation of the reflection system

We define a model of the reflection system for the single beam and multiple beam structures of auxiliary beam TSI suppression in Section 3.1. Then, in Section 3.2 we show how the reflection system can be estimated. In Section 3.3 we present theoretical expressions for the quality of the estimated reflection system.

3.1 Model of the reflection system

We model the TSI signal in the main channel $r(t)$ with a linear regression

$$r(t) = \boldsymbol{\varphi}^{\mathrm{T}}(t)\boldsymbol{h} \tag{4}$$

The vector $\boldsymbol{\varphi}^{\mathrm{T}}(t)$ only contains signals $a(t)$ or $a_k(t)$ (see below) and $\boldsymbol{h}$ are the impulse response coefficients in the

model of the reflection system $\boldsymbol{H}_{\mathrm{MA}}(q)$ with $\boldsymbol{H}_{\mathrm{MA}}(q)$ being defined by (2). The elements of $\boldsymbol{\varphi}^{\mathrm{T}}(t)$ are called *regressors*. Since $\boldsymbol{\varphi}^{\mathrm{T}}(t)$ only contains input signals of the system, (4) is a finite impulse response (FIR) system. Other model structures would also be possible, for example, auto-regression with extra inputs (ARX) or output error (OE) [9]. Especially for the single beam structure, FIR model of the reflection system $\boldsymbol{H}_{\mathrm{MA}}(q) = H(q)$ is natural because the reflection system can be seen as created by reflections of the transmitted jammer signal at a finite number of point scatterers with different delays.

In the single beam structure, the vector $\boldsymbol{\varphi}^{\mathrm{T}}(t)$ contains the direct jammer signals

$$\boldsymbol{\varphi}^{\mathrm{T}}(t) = [a(t),\ \ldots,\ a(t - T_{\mathrm{SA}} + 1)]$$

and

$$\boldsymbol{h} = [h(0),\ \ldots,\ h(T_{\mathrm{SA}} - 1)]^{\mathrm{T}} \tag{5}$$

where T_{SA} is the maximum time delay for this structure.

In the multiple beam structure the vector $\boldsymbol{\varphi}^{\mathrm{T}}(t)$ contains the received jammer signals in the $M-1$ auxiliary channels

$$\boldsymbol{\varphi}^{\mathrm{T}}(t) = [a_1(t),\ \ldots,\ a_1(t - T_{\mathrm{GLC}} + 1),\ \ldots,\ a_{M-1}(t),\ \ldots,\ a_{M-1}(t - T_{\mathrm{GLC}} + 1)]$$

where $a_i(t)$ is the signal in the ith auxiliary channel at fast time t and T_{GLC} is the maximum time delay for this structure. Here, the impulse response $\boldsymbol{h}$ of the system $\boldsymbol{H}_{\mathrm{MA}}(q)$ (2) is

$$\boldsymbol{h} = [h_1(0),\ \ldots,\ h_1(T_{\mathrm{GLC}} - 1),\ \ldots,\ h_{M-1}(0),\ \ldots,\ h_{M-1}(T_{\mathrm{GLC}} - 1)]^{\mathrm{T}}$$

where $h_i(\tau)$ are the coefficients for the ith auxiliary channel at fast time delay τ.

The number of coefficients in $\boldsymbol{h}$ is $n = T_{\mathrm{SA}}$ for the single beam structure and $n = T_{\mathrm{GLC}}(M-1)$ for the multiple beam structure if there are no 'holes' in the possible sequence of coefficients. Note that it is not necessary that the coefficients are consecutive in time and antenna channels. There may be 'holes' in the sequence. We may keep the most important coefficients (the most important scatterers), discard the other and obtain a better estimate of the reflection system. This is a problem in itself. It is related to 'compressed sensing/sampling' [18]. See [9, 19, 20] for general information on how to choose regressors/coefficients. We will see in Section 5.3 that the choice of proper coefficients is important for radar performance.

3.2 Estimation of the reflection system

There are several methods in the literature to estimate a system like the reflection system without the noise $\boldsymbol{v}_{\mathrm{A}}(t)$ in the auxiliary channels. In [10], we saw that the least squares (LS) method [21] and the prediction error method (PEM) [9], well-known in the field of 'system identification', are equivalent for this system. The Wiener filter, which minimises the minimum mean square error (MMSE) [22], can also be employed for the reflection system estimation [5]. Compared with the PEM/LS method, the Wiener/MMSE filter uses ideal ensemble mean values instead of averages of measured data. The ensemble mean values must be estimated and natural choices are the averages used in the PEM/LS method. Then the PEM, LS, Wiener and MMSE methods will give exactly the same estimator of the reflection system. Therefore the expressions for the quality of the estimated reflection system in Section 3.3 will be valid for all these methods.

We will here show how the reflection system can be estimated with the (deterministic) LS [21]. We can write (1) in a different way

$$\boldsymbol{m}(t_0) = \boldsymbol{r}(t_0) + \boldsymbol{e}(t_0) \tag{6}$$

and the estimate of the TSI signal

$$\hat{\boldsymbol{r}}(t_0) = \boldsymbol{A}(t_0)\hat{\boldsymbol{h}}$$

where $\boldsymbol{m}(t_0) = [m(t_0),\ \ldots,\ m(t_0 + N - 1)]^{\mathrm{T}}$, $\boldsymbol{r}(t_0) = [r(t_0),\ \ldots,\ r(t_0 + N - 1)]^{\mathrm{T}}$, $\boldsymbol{e}(t_0) = [e(t_0),\ \ldots,\ e(t_0 + N - 1)]^{\mathrm{T}}$, $\hat{\boldsymbol{r}}(t_0) = [\hat{r}(t_0),\ \ldots,\ \hat{r}(t_0 + N - 1)]^{\mathrm{T}}$ and

$$\boldsymbol{A}(t_0) = \begin{bmatrix} \boldsymbol{\varphi}^{\mathrm{T}}(t_0) \\ \vdots \\ \boldsymbol{\varphi}^{\mathrm{T}}(t_0 + n - 1) \\ \vdots \\ \boldsymbol{\varphi}^{\mathrm{T}}(t_0 + N - 1) \end{bmatrix} \tag{7}$$

In (6) and (7) the time index t_0 indicates the point of time when the estimation is performed. In the following, t_0 will be omitted in order to simplify the notation. The quantity N is the number of 'estimation data' or 'identification data'. The estimation data consists of $a(t)$ or $a_k(t)$ in $\boldsymbol{A}$ and of $m(t)$ in $\boldsymbol{m}$.

The estimation problem is with this notation for both the single and multiple beam structures

$$\hat{\boldsymbol{h}} = \arg\min_{\boldsymbol{h}} V_N(\boldsymbol{h}) \tag{8}$$

with the loss function $V_N(\boldsymbol{h})$

$$V_N(\boldsymbol{h}) = \|\boldsymbol{m} - \hat{\boldsymbol{m}}\|^2 \tag{9}$$

where $\|\cdot\|$ denotes the Euclidean norm of a vector. Without radar returns in the main channel we choose $\hat{\boldsymbol{m}} = \hat{\boldsymbol{r}} = \boldsymbol{A}\hat{\boldsymbol{h}}$

Equation (8) has the solution

$$\hat{\boldsymbol{h}} = \arg\min_{\boldsymbol{h}} V_N(\boldsymbol{h}) = (\boldsymbol{A}^{\mathrm{H}}\boldsymbol{A})^{-1}\boldsymbol{A}^{\mathrm{H}}\boldsymbol{m} \tag{10}$$

If we define $N\boldsymbol{f}_N = \boldsymbol{A}^{\mathrm{H}}\boldsymbol{m}$ and $N\boldsymbol{R}_N = \boldsymbol{A}^{\mathrm{H}}\boldsymbol{A}$, that is

$$\boldsymbol{f}_N = \frac{1}{N}\sum_{t=0}^{N-1} \boldsymbol{\varphi}^*(t)m(t) \text{ and } \boldsymbol{R}_N = \frac{1}{N}\sum_{t=0}^{N-1} \boldsymbol{\varphi}^*(t)\boldsymbol{\varphi}^{\mathrm{T}}(t) \tag{11}$$

we can write the solution (10) as

$$\hat{\boldsymbol{h}} = \boldsymbol{R}_N^{-1}\boldsymbol{f}_N \tag{12}$$

We see that this is also the PEM estimate [9]. Furthermore, we realise the matrix $\boldsymbol{R}_N$ is the sample matrix estimate of the ubiquitous interference covariance matrix in adaptive

doi: 10.1049/iet-rsn.2011.0407

beamforming and STAP [4, 8]. Thus (12) is the usual SMI filter weights of the SLC architecture of adaptive beamforming and STAP [4, 8]. This means that our results apply to the usual adaptive beamforming and STAP filter.

We now generalise the LS estimation to the weighted least squares problem (WLS) by introducing the weighting matrix $\boldsymbol{W}$

$$\hat{\boldsymbol{h}} = \arg\min_{\boldsymbol{h}} V_N(\boldsymbol{h}) \tag{13}$$

with the loss function $V_N(\boldsymbol{h})$ now using a weighted norm

$$\begin{aligned} V_N(\boldsymbol{h}) &= \|\boldsymbol{m} - \hat{\boldsymbol{m}}\|_{\boldsymbol{W}}^2 = \|\boldsymbol{m} - \boldsymbol{A}\boldsymbol{h}\|_{\boldsymbol{W}}^2 \\ &= (\boldsymbol{m} - \boldsymbol{A}\boldsymbol{h})^{\mathrm{H}}\boldsymbol{W}(\boldsymbol{m} - \boldsymbol{A}\boldsymbol{h}) \end{aligned} \tag{14}$$

and with the solution [21]

$$\hat{\boldsymbol{h}} = \arg\min_{\boldsymbol{h}} V_N(\boldsymbol{h}) = (\boldsymbol{A}^{\mathrm{H}}\boldsymbol{W}\boldsymbol{A})^{-1}\boldsymbol{A}^{\mathrm{H}}\boldsymbol{W}\boldsymbol{m} \tag{15}$$

if $(\boldsymbol{A}^{\mathrm{H}}\boldsymbol{W}\boldsymbol{A})$ is invertible. With $\boldsymbol{W} = \boldsymbol{I}$ the solution (15) is the same as the unweighted LS solution (10).

The weighting matrix $\boldsymbol{W}$ in WLS is useful when the noise $\boldsymbol{e}$ is not white. The noise $\boldsymbol{e}$ could be non-white when the target is distributed or the clutter is correlated, in both cases when the radar resolution is high. By choosing the weighting matrix as

$$\boldsymbol{W} = (\boldsymbol{R}_{\boldsymbol{e}}^{*})^{-1} \tag{16}$$

with $\boldsymbol{R}_{\boldsymbol{e}} = \mathrm{E}\{(\boldsymbol{e} - \mathrm{E}\{\boldsymbol{e}\})^{*}(\boldsymbol{e} - \mathrm{E}\{\boldsymbol{e}\})^{\mathrm{T}}\}$ we achieve the smallest variance of the estimate $\hat{\boldsymbol{h}}$. This can be realised by using the Gauss–Markov theorem in [21] and our definition of the covariance matrix in calculations similar to the ones in [21]. This estimate $\hat{\boldsymbol{h}}$ is called the 'best linear unbiased estimate' (BLUE), the 'minimum variance unbiased estimator' (MVUE) or the 'Markov estimate'. See also [9].

If the noise $v(t)$ in the auxiliary channels is not negligible, an approach is to use total least squares (TLS) [21, 23]. In [24], LS and TLS were compared in three radar applications for 'cancellation of electromagnetic noise-like interference in modern radar systems'. TLS gave better performance in two of the applications and LS in one. TLS was less robust than LS and required more computations. The conclusion was that LS is the preferred choice. In our application, the single auxiliary beam structure might cope better with the noise $v(t)$ in the auxiliary channel than the multiple beam structure because the jammer signal is stronger compared with the noise. Therefore LS could be appropriate for single beam and TLS for multiple beam TSI suppression.

Important aspects on employing auxiliary beam TSI suppression is the point of time to estimate the reflection system, the point of time to apply the estimate and what estimation data to choose. Since the TSI is non-stationary, the reflection system must be updated regularly, typically once for each pulse repetition interval (PRI) [4, 7]. The application of the system estimate should be as close as possible in time to the estimation data and the estimation data should be free of monostatic clutter [4, 7]. The single beam structure might cope better with monostatic clutter and targets in the estimation data because the direct jammer signal is strong in the auxiliary channel because the beam is aimed directly towards the jammer.

We will see in this article that the number of estimation data N should be large for good quality of the estimated reflection system and for good radar performance (SINR). However, if we choose too many estimation data some of them will be outdated because of the non-stationarity of the TSI. This will result in lower performance [7]. See Rabideau [7] for suggestions on how to obtain estimation data and how to apply the suppression filter, that is, the reflection system.

To cope with large signal dimensions and lack of sufficient estimation data in STAP, rank reduction methods are suggested in the literature. In our auxiliary beam TSI suppression architecture, rank reduction can be performed by a matrix multiplication on the received radar snapshot, see [8]. The beamforming matrix $\boldsymbol{B}_{\mathrm{A}}$ in Fig. 1 may contain a matrix for spatial rank reduction.

3.3 Quality of the estimated reflection system

3.3.1 Bias of the estimate: Assume that the (true) received signal in the main beam is

$$\boldsymbol{m} = \boldsymbol{A}\boldsymbol{h}_0 + \boldsymbol{e} \tag{17}$$

where the jammer signals in $\boldsymbol{A}$ are deterministic, $\boldsymbol{h}_0$ is the true impulse response of the reflection system and the stochastic vector $\boldsymbol{e} = \boldsymbol{s} + \boldsymbol{n}$ is our 'noise' (consists of target and clutter reflections $\boldsymbol{s}$ and the receiver noise $\boldsymbol{n}$). Then, from (15) and (17) the WLS estimate of $\boldsymbol{h}$ will be

$$\begin{aligned} \hat{\boldsymbol{h}} &= (\boldsymbol{A}^{\mathrm{H}}\boldsymbol{W}\boldsymbol{A})^{-1}\boldsymbol{A}^{\mathrm{H}}\boldsymbol{W}\boldsymbol{m} \\ &= (\boldsymbol{A}^{\mathrm{H}}\boldsymbol{W}\boldsymbol{A})^{-1}\boldsymbol{A}^{\mathrm{H}}\boldsymbol{W}(\boldsymbol{A}\boldsymbol{h}_0 + \boldsymbol{e}) \\ &= \boldsymbol{h}_0 + (\boldsymbol{A}^{\mathrm{H}}\boldsymbol{W}\boldsymbol{A})^{-1}\boldsymbol{A}^{\mathrm{H}}\boldsymbol{W}\boldsymbol{e} \end{aligned} \tag{18}$$

The bias of the estimated impulse response is

$$\begin{aligned} \boldsymbol{b} &= \mathrm{E}\{\hat{\boldsymbol{h}}\} - \boldsymbol{h}_0 \\ &= \mathrm{E}\{(\boldsymbol{A}^{\mathrm{H}}\boldsymbol{W}\boldsymbol{A})^{-1}\boldsymbol{A}^{\mathrm{H}}\boldsymbol{W}\boldsymbol{e}\} \\ &= (\boldsymbol{A}^{\mathrm{H}}\boldsymbol{W}\boldsymbol{A})^{-1}\boldsymbol{A}^{\mathrm{H}}\boldsymbol{W}\boldsymbol{m}_{\boldsymbol{e}} \end{aligned} \tag{19}$$

where $\boldsymbol{m}_{\boldsymbol{e}} = \mathrm{E}\{\boldsymbol{e}\}$. If the mean value of $\boldsymbol{e}$ is zero, that is, $\boldsymbol{m}_{\boldsymbol{e}} = 0$, the bias of the estimate $\hat{\boldsymbol{h}}$ will be zero. This can also be realised using results from system identification by noting that our FIR model $\boldsymbol{m} = \boldsymbol{A}\boldsymbol{h} + \boldsymbol{e}$ is at the same time an OE model [9]. It is known that it is possible to estimate OE models without bias if the true system can be described exactly by the model. This is valid even if the noise model cannot describe the true noise system. However, this would not be the case if we had general ARX structures [9]. These would not be of the OE structure. Ljung [9] has more information about this. If the mean value of $\boldsymbol{e}$ is not zero, then the bias of the estimate $\hat{\boldsymbol{h}}$ will probably not be zero.

If the criterion is unweighted, that is, $\boldsymbol{W} = \boldsymbol{I}$, the bias simplifies to

$$\boldsymbol{b} = \frac{1}{N}\boldsymbol{R}_N^{-1}\boldsymbol{A}^{\mathrm{H}}\boldsymbol{m}_{\boldsymbol{e}} \tag{20}$$

Since $\boldsymbol{A}$ consists of the jammer signal $d(t)$, we obtain the following

$$\boldsymbol{b} \propto 1/\sqrt{\lambda_{\mathrm{d}}} \tag{21}$$

where $\propto$ means 'proportional to' and λ_d is the jammer power in the estimation data.

We see from (19)–(21) that the bias depends on the mean value of $\boldsymbol{e}$, the received jammer signals in $\boldsymbol{A}$ (especially the jammer power λ_d), the weighting matrix $\boldsymbol{W}$ and the number of estimation data N. We realise from (18) that the bias is independent of the colour of the noise $e(t)$.

We have performed some simulations to validate the quality expressions for the reflection system. With the ideal radar setup and ideal reflection system in Section 5.1, our theoretical bias and estimated bias (considered the truth) agreed excellently. For the realistic setup and realistic system, the bias agreement was not so good.

3.3.2 Covariance of the estimate: If there is no bias, that is, $\mathrm{E}\{\hat{\boldsymbol{h}}\} = \boldsymbol{h}_0$, in the estimated coefficients $\hat{\boldsymbol{h}}$, the covariance matrix of $\hat{\boldsymbol{h}}$ is, from (18)

$$\begin{aligned}\boldsymbol{P}_N &= \mathrm{Cov}\{\hat{\boldsymbol{h}}\} = \mathrm{E}\{(\hat{\boldsymbol{h}} - E\{\hat{\boldsymbol{h}}\})^*(\hat{\boldsymbol{h}} - \mathrm{E}\{\hat{\boldsymbol{h}}\})^{\mathrm{T}}\} \\ &= \mathrm{E}\{(\boldsymbol{A}^{\mathrm{H}}\boldsymbol{W}\boldsymbol{A})^{-*}\boldsymbol{A}^{\mathrm{T}}\boldsymbol{W}^*\boldsymbol{e}^*\boldsymbol{e}^{\mathrm{T}}\boldsymbol{W}^{\mathrm{T}}\boldsymbol{A}^*(\boldsymbol{A}^{\mathrm{H}}\boldsymbol{W}\boldsymbol{A})^{-\mathrm{T}}\} \\ &= (\boldsymbol{A}^{\mathrm{T}}\boldsymbol{W}^*\boldsymbol{A}^*)^{-1}\boldsymbol{A}^{\mathrm{T}}\boldsymbol{W}^*\boldsymbol{R}_{\boldsymbol{e}}\boldsymbol{W}^{\mathrm{T}}\boldsymbol{A}^*(\boldsymbol{A}^{\mathrm{T}}\boldsymbol{W}^{\mathrm{T}}\boldsymbol{A}^*)^{-1} \end{aligned} \tag{22}$$

where $\boldsymbol{B}^{-*} = (\boldsymbol{B}^{-1})^* = (\boldsymbol{B}^*)^{-1}$ and $\boldsymbol{B}^{-\mathrm{T}} = (\boldsymbol{B}^{-1})^{\mathrm{T}} = (\boldsymbol{B}^{\mathrm{T}})^{-1}$.

If the noise $\boldsymbol{e}$ is white, that is, its covariance matrix $\boldsymbol{R}_{\boldsymbol{e}} = \lambda_e\boldsymbol{I}$, where λ_e is the power of $e(t)$ in the estimation data, and the criterion is unweighted, that is, $\boldsymbol{W} = \boldsymbol{I}$, the covariance simplifies to

$$\boldsymbol{P}_N = \lambda_e(\boldsymbol{A}^{\mathrm{T}}\boldsymbol{A}^*)^{-1} = \lambda_e((\boldsymbol{A}^{\mathrm{H}}\boldsymbol{A})^{-1})^* = \frac{1}{N}\lambda_e(\boldsymbol{R}_N^{-1})^* \tag{23}$$

where $\boldsymbol{R}_N$ is given by (11). When we derive the remaining TSI power and SINR after suppression (Section 4.1) we need (23). In [9], similar calculations as here are performed but only for systems with real valued signals. The application of TSI suppression is not treated in [9, 21]. Since $\boldsymbol{A}$ consists of the jammer signal $d(t)$, the following is also valid

$$\boldsymbol{P}_N \propto 1/(\mathrm{E}\{d^2(t)\}) = 1/\lambda_{\mathrm{d}} \tag{24}$$

We see, stronger the jammer better the $\hat{\boldsymbol{h}}$.

The true power λ_e of $\boldsymbol{e}$ in (23) is not known but can be estimated. If $\mathrm{E}\{\boldsymbol{e}\} = 0$ and $\boldsymbol{e}$ is white, an unbiased estimate is given by [9]

$$\hat{\lambda}_e = \frac{N}{N-n}V_N(\boldsymbol{h})$$

where $V_N(\boldsymbol{h})$ is the loss function (9) or (14). Thus an estimate of $\boldsymbol{P}_N$ in the white noise case is

$$\hat{\boldsymbol{P}}_N = \frac{1}{N}\hat{\lambda}_e(\boldsymbol{R}_N^{-1})^* \tag{25}$$

When the bias of $\hat{\boldsymbol{h}}$ is zero and n and N are large, we have approximately for the variance of the frequency function of the estimated jammer reflection system $\hat{H}(q)$ [9]

$$\mathrm{Var}\{\hat{H}(e^{j\omega})|\boldsymbol{h})\} \approx \frac{n}{N}\frac{\Phi_e(\omega)}{\Phi_d(\omega)} \tag{26}$$

where $\Phi_e(\omega)$ and $\Phi_d(\omega)$ are the frequency spectra at estimation for $e(t) = s(t) + n(t)$ and $d(t)$, respectively. Here we clearly see that increasing the model order n makes the estimated model worse but increasing the number of estimation data N makes the model better. Increasing the 'noise' (target, clutter and receiver noise power) and/or decreasing the jammer signal power at estimation time will make the estimated model worse and vice versa.

3.3.3 Noise in a single auxiliary channel: We now look at what happens for the single auxiliary beam case if we have estimated the reflection system as in Section 3.2, but there is noise present in the auxiliary channel at estimation time, that is, $v(t) \neq 0$. Then $\hat{\boldsymbol{h}}$ in (12) and (15) will not be optimal but we can still compute the covariance $\boldsymbol{P}_N = \mathrm{Cov}\{\hat{\boldsymbol{h}}\}$. We assume now that $d(t)$ and $v(t)$ are uncorrelated in time and with each other. This assumption should be valid, except perhaps for a repeater jammer, when $d(t)$ might be correlated in time. We have not seen any literature about TSI and its suppression for repeater jammers. Then

$$\boldsymbol{R}_N = \frac{1}{N}\left(\sum_{t=0}^{N-1}\boldsymbol{\varphi}^*(t)\boldsymbol{\varphi}^{\mathrm{T}}(t)\right) \simeq (\lambda_{\mathrm{d}} + \lambda_v)\boldsymbol{I}_n \tag{27}$$

where $\lambda_{\mathrm{d}} = \mathrm{E}\{|d(t)^2|\}$ and $\lambda_v = \mathrm{E}\{|v(t)^2|\}$ are the jammer power and auxiliary noise power in the estimation data and $\boldsymbol{I}_n$ is the $n \times n$ identity matrix. If $d(t)$ and $v(t)$ are ergodic processes then $\boldsymbol{R}_N$ will converge to the right side of (27) when $N \to \infty$. For limited N (27) will be an approximation. From (23) and (27) we now obtain the covariance matrix of the estimated reflection system

$$\boldsymbol{P}_N = \frac{1}{N}\lambda_e(\boldsymbol{R}_N^{-1})^* \simeq \frac{1}{N}\frac{\lambda_e}{\lambda_{\mathrm{d}} + \lambda_v}\boldsymbol{I}_n \tag{28}$$

Here we see how the number of estimation data, the power of jammer, auxiliary channel noise and main channel noise (target, clutter and receiver noise) at the estimation influence the variance of the estimated reflection system. It seems like in (28) that stronger noise in the auxiliary channel at the estimation will give a better estimated system and better TSI suppression. However, the estimated coefficients will probably obtain a bias because $v(t)$ is a false 'jammer signal' which is not present in the main channel. This we have seen by simulations. We will need (28) in Section 4.1.

In our simulations with the ideal radar setup and ideal reflection system in Section 5.1, our theoretical variance and estimated variance (considered the truth) was excellent. For the realistic setup and realistic system, the agreement was rather good. We noted that it is important to take the noise $v(t)$ in the auxiliary channel into account as in (28).

4 Theory for TSI power and SINR

In this section, we derive theoretical expressions for the remaining TSI power after suppression and the SINR in the single auxiliary beam structure.

4.1 Remaining TSI power after suppression

First, we derive expressions for the remaining TSI power in the main channel before and after suppression. These

doi: 10.1049/iet-rsn.2011.0407

quantities are the key quantities from which we can derive other quantities like the SINR.

We model the true reflection system coefficients $h(t)$ as stochastic and the estimated reflection system coefficients $\hat{h}(t)$ as the true coefficients $h(t)$ plus zero mean uncorrelated errors $\varepsilon(t)$

$$\hat{h}(t) = h(t) + \varepsilon(t) \tag{29}$$

This implies that the bias of the estimated coefficients will be zero (Section 3.3.1) and the vectors $\boldsymbol{h}$ and $\hat{\boldsymbol{h}}$ in (5), (12) and (15) will be stochastic.

The signals $r(t)$ and $\hat{r}(t)$ are then stochastic processes which are statistically dependent on $\boldsymbol{h}$. The powers, expectations and variances which we compute are conditioned on $\boldsymbol{h}$. When we write $\mathrm{V}\{\hat{h}(t)\}$, we mean $\mathrm{V}\{\hat{h}(t)\} = \mathrm{Var}\{\hat{h}(t)|\boldsymbol{h}\}$, which is the variance of the coefficients of the estimated reflection system when $\boldsymbol{h}$ is known. This variance is the diagonal element of $\boldsymbol{P}_N$ in (22), (23) and (28).

If we assume $d(t)$ is a white process, we can write the TSI power in the main channel without suppression as

$$\begin{aligned}\mathrm{Power}\{r(t)\} &= \mathrm{E}\{|r(t)|^2|\boldsymbol{h}\} = \mathrm{E}\left\{\left|\sum_{\tau=0}^{n-1} h(\tau)d(t-\tau)\right|^2 |\boldsymbol{h}\right\} \\ &= \mathrm{E}\left\{\sum_{\tau=0}^{n-1} |h(\tau)|^2 |d(t-\tau)|^2 |\boldsymbol{h}\right\} \\ &= P_d \sum_{\tau=0}^{n-1} \mathrm{E}\{|h(\tau)|^2|\boldsymbol{h}\} \\ &= P_d \sum_{\tau=0}^{n-1} |h(\tau)|^2 = P_d\|\boldsymbol{h}\|^2\end{aligned} \tag{30}$$

The third equality follows from $d(t)$ being uncorrelated in time. The quantity P_d is the jammer power during TSI suppression filtering. $\|\boldsymbol{h}\|$ is the Euclidean norm of vector $\boldsymbol{h}$ and is also a measure of the strength of the true reflection system. We see in (30) that the power of $r(t)$ is dependent on jammer power and the strength of the reflection system, as expected.

Now, we first note that

$$\begin{aligned}\mathrm{V}\{\hat{h}(t)\} &\equiv \mathrm{Var}\{\hat{h}(t)|\boldsymbol{h}\} \\ &= \mathrm{E}\{|\varepsilon(t)|^2|\boldsymbol{h}\} = \mathrm{E}\{|\varepsilon(t)|^2\}\end{aligned} \tag{31}$$

by utilizing (29), the zero mean of $\varepsilon(t)$, and that $h(t)$ and $\varepsilon(t)$ are uncorrelated with each other. We observe that the variance of the estimated reflection system is independent of the strength of the true reflection coefficients $|h(t)|$.

Then, if we assume the following: the number of estimated system coefficients is the same as the number of true coefficients (=n); the delays are the same in the estimated and the true systems; $d(t)$ and $v(t)$ are white stationary processes in time; $d(t)$, $v(t)$, $h(t)$ and $\varepsilon(t)$ are uncorrelated with each other, we obtain the power of the remaining TSI signal in the main channel after suppression as (see Appendix)

$$\mathrm{Power}\{r(t) - \hat{r}(t)\} = (P_d + P_v)\mathrm{Tr}\{\boldsymbol{P}_N\} + P_v\|\boldsymbol{h}\|^2 \tag{32}$$

where P_v is the power of $v(t)$ during TSI suppression filtering, $\boldsymbol{P}_N$ is given in (22), (23) or (28) and $\mathrm{Tr}\{\boldsymbol{B}\}$ is the trace of a square matrix $\boldsymbol{B}$ (= the sum of the diagonal elements). We see that, $\mathrm{Power}\{r(t) - \hat{r}(t)\}$ is dependent on jammer power and auxiliary channel noise power at TSI suppression, the variance of the estimated coefficients and the strength of the true system. Note that in the term $P_v\|\boldsymbol{h}\|^2$, P_v belongs to the auxiliary channel and $\|\boldsymbol{h}\|^2$ to the main channel.

The signal $e(t) = s(t) + n(t)$ does not seem to matter for this computation. It is not part of the calculation of the remaining TSI signal or power in (32). However, $e(t)$ matters for estimation of the reflection system and therefore also for the remaining TSI signal or power, as we will see.

Now, we utilise (28). For limited N this equation is an approximation as noted in Section 3.3.3. For us it is only important that the diagonal elements are sufficiently correct because of the trace operation in (32) which gives with (28)

$$\mathrm{Tr}\{\boldsymbol{P}_N\} \simeq \mathrm{Tr}\left\{\frac{1}{N}\frac{\lambda_e}{\lambda_\mathrm{d} + \lambda_v}\boldsymbol{I}_n\right\} = \frac{n}{N}\frac{\lambda_e}{(\lambda_\mathrm{d} + \lambda_v)} \tag{33}$$

If we insert this in (32) we arrive at

$$\mathrm{Power}\{r(t) - \hat{r}(t)\} = (P_\mathrm{d} + P_v)\frac{n}{N}\frac{\lambda_e}{(\lambda_\mathrm{d} + \lambda_v)} + P_v\|\boldsymbol{h}\|^2 \tag{34}$$

We see that the remaining TSI power also is dependent on the model order n, the number of estimation data N and signal powers [jammer, auxiliary channel noise and $e(t)$] during the estimation.

It appears in (34) as if a stronger noise in the auxiliary channel at estimation gives a lower TSI power. See Section 3.3.3 for a comment on this.

If $P_d = \lambda_\mathrm{d}$ and $P_v = \lambda_v$ then (34) simplifies to

$$\mathrm{Power}\{r(t) - \hat{r}(t)\} = \frac{n}{N}\lambda_e + P_v\|\boldsymbol{h}\|^2 \tag{35}$$

which is independent of jammer power.

4.2 Signal-to-interference plus noise ratio

Now, we will derive expressions for the SINR for the single auxiliary beam structure. The SINR is the principal radar performance measure, directly affecting the probability of detection, detection range and estimation accuracy.

The SINR without TSI suppression is, using (30)

$$\mathrm{SINR}_\mathrm{wo} = \frac{P_s}{\mathrm{Power}\{r(t)\} + P_n} = \frac{P_s}{P_d\|\boldsymbol{h}\|^2 + P_n} \tag{36}$$

where P_s is the target power and P_n the receiver noise in the main channel at TSI suppression filtering. We assume absence of monostatic clutter at suppression. Such clutter could be handled separately as described in [7]. This SINR is dependent on jammer power and the strength of the true reflection system.

The SINR with TSI suppression is using (32)

$$\begin{aligned}\mathrm{SINR}_w &= \frac{P_s}{\mathrm{Power}\{r(t) - \hat{r}(t)\} + P_n} \\ &= \frac{P_s}{(P_d + P_v)\mathrm{Tr}\{\boldsymbol{P}_N\} + P_v\|\boldsymbol{h}\|^2 + P_n}\end{aligned} \tag{37}$$

This SINR is dependent on jammer power and auxiliary channel noise power during TSI filtering, the variance of the estimated reflection system coefficients and on the strength of the true reflection system.

Using the expression in (34) we also obtain

$$\mathrm{SINR}_{\mathrm{w}} \simeq \frac{P_s}{(P_d + P_v)\frac{n}{N}\frac{\lambda_e}{(\lambda_d+\lambda_v)} + P_v\|\boldsymbol{h}\|^2 + P_n} \tag{38}$$

Here we note that the SINR also is dependent on the model order n, the number of estimation data N and the jammer power, auxiliary channel noise power and power of $e(t)$ during the estimation.

With $P_d = \lambda_d$ and $P_v = \lambda_v$ this simplifies to

$$\mathrm{SINR}_{\mathrm{w}} \simeq \frac{P_s}{\frac{n}{N}\lambda_e + P_v\|\boldsymbol{h}\|^2 + P_n} \tag{39}$$

which is independent of jammer power. Thus, the SINR should be able to be independent of jammer power. The reason is that a stronger jammer at filtering is balanced by a better estimate of the reflection system. We see that when $N \to \infty$, there will still be an SINR loss because of noise in the auxiliary channel. This is not the case in the expression in [11]. The SINR expressions in [8] show no dependence on the number of estimation data because they assume known TSI properties.

5 Simulations of TSI power and SINR

In this section, we validate our theory for TSI power and SINR against simulations. We will see that the theory agrees well with the simulations despite the fact that the assumptions for the optimal TSI filter are not completely fulfilled. The exception is when there are missing true delays in the model of the reflection system but we have an explanation for this.

5.1 Simulation setup

The simulation scenarios consist of two parts, definition of the true reflection system and definition of the rest of the scenario. The latter we call the 'radar setup'.

In the 'ideal radar setup' there is no noise $v(t)$ in the auxiliary channel and no target in the estimation data. In the 'realistic radar setup' there is one point target (power 20 dB) at range $N_R/2$ in the estimation data and noise $v(t)$ (zero-mean white complex Gaussian with power 0 dB). The number N_R is the number of range bins.

Four different true reflection systems have been employed. The 'ideal system' is a simple reflection system with $n = 10$ complex coefficients with amplitude $0.1 = -20$ dB and uncorrelated uniform random phase, see Fig. 4. The (more) 'realistic system' has uncorrelated complex Gaussian coefficients with delay dependent variance $[0{,}1\ \exp(-t/10)]^2$, see Fig. 4. The number of true coefficients is the same as the number of estimation data, which usually is much larger than the number of estimated coefficients. The system 'fullconst + s', is like the ideal system but has one more coefficient, which is weak (amplitude $0.01 = -40$ dB). The system 'fullconst + 1', is like 'fullconst + s' but the extra coefficient is strong (amplitude $0.1 = -20$ dB).

Especially in wireless communications, reflection systems have been studied, for example, in [25–27]. The measurements in [26] are somewhat similar to our ideal system. Our more realistic reflection system does not behave exactly as the measurements in [25, 27] but has a character similar to them. The simulations assume either that no monostatic clutter is present or that it can be suppressed separately (see Section 1).

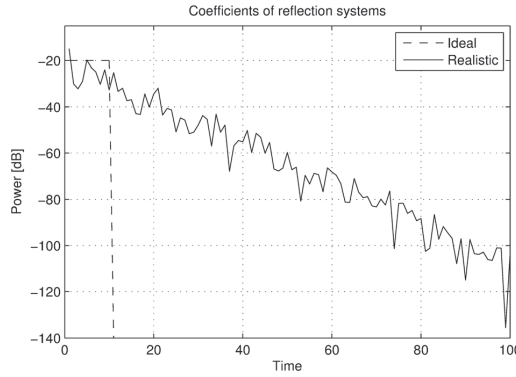

Fig. 4 *Absolute value of the impulse response coefficients of the ideal and realistic system types used in the simulations*
Only one realisation of the realistic system is shown

For both radar setups the noise $n(t)$ in the main channel was zero-mean white complex Gaussian with power 0 dB. Also at suppression filtering there was a point target (power 20 dB) at range $N_R/2$. The jammer power P_d at suppression was either constant at $P_{\mathrm{d}} = \mathrm{E}\{d^2(\mathrm{t})\} = 20$ dB or varied from -20 to $+60$ dB in steps of 1 dB. In most simulations $\lambda_d = P_d$ but in Section 5.4, λ_d is fixed at $\lambda_d = 20$ dB. There were different random reflection systems for each used number of data N but the same random system was employed for all used different jammer powers P_d. The estimated system was always of FIR structure with $n = 10$ coefficients. The number of Monte Carlo simulations was 100.

We will in the simulation results show two types of graphs. First, we will show graphs of the power of the TSI signal in the main channel without suppression, $r(t)$, and with suppression, $r(t) - \hat{r}(t)$ (also called the 'remaining TSI signal'). Both theoretical values according to (30) and (34) and values estimated from the simulations are displayed. This will give four curves in each graph, labelled 'Theo r(t)' (30), 'Theo8 r(t)-rHat(t)' (34), 'Sim r(t)' (estimated, without suppression) and 'Sim r(t)-rHat(t)' (estimated, with). See Fig. 5 for an example.

Second, we will show graphs of the SINR with or without TSI suppression. Both theoretical values from (36) and (38) and values estimated from the simulations are displayed. The four curves are labelled 'Theo wo.' (36), 'Theo8 w.' (38), 'Est wo.' (estimated, without suppression) and 'Est w.' (estimated, with). See Fig. 5 for an example.

The values estimated from the simulations are considered the truth in all graphs.

5.2 Results for the ideal and realistic scenario

With the ideal radar setup and the ideal true system the theory agrees very well with the simulations (not shown here). With the realistic radar setup and the realistic true system the theory for the TSI power and the SINR after suppression only agrees with the simulations for jammer power $P_d \leq 10$ dB (Fig. 5). We will see the reason for the failure in Section 5.3. For the

doi: 10.1049/iet-rsn.2011.0407

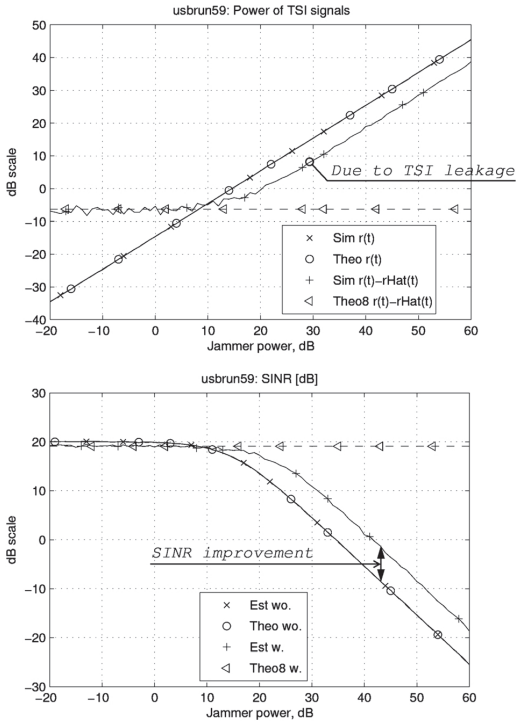

Fig. 5 *Power of TSI signals and SINR as a function of jammer power $P_d = \lambda_d$*

Realistic radar setup with realistic true system
Top, TSI signal power
Bottom, SINR

ideal true system the TSI suppression always succeeds in keeping a constant SINR despite an increasing jammer power, which is also predicted by (39). See the 'ideal' curve in Fig. 6. For the realistic true system the constant SINR cannot be maintained but we can define an 'SINR improvement' as the difference between SINR with TSI suppression and SINR without TSI suppression (Fig. 5).

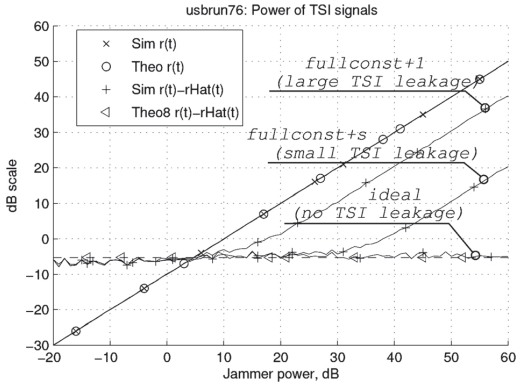

Fig. 6 *Power of TSI signals as a function of jammer power $P_d = \lambda_d$*

Realistic radar setup $N = 100$. True systems: 'ideal', 'fullconst + s' and 'fullconst + 1'

5.3 Results for missing delays

Fig. 6 shows the TSI signal power as a function of jammer power for different true systems. The realistic radar setup was employed. As a function of jammer power there are different deviations of the theory from the simulation depending on the true system. As a function of number of data, only for the true system 'fullconst + 1' the theoretical value of the remaining TSI power differs significantly from the estimated one (not shown here).

For the ideal true system the estimated system has all delays which are present in the true one and the theory agrees with the simulation in Fig. 6. In the true systems 'fullconst + s' and 'fullconst + 1' there is an extra delay in the system which is not present in the estimated one. The true system 'fullconst + s' has a small extra coefficients for the extra delay, causing a weak TSI signal to slip into the main channel. The true system 'fullconst + 1' has a strong extra coefficient causing a stronger TSI signal to slip in. Since the estimated system does not have a coefficient for the extra delay, it has no chance to cancel this extra TSI signal. We call this phenomenon 'TSI leakage' and it can be seen as the disagreement between theory and simulation in Fig. 6.

5.4 Different jammer power for estimation and filtering

Fig. 7 displays what happens if the jammer power is not the same for estimation and filtering. The graph depicts the TSI signal power as a function of jammer power P_d at suppression for different true systems while the estimation jammer power is fixed at $\lambda_d = 20$ dB.

For the case without TSI leakage (ideal true system) our theory agrees well with the simulation. Also for the case with small TSI leakage (true system 'fullconst + s') the theory agrees. Only for the true system 'fullconst + 1' the theoretical value of the remaining TSI power differs significantly from the estimated one.

6 Discussion about radar performance

In the derivations of the theory in Section 4 we have utilised a number of assumptions. We have seen that having correct delays in the estimated reflection system is very important and our theory will fail if this is not the case. The important thing is that the estimated system is not missing delays with

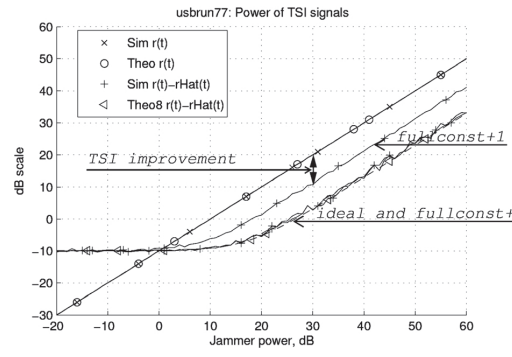

Fig. 7 *Power of TSI signals as a function of jammer power P_d at suppression while $\lambda_d = 20$ dB is fix*

Realistic radar setup. True systems: 'ideal', 'fullconst + s' and 'fullconst + 1'

strong system coefficients. Compare the result for the systems 'fullconst + s' and 'fullconst + 1'. In reality, the true reflection system will most likely not be limited in delay but the impulse response will wear off indefinitely. This would make it impossible to completely cancel the TSI. We will not achieve a constant SINR independent of jammer power. We will instead obtain a certain SINR improvement. One way to increase SINR improvement could be, not to choose the delays in the estimated reflection system consecutively but choose the delays with the strongest true coefficients. See Section 3.1 and the references there. In the opposite case, if we had too many delays in the estimated system, the filter would have the ability to cancel all leaking TSI signals but it also would give a higher variance of the estimated system coefficients, see (26), and therefore lower SINR, (38). It will be a trade-off.

It is often suggested in the literature [3, 28, 29], that $R_{\text{ft}} = R_{\text{tsi}}$ for the required number of fast-time taps R_{ft}, where R_{tsi} is the maximum delay of the true reflection system. We have not seen a proof for that. In [30], the condition

$$R_{\text{ft}} > \frac{N_d(R_{\text{tsi}} - 1)}{L - N_d} \tag{40}$$

or the required number R_{ft} which 'guarantees hot-clutter rejectability' for fully adaptive fast-time STAP is given. In (40), L is the number of antenna channels and N_{d} the number of jammers. Equation (40) is a sufficient but not necessary condition and it does not guarantee the resulting SINR. We can realise from (40) that to some extent there is a trade-off between spatial and temporal degrees of freedom (DoFs) in order to suppress the TSI. Using (40) we can also see that the requirements on R_{ft} can be both $R_{\text{ft}} \ll R_{\text{tsi}}$ or $R_{\text{ft}} \gg R_{\text{tsi}}$ depending on the case. In our simulations we have seen that $R_{\text{ft}} \geq R_{\text{tsi}}$ is necessary to avoid TSI leakage, which is in agreement with [3, 28, 29]. However, we have no extra spatial DoFs to play with as in (40).

Another assumption to question is whether the jammer transmits white noise. This is a very common assumption and reasonable but we have not investigated what happens for non-white jamming. We have not seen any literature on TSI suppression for non-white jamming. We also assume that the signal $e(t) = s(t) + n(t)$ is white. It is reasonable that the receiver noise $n(t)$ is white. Also a point target in $s(t)$ will have a white spectrum. If the radar range resolution is very high, it could resolve the target into several dependent scatterers and the target signal could be correlated. Also any remaining clutter [part of $e(t)$] could be correlated for high radar resolution.

A fourth assumption to consider is that the number of estimation data should be large. For a 1D filter in fast-time as our TSI filter, the problem is not as large. In a simple simulation our theory gave an error in the theoretical SINR of about 3 dB for $N = n$, 0.7 dB for $N = 2n$, 0.5 dB for $N = 3n$ and 0.3 dB for $N = 4n$.

Yet another assumption is that the bias in the estimated coefficients of the reflection system should be zero in (23), (28) and (29). In Section 3.3.1 we saw that the bias can be zero according to the theory but in the simulations it was not zero. Despite that, our theory for TSI power and SINR agrees with our simulations. The theory is robust to this assumption.

Our expressions for SINR work even if there is a target signal in the estimation data. A target is not allowed to be present [31] for the SINR loss expression in [11].

A derivation of the TSI power and SINR for the multiple beam structure would be more complicated than for a single beam. However, it is probable that the TSI power and SINR for multiple beams should qualitatively behave as the ones for a single beam. The interpretation of $\|\boldsymbol{h}\|^2$ in our TSI power and SINR expressions must be changed since for multiple beams, $\boldsymbol{h}$ are the coefficients of the true system $\boldsymbol{H}_{\text{MA}}(q)$ in (2). For the multiple beam structure, (40) tells us that the number of delays need not always be the same in the estimated reflection system and in the true system for good suppression.

7 Conclusions

7.1 Conclusions for the reflection system (Section 2 and 3)

We have presented a new way to view auxiliary beam TSI suppression, centred around the reflection system.

We have put the single beam and multiple beam structures of the auxiliary beam TSI suppression in a common framework.

We see that the reflection system is the same as the usual adaptive filter weights in the well-known SMI SLC of adaptive beamforming and STAP. Our matrix $\boldsymbol{R}_N$ is the sample matrix estimate of the ubiquitous interference covariance matrix. Thus, our results apply also to this usual filter [except (28)].

We present theoretical expressions of the quality (bias and variance) of the estimate of the reflection system and see how some factors influence the quality. The variance expressions are needed when we derive the performance of the radar system.

We have also discussed several other aspects on using auxiliary beam TSI suppression, like only modelling the most important scatterers and estimating with different kinds of noise.

7.2 Conclusions for radar performance (Section 4–6)

We have studied radar performance for the single auxiliary beam TSI suppression structure. Our main results are theoretical expressions for remaining TSI power and SINR after suppression filtering, (32), (34), (35), (37)–(39). Since the SINR is directly connected to the radar performance, with these expressions, it is possible to see what factors affect the performance and how they do it. Among others we note that ideally the TSI suppression should be able to keep the SINR constant regardless of jammer power. The TSI power and SINR should also in the multiple auxiliary beam structure qualitatively behave as our theoretical expressions.

In all simulations (single auxiliary beam) where the estimated reflection system has all the delays of the true system the theory agrees very well with the simulations, which are considered the truth. However, when the estimated system is missing one or more delays of the true system, the TSI filter cannot suppress the TSI signal with these delay(s) and TSI power will slip into the main radar channel. This phenomenon, which we call 'TSI leakage', has a very large impact on the performance. The SINR cannot be kept constant. We instead can define an 'SINR improvement'. Since, in the multiple auxiliary beam structure, spatial and temporal DoF can in some extent be traded against each other, this paragraph is not expected to be valid for multiple beams.

doi: 10.1049/iet-rsn.2011.0407

8 References

1 Bürger, W.K.: 'Sidelobe forming for ground clutter and jammer suppression for airborne active array radar'. Proc. IEEE Int. Symp. Phased Array Systems and Technology, 2003, Boston, Massachusetts, USA, 14–17 October 2003, pp. 271–276

2 Farina, A.: 'Antenna-based signal processing techniques for radar systems' (Artech House, 1992, ISBN 0-89006-396-6)

3 Fante, R.L., Torres, J.A.: 'Cancellation of diffuse jammer multipath by an airborne adaptive radar', *IEEE Trans. Aerosp. Electron. Syst.*, 1995, **31**, (2), pp. 805–820

4 Gabel, R.A., Kogon, S.M., Rabideau, D.J.: 'Algoritms for mitigating terrain-scattered interference', *IEE Electron. Commun. Eng. J.*, Special issue on space-time adaptive processing, 1999, **11**, (1), pp. 49–56

5 Kogon, S.M., Williams, D.B., Holder, E.J.: 'Beamspace techniques for hot clutter cancellation'. Proc. IEEE ICASSP Int. Conf. on Acoustics, Speech and Signal Processing, Atlanta, Georgia, USA, 7–10 May 1996, pp. 1177–1180

6 Kogon, S., William, D., McClellan, J.: 'Factored mitigation of terrain scattered interference and monostatic clutter'. Proc. 30th Asilomar Conf. Signals, Systems, and Computers, Pacific Grove, CA, USA, 3–6 November 1996, pp. 526–530

7 Rabideau, D.J.: 'Clutter and jammer multipath cancellation in airborne adaptive radar', *IEEE Trans. Aerosp. Electron. Syst.*, 2000, **36**, (2), pp. 565–583

8 Guerci, J.R., Goldstein, J.S., Reed, L.S.: 'Optimal and adaptive reduced-rank STAP', *IEEE Trans. Aerosp. Electron. Syst.*, 2000, **36**, (2), pp. 647–663

9 Ljung, L.: 'System identification', (Prentice-Hall 1999, ISBN-0-13-656695-2)

10 Björklund, S., Nelander, A.: 'Theoretical aspects on a method for terrain scattered interference mitigation in radar'. Proc. 2005 IEEE Int. Radar Conf., Arlington, Virginia, USA, 9–12 May 2005, pp. 663–668

11 Reed, I.S., Mallett, J.D., Brennan, L.E.: 'Rapid convergence rate in adaptive arrays', *IEEE Trans. Aerosp. Electron. Syst.*, 1974, **10**, (6), pp. 853–863

12 Brennan, L.E.: 'Preliminary results of hot clutter cancellation tests using WSMR data'. Proc. 3rd Adaptive Sensor Array Processing Workshop 1995 (ASAP-95), March 1995, vol. 2, pp. 515–537

13 Coutts, S.D.: 'Moutaintop jammer multipath mitigation experiment'. Proc. Second Adaptive Sensor Array Processing Workshop, MIT Lincoln Laboratory, 15–17 March 1994, 2, pp. 595–624

14 Gabel, R.A.: 'TSI mitigation weight training experiments'. Proc. Third ARPA Mountaintop Hot Clutter TIM, 1995, pp. 249–294

15 Gustafsson, F.: 'Adaptive filtering and change detection', (Wiley 2000, ISBN 0-471-49287-6)

16 Johnson, D.H., Dudgeon, D.E.: 'Array signal processing. concepts and techniques', (Prentice-Hall 1993, ISBN 0-13-048513-6)

17 Rabideau, D.J.: 'Modulation of signals in rapidly updated adaptive filters: theory, mitigation, and applications'. Proc. 31th Asilomar Conf. on Signals, Systems, and Computers, Pacific Grove, CA, USA, 2–5 November 1997, pp. 1665–1669

18 Candès, E., Wakin, M.B.: 'An introduction to compressive sampling', *IEEE Signal Process. Mag.*, 2008, **5**, (2), pp. 21–30

19 Lind, I.: 'Regressor and structure selection – uses of ANOVA in system identification' PhD thesis no. 1012, Linköping University, May 2006

20 Ohlsson, H.: 'Regularization for sparseness and smoothness. Applications in system identification and signal processing', PhD thesis, No. 1351, Linköping University, Sweden 2010

21 Kailath, T., Sayed, A.H., Hassibi, B.: 'Linear estimation' (Prentice-Hall 2000, ISBN 0-13-022464-2)

22 Gustafsson, F., Ljung, L., Millnert, M.: 'Signal processing', (Studentlitteratur 2010, ISBN 9789144058351)

23 Huffel, S.V., Vandewalle, J.: 'The total least squares problem: computational aspects and analysis', SIAM 1991, ISBN 0-89871-275-0

24 Farina, A., Golino, G., Timmoneri, L.: 'Comparison between LS and TLS in adaptive processing for radar systems', *IEE Proc. Radar Sonar Navig.*, 2003, **150**, (1), pp. 2–6

25 Ahlin, L., Zander, J.: 'Principles of wireless communications', (Studentlitteratur 1998, ISBN 91-44-00762-0)

26 Driessen, P.F.: 'Prediction of multipath delay profiles in mountainous terrain', *IEEE J. Sel. Areas Commun.*, 2000, **18**, (3), pp. 336–346

27 Turkmani, A.M.D., Demery, D.A., Parsons, J.D.: 'Measurement and modelling of wideband mobile radio channels at 900 MHz', *IEE Proc. I, Commun. Speech Vis.*, 1991, **138**, (5), pp. 447–457

28 Griffiths, L.J.: 'Linear constraints in hot clutter cancellation'. Proc. ICASSP Int. Conf. Acoustics, Speech, and Signal Processing, 7–10 May 1996, Atlanta, Georgia, USA, pp. 1181–1184

29 Kogon, S.M., Williams, D.B., Holder, E.J.: 'Exploiting coherent multipath for mainbeam jammer suppression'; *IEE Proc. Radar Sonar Navig.*, 1998, **145**, (5), pp. 303–308

30 Abramovich, Y.I., Spencer, N.K., Anderson, S.J., Gorokhov, A.Y.: 'Stochastic-constraints method in nonstationary hot-clutter cancellation – Part I: fundamentals and supervised training applications', *IEEE Trans. Aerosp. Electron. Syst.*, 1998, **34**, (4), pp. 1271–1292

31 Ward, J.: 'Space-time adaptive processing for airborne radar', MIT Lincoln Laboratory, Technical Report 1015, 1994

9 Appendix: Derivation of theoretical TSI power

We will derive equation (32) for the power of the remaining TSI signal in the main channel after suppression. We start without noise $v(t)$ in the auxiliary channel.

We assume the number of estimated system coefficients is the same as the number of true coefficients ($=n$) and the delays are the same in the estimated and the true systems. The TSI power in the main channel after suppression is

$$
\begin{aligned}
P_{r-\hat{r}} &= \text{Power}\{r(t)-\hat{r}(t)\} \\
&= E\left\{\left|\sum_{\tau=0}^{n-1} h(\tau)d(t-\tau) - \sum_{\nu=0}^{n-1}[h(\nu)+\varepsilon(\nu)]d(t-\nu)\right|^2 |\boldsymbol{h}\right\} \\
&= \sum_{\tau=0}^{n-1}\sum_{\nu=0}^{n-1} \text{E}\{h^*(\tau)h(\nu)d^*(t-\tau)d(t-\nu)|\boldsymbol{h}\} \\
&\quad - \sum_{\tau=0}^{n-1}\sum_{\nu=0}^{n-1} \text{E}\{h^*(\tau)[h(\nu)+\varepsilon(\nu)]d^*(t-\tau)d(t-\nu)|\boldsymbol{h}\} \\
&\quad - \sum_{\tau=0}^{n-1}\sum_{\nu=0}^{n-1} \text{E}\{[h^*(\tau)+\varepsilon^*(\tau)]h(\nu)d^*(t-\tau)d(t-\nu)|\boldsymbol{h}\} \\
&\quad + \sum_{\tau=0}^{n-1}\sum_{\nu=0}^{n-1} \text{E}\{[h^*(\tau)+\varepsilon^*(\tau)][h(\nu)+\varepsilon(\nu)] \\
&\qquad \times d^*(t-\tau)d(t-\nu)|\boldsymbol{h}\} \qquad (41)
\end{aligned}
$$

When all terms of the type $[h(\nu)+\varepsilon(\nu)]$ are split into double sums of themselves, we obtain nine double sums from (41).

If we assume $d(t)$ is uncorrelated with $h(t)$ and $\varepsilon(t)$, then

$$
\begin{aligned}
&\text{E}\{[h^*(\tau)+\varepsilon^*(\tau)][h(\nu)+\varepsilon(\nu)]d^*(t-\tau)d(t-\nu)|\boldsymbol{h}\} \\
&= \text{E}\{[h^*(\tau)+\varepsilon^*(\tau)][h(\nu)+\varepsilon(\nu)]|\boldsymbol{h}\} \\
&\quad \times \text{E}\{d^*(t-\tau)d(t-\nu)|\boldsymbol{h}\}
\end{aligned}
$$

and the same for similar terms in (41).

If we assume $d(t)$ is white in time, only terms in the double sums in (41) with $\tau=\nu$ will survive and the double sums become single sums. We also assume $d(t)$ is stationary and independent of $\boldsymbol{h}$. Then, the factors $\text{E}\{d^*(t-\tau)d(t-\tau)|\boldsymbol{h}\} = \text{E}\{|d(t)|^2\} = P_d$ in (41), where P_d is the jammer power during TSI suppression filtering.

Since $h(t)$ and $\varepsilon(t)$ are uncorrelated

$$
\begin{aligned}
&\text{E}\{[h^*(\tau)+\varepsilon^*(\tau)][h(\tau)+\varepsilon(\tau)]|\boldsymbol{h}\} = \text{E}\{h^*(\tau)h(\tau)|\boldsymbol{h}\} \\
&\quad + \text{E}\{h^*(\tau)\varepsilon(\tau)|\boldsymbol{h}\} + \text{E}\{\varepsilon^*(\tau)h(\tau)|\boldsymbol{h}\} + E\{\varepsilon^*(\tau)\varepsilon(\tau)|\boldsymbol{h}\} \\
&= \text{E}\{|h(\tau)|^2|\boldsymbol{h}\} + 0 + 0 + \text{E}\{|\varepsilon(\tau)|^2|\boldsymbol{h}\}
\end{aligned}
$$

and the same for similar terms in (41).

Now remains from (41)

$$\begin{aligned} P_{r-\hat{r}} &= P_d \sum_{\tau=0}^{n-1} \mathrm{E}\{|h(\tau)|^2|\boldsymbol{h}\} - P_d \sum_{\tau=0}^{n-1} \mathrm{E}\{|h(\tau)|^2|\boldsymbol{h}\} \\ &\quad - P_d \sum_{\tau=0}^{n-1} \mathrm{E}\{|h(\tau)|^2|\boldsymbol{h}\} + P_d \sum_{\tau=0}^{n-1} \mathrm{E}\{|h(\tau)|^2|\boldsymbol{h}\} \\ &\quad + P_d \sum_{\tau=0}^{n-1} \mathrm{E}\{|\varepsilon(\tau)|^2|\boldsymbol{h}\} \\ &= P_d \sum_{\tau=0}^{n-1} \mathrm{E}\{|\varepsilon(\tau)|^2|\boldsymbol{h}\} \end{aligned} \tag{42}$$

Using (31), (42) and the trace operator we arrive at

$$P_{r-\hat{r}} = P_d \sum_{\tau=0}^{n-1} \mathrm{V}\{\hat{h}(\tau)\} = P_d \mathrm{Tr}\{\boldsymbol{P}_N\} \tag{43}$$

where $\boldsymbol{P}_N$ is the covariance matrix of $\hat{\boldsymbol{h}}$.

Now we turn to the somewhat more complicated case with noise $v(t)$ in the auxiliary channel.

$$\begin{aligned} P_{r-\hat{r}} &= \mathrm{Power}\{r(t) - \hat{r}(t)\} \\ &= \mathrm{E}\left\{ \left| \sum_{\tau=0}^{n-1} h(\tau) d(t-\tau) - \sum_{\nu=0}^{n-1} [h(\nu) + \varepsilon(\nu)] \right.\right. \\ &\quad \left.\left. \times [d(t-\nu) + v(t-\nu)] \right|^2 |\boldsymbol{h} \right\} \end{aligned} \tag{44}$$

While we in (41) only had 9 double sums, we in (44) have 25.

If we assume that $v(t)$ is a white stationary process in time and that $d(t)$ and $h(t)$ are uncorrelated with $v(t)$ and use that $h(t)$ and $\varepsilon(t)$ are uncorrelated, we can see that the new double sums also become single sums and that most of the new sums will be zero. The only new non-zero sums of $P_{r-\hat{r}}$ are

$$\begin{aligned} &\sum_{\tau=0}^{n-1} \mathrm{E}\{|h(\tau)|^2|\boldsymbol{h}\} \mathrm{E}\{|v(t-\tau)|^2|\boldsymbol{h}\} \\ &\quad + \sum_{\tau=0}^{n-1} \mathrm{E}\{|\varepsilon(\tau)|^2|\boldsymbol{h}\} \mathrm{E}\{|v(t-\tau)|^2|\boldsymbol{h}\} \end{aligned} \tag{45}$$

The factors $\mathrm{E}\{|v(t-\tau)|^2|\boldsymbol{h}\} = \mathrm{E}\{|v(t)|^2|\boldsymbol{h}\} = P_v$ are the power of noise $v(t)$ during TSI suppression. Using $\mathrm{E}\{|h(\tau)|^2|\boldsymbol{h}\} = |h(\tau)|^2$ and (31) the new terms in (45) will be

$$P_v \sum_{\tau=0}^{n-1} |h(\tau)|^2 + P_v \sum_{\tau=0}^{n-1} \mathrm{V}\{\hat{h}(\tau)\} \tag{46}$$

By adding the new terms in (46) to (43) and using $\|\boldsymbol{h}\|^2 = \sum_{\tau=0}^{n-1} |h(\tau)|^2$ and the trace operator we finally arrive at

$$\begin{aligned} P_{r-\hat{r}} &= (P_d + P_v) \sum_{\tau=0}^{n-1} \mathrm{V}\{\hat{h}(\tau)\} + P_v \sum_{\tau=0}^{n-1} |h(\tau)|^2 \\ &= (P_d + P_v) \mathrm{Tr}\{\boldsymbol{P}_N\} + P_v \|\boldsymbol{h}\|^2 \end{aligned}$$

which is (32).

doi: 10.1049/iet-rsn.2011.0407

Publication 4: Measurement of Rank and Other Properties of Direct and Scattered Signals

Svante Björklund, Per Grahn, Anders Nelander, Mats I. Pettersson: "Measurement of Rank and Other Properties of Direct and Scattered Signals", International Journal of Antennas and Propagation, 2016 [6]. <https://www.hindawi.com/journals/ijap/2016/5483547/>. Published by Hindawi Publishing Corporation.

Hindawi Publishing Corporation
International Journal of Antennas and Propagation
Volume 2016, Article ID 5483547, 17 pages
http://dx.doi.org/10.1155/2016/5483547

Research Article

Measurement of Rank and Other Properties of Direct and Scattered Signals

Svante Björklund,[1] Per Grahn,[1] Anders Nelander,[1] and Mats I. Pettersson[2]

[1]*The Swedish Defence Research Agency (FOI), P.O. Box 1165, 581 11 Linköping, Sweden*
[2]*The Blekinge Institute of Technology, 371 79 Karlskrona, Sweden*

Correspondence should be addressed to Svante Björklund; svabj@foi.se

Received 15 April 2016; Revised 12 July 2016; Accepted 25 July 2016

Academic Editor: Wenchong Xie

We have designed an experiment for low-cost indoor measurements of rank and other properties of direct and scattered signals with radar interference suppression in mind. The signal rank is important also in many other applications, for example, DOA (Direction of Arrival) estimation, estimation of the number of and location of transmitters in electronic warfare, and increasing the capacity in wireless communications. In real radar applications, such measurements can be very expensive, for example, involving airborne radars with array antennas. We have performed the measurements in an anechoic chamber with several transmitters, a receiving array antenna, and a moving reflector. Our experiment takes several aspects into account: transmitted signals with different correlation, decorrelation of the signals during the acquisition interval, covariance matrix estimation, noise eigenvalue spread, calibration, near-field compensation, scattering in a rough surface, and good control of the influencing factors. With our measurements we have observed rank, DOA spectrum, and eigenpatterns of direct and scattered signals. The agreement of our measured properties with theoretic and simulated results in the literature shows that our experiment is realistic and sound. The detailed description of our experiment could serve as help for conducting other well-controlled experiments.

1. Introduction

In this article we have designed an experiment for low-cost indoor measurements of rank and other properties of direct and scattered signals with radar applications in mind. In real radar applications, such measurements can be very expensive, for example, involving airborne radars with array antennas.

In this introductory section we first in Section 1.1 define the signal rank and mention some other signal properties. Then in Section 1.2 we present radar applications and other applications where the signal rank is important. Section 1.3 tells what we have done in this article and gives an outline of the rest of the article.

1.1. Signal Rank and Other Signal Properties. In many applications of array antennas the *covariance matrix* $\mathbf{R} = E\{\mathbf{x}\mathbf{x}^H\}$ of the received signal vector $\mathbf{x}$ is utilized. The vector $\mathbf{x}$ usually contains the signals from the antenna channels and possibly some temporal dimension. The vector can be called a *space* (or *space-only*) *snapshot* or *space-time snapshot*, respectively.

The rank of the covariance matrix for the case with $\mathbf{x}$ containing only external signals and without the white receiver noise is important in radar applications and in many other applications (see Section 1.2). It states how many, in some sense, independent signals impinge on the antenna. We talk about the *signal rank*, which is the rank of this covariance matrix.

As $\mathbf{R}$ usually is unknown, it must be estimated in the algorithms that use it. A common estimate is [1, 2]

$$\hat{\mathbf{R}} = \frac{1}{N_R}\sum_{n=1}^{N_R}\mathbf{x}_n\mathbf{x}_n{}^H, \tag{1}$$

where $\mathbf{x}_n$ are training snapshots and N_R is the number of such snapshots. These training snapshots must be selected wisely, depending on the application, and their acquisition will take

some time, the *acquisition interval*. The acquisition of the training data and the estimation of the covariance matrix influence the rank.

Other signal properties than the rank which we consider in this article are the DOA (Direction of Arrival) spectrum and eigenpatterns. The DOA spectrum shows the distribution of received power from different DOAs. Eigenpatterns are formed by using the eigenvectors of $\widehat{\mathbf{R}}$ as beamforming weights when plotting the antenna array factor. See Section 3.5 for more details.

1.2. Applications. In *interference* suppression in radar, the rank of direct and scattered signals is important. Such interference can be *direct path jamming* (signals from a jammer travelling one-way line-of-sight to the radar), *clutter* (signals from the radar transmitter travelling to a surface, where they are undesirably scattered back to the radar, also called *cold clutter*), and *hot clutter* (signals travelling one-way from a jammer to the radar, not directly but scattered on a surface). The received radar signal in a pulse-Doppler radar can be stored in a *radar data cube* with dimensions for antenna channels (*space*), pulses (*slow-time*), and range bins (*fast-time*). Suppression of interference is commonly performed with linear filters, which can be one-dimensional, two-dimensional, or three-dimensional. For suppression of direct path jamming, space-only snapshots are usually employed, for cold clutter usually space-slow-time and for hot clutter usually space-fast-time.

The output of the suppression filter is $y = \mathbf{w}_a^H \mathbf{x}$, where $\mathbf{x}$ is a received snapshot. The filter weights are usually computed as [3–5]

$$\mathbf{w}_a = \mu \mathbf{R_{qq}}^{-1} \mathbf{w}_0, \tag{2}$$

where μ is a scalar and $\mathbf{R_{qq}}$ is the covariance matrix of the interference plus (receiver) noise signal vector $\mathbf{x_q}$. The vector $\mathbf{w}_0$ contains the weights without adaptation. It is usually the steering vector towards the target, possibly with tapering to reduce the sidelobes [5]. The use of filter (2) is commonly called *adaptive beamforming* for space-only snapshots or STAP (*Space-Time Adaptive Processing*) for space-time snapshots (this is also called *optimal* beamforming and *optimal* STAP if $\mathbf{R_{qq}}$ is known and *adaptive* beamforming and *adaptive* STAP if $\mathbf{R_{qq}}$ is estimated). The interference rank determines the needed DoFs (degrees of freedom = number of filter coefficients minus one) of the filter and the needed number of training snapshots (see, e.g., [4]). The DoF should be at least as many as the rank. There are many proposed methods, called *reduced rank methods*, for the suppression, with the DoFs adapted to the rank; for example, see [4, 6, 7].

Clutter in bistatic radar (the transmitter and receiver geographically separated) is similar to the case of hot clutter in normal (monostatic) radar. It has been suggested that also bistatic clutter should be suppressed by STAP [8]. Many high resolution DOA, Doppler, and range estimation methods in radar also need to know the signal rank.

In applications other than radar, the signal rank is also needed. In Electronic Support Measures (ESM), a kind of electronic warfare, the objective is to learn as much as possible about noncooperative radar and radio transmitters. Among other things, it is desired to estimate the number and location of the transmitters. This information can be used as information only or as a help for jamming. Some methods for estimating the number of emitters and their location need the signal rank. In wireless communication it is suggested to use adaptive beamforming and DOA estimation methods for interuser interference suppression and signal separation [1]. For estimating multipath channel models in wireless communication, DOA estimation can be used [9]. For adaptive beamforming and DOA estimation the signal rank is often needed. In MIMO (Multiple Input Multiple Output) communications, the signal rank is directly related to the transmission capacity.

1.3. Description of Work and Outline of Article. This article describes how we have designed and executed low-cost indoor measurements of direct and scattered signals. Direct signals travel one-way in line-of-sight from transmitter antenna to receiver antenna. Scattered signals do not travel in line-of-sight but are scattered on a surface on the way. We have performed the measurements in an anechoic chamber with an experimental array antenna where the received signals arrived directly from the transmitter(s) (direct signals) or were scattered on a moving rough surface reflector (scattered signals). Our experiment takes several aspects into account: transmitted signals with different correlation, decorrelation of the signals during the acquisition interval, covariance matrix estimation, noise eigenvalue spread, calibration, near-field compensation, and scattering on a rough surface. An advantage of indoor measurements in an anechoic chamber compared to outdoor measurements is the good control of the influencing factors, which is necessary to draw objective conclusions.

The main result of this paper is the design of the experiment for characterization of signal properties of direct and scattered signals. Also our measured signal properties could be seen as results. They agree with theoretic and simulated results in the literature. We have not seen such measured results but they should exist.

In [10], how the space-only rank of direct path signals was dependent on several factors for our experimental array antenna was studied. Also, noise properties were studied. Part of the material in this paper has earlier been published in [11] but the current article contains more details and a significantly deeper analysis.

In Section 2 we will discuss the relation between rank and eigenvalues and also motivate why we can measure space-time rank with space-only snapshots. Then in Section 3 the experimental setup is described and Section 4 gives some measurement results. A discussion is carried out in Section 5 and, finally, conclusions are presented in Section 6.

2. Some Preliminaries

What now follows is a discussion of some topics that are needed for and which motivate the article.

2.1. Rank and Eigenvalues. The rank of a covariance matrix is equal to the number of eigenvalues larger than zero.

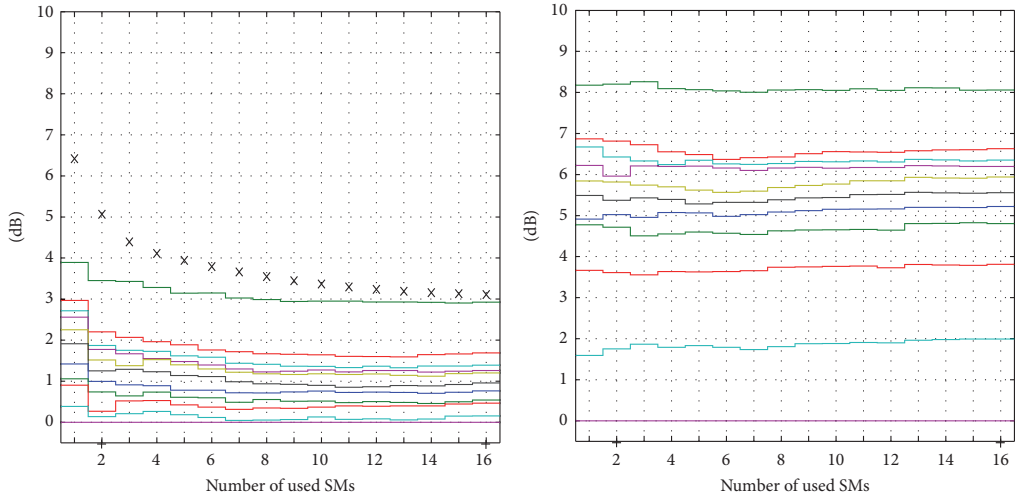

Figure 1: Noise eigenspectrum in measurement C1W (one transmitter and reflector; see Table 1). (b) With spatial calibration using a decoupling matrix and (a) without calibration. dB scale. See Section 3.3 for "SM." See Section 3.5 for an explanation of the figure.

However, what matters for interference suppression [4] and number of sources and DOA estimation [1] is the number of eigenvalues larger than the white noise power. This number is called the *effective rank* [4]. Theoretically, for a known covariance matrix and for white noise as the only signal, all eigenvalues will be equal and also equal to the noise power. This level is called *the noise floor*. Thus, the effective rank is the number of eigenvalues larger than the noise floor. These eigenvalues are caused by external signals, like targets, clutter, jammers, or radio transmitters and are called *signal* or *interference eigenvalues*. The smaller eigenvalues are caused by the receiver noise and are called *noise eigenvalues*.

In reality the noise eigenvalues will not be equal. There are two reasons. First, the estimated eigenvalues will be different, even if the true covariance matrix has equal eigenvalues, because of estimation errors [4, 10]. If these incorrectly estimated noise eigenvalues are used in the optimal filter (2), the performance will be degraded [4]. Two possible solutions are to set the noise eigenvalues to their correct value (by calibration or appropriate estimation [12]) or to use diagonal loading [4]. When setting the correct noise eigenvalue, the number of signals/interference eigenvalues must be known.

The second reason for different noise eigenvalues is that the true eigenvalues really are different due to system nonidealities, like unequal noise power in the channels or correlation between the channels, or due to the used calibration, for example, with a decoupling matrix (Figure 1 and Section 3.2). These true unequal noise eigenvalues should not be made equal since the optimal filter (2) needs the true covariance matrix, including true unequal noise eigenvalues.

To determine the number of signals/interference eigenvalues (of direct and scattered signals) we compute in this article a threshold λ_T as the maximum eigenvalue of a measured and estimated noise-only covariance matrix, normalized with the minimum eigenvalue. The threshold then includes the effects due to finite number of snapshots and to nonidealities of the system like unequal and correlated channel noise. The eigenvalues below the threshold are caused by the system (noise and nonidealities) and weak signal/interference eigenvalues. The eigenvalues above the threshold will then, hopefully, only be caused by the external signal/interference sources. Eigenvalues above the threshold will be called *large eigenvalues*.

2.2. Hot Clutter and Space-Only Data. Hot clutter suppression is an important use of our results. Therefore we here explain why our space-only measurements of direct and scattered signals are relevant for hot clutter.

The theoretic results in [14] about the estimated space-fast-time hot clutter covariance matrix indicate that the rank of this matrix can be measured by the space-only covariance matrix, if the number of scatterers seen by the receiver is less than the size of the space-only snapshot (which is the case in our measurements since in all experiments the number of large eigenvalues, max 10, is less than the size of the snapshot, 12; see Table 2). Fast-time effects, like jammer and system bandwidth and time-delay to the scatterers, are included in the theoretic model and affect the space-only rank through varying decorrelation of the signals from different scatterers. What determine the rank of space-only or space-fast-time signals are the scatterers and not the number of used samples in space or fast-time. Note that the results in [14] are valid for the estimated covariance matrix (1). This is the covariance matrix that must be used in the signal processing. This is also

the one which is used in the analysis of our measurements. With an estimated covariance matrix the acquisition interval, during which decorrelation can occur, is inevitable.

In [15] the authors measure channel rank in indoor wireless communications by the rank of the time-only covariance matrix of the received signal. They say that in narrowband systems the channel rank is equal to the number of resolvable multipaths for uncorrelated scattering, which with our terminology is the number of uncorrelated sources. This confirms that what determine the rank are the scatterers and not the number of used samples in space or time.

3. Experimental Setup

3.1. The Experimental Array Antenna. The experimental receiver antenna [10, 16] used in this article was designed and built by FOI (the Swedish Defence Research Agency). The high quality antenna has sidelobe levels below −60 dB [10, 16] and DOA estimation resolution below one-tenth of the conventional beamwidth [10, 17]. The antenna consists of a horizontal receiving linear array of 12 antenna elements with slightly less than half a wavelength separation (45 mm), 12 receiver modules, 12 A/D converters (12 bits), and 12 buffer memories. The antenna has an agile frequency band of 2.8–3.3 GHz and an instantaneous bandwidth of 5 MHz. The antenna elements are vertically polarized and have a horizontal 3 dB beamwidth of about 115° and a vertical beamwidth of about 15° [10]. The horizontal beamwidth of the whole array is about 10°. The receiver modules were manufactured by Ericsson Microwave Systems (today Saab Electronic Defence Systems). From the buffer memories the signals are transferred to a standard computer, where the IQ-conversion, DDC (digital downconversion and downsampling with a factor of 4), calibration correction, and spatial signal processing are performed in nonreal time. See the hardware block diagrams in [16].

The noise properties of our experimental antenna have been investigated by Pettersson in [10]. He stated that the noise sources, without external transmitters, are mainly internal thermal noise from the receiver modules and external thermal noise from the anechoic chamber walls. With external transmitters, there may be additional noise sources, like sampling jitter and phase noise of the signal generators. The true noise power is different in the channels [10] and it may differ by up to 1.5 dB. The noise also has a small correlation between the channels. The absolute value of the nondiagonal elements of the noise covariance matrix can be up to about one-tenth of the diagonal elements [10]. These two noise properties will give spread of the estimated noise eigenvalues; see Section 2.1.

3.2. Calibration. Accurate channel equalization (for frequency response) and spatial channel calibration (for mutual coupling) are utilized [10, 16]. The spatial calibration can be performed with three different methods [10]

(i) with a DOA correction table on the steering vectors,

(ii) with a decoupling matrix on the steering vectors,

(iii) with a decoupling matrix on the antenna signals $\mathbf{x}$.

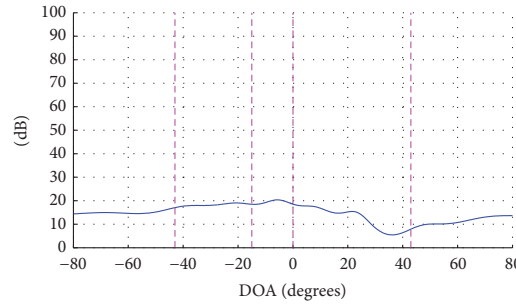

Figure 2: Capon DOA spectrum without spatial calibration. Otherwise the same measurement (U2SS, two uncorrelated strong transmitters; see Table 1) and processing as in Figure 10. See Section 3.5 for an explanation of the figure.

The fourth potential method, using a DOA correction table on the antenna signals, is not possible because these signals do not correspond to a single and known DOA. We prefer using a correction table on the steering vectors (method (i)) whenever possible. We have not found any drawbacks with storing such a table instead of only a decoupling matrix, which is contrary to the opinion in [18].

If in STAP the spatial calibration is performed on the antenna signals $\mathbf{x}$ (by method (iii)), then the same calibration should be done on the antenna signals $\mathbf{x}_n$ utilized for the estimation of the interference covariance matrix (1). The reason is to keep the STAP filter (2) optimal, for example, keeping the filter as a matched filter. However, if the spatial calibration is applied on the signals, the internal noise will become more correlated, due to the decoupling matrix [10], and the spread of the noise eigenvalues will be increased (Figure 1 and Section 2.1).

Without any spatial calibration the interference suppression performance will be degraded significantly. See Figure 2 for an example with a Capon DOA spectrum (Section 3.5) and compare with Figure 10 where spatial calibration is applied (via a DOA correction table on the steering vectors). See also [18]. The Capon spectrum is a form of the STAP filter (2).

3.3. Reflector and Data Acquisition. The measurements were performed in an anechoic chamber at FOI. Both the array antenna and the reflector were horizontally oriented (Figure 3). The reflector, made of a fine-meshed aluminum net of size 4.0 m × 1.5 m, was irregularly dented. It was designed to simulate a rough surface with a Gaussian height distribution (with a standard deviation somewhat less than one wavelength) and a Gaussian height correlation function (with a correlation distance of some wavelengths). This surface was chosen to obtain a sufficient number of scattering points from hills and valleys and sufficient roughness to have more than a wavelength bistatic range variation due to the surface roughness. We did not aim to model different terrain types but to achieve multipaths and obtain decorrelation by movement.

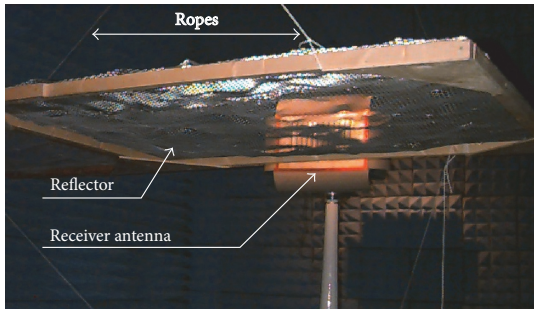

Figure 3: The reflector and the receiver antenna in the anechoic chamber. Photo from [13].

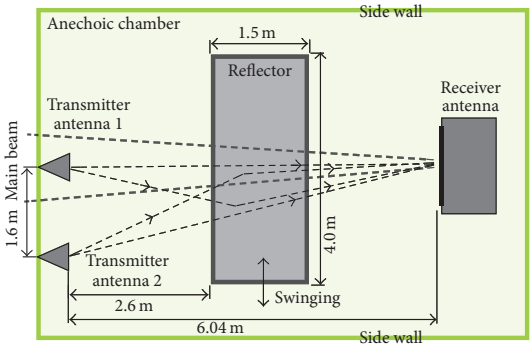

Figure 4: Top view of transmitter and receiver antennas and the reflector in the anechoic chamber. The drawing is not to scale.

The reflector was suspended from the ceiling using thin ropes at a height which gave grazing angles of about 9°. This grazing angle was just outside of the 3 dB elevation beamwidth (7.5°) of the experimental antenna. This geometry was chosen to have an unobstructed view of the antenna for the direct path signal and to have a sufficient delay corresponding to about one wavelength to obtain a large phase shift for the scattered signals. See Figures 4 and 5 for placement of the equipment in the chamber. The suspension allowed the reflector to swing easily from one side to the other.

When the reflector was swinging back and forth, with a deviation of one to two wavelengths, several submeasurements (SMs) were conducted with a delay of 15 s between the SMs. Each SM contained 256 snapshots (after downconversion and downsampling) and took 40 μs to measure. These snapshots were utilized to estimate a covariance matrix (1). The used covariance matrix in the analysis (Section 3.5) is the average of the covariance matrices from the used SMs. The total time for all SMs was about 3 min for 12 SMs (3072 snapshots), 4 min for 16 SMs (4096 snapshots), and 6 min for 24 SMs (6144 snapshots). Increasing the number of used SMs in this study corresponds to increasing the acquisition interval in [14, 19] (denoted as T in [19]). An acquisition interval is needed to estimate the covariance matrix (1).

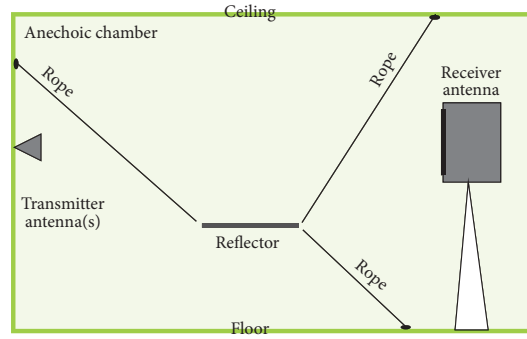

Figure 5: Side view of transmitter and receiver antennas and the reflector in the anechoic chamber. The drawing is not to scale.

By utilizing several SMs and a swinging reflector we could simulate decorrelation of the direct and scattered signals. The movement of the reflector gave a random component in the phase of the signal. By this the different multipath signals decorrelated with each other and with the direct signal. The movement of the reflector also enabled us to measure an "average" reflector instead of a particular one by using the same reflector at different positions.

The use of the reflector was not meant to replicate the exact generation of cold or hot clutter or any other signal/interference. In applications the decorrelation can occur due to movement of transmitter and receiver, nonzero bandwidth, and so forth (see above and Section 5).

3.4. Transmitters. We used one or two transmitter antennas, which were positioned at about the same height as the receiver antenna. The transmitter antenna 1 was located at the broadside of the receiver antenna and antenna 2 was shifted in DOA (Direction of Arrival) by 15°, which is 1.5 beamwidths of the receiver antenna; see Figure 4. Transmitter antenna 1 was a rectangular standard gain horn with a horizontal 3 dB beamwidth of 30°. The second transmitter antenna was a conical ridge horn. The receiver antenna was directed towards transmitter antenna 1, which had DOA 0° seen from the receiver antenna array center.

The distance between the transmitter antenna 1 and the receiver antennas was 6.0 m, which is on the limit to be considered a far-field distance for one antenna element. Near-field corrections in the receiver antenna were therefore applied [10, 16]. The far-field (Fraunhofer) region for the receiving antenna is beyond 5 m [20], and the radiating near-field (Fresnel) region is between 0.7 and 5 m. This means that the reflector is in the Fresnel region with almost three times the distance from the reactive near-field. We can therefore assume that there is no coupling between the antenna and the reflector and that the reflector will not influence the receiving antenna properties. By this we conclude that the antenna setup will not influence the decorrelation properties investigated in the article.

One or two commercially available signal generators were used for the transmitters. The transmitted waveforms were

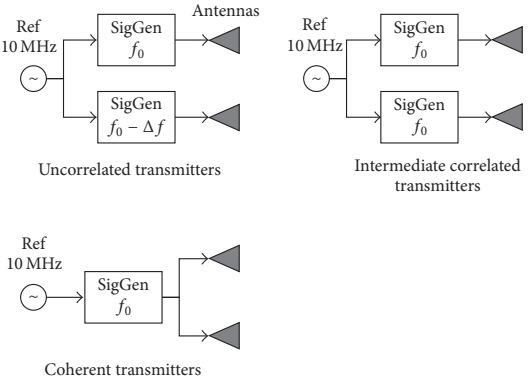

Figure 6: Generation of uncorrelated, intermediate correlated, and coherent transmitters. An integral number of periods of the uncorrelated signals fit exactly in the acquisition interval. The frequency f_0 was about 3 GHz and Δf about 0.4 MHz.

pure sinusoids, that is, the carrier signal without modulation. Measurements were conducted with coherent, intermediate correlated, and uncorrelated transmitted signals (Figure 6). The coherent signals originated from the same signal generator which fed both antennas. The uncorrelated signals were generated by two signal generators with different frequencies. The frequencies were selected so that integer numbers of periods of the sinusoid signal of each transmitter (after downconversion and downsampling) were received during the data acquisition interval. The two transmitted signals then seemed uncorrelated over this interval. This matter is treated in [10]. We believe that the accuracy of the frequencies of the transmitters and the internal oscillators of the receivers was sufficiently good to give sufficiently low correlation between the signals which should be "uncorrelated." Completely uncorrelated signals are not necessary. Even if the signals are somewhat correlated, the same qualitative behavior is achieved regarding the eigenanalysis [21]. A similar condition for space uncorrelation was noted in [19]. The intermediate correlated signals were generated by two signal generators with the same frequency. The two signal generators were in all cases phase-locked with a 10 MHz signal. The intermediate correlated signals should therefore be close to coherent. The used frequencies for the transmitters were 2999.596875 MHz and 2999.193750 MHz. These frequencies fulfill the requirements described above.

Table 1 lists important measurement parameters of our measurements. The two transmitters were selected to be either nearly equal in strength or very different in strength. This later case could imitate a situation with a weak target signal and a strong jammer. The difference in power, 45 dB, was chosen so that the power of the weak transmitter would be similar to the power of the reflections from the stronger transmitter.

3.5. Methods of Reflection Analysis. Our first analysis type employed to describe the direct and scattered signals is the

Table 1: Parameters of the measurements.

Name	Number of transmitters	Correlation	PG[a] Tx 1[b] [dB]	PG[a] Tx 2[b] [dB]	SNR[c] [dB]
C1S	1	—	0.5	—	41
C2SS	2	Coherent	0.5	−4.2	45
U2SS	2	Uncorrelated	0.5	−4.5	40, 32
I2SS	2	Intermediate	High	High	42
C1W	1	—	−39.5	—	14
C2SW	2	Coherent	0.5	−44.2	43
U2SW	2	Uncorrelated	0.5	−44.5	44, −3

[a]PG is the *effective isotropic radiated power* [dBm].
[b]The DOA was 0° for transmitter 1 (Tx 1) and −15° for transmitter 2 (Tx 2).
[c]The SNR is for one antenna channel (mean value between the channels) and one time sample after IQ, DDC, and calibration and is estimated from data (by the frequency spectrum, not the Capon spectrum). For measurements C2SS, I2SS, and C2SW the stated SNR is for the sum of the two transmitters. The reason for this is that the transmitters could not be separated in the SNR estimation.

Table 2: Summary of eigenspectra results[a].

Name	Figure	1 SM	Increase per SM[b]	12 SMs	24 SMs
C1S	Figure 8	1	1	8	8
C2SS	Figure 9	1	≤1	7	8
U2SS	Figure 10	2	2 (up to 6 SM), ≤1 (above 6 SM)	10	10
I2SS	Figure 11	2	≤1	9	10
C1W	Figure 12	1	0	1	1
C2SW	Figure 13	1	≤1	8	8
U2SW	Figure 14	2	1	8	8

[a]The table gives the number of large eigenvalues, that is, eigenvalues larger than the threshold λ_T. Often the last large eigenvalue came later than the rest.
[b]Approximate values.

Capon DOA spectrum [22] (also called MVDR, Minimum Variance Distortionless Ratio),

$$P_{\text{capon}}(\theta) = \frac{1}{\mathbf{a}^H(\theta)\,\hat{\mathbf{R}}^{-1}\,\mathbf{a}(\theta)}, \tag{3}$$

where $\mathbf{a}(\theta)$ is the spatial steering vector and $\hat{\mathbf{R}}$ is the estimated covariance matrix in (1). The steering vector is a model of how the receiver perceives an impinging signal from direction θ. For us $\mathbf{a}(\theta)$ was measured in the anechoic chamber and tabulated for $-80^\circ \le \theta \le 80^\circ$ with a step of 0.5°. For angles θ between the ones in the table the vector $\mathbf{a}(\theta)$ was interpolated linearly. The calibration correction for antenna element coupling, amplitude and phase drift, and near-field were all done on the steering vectors. This is method (i) in Section 3.2 (DOA correction table on the steering vectors). See [10, 16] for more information.

The Capon spectrum shows the distribution of received power from different DOAs unless the signals are coherent. The Capon spectrum also gives an indication of how well optimal beamforming and STAP can suppress scattered signals, since it is computed according to (2), with special

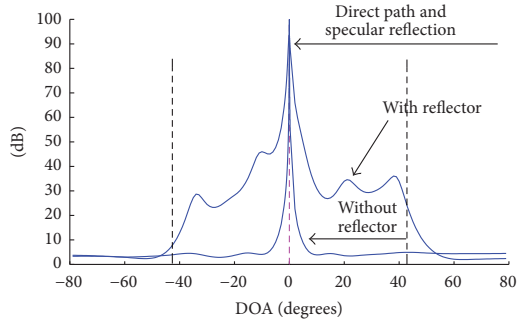

Figure 7: Capon DOA spectra with the reflector (measurement C1S in Table 1, same result as Figure 8) and without the reflector plotted on top of each other. The region between the left and right vertical dashed lines is the reflection region, that is, where reflections are possible because of the presence of the reflector. The middle dashed line(s) is the true DOA of the direct signal(s). 24 SMs.

choices of the covariance matrix and the scalar μ. For the Capon spectra, 24 SMs were used. As an example of the influence of the reflector, Figure 7 shows the Capon spectra for experiments with and without the reflector.

The second analysis type is the *eigenspectrum*, which is the eigenvalues of the antenna signal covariance matrix, usually sorted in decreasing order. We have plotted the eigenvalues in an uncommon manner. They are not plotted in decreasing order for a single covariance matrix but all eigenvalues for the same covariance matrix are plotted in the same "column." The different columns are used for covariance matrices with different number of SMs. We have computed the eigenvalues for an increasing number of used SMs, up to a maximum of 24. However, in the graphs in this article only up to 16 SMs are plotted, due to space limitations. See Figure 8(b) for an example. The eigenspectrum illustrates the signal/interference rank. In each presentation we have normalized the eigenvalues to the smallest one. No spatial calibration was performed for the eigenspectra results (except as an illustration in Figure 1). For interference suppression this is not necessary, since when computing the optimal weights in (2), the calibration can and should be performed on the quiescent weight vector $\mathbf{w}_0$ (method (i) in Section 3.2) instead of the covariance matrix (via a decoupling matrix on the received signals used to estimate the covariance matrix, method (iii)). Done differently, the noise eigenvalue spread would increase (Figure 1) and the noise eigenvectors would influence the optimal filter (2) more and perhaps require more DoFs. In this paper we determine the interference rank by the threshold described in Section 2.1. In the graphs the threshold is marked by the symbol "×"; see Figure 8.

We also present *eigenpatterns* (eigenvector antenna array factors) [23]. Eigenpatterns are formed by using the eigenvectors of the antenna signal covariance matrix as beamforming weights when plotting the antenna array factor. Since the element pattern is not included in the steering vector, our eigenpatterns will not be antenna patterns. For the eigenpatterns the spatial calibration was performed using a decoupling matrix on the training signals (method (iii) in Section 3.2). See [10, 16] for more information. Since the reflector is not placed in the extreme near-field and the eigenpatterns are transformed to the far-field (by near-field compensation on the training signals and by the used far-field steering vector), there should be no significant differences in the eigenpatterns compared to the case where the reflector is in the far-field.

4. Measurement Results

4.1. Capon DOA Spectra and Eigenspectra. The Capon DOA spectrum and the eigenspectrum for measurement C1S (a single, strong transmitter; see Table 1) are shown in Figure 8. A clear peak at DOA 0° is seen in Figure 8(a). This is the direction of the transmitter. The peak contains both the direct signal and the specular reflection. In the figure the extension of the reflector is given by dashed vertical lines. As seen in the figure, most reflections from the reflector are about 60 dB lower than the peak. We see that the whole reflector is covered by the power from the transmitting antennas. In Figure 8(b), the number of large eigenvalues, that is, above the threshold (Section 2.1), starts with one and increases by one for each new SM, except for the last large eigenvalue, up to a maximum of eight. This means that we can consider the signal/interference rank to be about one to eight, depending on the level of decorrelation, of which the direct signal is one. Table 2 summarizes all eigenspectra.

Figure 9 presents results from measurement C2SS (two strong coherent transmitters). Here, the Capon spectrum peak for DOA 0° is considerably lower, 30 dB, than in Figure 8. The second direct signal peak is also weak and has some bias in DOA. Most parts of the reflection region are weaker than in Figure 8. The probable reason for the low levels is the mutual cancellation of the signals from the two transmitters due to the coherence between them [21, 24]. The eigenspectrum is similar to Figure 8. This similarity means that two coherent transmitters are seen as a single transmitter. The largest eigenvalue in Figure 9 has nearly the same size as in Figure 8, despite the largest peak being lower in Figure 9 than in Figure 8. This is possible since the eigenvalues do not correspond directly to the power of the signal sources but the

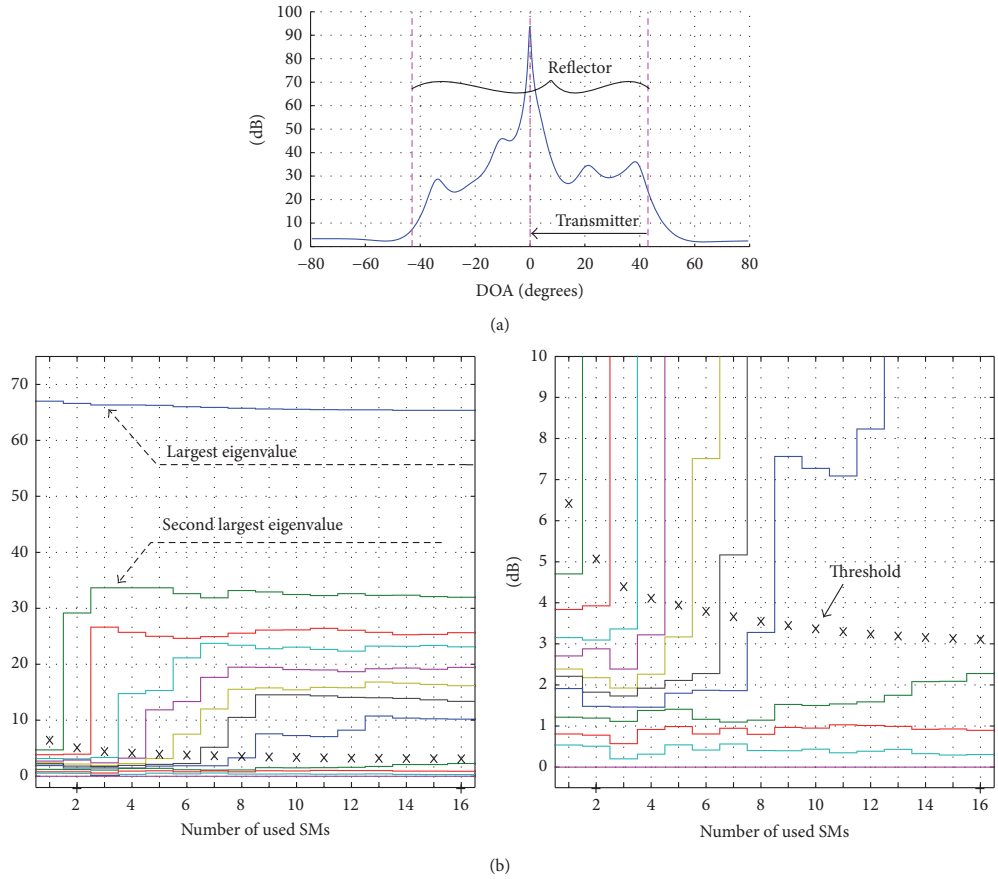

Figure 8: Measurement C1S. A single strong transmitter. (a) Capon DOA spectrum. Figure description in Figure 7. (b) Eigenspectrum. Zoom-in to the right. dB scale. See Section 3.3 for "SM."

sum of the signal eigenvalues λ_l is equal to the sum of the signal powers P_l [21]:

$$\sum_{l=1}^{L} P_l = \sum_{l=1}^{L} \lambda_l, \tag{4}$$

where L is the number of signal sources.

The case with two strong uncorrelated transmitters (measurement U2SS) is depicted in Figure 10. Both direct signals (including specular reflections) are clearly seen. Also the reflection region is clearly visible. When studying the eigenspectrum, we note a difference to the previous measurements. Here it starts with two large eigenvalues for the first SMs and initially increases by two for each new SM (up to six). Then it increases slower, probably because some eigenvalues are below the noise floor, up to ten large eigenvalues on the remaining SMs.

Figure 11 shows Capon spectrum and eigenspectrum for the case with two strong and intermediate correlated transmitters (measurement I2SS). The Capon spectrum seems to be nearly identical with the case of uncorrelated transmitters (compare Figures 10 and 11). The eigenspectrum starts with two large eigenvalues and then increases by only one for each extra SM, except for no change between 3 and 4 SMs. The maximum number of large eigenvalues is ten as for uncorrelated transmitters (U2SS) but the final large eigenvalues require more SMs and therefore more decorrelation than for uncorrelated transmitters. The more uncorrelated the transmitters are, the more equal in size the eigenvalues are in the simulations in [19, 21]. In measurement I2SS the transmitters were more correlated than in U2SS. The eigenvalues were probably therefore more unequal and some were too small to cross the threshold and become "large" ones. Thus, the signal/interference rank increases as the correlation between the transmitters decreases.

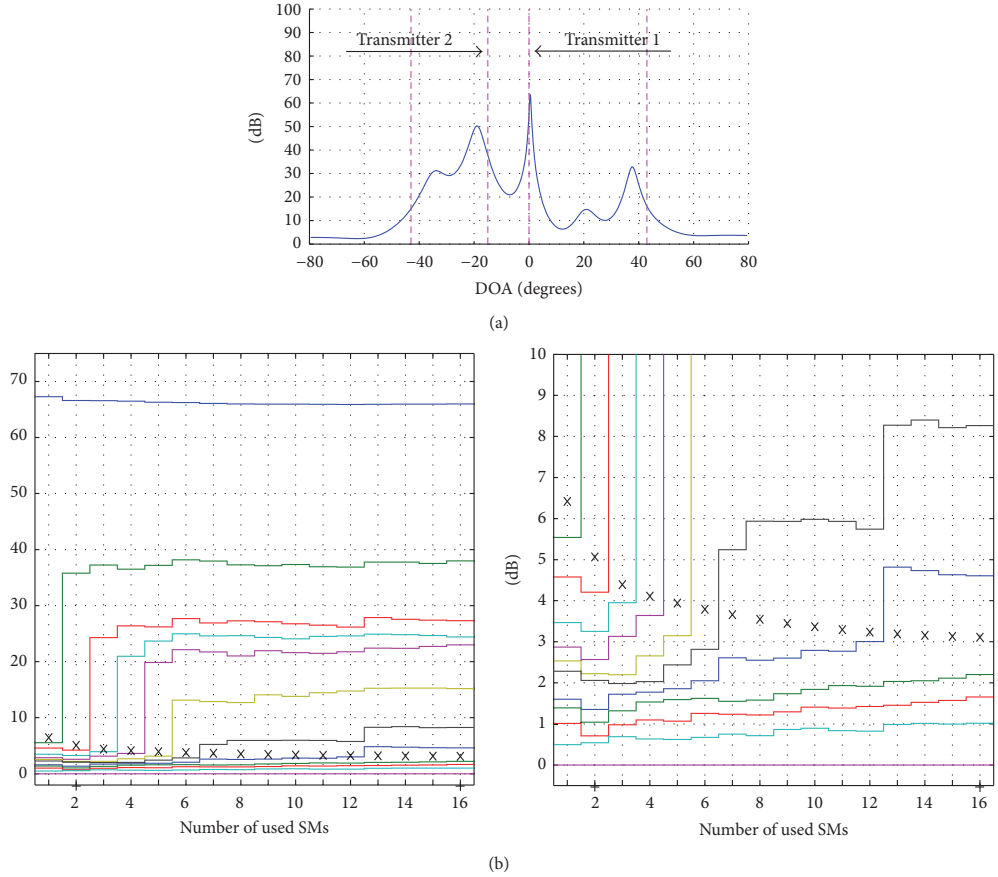

Figure 9: Measurement C2SS. Two coherent strong transmitters. (a) Capon DOA spectrum. (b) Eigenspectrum. Zoom-in to the right. dB scale. See Section 3.3 for "SM."

In Figure 11, we observed that there are two large eigenvalues for a single SM. By changing the analysis to use only 1 SM in 16 repetitions, we obtained two large eigenvalues in 13 repetitions, we obtained one large eigenvalue in 1 repetition, and we obtained three large eigenvalues in 2 repetitions. This shows that with a high probability there will be two large eigenvalues for 1 SM.

We now turn to the case with a single weak transmitter (measurement C1W). The Capon spectrum (Figure 12) tells us that the peak is 40 dB lower than in Figure 8, which is as expected since the transmitted power was this much lower. The reflection region is not seen at all. The explanation is that the scattered signals are weaker than the noise. The eigenspectrum in Figure 12 contains the same information. It has only one large eigenvalue for all SMs, because of the weak transmitter. All but one eigenvalue are below the noise. See also the discussion about the iceberg effect in Section 5.

The Capon DOA spectrum in Figure 13 for two coherent and different strong transmitters (measurement C2SW) resembles the one for a single strong transmitter (Figure 8) very much. Also the eigenspectra (Figure 13(b)) are fairly similar for few SMs (compare Figures 8(b) and 13(b)). For up to 6 SMs, the number of large eigenvalues increases by one for each SM as in Figure 8 but the 7th large eigenvalue does not show up until SM 11 for C2SW. The probable reason for the similarity is that the weak transmitter is too weak to disturb the strong transmitter.

In measurement U2SW (two uncorrelated transmitters with different strength) the Capon DOA spectrum (Figure 14) is also rather similar to the one with a single strong transmitter (Figure 8). The direct signal is about 3 dB lower and the valleys of the reflection region are deeper. Interestingly, the eigenspectrum (Figure 14) starts with two large eigenvalues, which indicates two noncoherent transmitters despite the low power of the weak transmitter, below the noise (SNR $\approx$ -3 dB). This is also possible because of (4). Then the number of large eigenvalues increases by one for each additional SM, which could indicate a single transmitter. It ends with eight

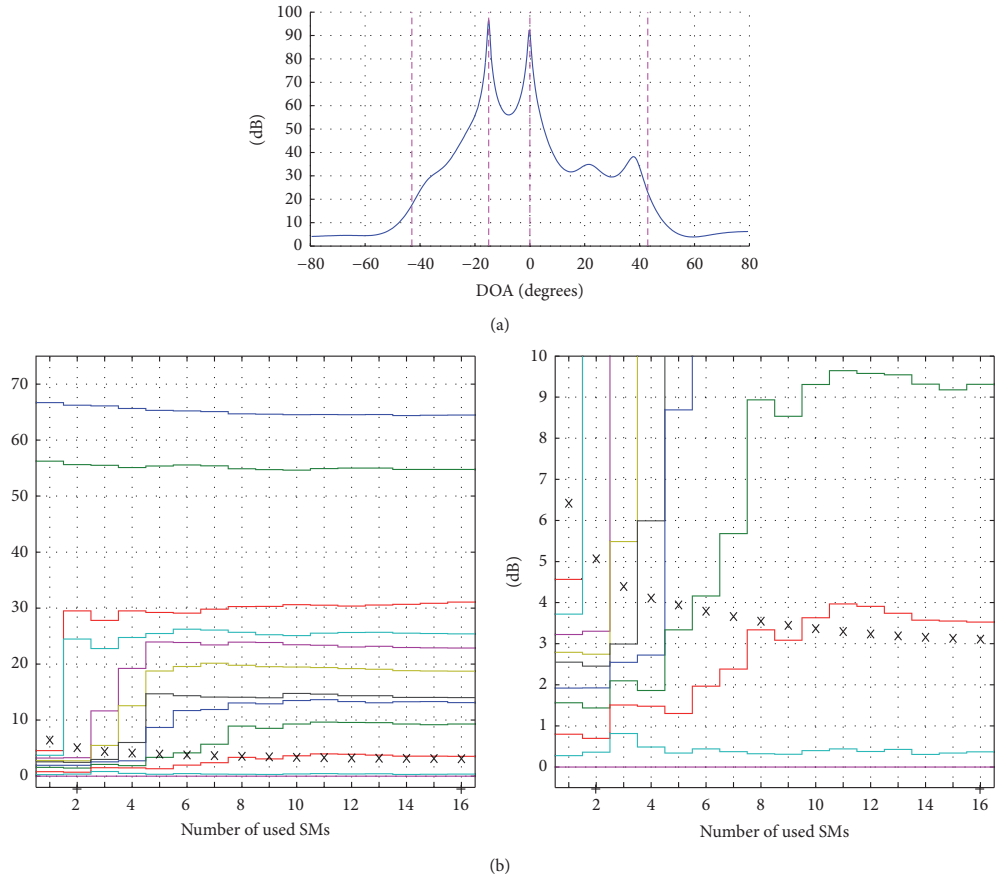

Figure 10: Measurement U2SS. Two uncorrelated strong transmitters. (a) Capon DOA spectrum. (b) Eigenspectrum. Zoom-in to the right. dB scale. See Section 3.3 for "SM."

large eigenvalues as for a single strong transmitter. There are probably several signal/interference eigenvalues below the noise.

4.2. Eigenpatterns. Figures 15 and 16 give some examples of eigenpatterns. More eigenpatterns can be found in [13] according to Table 3. We notice that each eigenpattern has one or more large lobes. When the peak of the highest lobe is within the reflection region (where the reflector can give scattered signals, denoted with the outermost dashed vertical lines), we say that the eigenpattern *covers* the reflection region. When the peak is outside this region we say that the eigenpattern covers the region outside.

In our measurements the eigenpatterns corresponding to the largest eigenvalues usually cover the reflection region. The remaining eigenpatterns cover the region outside. The one or two largest eigenvalues have eigenpatterns which are directed towards the strong direct signals and the other eigenpatterns usually have nulls in these directions (Figures 15 and 16). Actually, the eigenpatterns, associated with the eigenvectors, must be as "different" as possible since they are orthogonal.

There is approximately the same number of covering eigenpatterns for 1 SM ("without order") as for 12 SMs; see Table 3.

Strangely enough, there is about the same number of eigenpatterns covering the reflection region for 1 SM as there are large eigenvalues using all (24) SMs, especially "without order" (compare Tables 2 and 3). Exceptions are the measurement C1W which has 7 covering eigenpatterns (Figure 16) despite only 1 large eigenvalue and U2SS and I2SS, which have somewhat fewer covering eigenpatterns than eigenvalues. C1W seems to observe all distinct sources with its eigenpattern but not with its eigenvalues. Remember some signal eigenvalues are below the noise floor in the eigenspectra.

For the weak direct signal in the presence of a strong direct signal, its eigenpattern has a bias in DOA. Also for the case with two equal strong coherent transmitters there

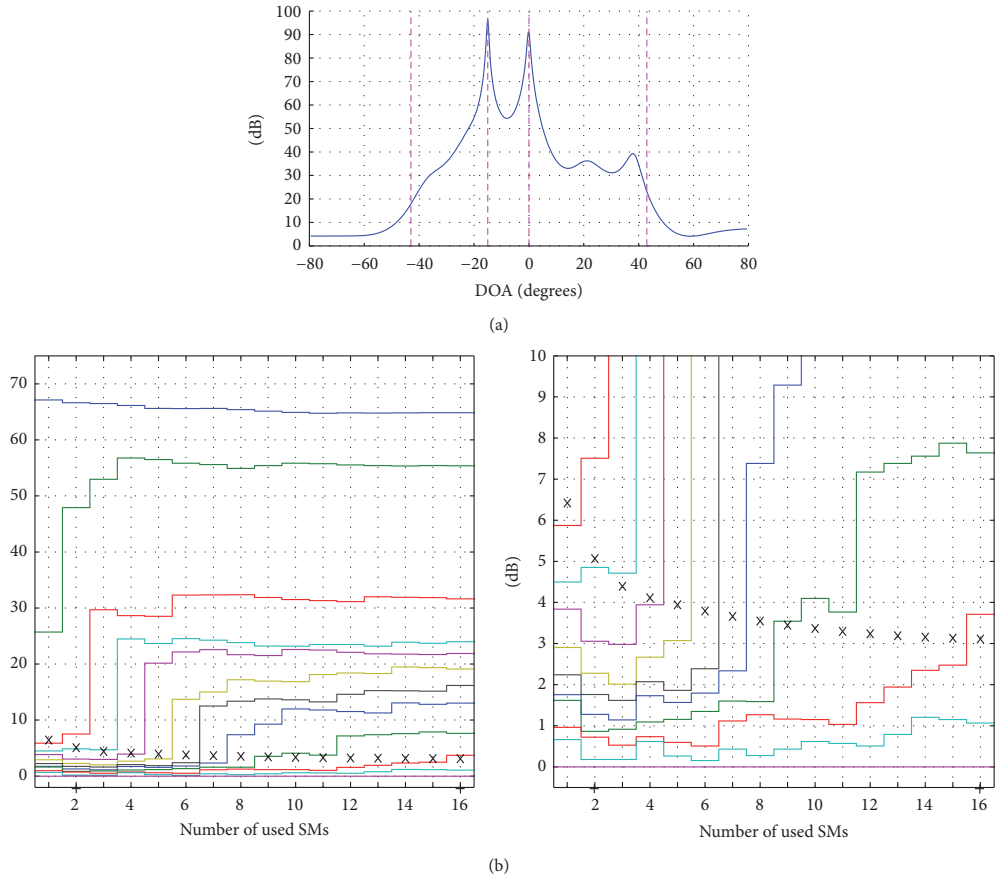

Figure 11: Measurement I2SS. Two intermediate correlated strong transmitters. (a) Capon DOA spectrum. (b) Eigenspectrum. Zoom-in to the right. dB scale. See Section 3.3 for "SM."

Table 3: Summary of eigenpattern results[a].

Name	1 SM w ord[b]	1 SM w/o ord[c]	Figure	12 SMs	Figure
C1S	8	8	6.8 in [13]	8	6.9 in [13]
C2SS	8	8	Figure 15	7-8	6.33 in [13]
U2SS	5	7	6.24 in [13]	8	6.25 in [13]
I2SS	2	6	6.36 in [13]	8	6.37 in [13]
C1W	7	7	Figure 16	7-8	6.21 in [13]
C2SW	5	7	6.16 in [13]	8	6.17 in [13]
U2SW	8	8	6.28 in [13]	8	6.29 in [13]

[a]The table gives the number of eigenpatterns covering the reflection region.
[b]"w ord" stands for "with order" and means the number of covering eigenpatterns in an uninterrupted sequence from the first one.
[c]"w/o ord" means "without order" and means the total number of covering eigenpatterns.

is a bias, although less than for two signals with unequal strength.

4.3. Summary of the Measurement Results. We have from the measurements obtained results on the rank and other properties of direct and scattered signals. We see that the signal/interference rank depends on the number of transmitters, the SNR (Signal to Noise Ratio), the correlation between the transmitters, and the degree of decorrelation of the transmitter signals that occurs during the data acquisition.

Without decorrelation, the direct and scattered signals of a transmitter will all be coherent. If the scattered signals decorrelate with each other and with the direct signal, the rank is increased. Two coherent transmitters appear as a single transmitter regarding the signal/interference rank. Two strong uncorrelated transmitters give rise to the double number of sources compared to a single transmitter.

With higher SNR, more eigenvalues of the eigenspectrum tail will appear above the noise level, and the rank will be higher.

The eigenpatterns show the reflection region and the DOAs to the direct signals. The eigenpattern can tell us the number of signal sources when the signals still are coherent.

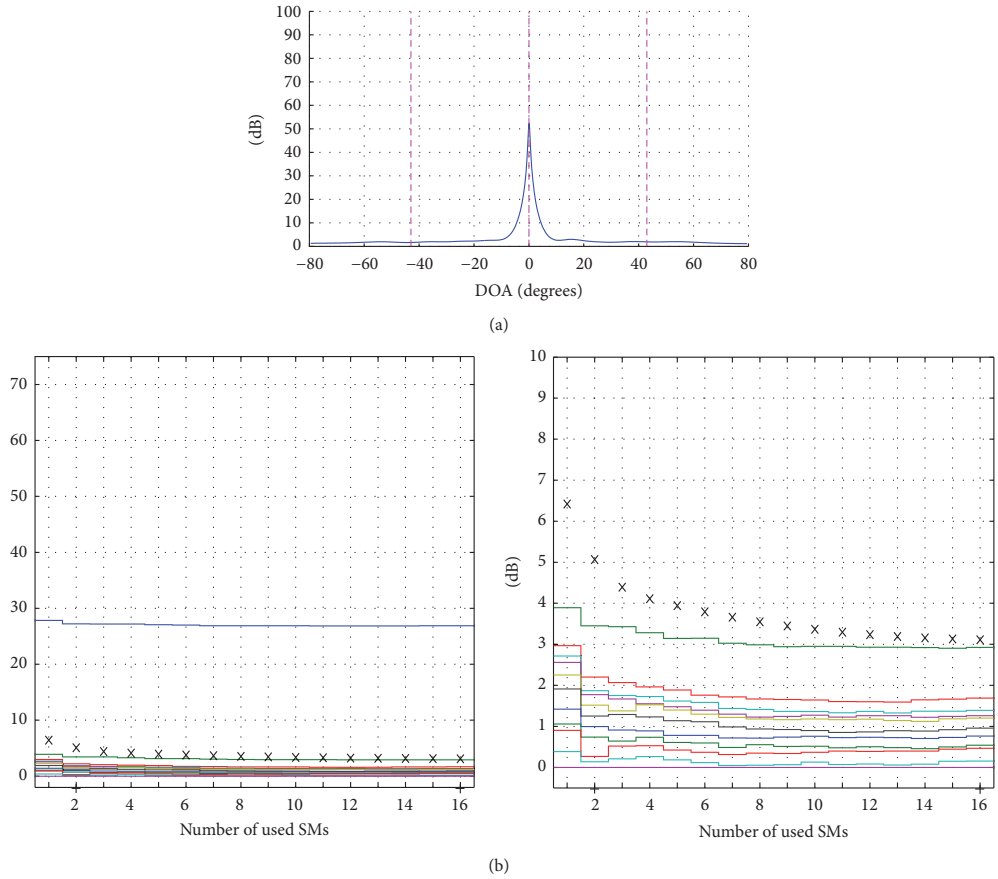

Figure 12: Measurement C1W. A single weak transmitter. (a) Capon DOA spectrum. (b) Eigenspectrum. Zoom-in to the right. dB scale. See Section 3.3 for "SM."

Alternatively, they can tell us the extent of the reflection region if the number of signal sources is known.

5. Discussion

5.1. Discussion about the Experimental System. To show the eigenvalues for an increasing number of used SMs when the reflector is moving gives the possibility to study the signal/interference rank for different degrees of decorrelation. In a real case, decorrelation can occur as a result of platform motion (comparing with [19]), internal clutter motion, nonzero bandwidth [25], long acquisition interval for estimating the covariance matrix, carrier frequency changes, and so forth.

Note that we are studying the estimated covariance matrix (1), not the true covariance matrix. It is the estimated matrix which must be used in algorithms. The measured signal snapshots were space-only snapshots. However, the time dimension enters via the acquisition interval, during which decorrelation of the signals can occur (see also Sections 2.2 and 3.3). This will increase the rank. The decorrelation increases if the acquisition interval is prolonged (more SMs) as in [14].

The Capon spectrum gives a good picture of the impinging power from the direct and scattered signals if the transmitters are noncoherent.

The measurement result will be influenced by different transmitter signals. With a different frequency of the pure sinusoid, there will be different differences in amplitude and phase between the scatterers on the reflector. If the frequency is changed much, the number of scatters will change and thereby the signal rank will change too, with a higher number and higher rank with a higher frequency. Now the signal bandwidth is low and the scatterers on the reflector cannot be resolved in range (= fast-time). A bandwidth in the order of 100 MHz would be needed to resolve in range. If the

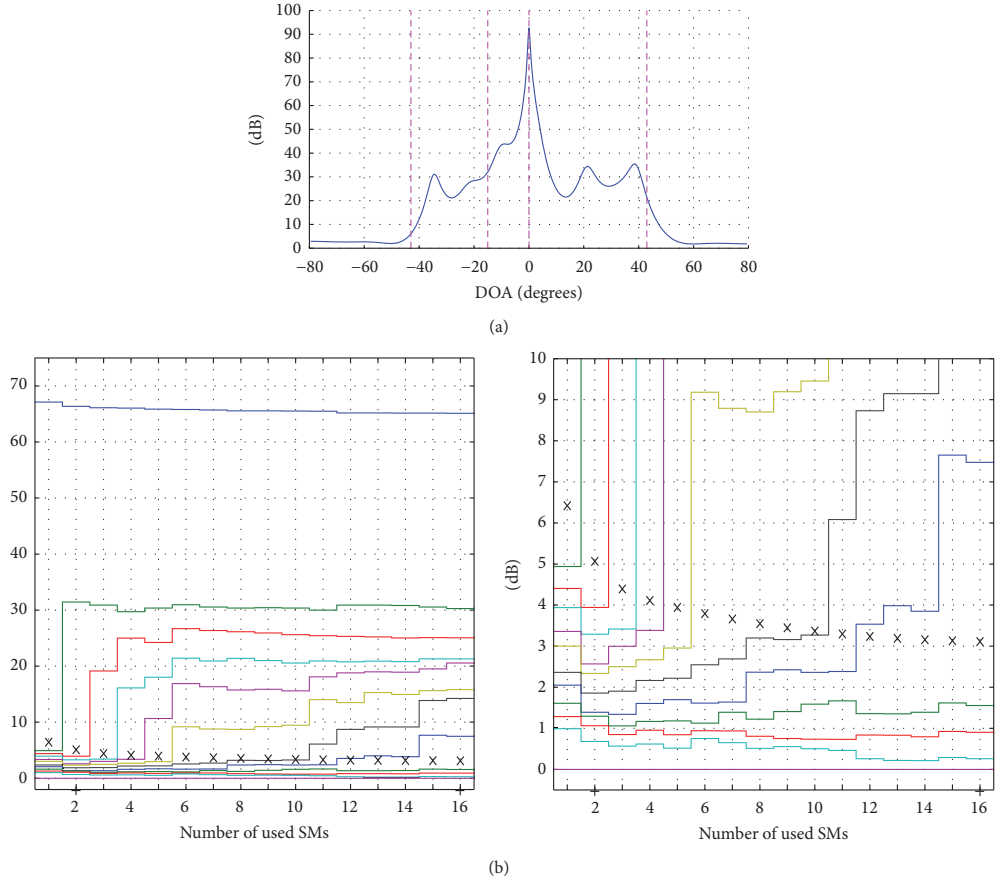

Figure 13: Measurement C2SW. Two coherent transmitters, one strong and one weak. (a) Capon DOA spectrum. (b) Eigenspectrum. Zoom-in to the right. dB scale. See Section 3.3 for "SM."

transmitter signals are different from pure sinusoids, the emulation of uncorrelated transmitted signals probably had to be performed in a different way.

The measurement quality was considered before, during, and after conducting the experiments, for example, with a written experimental design [26] and estimation of uncertainty in the position measurements of the antennas and the reflector. See [13] for further information on this.

5.2. More Comparison of the Measurements with the Literature. The literature [19, 21, 27] says that each noncoherent monochromatic source with a different DOA gives rise to a large eigenvalue, which is in accordance with our measurements C1S, C2SS, and U2SS.

The more uncorrelated the sources are the more equal in size the eigenvalues are in the experiments in [19, 21]. In particular, uncorrelated sources with well separated DOAs give each an eigenvalue of similar size according to [21]. These statements are in accordance with our measurements I2SS and U2SS. In [25] a theoretic expression for the size of the two eigenvalues of two uncorrelated zero bandwidth signals is derived. In our measurements U2SS and U2SW the difference between the two largest eigenvalues for 1 SM was about 6 dB larger than the prediction of the theory. The discrepancy could be due to a nonideal measurement system and to a nonzero bandwidth because of time limited measurements.

The result that the eigenspectrum starts with a single eigenvalue for (one or two) coherent transmitters for a single SM (a very short acquisition interval) in our measurements agrees with the result in [14] showing that the rank will be one for the case without motion and with zero jammer bandwidth and for the case with motion of radar and/or jammer, zero bandwidth, and a "vanishing short" acquisition interval. One of our results is that the number of large eigenvalues will increase up to a limit when the number of SMs is increased. This result is in agreement with the result in [14] showing that each scatterer will appear as an independent source when the acquisition interval goes to infinity.

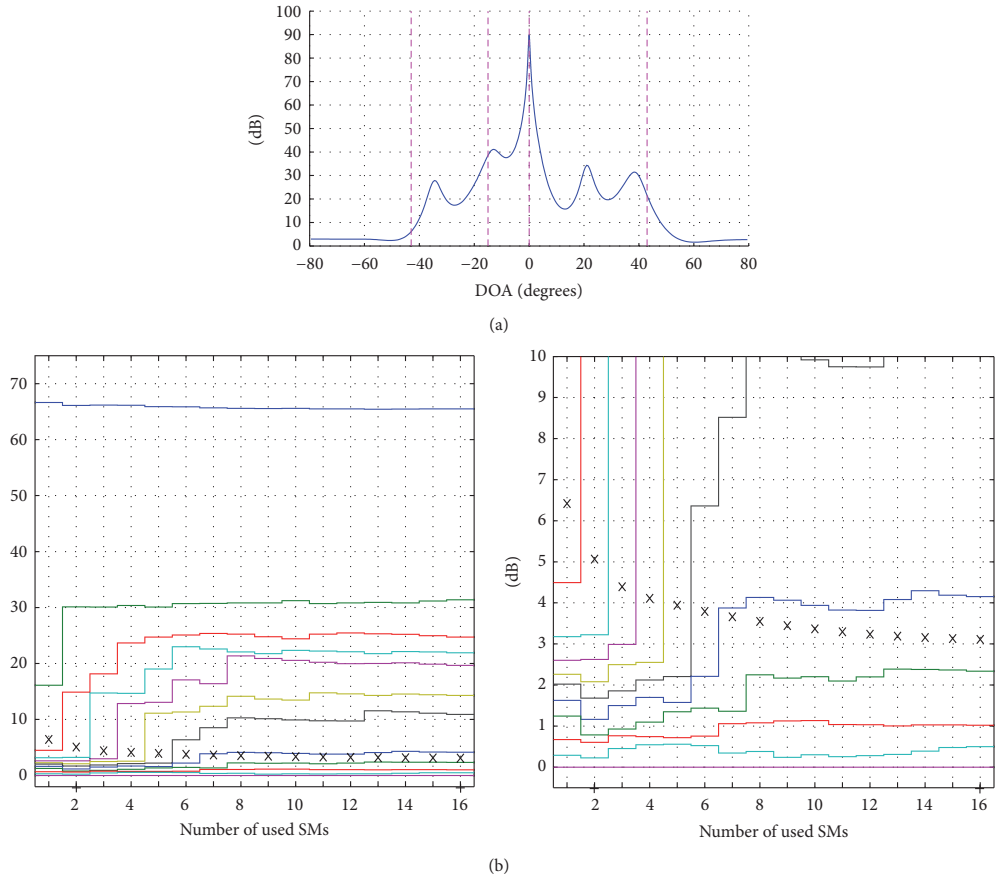

Figure 14: Measurement U2SW. Two uncorrelated transmitters, one strong and one weak. (a) Capon DOA spectrum. (b) Eigenspectrum. Zoom-in to the right. dB scale. See Section 3.3 for "SM."

We noticed by our measurements that the number of large eigenvalues depends on the signal power in comparison to the noise floor (compare measurement C1S in Figure 8 with C1W in Figure 12 and measurement U2SS with U2SW). The higher the signal power is, the more the eigenvalues of the spectrum tail will appear above the noise level. It is like an iceberg lifting above the ocean surface. This phenomenon is therefore called the *iceberg effect*. It is described in [4, 27] and there illustrated by simulations.

We found that the number of eigenpatterns which cover the reflection region (by the number of eigenpatterns which have their highest peak within the reflection region) is nearly independent of the number of used SMs. To estimate the number of signals using the eigenvalues we need many SMs but with the eigenpatterns it is enough with a few. Thus, it seems like the fact that the eigenpatterns are better for the estimation of the number of signals than the eigenvalues. Nevertheless, it is well-known that the number of large eigenvalues determines the required DoFs for interference suppression [4]. In [27] it is noticed, probably from simulations, that the eigenpatterns corresponding to the signal sources were "essentially unaffected" by a "modest amount" of interference subspace leakage, which is in agreement with our results.

We conclude that our measurement results agree in most cases with theoretic and simulated results presented in the literature.

6. Conclusions

We have designed an experiment for low-cost indoor measurements of direct and scattered signals with radar applications in mind. We have good control of the influencing factors, which is necessary to draw objective conclusions. The detailed description of our experiment could serve as a help for conducting other well-controlled experiments. Our experimental design has some characteristics:

(i) Emulation of coherent, intermediate correlated, and uncorrelated signal sources (Section 3.4).

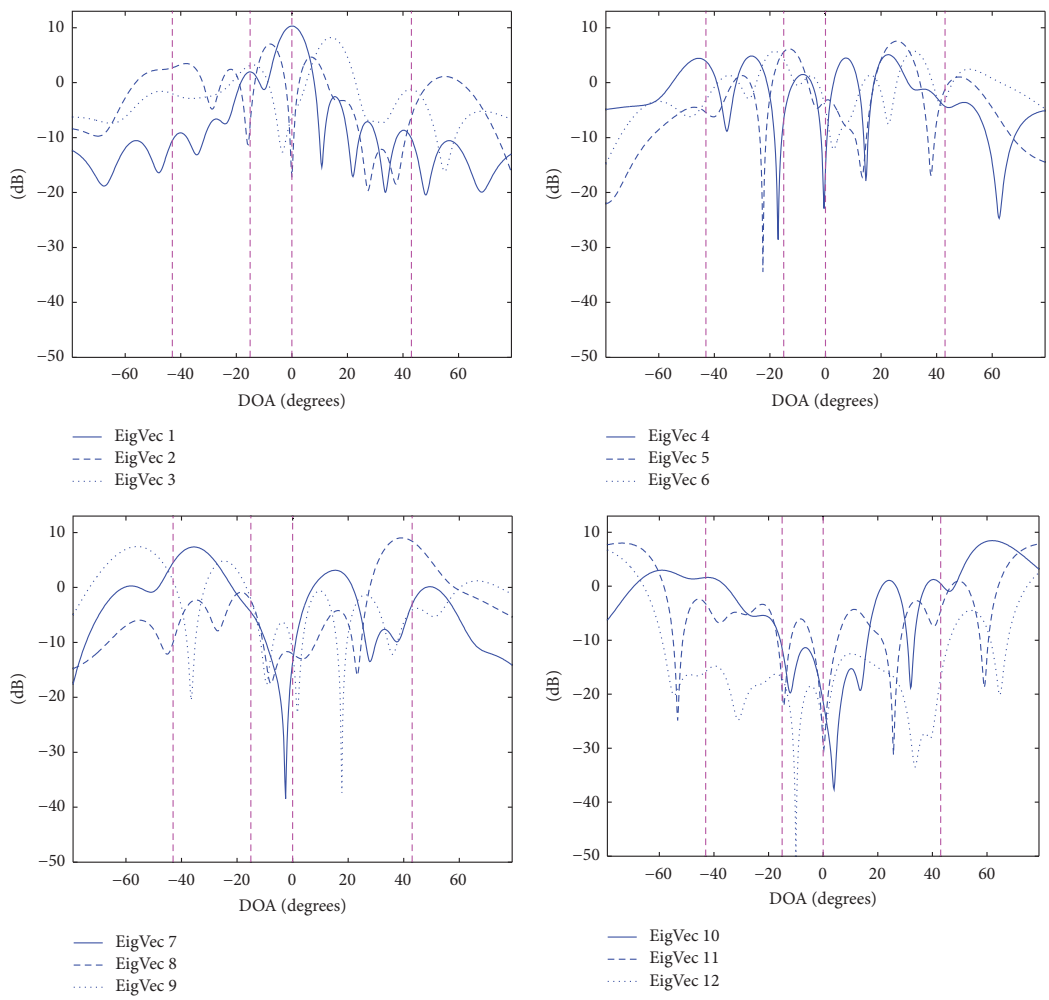

Figure 15: Eigenpatterns for measurement C2SS (two coherent strong transmitters). 1 SM. Dashed vertical lines are the true DOAs of the transmitter(s) and the nearest left and right corner of the reflector. Figure 6.32 in [13].

(ii) Calibration: when to calibrate and when not and also how to calibrate in different cases (Sections 3.2 and 3.5).

(iii) Near-field compensation: relation to receiving antenna properties, decorrelation, and eigenpatterns (Sections 3.4 and 3.5).

(iv) Noise eigenvalue spread: relation to calibration, hardware quality, and signal rank (Sections 2.1, 3.2, and 3.5).

(v) Emulation of a rough surface by a reflector (Section 3.3).

(vi) Decorrelation of the signals by movement of the reflector (Section 3.3).

(vii) Acquisition interval for the estimation of the covariance matrix and its effects on the rank (Section 3.3).

(viii) Analysis methods: Capon DOA spectrum, eigenspectrum, and eigenpatterns (Section 3.5).

Section 4.3 summarizes our measured properties of direct and scattered signals. The agreement of our measured properties with theoretic and simulated results presented in the literature shows that our experimental design is realistic and sound.

Competing Interests

The authors declare that they have no competing interests.

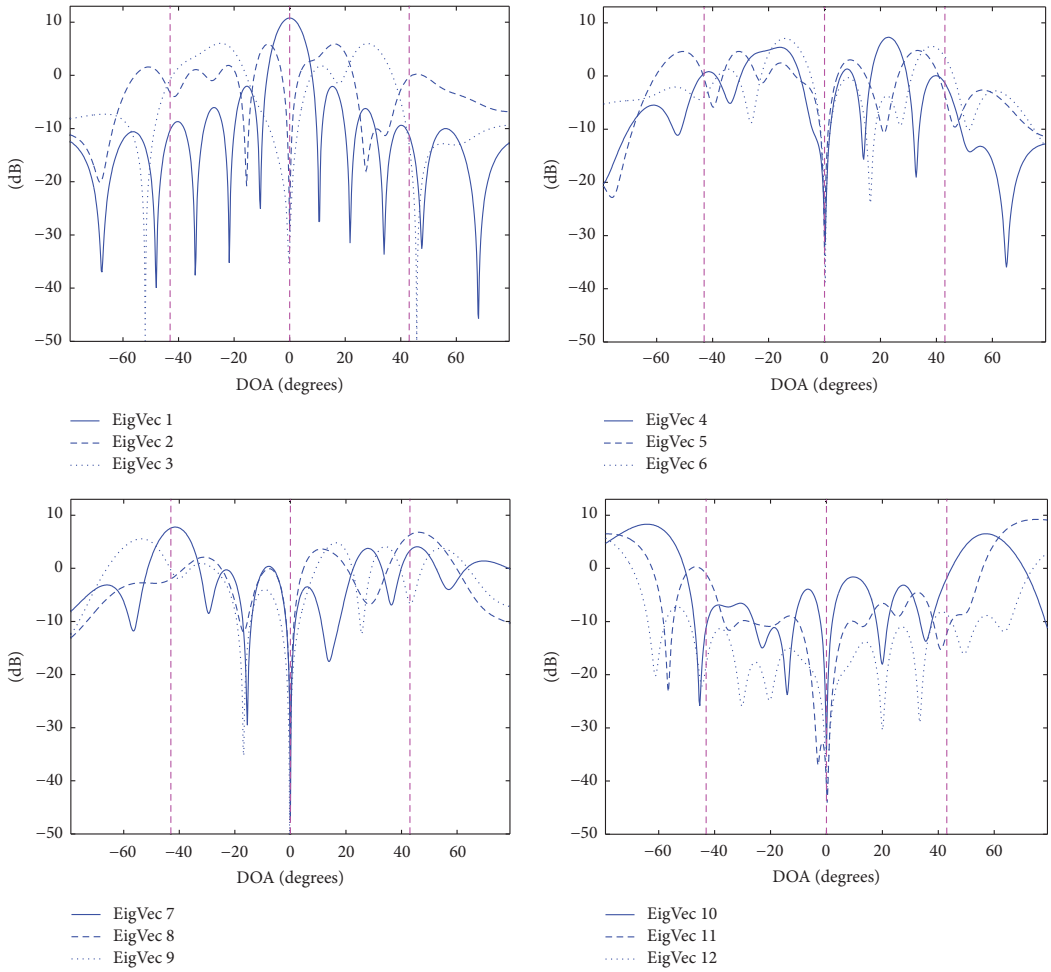

Figure 16: Eigenpatterns for measurement C1W (a single weak transmitter). 1 SM. Dashed vertical lines are the true DOAs of the transmitter(s) and the nearest left and right corner of the reflector. Figure 6.20 in [13].

Acknowledgments

This work has been financially supported by the Swedish Armed Forces, the Swedish Defence Materiel Administration, and the Swedish Knowledge Foundation.

References

[1] H. Krim and M. Viberg, "Two decades of array signal processing research: the parametric approach," *IEEE Signal Processing Magazine*, vol. 13, no. 4, pp. 67–94, 1996.

[2] I. S. Reed, J. D. Mallett, and L. E. Brennan, "Rapid convergence rate in adaptive arrays," *IEEE Transactions on Aerospace and Electronic Systems*, vol. 10, no. 6, pp. 853–863, 1974.

[3] L. E. Brennan and I. S. Reed, "Theory of adaptive radar," *IEEE Transactions on Aerospace and Electronic Systems*, vol. 9, no. 2, pp. 237–252, 1973.

[4] J. R. Guerci, *Space-Time Adaptive Processing for Radar*, Artech House, 2003.

[5] J. Ward, "Space-time adaptive processing for airborne radar," Tech. Rep. 1015, MIT Lincoln Laboratory, 1994.

[6] M. C. Wicks, M. Rangaswamy, and R. Adve, "Space-time adaptive processing: a knowledge-based perspective for airborne radar," *IEEE Signal Processing Magazine*, vol. 23, no. 1, pp. 51–65, 2006.

[7] J. R. Guerci, J. S. Goldstein, and I. S. Reed, "Optimal and adaptive reduced-rank STAP," *IEEE Transactions on Aerospace and Electronic Systems*, vol. 36, no. 2, pp. 647–663, 2000.

[8] W. L. Melvin and M. E. Davis, "Adaptive cancellation method for geometry-induced nonstationary bistatic clutter environments," *IEEE Transactions on Aerospace and Electronic Systems*, vol. 43, no. 2, pp. 651–672, 2007.

[9] M. Viberg, "Direction-of-arrival estimation," in *Smart Antennas: State of the Art*, chapter 16, Hindawi Publishing Corporation, New York, NY, USA, 2005.

[10] L. Pettersson, "An S-band digital beamforming antenna: design, procedures and performance," FOA Report FOA-R—99-01162-408—SE, 1999.

[11] S. Björklund, P. Grahn, and A. Nelander, "Analysis of array antenna measurements with a rough surface reflector," in *Proceedings of the 34th Asilomar Conference on Signals, Systems, and Computers*, pp. 1135–1139, Pacific Grove, Calif, USA, November 2000.

[12] X. Mestre, "Improved estimation of eigenvalues and eigenvectors of covariance matrices using their sample estimates," *IEEE Transactions on Information Theory*, vol. 54, no. 11, pp. 5113–5129, 2008.

[13] S. Björklund, P. Grahn, A. Nelander, and A. Alm, "Hot clutter reduction in radar. Measurement report for anechoic chamber measurements in spring 2000," Tech. Rep. FOA-R—00-01806-408—SE, 2000.

[14] P. M. Techau, J. R. Guerci, T. H. Slocumb, and L. J. Griffiths, "Performance bounds for hot and cold clutter mitigation," *IEEE Transactions on Aerospace and Electronic Systems*, vol. 35, no. 4, pp. 1253–1265, 1999.

[15] R. Cepeda, C. Vithanage, and W. Thompson, "From wideband to ultrawideband: channel diversity in low-mobility indoor environments," *IEEE Transactions on Antennas and Propagation*, vol. 59, no. 10, pp. 3882–3889, 2011.

[16] L. Pettersson, M. Danestig, and U. Sjostrom, "An experimental S-band digital beamforming antenna," *IEEE Aerospace and Electronic Systems Magazine*, vol. 12, no. 11, pp. 19–26, 1997.

[17] S. Björklund and A. Heydarkhan, "High resolution direction of arrival estimation methods applied to measurements from a digital array antenna," in *Proceedings of the IEEE Sensor Array and Multichannel Signal Processing Workshop (SAM '00)*, pp. 464–468, Cambridge, Mass, USA, March 2000.

[18] E. M. Friel and K. M. Pasala, "Effects of mutual coupling on the performance of STAP antenna arrays," *IEEE Transactions on Aerospace and Electronic Systems*, vol. 36, no. 2, pp. 518–527, 2000.

[19] F. Haber and M. Zoltowski, "Spatial spectrum estimation in a coherent signal environment using an array in motion," *IEEE Transactions on Antennas and Propagation*, vol. AP-34, no. 3, pp. 301–310, 1986.

[20] C. A. Balanis, *Antenna Theory. Analysis and Design*, John Wiley & Sons, New York, NY, USA, 2nd edition, 1997.

[21] A. Farina, *Antenna-Based Signal Processing Techniques for Radar Systems*, Artech House, Norwood, Mass, USA, 1992.

[22] J. Capon, "High-resolution frequency-wavenumber spectrum analysis," *Proceedings of the IEEE*, vol. 57, no. 8, pp. 1408–1418, 1969.

[23] W. F. Gabriel, "Using spectral estimation techniques in adaptive processing antenna systems," *IEEE Transactions on Antennas and Propagation*, vol. AP-34, no. 3, pp. 291–300, 1986.

[24] V. U. Reddy, A. Paulraj, and T. Kailath, "Performance analysis of the optimum beamformer in the presence of correlated sources and its behavior under spatial smoothing," *IEEE Transactions on Acoustics, Speech, and Signal Processing*, vol. 35, no. 7, pp. 927–936, 1987.

[25] M. Zatman, "How narrow is narrowband?" *IEE Proceedings—Radar, Sonar and Navigation*, vol. 145, no. 2, pp. 85–91, 1998.

[26] S. Björklund, "Hot clutter reduction in radar. Experimental design for anechoic chamber measurements," Technical Report FOA Memo 00-3316/L, 2000.

[27] J. R. Guerci and J. S. Bergin, "Principal components, covariance matrix tapers, and the subspace leakage problem," *IEEE Transactions on Aerospace and Electronic Systems*, vol. 38, no. 1, pp. 152–162, 2002.

Publication 5: Clutter Properties for STAP with Smooth and Faceted Cylindrical Conformal Antennas

Clutter Properties for STAP with Smooth and Faceted Cylindrical Conformal Antennas

Svante Björklund[1], Tomas Boman[2],
Anders Nelander[3]
[123]Swedish Defence Research Agency (FOI)
[123]P.O. Box 1165, SE-581 11 Linköping, Sweden
[1]svabj@foi.se, [2]tombom@foi.se, [3]andnel@foi.se

Svante Björklund[1]
[1]Blekinge Institute of Technology
[1]Ronneby, Sweden

Abstract - **Conformal antennas, which assume the shape of the platform, have several advantages; like reduced weight and space, aerodynamic design and increased field of view. We are interested in detection of moving ground targets with air-borne radar with faceted or smooth vertical half-cylinder or planar antennas with different subarray sizes. We simulate radar systems and study clutter properties which are important for suppressing the clutter with STAP (Space-Time Adaptive Processing), properties by which we can compare the antennas. We use old analysis tools and propose some new which are easy to interpret and draw conclusions from. We find that the faceted and smooth half-cylinder antennas have no significant differences in clutter suppression performance. The plane antenna has poorer performance. The subarray division is more important than the antenna geometry. The number of antenna channels is related to the clutter rank and the clutter fraction of the signal space.**

I. Introduction

Lately there has been a large interest in sensors for small platforms like UAVs (Unmanned Aerial Vehicle) for surveillance and information acquisition about ground targets, in for example task forces and on a tactical level [5].

It is desired that the UAV has several functions, like detection, positioning and identification of stationary and moving ground targets, tactical mapping of unknown terrain, seeing and avoiding other aerial vehicles, communication and in some cases electronic warfare functions. Probably a combination of microwave and EO (electro-optical) systems is needed. These systems have different advantages and drawbacks. In this paper we only address microwave systems.

The microwave sensing of stationary targets can be performed by SAR (Synthetic Aperture Radar) and moving targets by radar with GMTI (Ground Moving Target Indication) using STAP (Space Time Adaptive Processing) [7, 18].

In order to save space, weight, costs and energy consumption the same microwave hardware should be used for several or all functions, if possible. On UAVs a conformal array antenna, which assumes the shape of the platform (Fig. 1 and 2), has several advantages. It can reduce weight, space and radar cross section. It has an aerodynamic design and can increase the field of view and the antenna aperture size. It also avoids the signal modulation a rotating antenna would cause.

At FOI an experimental conformal antenna for a small tactical UAV or an aircraft mounted pod has been designed, built and evaluated [12, 15], see Fig. 1. The antenna consists of planar facets on a vertical half-cylinder. An antenna with facets instead of a continuously bent antenna aperture is often easier to manufacture.

This paper contains simulation results of clutter properties which are important for the employment of STAP for GMTI in UAV borne radar with faceted (of the FOI type) and smooth cylindrical conformal antennas (Fig. 1, 2 and 4). The purpose is to compare different antennas, including their geometry and subarray division, regarding clutter suppression. The paper is based on the report [1] and the conference paper [2]. We have made these developments compared to [2]: Improved power calculations, directive transmitter antennas, antenna

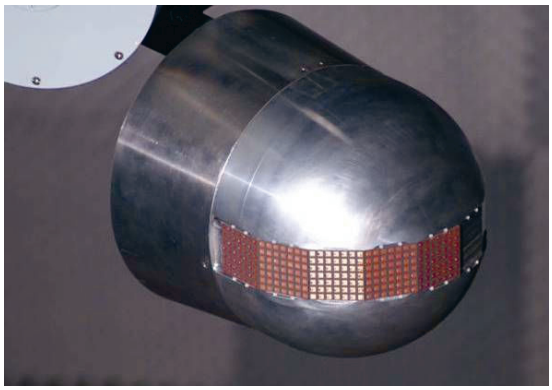

Figure 1. Experimental conformal antenna designed and built by FOI. It has planar facets on a vertical half-cylinder. Photo from [6].

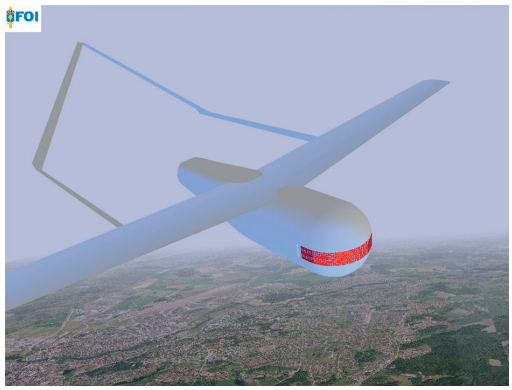

Figure 2. The FOI experimental conformal antenna mounted on a UAV. Image from [6].

scanning of transmitter and receiver subarrays and also new methods for comparison of antenna geometries and divisions.

STAP with conformal antennas has not been reported much in the literature. In [8] they model conformal antennas and compute SINR performance for an airborne radar against moving targets with clutter background. A continued work is reported in [9]. In [8, 9] they used conformal antennas with other geometries than we do. They also ignored the influence of the polarization, which is questionable. We have taken the polarization into account. Reference [17] is about range dependence compensation of training data from a partially calibrated conformal antenna in bistatic radar. A method for managing clutter range dependence with conformal arrays is proposed in [10].

II. Simulations

The simulation program, written in Matlab, mainly computes and displays clutter properties, SINR (Signal to Interference plus Noise Ratio) and antenna patterns as functions of antenna and waveform design of the radar, clutter and target models and positions and velocities.

The scenario is similar to the one in [2], making comparisons possible. The simulation scenario is depicted in Fig. 3 with the ground surface, surface elements, a target and the radar. We let only a rectangular flat ground surface of size 10 km x 10 km contribute to the clutter in the simulations. The horizons are not taken into consideration. The surface is divided into equally large, rectangular elements $(\Delta X, \Delta Y)$=(50 x 50m). The equal size compared to the usual division of the surface elements according to the radar coordinates (azimuth, elevation and range) has the advantage that the clutter statistical properties will be the same for all elements just because they have the same size.

The specific RCS (Radar Cross Section) $[m^2/m^2]$ of the ground is modelled by the (monostatic) *constant gamma model* [14] $\sigma = \gamma \sin\theta_i$, where θ_i is the grazing angle and $\gamma = -14$ dB, applicable to "open woods" [14, p. 333]. This is a simple but common model. The radar platform is located above the center of the ground surface at an altitude of 300 m and is moving with 45 m/s in the global $\hat{X}$ direction (Fig. 3).

The radar carrier frequency is 35 GHz. The radar range resolution is ΔR=200 m. The number of radar pulses in a CPI (Coherent Processing Interval) is $M = 16$. The PRF is 3.75 kHz, the maximum unambiguous radial velocity is 8.0 m/s and the velocity resolution is 1 m/s. The choice of ΔX, ΔY, ΔR and M is limited by the simulation computational load. Since the radar unambiguous range (40 km) is larger than the maximum range for all ground elements, there will be no range aliasing. We have simulated several receiver antennas, both conformal ones (faceted and smooth half-

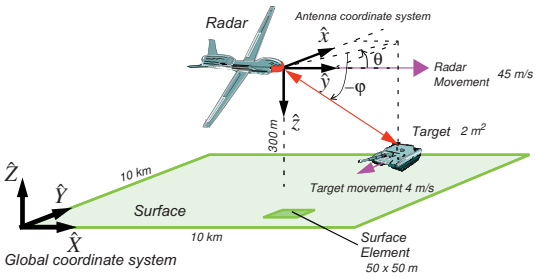

Figure 3. Simulation scenario with radar, ground surface, surface element and ground target. The radar is located above the center of the ground surface and is moving in the global x direction. Angle azimuth θ, elevation φ.

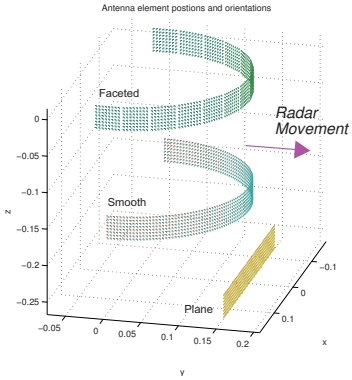

Figure 4. Element placement for the faceted (Fpq) and smooth (Spq) cylindrical antennas and for the plane (Ppq) antenna. Figure from [2].

cylindrical) and plane ones. We use the plane antennas for comparison. We have recently simulated antennas with three different geometries (placement and orientation of the antenna elements), *Fpq*, *Spq* and *Ppq* (Fig. 4). The symbols *pq* denote the subarray divisions described below.

- *Fpq*: Faceted antenna on a forward-looking vertical half cylinder (radius 0.15 m) with 14 facets with 8x8 antenna elements each, totally 896 elements. Within each facet the elements are separated half a wavelength. See Fig. 4.
- *Spq*: Smooth antenna on a forward-looking vertical half cylinder (radius 0.15 m) with 8 elements vertically, totally 896 elements. The element separation is approximately half a wavelength. See Fig. 4.
- *Ppq*: Plane forward-looking antenna with 8 elements vertically and 64 horizontally, totally 512 elements. The element separation is half a wavelength. See Fig. 4. The aperture width is 0.27 m, which is somewhat less than the projection to the front of the faceted or smooth cylindrical antennas (0.30 m). On the other hand, all elements of the plane antenna are directed to the front and will be more effective than most element of the faceted and smooth antennas when looking to the front and therefore compensate for the smaller number of antenna elements and smaller forward-looking aperture. Looking far to the side with this antenna will give poorer performance than with the half-cylinder antennas.

For each of the three antenna geometries described above four different subarray divisions are used. All subarrays are non-overlapping and have 8 vertical elements. The number of horizontal elements in the subarrays are 8, 4, 2 or 1. This gives totally 12 receiver antennas with the names F88, F84, F82, F81, S88, S84, S82, S81, P88, P84, P82 and P81. The faceted and smooth cylindrical antennas have 14, 28, 56 or 112 subarrays and antenna channels. The plane forward-looking antennas have 8, 16, 32 or 64 subarrays. None of the subarrays use tapering. Compare with the antennas in [8].

The receiver subarrays are with all antennas scanned to one of the 14 azimuth angles [-90 -76 -62 -48 -35 -21 -7 7 21 35 48 62 76 90] degrees relative the forward direction (the global x direction in Fig. 3), which also are the normal directions of the facets of the facetted antenna. The subarrays are scanned to the elevation -5.7 degrees, which gives an intersection of the antenna beam with the ground at 3 km. In [2] the subarrays were not scanned but had a pointing direction fixed to the forward direction. By a fix pointing direction we only get the clutter properties for a radar field of view within the fix subarray main beam. Our new simulations are therefore an improvement in this aspect.

For the transmission, an 8x8 subarray of the antenna was employed. With the antenna gain 23 dB a transmitted power of 16 W (0.25 W per element) is enough for a designed detection range of 5 km for a target with RCS $2\ \mathrm{m}^2$. An isotropic transmitter antenna, as in [2], would require a mean transmitted power of 50 kW, which would be unreasonable. For the facetted and smooth cylindrical antennas, the subarray in the configuration F88 or S88, respectively, whose normal direction was closest to the receiver subarray scanning was used as the transmitter. For the plane antenna a fix subarray of the middle 8x8 elements was utilized for the transmission. In all cases, the transmitter antenna was scanned to the same direction as the receiver subarrays. Compared to an isotropic transmitter antenna the field of view is limited by the transmitter main beam, see Fig. 5.

The transmitter and receiver antenna elements have in their forward direction the amplitude pattern $f_e(\beta) = \cos\beta$, where β is the angle with the element normal vector. The pattern is zero in element back direction. This gives zero clutter power from the back direction of the transmitter facet in Fig. 5. The antenna elements are vertically polarized.

For each clutter element and for the target the RCS, range, viewing angles, antenna gains and Doppler frequency are computed. The received clutter and target signal correlation matrices[1] and powers are then computed. This is done in a similar manner as in [13]. The clutter signal from all surface elements are assumed statistically independent, as in [13].

III. Space-Time Adaptive Processing

The adaptive space-slow-time processing which we are interested in is performed by the following well-known linear filter. See for example [3, 7, 18]. The output of the filter is $y = \mathbf{w}_a^H \mathbf{x}$, where $\mathbf{x}$ is a radar snapshot (the stacked signals from the antenna channels and radar pulses). The filter weights are computed according to equation (1)

$$\mathbf{w}_a = \mu \mathbf{R}_{\mathbf{qq}}^{-1} \mathbf{w}_0, \qquad (1)$$

1. Often called *covariance matrix* in the literature.

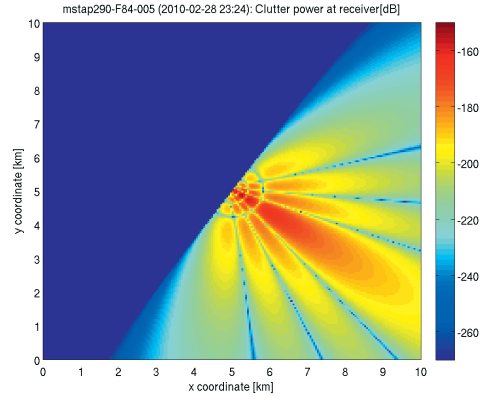

Figure 5. Clutter power at the receiver antenna before beamforming vs. different surface positions of the clutter cells. Antenna F84. Scanning to $-35°$.

where μ is a scalar that can be chosen in different ways, $\mathbf{R}_{\mathbf{qq}} = \mathrm{E}\{\mathbf{x}_\mathbf{q}\mathbf{x}_\mathbf{q}^H\}$ is the correlation matrix of the interference $\mathbf{x}_\mathbf{q}$ (clutter, receiver noise, etc.) and $\mathbf{w}_0$ is a constraint vector, which depends on DOA (Direction of Arrival) and Doppler to investigate ("the steering vector"). Fully adaptive STAP is assumed to be used, i.e. all digital antenna channels and all radar pulses are utilized. However, analog beamforming to subarrays are employed, giving fewer antenna channels than antenna elements. The true space-slow-time correlation matrix is used. It is not estimated from data, as must be done in reality, but computed theoretically. This will give *optimal STAP*.

IV. Performance Measures

We have used several performance measures to compare different antenna geometries and subarray divisions.

Fig. 7-12 display interference (clutter plus receiver noise) DOA Doppler Spectra for some of the different receiver antennas described above. An interference DOA Doppler Spectrum (DDS) displays the interference power as experienced by the radar, for a certain range bin (3000 m in this paper), distributed in DOA and Doppler. It is desired that the parts of the DOA-Doppler spectrum which is stronger than the receiver noise occupy as little as possible of the spectrum. These parts are due to the clutter. This gives more signal space where targets

can be detected. Close to the strong clutter in the spectrum we cannot expect to being able to detect targets. It is also desired that the clutter looks the same in many neighboring range bins since these bins usually are used to estimate the clutter properties, i.e. the correlation matrix $\mathbf{R}_{qq}$. The DOA-Doppler plots in this report were estimated by the Capon method [4], as in [11], which should give a true power measure with good resolution. Because of the scanning of the receiver subarrays and the transmitter antenna, we have merged 14 (the number of scanning angles) DDSs for different DOA subintervals, each with the width of the transmitter beam, to form a single DDS with DOAs in the whole interval $[-90°, 90°]$.

We have further processed the interference DOA Doppler spectrum by sorting all its values in decreasing order, getting the interference Sorted DOA Doppler Spectrum (SDDS). See Fig. 13 for an example. The spectra for different cases, like different antennas, are then easier to compare. The sorted spectrum can also be used in quantitative statements, which is difficult with the unsorted spectra in Fig. 7-12. Our sorted interference DOA Doppler spectrum is a similar concept as the "rank-ordered SINR loss" in [16].

A step further we get the Clutter DOA Doppler Fraction (CDDF) which we define as the fraction of the interference DOA Doppler spectrum larger than 3dB above the white noise power. We must set threshold above the noise level because no values of the spectrum is below the noise, see Fig. 13. We assume that only 3dB or more above the noise the clutter will have any significance. The CDDF is similar to the "Usable Doppler Space Fraction" (UDSF) in [18].

Fig. 6 shows the clutter eigenspectrum for some of the receiver antennas. A clutter eigenspectrum depicts the eigenvalues of the clutter correlation matrix $\mathbf{R}_{qq}$, sorted in descending order. It tells us how difficult it is to suppress the clutter and how much radar resources are needed. It is the number of eigenvalues larger than the receiver noise that matters for the clutter suppression. This number is called the "effective rank" [7]. The effective rank is related to the number of antenna channels and radar pulses needed for clutter suppression. It gives an indication of the computational burden and the amount of training data needed to estimate the properties of the interference and compute the suppression filter. The latter is very important, since it is usually difficult to acquire enough training data of high quality. The eigenspectrum is a major analysis tool for interference suppression in radar. Also the eigenspectra let us compare different antenna geometries and subarray divisions. We have in this paper computed the eigenspectra for the slant range 3000 m and the receiver subarray and transmitter antennas were be scanned to $-34°$.

Also from the eigenspectrum we have taken a step further and computed the Clutter Rank Fraction (CRF) which is the fraction of eigenvalues larger than the white noise power. This quantity, like the DDS, also measures how much of the signal space the clutter occupies and therefore how difficult it is to suppress. Computing the fraction is also a concept like the CDDF and UDSF.

The new performance measures in this paper (SDDS, CDDF and CRF) are easier to interpret and draw conclusions from compared to the ones in [2], the DDS and eigenspectrum. All performance measures we have used are independent of the STAP method.

V. Simulation results

Fig. 7-12 display interference DOA Doppler Spectra (DDS) for some of the different receiver antennas described above. The ambiguity in Doppler is clearly visible. The plane antenna has many more strong clutter ridges. Note the differences to the corresponding DDSs in [2]. The main reason for the less clutter here and the cleaner spectrum should be the directive transmitter antenna and the scanning of the receiver subarrays and the transmitter antenna. The absolute power levels in the DDS here and the DDSs in [2] cannot be compared because the simulations are different.

Table I shows the effective clutter rank, Table II the clutter rank fraction (CRF) and Table III the Clutter DOA Doppler Fraction (CDDF) for our 12 antennas. We see that the effective rank decreases (better) with fewer antenna channels (larger

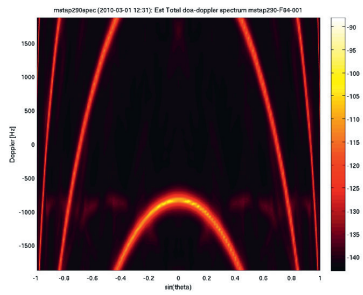

Figure 7. Interference DOA Doppler spectrum. Antenna F84. Slant range 3 km.

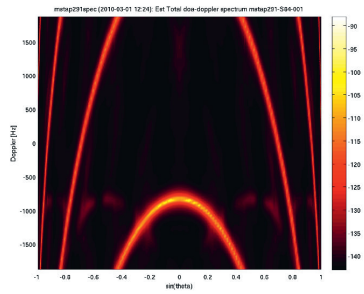

Figure 8. Interference DOA Doppler spectrum. Antenna S84. Slant range 3 km.

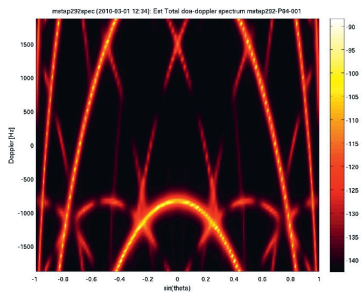

Figure 9. Interference DOA Doppler spectrum. Antenna P84. Slant range 3 km.

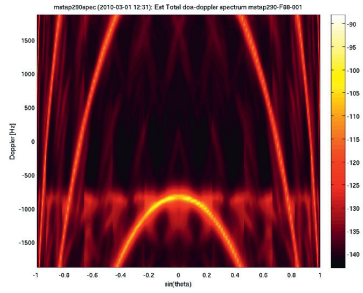

Figure 10. Interference DOA Doppler spectrum. Antenna F88. Slant range 3 km.

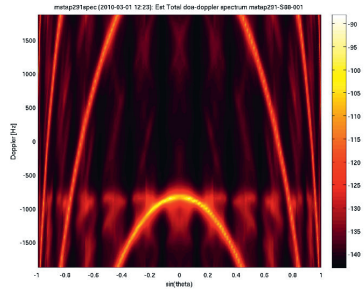

Figure 11. Interference DOA Doppler spectrum. Antenna S88. Slant range 3 km.

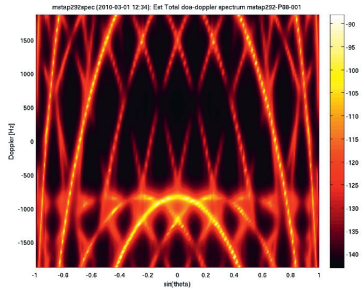

Figure 12. Interference DOA Doppler spectrum. Antenna P88. Slant range 3 km.

subarrays) and the effective rank is about the same for the faceted and smooth cylindrical antennas while smaller for the plane antenna (which has fewer channels). We see that the clutter rank fraction (CRF) increases (worse) with fewer antenna channels (larger subarrays). The CRF is about the same for the faceted and smooth antennas while larger (worse) for the plane antenna. We see that clutter DOA Doppler fraction (CDDF) increases (worse) with fewer antenna channels (larger subarrays). Again faceted and smooth antennas have about the same values while the plane antenna has a higher CDDF (worse). For all antenna types the CDDF difference is larger between large subarrays than between small ones. Note also that for the largest subarrays the CDDF is not worse for the plane antenna than for the other ones.

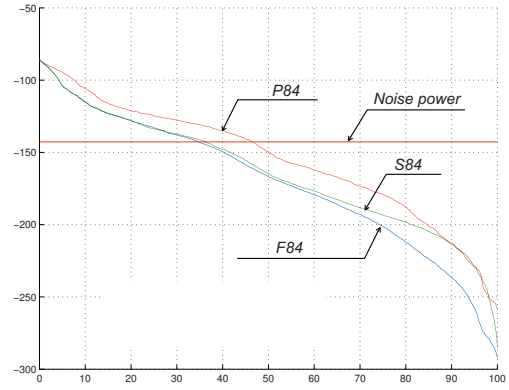

Figure 6. Clutter eigenspectrum. Comparing antennas F84, S84 and P84. Slant range 3km. Scan angles $-34°$.

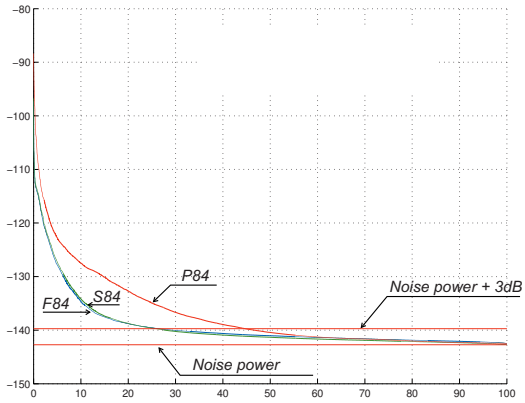

Figure 13. Interference Sorted DOA Doppler spectrum (SDDS). Comparing antennas F84, S84 and P84. Slant range 3km.

TABLE I. Effective Clutter Rank (number of eigenvalues larger than the white noise power).

	Faceted Fpq	Smooth Spq	Plane Ppq
pq=81	169	187	150
82	160	174	142
84	156	162	119
88	133	128	90

TABLE II. Clutter Rank Fraction (CRF, fraction of eigenvalues larger than the white noise power).

	Faceted Fpq	Smooth Spq	Plane Ppq
pq=81	9 %	10 %	15 %
82	18 %	19 %	28 %
84	35 %	36 %	47 %
88	60 %	57 %	71 %

VI. Further Discussion

The difference between smooth and faceted antennas is not expected to be large, provided that the elements in different facets can be used simultaneously without problems. In our simulations the smooth and facetted antennas have similar properties.

TABLE III. Clutter DOA Doppler Fraction (CDDF, fraction of the interference DOA Doppler spectrum larger than 3dB above the white noise power).

	Faceted Fpq	Smooth Spq	Plane Ppq
pq=81	14 %	15 %	23 %
82	16 %	17 %	29 %
84	27 %	26 %	45 %
88	77 %	71 %	75 %

The antenna elements in a smooth array can be combined into almost arbitrary sub-arrays, but it would be difficult to make subarrays of a faceted array that overlap between facets. This is a reason for not using overlapping subarrays in the simulations.

From an antenna point of view, the smooth antenna has an advantage in that all elements but a few at the outer edges can be considered equal, both in terms of radiation pattern and in terms of matching properties. The faceted antenna is on the other hand easier to manufacture and repair since each facet can be replaced independent of the other facets.

Our conformal antennas are able to form good transmitter and receiver subarray patterns in all directions between $-90°$ and $90°$ because there will always be a part of the antenna aperture nearly orthogonal to the desired direction. The plane antenna cannot do this far from broadside. For the antennas with the small subarrays (1-4 elements wide) the field of view will be limited by the transmitter antenna beamwidth.

We believe now that the antennas with the fewest antenna channels (largest subarrays) are useful for clutter suppression. This is nearly contrary to the conclusion in [2]. Our changed opinion is due to our

better analysis tools now. Some other conclusions are the same as in [2].

VII. Conclusions

We draw the following conclusions from our work:

- The faceted and smooth half-cylinder antennas have no significant differences in clutter suppression performance. The plane antenna has poorer performance.
- The subarray division is more important than the geometry of the antenna.
- The number of antenna channels is related to the clutter rank and the clutter fraction of the signal space. With fewer antenna channels a larger percentage of the channels is needed for the clutter suppression but also with fewer channels less resources (computational and training data) are needed for the suppression.
- We propose new performance measures (SDDS, CRF and CDDF), which seem to be easy to interpret and draw conclusions from.

References

[1] Björklund S., "*STAP for Detection of Ground Targets, Simulation Program and First Results*", Report FOI Memo 2517, FOI September 2008.

[2] Björklund S.: "*Space-Time Adaptive Processing with a Half-Cylinder Faceted Conformal Antenna*", International Radar Conference, RADAR 2009, Bordeaux, France, October 12-16, 2009.

[3] Brennan L.E., Reed I.S.: "*Theory of Adaptive Radar*", IEEE Trans AES., Vol. 9, No. 2, March 1973, pp 237-252.

[4] Capon J. : "*High-Resolution Frequency Wavenumber Spectrum Analysis*", Proceedings of the IEEE, Vol. 57, No. 8, pp. 1408-1418, Aug 1969.

[5] Erickson R.: "*Kompakta radarsystem på små farkoster - den internationellla utvecklingen*" ("*Compact Radar Systems on Small Platforms - The International Development*"), In Swedish, FOI Memo 2379, 2008.

[6] Erickson R., Martin T., Pettersson L., Grahn P., Boman T., Björklund S., Malmqvist R., Nelander A.: "*Flexibla mikrovågssystem - Årsrapport 2007*" ("*Flexible Microwave Systems - Annual Report 2007*"), In Swedish, FOI Memo 2243, FOI 2007.

[7] Guerci J.R.: "*Space-Time Adaptive Processing for Radar*", Artech House 2003, ISBN 1-58053-377-9.

[8] Hersey R.K., Melvin W.L., McCellan J.H.: "*Clutter-limited detection performance of multi-channel conformal arrays*", Signal Processing 84 (2004), pp. 1481-1500.

[9] Hersey R.K., Melvin W.L., McCellan J.H., Culpepper E.: "*Adaptive ground clutter suppression for conformal array radar systems*", IET Radar, Sonar and Navigation, Vol. 3, Iss. 4, 2009, pp. 357-372.

[10] Jaffer A.G, Ho P.T., Himed B.: "*Adaptive Compensation for Conformal Array STAP by Configuration Parameter Estimation*", 2006 IEEE Conference on Radar, Verona, NY, USA, April 24-27, 2006.

[11] Klemm R.: "*Comparison Between Monostatic and Bistatic Antenna Configureations for STAP*", IEEE Trans. AES (Transaction on Aerospace and Electronics Systems), vol. 36, no. 2, Aprill 2000, pp 596-608.

[12] Martin T., Erickson R.: "*Utvärdering av konform experimentantenn*" ("*Evaluation of Conformal Experimental Antenna*"), In Swedish, FOI Memo 2167, FOI 2007.

[13] Melvin W.L., Davis M.E.: "*Adaptive Cancellation Method for Geometry-Induced Nonstationary Bistatic Clutter Environments*", IEEE Transactions on Aerospace and Electronic Systems, Vol. 43, No. 2, April 2007, pp. 651-672.

[14] Nathanson F.E.: "*Radar Design Principles. Second Edition*", McGraw-Hill 1991, ISBN 0-07-046052-3.

[15] Pettersson L., Martin T., Huss L.-G., Erickson R., Lundén O., Leijon S.: "*Experimental investigation of a conformal array antenna on a UAV-nose mock-up*", Fifth European Workshop on Conformal Antennas, Bristol, UK, September 10-11, 2007.

[16] Rabideau D.J.: "*Clutter and Jammer Multipath Cancellation in Airborne Adaptive Radar*", IEEE Trans. AES (Transaction on Aerospace and Electronics Systems), vol. 36, no. 2, April 2000, pp 565-583.

[17] Ries P., Lapierre F.D., Lesturgie M., Verly J.G.: "*Handling partially calibrated conformal antenna arrays in range-dependence compensation for airborne bistatic space-time adaptive processing radar*", IET Radar Sonar and Navigation, Vol. 3, Iss. 4, 2009, pp. 373-383.

[18] Ward J., "*Space-Time Adaptive Processing for Airborne Radar*", MIT Lincoln Laboratory, Technical Report 1015, 1994.

Publication 6: Clutter Properties for a Side-Looking Radar with Planar Regular and Irregular Subarrays

Svante Björklund: "Clutter Properties for a Side-Looking Radar with Planar Regular and Irregular Subarrays", International Radar Symposium (IRS) 2015, Dresden, Germany, June 24-26, 2015. Reproduced with permission from DGON (German Institute of Navigation).

Clutter Properties for a Side-Looking Radar with Planar Regular and Irregular Subarrays

Svante Björklund

Swedish Defence Research Agency (FOI), P.O. Box 1165, SE-581 81 Linköping, Sweden
Blekinge Institute of Technology, SE-371 79 Karlskrona, Sweden
email: svabj@foi.se

Abstract: *The effect of the subarray design in a side-looking moving radar with a planar antenna on some clutter properties which are important for suppressing the clutter with STAP (Space-Time Adaptive Processing) is investigated by simulations. These properties are interference DOA Doppler Spectrum (DDS) and clutter rank. The conclusions from the work is that irregular antennas give less clutter in the DDS and that larger subarrays give lower clutter rank.*

1. Introduction

There are several ways to reduce the number of digital antenna channels of a radar and thereby reduce cost, space, weight, power consumption etc. The traditional way is to use subarrays with analog beamforming [1]. Other ways are minimum redundancy arrays [8], co-prime arrays [10] and MIMO (Multiple Input Multiple Output) arrays [4]. Often it is necessary to suppress the radar clutter from ground and sea in order to detect and locate targets. STAP (Space-Time Adaptive Processing) [6] can be used for the suppression. For efficient suppression, knowledge of clutter properties is needed, e.g. the clutter rank [7]. The clutter rank for antennas with subarrays has been treated in [5, 11].

The problem which we address in this paper is if and how the antenna subarray design of a moving radar affects some clutter properties which are important for suppressing the clutter with STAP. These properties are interference DOA Doppler spectrum (DDS) and the clutter rank, the latter also called clutter degrees of freedom. An application is "UAVs (Unmanned Aerial Vehicle) for surveillance and information acquisition about ground targets, in, for example, task forces and on a tactical level." [3], Figure 1. This paper is similar to [2] but uses a side-looking radar instead of a forward-looking and has a different antenna geometry and different subarray designs. This paper has been supported by The Swedish Armed Forces' R&D program.

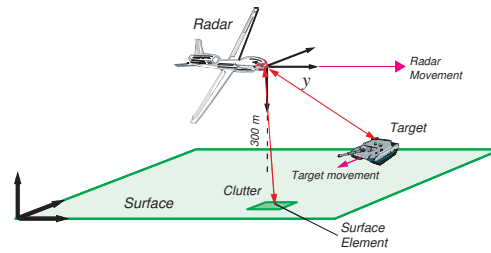

Figure 1: Simulation scenario.

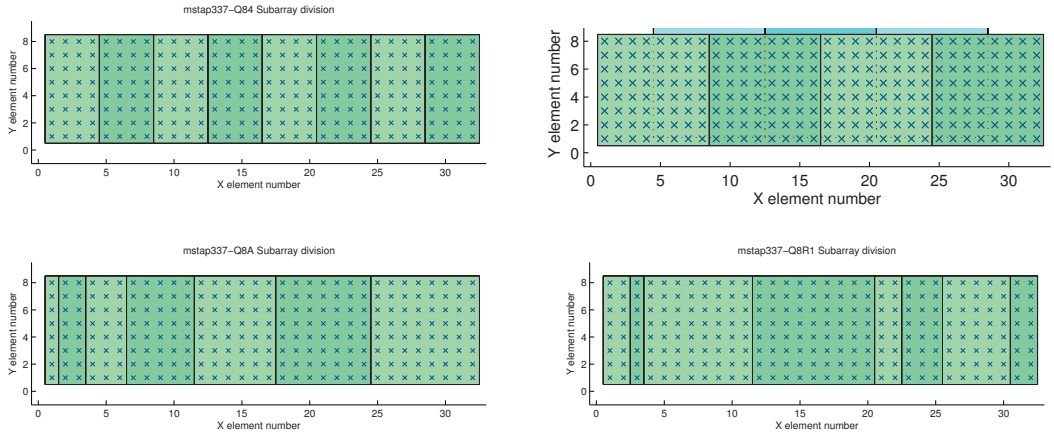

Figure 2: Subarray designs. Top left Q84, top right Q88o1, bottom left Q8A, bottom right Q8R1. The left side of the antennas is in the forward direction of the UAV.

2. Simulations

We obtain our results by simulations in a scenario with a UAV borne 35 GHz radar for detection of ground targets (Figure 1 and [3]). The radar, scenario and simulation setup are the same as in [2] except for the antennas used. Since the performance measures in Section 4. utilize the space-time covariance matrix of the received radar signals from clutter only or clutter plus receiver noise, we compute or "simulate" these matrices. The space dimension is the antenna channels from the subarrays of the antenna. The time dimension is the radar pulses or PRI (Pulse Repetition Interval). The number of antenna channels is 7 or 8. The true (not estimated) clutter covariance matrix is used and the receiver noise is white in space and time and has equal power in all channels.

3. Antennas

The antenna is a planar rectangular array with identical antenna elements positioned in a rectangular grid with equal inter-element distances. The antenna aperture is placed on the left side of the UAV, with its normal orthogonal to the direction of movement. The antenna has subarrays only in the horizontal direction. We have used four different subarray designs (see Figure 2):

Q84: Eight equally sized, non-overlapping, subarrays of width 4 elements. Up to seven times the same distance between pairs of subarray phase centers (not only neighboring subarrays) occurs (the first time and six repetitions of the same distance). This quantity is the same as the maximum of "spatial-frequency sensitivity" in [8].

Q88o1: Seven equally sized, overlapping, subarrays of width 8 elements. Up to six times the same distance between pairs of subarray phase centers occurs.

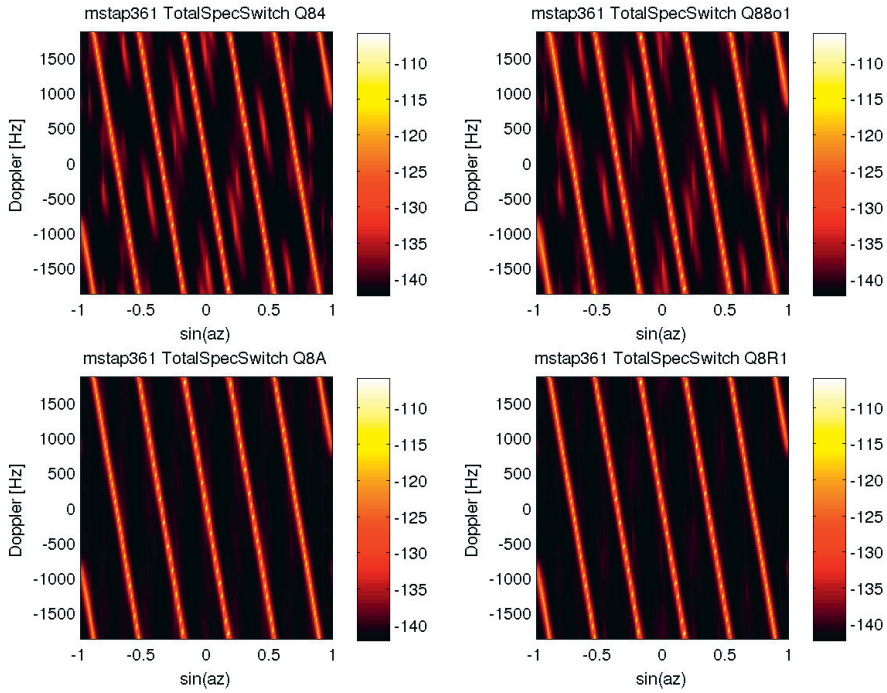

Figure 3: Interference DOA-Doppler spectra. Top left: Q84, top right: Q88o1, bottom left: Q8A, bottom right: Q8R1. Horizontal axis: sin(azimuth angle). Slant range 3000 m.

Q8A: Seven non-overlapping subarrays of different width. The design idea is to emulate the projection of a vertical half-cylinder antenna aperture to the side. In the forward direction of the UAV the subarrays get smaller and smaller like the projection of the half-cylinder antenna to the side direction. At most twice the same distance between pairs of subarray phase centers occurs.

Q8R1: Eight non-overlapping irregular subarrays. The widths of the subarrays are chosen so that the distance between the phase centers of pairs of subarrays repeat as few times as possible. Subarrays are often chosen so in order to reduce grating lobes. In [8], the antenna element positions are chosen so in order to increase the antenna aperture and its resolution without decreasing the angle between grating lobes. In our antenna Q8R1 the same phase center distance only occurs once (no repetition). This is desired in minimum-redundancy arrays [8].

4. Performance measures

We use the same performance measures as in [2], namely:

Interference DOA Doppler Spectrum (DDS), which is the clutter plus receiver noise power as sensed by the radar from different DOAs (Direction of Arrival) and Dopplers. See Figure 3. To generate these DDS we have split the view region $\pm 90^\circ$ into a number of smaller DOA regions.

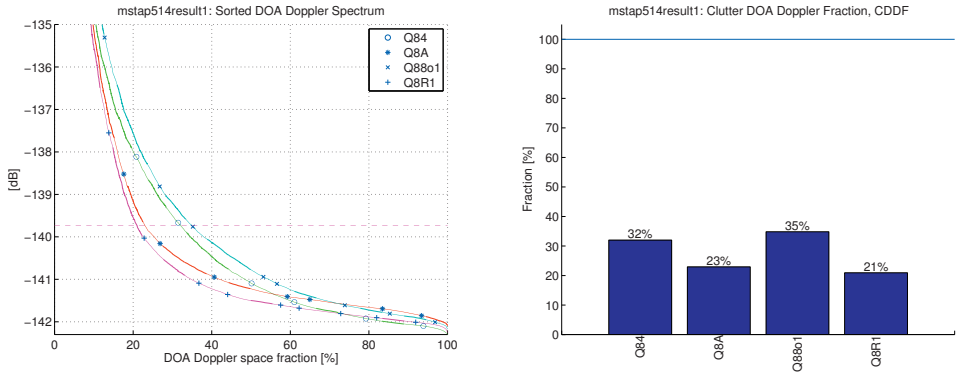

Figure 4: Interference DOA-Doppler spectra performance measures. Left: Sorted spectrum (SDDS). Right: DOA-Doppler fraction (DDF).

Each region corresponds to a Tx (transmitter) mainbeam antenna position and Rx (receiver) subarray antenna position (see [2]). The DDS is only computed in its DOA region, giving a subDDS. Then the subDDSs are joined together. This means that there is no clutter from sidelobes or backlobes in our DDS, contrary to what is usual. The whole our DDS is from the mainbeam of the Rx subarrays and from the Tx antenna. We want the clutter to occupy as little as possible of the DDS since where there is clutter, we cannot expect to detect targets. Vi have used the slant range 3000 m in this paper.

Interference Sorted DOA Doppler Spectrum (SDDS), which is the sorted values of the DDS in decreasing order. Then, different antennas are easier to compare. See Figure 4 left. We want the SDDS to be low.

Interference DOA Doppler Fraction (DDF), which we define as the fraction of the DDS which is more than 3dB above the receiver noise power. We assume that only the clutter 3dB above the noise will be a problem. See Figure 4 right. We want the DDF to be low.

Clutter eigenspectrum, which is the eigenvalues of the clutter covariance matrix sorted in decreasing order. See Figure 5 left. This spectrum gives information about how difficult the clutter is to suppress and and how much radar resources are required. We have in this paper used the eigenspectra for the single antenna scanning direction 55.4° relative the platform velocity vector and for slant range 3000 m.

Clutter Effective Rank (ER), which is the number of clutter eigenvalues larger than the receiver noise power. See Figure 5 right. This measure is very important when using STAP since it tells us the required radar radar resources and amount of data to estimate the clutter properties [6]. We want the ER to be low.

Clutter Effective Rank Fraction (ERF): The fraction of all eigenvalues which are above the noise power. See Figure 6. This measure tells us, like the interference DDF how much of the signal space the clutter occupies and therefore how large a clutter problem it is. We want the ERF low.

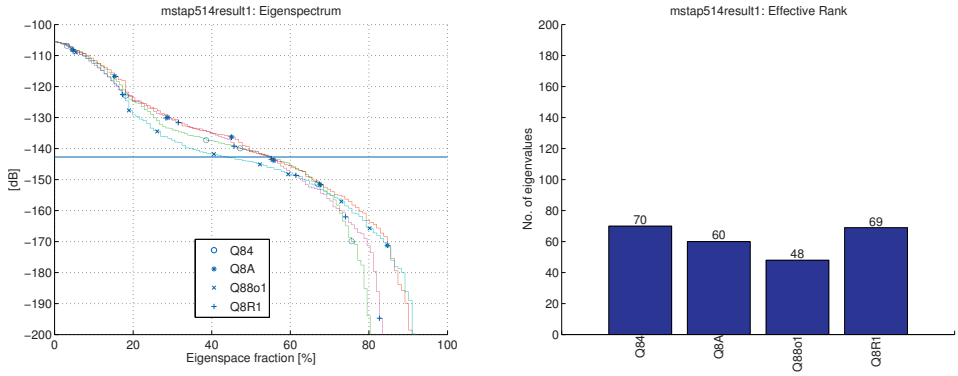

Figure 5: Clutter rank performance measures. Left: Eigenspectrum. Right: Clutter Effective Rank (ER). Slant range 3000 m.

5. Simulation results and discussion

The interference DDS for the four subarray designs are depicted in Figure 3. The solid lines is the clutter ridge. The interference SDDS and DDF are shown in Figure 4. The clutter eigenspectrum, ER and ERF are displayed in Figure 5 and 6.

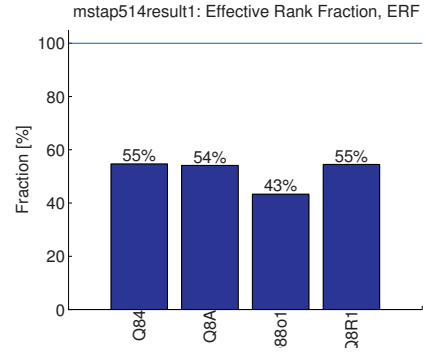

Figure 6: A clutter rank performance measures: Clutter Effective Rank Fraction (ERF).

We see in Figure 4 that the interference DDF is lower for the antennas with irregular subarrays, Q8A and Q8R1. The DDSs in Figure 3 are also cleaner compared to the extra clutter disturbances between the clutter ridges for the antennas with regular subarrays, Q84 and Q88o1. The reason for these differences could be grating lobes with Q84 and Q88o1, caused by the high repetition of the same distance between phase centers of the subarrays, up to 7 and 6 times for Q84 and Q88o1 compared to max 2 and 1 times for Q8A and Q8R1. These results also agree with the different results of planar and conformal antennas in [2], where the "irregular" conformal antennas have better interference DDS and DDF properties.

We see in Figure 5 and 6 two groups of subarray designs, namely Q84, Q8A and Q8R1 in one group and Q88o1 in the other. The Q88o1 gives better clutter rank properties. Q84, Q8A and Q8R1 have the same clutter ERF. The difference in ER is due to the different number of antenna channels. We note that Q84, Q8A and QR8R1 have in average about the same subarray width, namely 4.0-4.6 element distances. Q88o1 has a larger subarray width of 8 element distances. A probable reason for the lower clutter rank with Q88o1 is that the wider subarrays and therefore their narrower beams receive less clutter in the form of signal from fewer clutter scatterers and

a smaller Doppler spread. We note from our results that the properties of the clutter received by a radar depend on the radar design. This is in agreement with [9].

6. Conclusions

We draw the following conclusions from our work:

- Irregularity in the form of irregular subarrays or a non-planar aperture results in less clutter in the interference DOA Doppler spectrum.
- Larger subarrays give lower clutter rank. The reason is probably the narrower beam in which the signal of fewer clutter scatterers enter and the Doppler spread is smaller.
- None of the tested subarray designs is the best for all our performance measures. The irregular subarray designs are better for the DOA Doppler spectrum. The design with overlapping large subarrays is the best for the clutter rank.

References

[1] David Aalfs. *Principles of Modern Radar, Advanced Techniques*, chapter Adaptive Digital Beamforming, pages 401–452. Scitech Publishing, 2013. ISBN 978-1-891121-53-1.

[2] Svante Björklund, Tomas Boman, and Anders Nelander. Clutter properties for STAP with smooth and faceted cylindrical conformal antennas. In *2010 IEEE International Radar Conference*, Washington DC, USA, May 10-14 2010.

[3] Svante Björklund, Tomas Boman, and Anders Nelander. UAVs (unmanned aerial vehicle) for surveillance and information acquisition about ground targets. Back cover figures and text in IEEE Aerospace and Electronic Systems Magazine, Vol 26, No. 3, March 2011.

[4] Michael S. Davis. *Principles of Modern Radar, Advanced Techniques*, chapter MIMO Radar, pages 119–145. Scitech Publishing, 2013. ISBN 978-1-891121-53-1.

[5] L. B. Fertig. Estimation of space-time clutter rank for subarrayed data. In *38th Asilomar Conference on Signals, Systems, and Computer*, pages 289–292, November 2004.

[6] J.R. Guerci. *Space-Time Adaptive Processing for Radar*. Artech House, 2003.

[7] J.R. Guerci, J.S. Goldstein, and L.S. Reed. Optimal and adaptive reduced-rank stap. *IEEE Transactions on Aerospace and Electronics Systems*, 36(2):647–663, April 2000.

[8] A. Moffet. Minimum-redundancy linear arrays. *IEEE Transactions on Antennas and Propagation*, 16(2):172–175, March 1968.

[9] P. Ries, X. Neyt, F.D. Lapierre, and J.G. Verly. Fundamentals of spatial and Doppler frequencies in radar STAP. *IEEE Transactions on Aerospace and Electronic Systems*, 44(3), July 2008.

[10] P.P. Vaidyanathan and P. Pal. Sparse sensing with co-prime samplers and arrays. *Signal Processing, IEEE Transactions on*, 59(2):573–586, Feb 2011.

[11] Z. Zenghui, Z. Jubo, and W. Yongliang. Local degrees of freedom of clutter for airborne space-time adaptive processing radar with subarrays. *IET Radar, Sonar and Navigation*, 6(3), March 2012.

Publication 7: Three-Dimensional DPCA with Rotating Antenna for Clutter Cancellation

Three-Dimensional DPCA with Rotating Antenna for Clutter Cancellation

Svante Björklund
Swedish Defence Research Agency (FOI), SE-581 11 Linköping, Sweden
Email: svabj@foi.se

***Abstract*—In moving radar, e.g. airborne radar, the clutter from land and sea needs to be suppressed in order to detect the target. One approach to total cancellation of the clutter is Displaced Phase Center Antenna (DPCA). DPCA assumes that the antenna elements are positioned on a line parallel to the velocity vector of the radar platform so that the elements can take each others positions at different points of times. In a previous paper we saw that it is possible with other antenna element positions, e.g. in three dimensions, for a total cancellation of the clutter. We arrived at a theoretical condition for this. In this new paper we extend the condition with rotating array antennas. We also formulate an optimization problem for, besides the clutter cancellation, also maximizing the target signal.**

I. Introduction

Several objectives have been employed for suppressing surface clutter in airborne radar: maximize the Signal to Interference plus Noise Ratio (SINR) [1], [2]; maximize detection probability while holding a constant probability of false detection [3], [4]; and total cancellation of the clutter signal with no thought of the target signal [5]. These objectives have led to Space-Time Adaptive Processing (STAP) (fully adaptive, reduced dimension and reduced rank [1], [6]); CFAR (Constant False Alarm Ratio) detection filters like Kelly's [7] and Adaptive Matched Filter (AMF) [8]; and Displaced Phase Center Antenna (DPCA) [1], [2], [5], [9], [10]. An assumption in DPCA is that the antenna elements lie on a line parallel to the velocity vector of the radar platform so that the elements can take each others position at different times.

In [11] we theoretically investigated whether it is possible with other antenna geometries, i.e. other antenna element positions, for a total cancellation of the clutter. We allowed the antenna elements to be placed in three dimensions (3D). We arrived at a condition for this. The (multipulse) DPCA conditions [5] is a solution. Our work was an extension of the work by Richardson [5] where he derived the multipulse DPCA solutions for a linear array antenna aligned with the radar platform velocity vector. In [11] we also had a discussion about the condition, antenna element positions, target signal, DPCA, model errors and radar parameters.

In this new paper we have reduced, changed and extended [11]. We have reused text and equations from [11]. We have reused Figure 1 in a modified form. Many equations are changed versions of the ones in [11]. The only reused and unchanged numbered equations are (6), (9), (11) and (12).

New material and results in this new paper are:

- Improvement of the explanation of the theory of the clutter cancellation condition, including two new figures. See Section II and Figure 2 and 4.
- Extension with theory for a rotating array antenna. In [11] there was an example with a rotating antenna but it was not covered by the theory. We have added a new example with a rotating antenna. See Figure Figure 3 and 4.
- Formulation of an optimization problem for, besides the clutter cancellation, also maximization of the target signal. See Section IV and V.

In Section II we set up a signal model for received clutter and derive the condition for its total cancellation after a clutter filter. Section III gives examples on possible antennas and movements. In Section IV we formulate the optimization problem of maximizing the target signal. Section V contains a discussion on the results and Section VI conclusions.

II. The condition including rotating antenna

In this section we will derive the condition for total clutter cancellation by three-dimensional DPCA with a rotating antenna. The derivation is originally a copy of the one in [11] but is changed and extended for rotating antennas. First, we will set up a signal model for the received radar signal from a clutter cell. Then we apply a 2D clutter filter in space and slow-time on the signal and finally we will see what is required for the clutter signal to vanish. The derivation is inspired by the one in [5] but ours is more general.

The phase shift from a fix point in space (= the phase center) to antenna element n (including antenna rotation) for radar pulse m and for the impinging signal from the i^{th} clutter cell is

$$\varphi_{s,n,m,i} = \mathbf{k}_i \cdot \mathbf{R}(m)\mathbf{r}_n = \frac{2\pi}{\lambda}\hat{\mathbf{k}_i} \cdot \mathbf{R}(m)\mathbf{r}_n \qquad (1)$$

where $\mathbf{r}_n$ is the position of the n^{th} element, $\mathbf{R}(m)$ is the antenna rotation matrix for the m^{th} pulse, and "$\cdot$" denote scalar product. Vectors $\mathbf{x}$ are denoted by a bold upright font. The wave vector from the i^{th}clutter cell is $\mathbf{k}_i = \frac{2\pi}{\lambda}\hat{\mathbf{k}}_i$ where $\hat{\mathbf{k}}_i$ is the unit direction vector from the clutter cell to the origin of the antenna and λ is the wavelength of the radar wave. We assume far field conditions.

A general rotation matrix $\mathbf{R}(m)$ for rotation with angular velocity ω around an arbitrary rotation axis $\mathbf{u} = (u_x, u_y, u_z)$, with $\|\mathbf{u}\| = 1$, can be expressed succinctly as [12]:

$$\mathbf{R}(m) = \cos\theta_m \mathbf{I} + \sin\theta_m [\mathbf{u}]_\times + (1-\cos\theta_m)\mathbf{u}\mathbf{u}^T \quad (2)$$

where $\mathbf{I}$ is the identity matrix, $\theta_m = \omega m T$ and

$$[\mathbf{u}]_\times = \begin{bmatrix} 0 & -u_z & u_y \\ u_z & 0 & -u_x \\ -u_y & u_x & 0 \end{bmatrix} \quad (3)$$

which is the the *cross product matrix* of u. The quantity T is the PRI (Pulse Repetition Interval).

The phase shift for the impinging signal from the i^{th} clutter cell at pulse repetition interval (PRI) m due to movement of the radar platform, i.e. the Doppler shift, is

$$\varphi_{t,m,i} = \mathbf{k}_i \cdot 2mT\mathbf{v} = \frac{2\pi}{\lambda} 2\hat{\mathbf{k}_i} \cdot \mathbf{v} m T \quad (4)$$

which contains the usual formula $f_{\text{d}} = 2v/\lambda$ for the monostatic Doppler frequency f_{d} with platform radial velocity v. The quantity $\mathbf{v}$ is the radar platform velocity vector.

The signal from the i^{th} clutter cell is

$$\begin{aligned} & s_i(n,m) \quad (5) \\ & = A_i(\hat{\mathbf{k}}_i, n, m) \exp(-j\frac{2\pi R_i}{\lambda}) \exp(-j\left[\varphi_{s,n,m,i} + \varphi_{t,m,i}\right]) \\ & = A_i(\hat{\mathbf{k}}_i, n, m) \exp(-j\frac{2\pi R_i}{\lambda}) \exp(-j\mathbf{k}_i \cdot [\mathbf{R}(m)\mathbf{r}_n + 2mT\mathbf{v}]) \end{aligned}$$

where the complex scalar $A_i(\hat{\mathbf{k}}_i, t)$ contains contributions from the mean specific RCS (m^2/m^2), RCS fluctuations, clutter cell area, grazing angle, range attenuation, propagation attenuation, and transmitter and receiver antenna gains. The factor $\exp(-j\frac{2\pi R_i}{\lambda})$ is the phase shift for the distance R_i from the clutter cell to the phase center of the antenna. We recognize in (5) the phase contributions due to the antenna element positions and due to the platform movement.

We apply a standard 2D clutter filter in space (antenna elements) and slow-time (the PRI dimension) on the signal from the i^{th} clutter cell

$$y_i = \sum_{n=0}^{N-1} \sum_{m=0}^{M-1} w_{nm}^* s_i(n,m) \quad (6)$$

where N is the number of antenna elements, M is the number of PRIs and w_{nm} is the filter coefficient for antenna element n and PRI m. Complex conjugate of a quantity a is denoted by a^*. If we insert (5) in (6) and ignore the phase caused by R_i (it will not matter for us), we obtain

$$y_i = \sum_{n=0}^{N-1} \sum_{m=0}^{M-1} w_{nm}^* A_i(\hat{\mathbf{k}}_i, n, m) \exp(-j\mathbf{k}_i \cdot [\mathbf{R}(m)\mathbf{r}_n + 2mT\mathbf{v}]) \quad (7)$$

To come further we assume that $A_i(\hat{\mathbf{k}}_i, n, m)$ is independent of n and m. If all antenna element patterns are equal, $A_i(\hat{\mathbf{k}}_i, n, m)$ will be independent of n. If the clutter signal is coherent in time during the integration interval, $A_i(\hat{\mathbf{k}}_i, n, m)$ will be independent of m. We now assume $A_i(\hat{\mathbf{k}}_i, n, m)$ independent of n and m. This will give

$$y_i = A_i(\hat{\mathbf{k}}_i) \sum_{n=0}^{N-1} \sum_{m=0}^{M-1} w_{nm}^* \exp(-j\mathbf{k}_i \cdot [\mathbf{R}(m)\mathbf{r}_n + 2mT\mathbf{v}]) \quad (8)$$

To totally cancel the clutter we require

$$y_i \equiv 0 \quad (9)$$

for all clutter cells i. This is, of course, totally unrealistic but it is the problem which we study in this paper and it is the same problem as for usual DPCA.

We can rewrite (8) and (9) as

$$\begin{aligned} y_i = A_i(\hat{\mathbf{k}}_i) & \left[\sum_{k=1}^{K_0} w_{n_{0,k} m_{0,k}}^* \exp(-j\mathbf{k}_i \cdot \left[\mathbf{R}(m)\mathbf{r}_{n_{0,k}} + 2m_{0,k}T\mathbf{v}\right]) \right. \\ & \left. + \sum_{q=1}^{Q} \sum_{k=1}^{K_q} w_{n_{q,k} m_{q,k}}^* \exp(-j\mathbf{k}_i \cdot \left[\mathbf{R}(m)\mathbf{r}_{n_{q,k}} + 2m_{q,k}T\mathbf{v}\right]) \right] \quad (10) \\ & \equiv 0 \end{aligned}$$

where

$$w_{n_{0,k} m_{0,k}} = 0 \quad (11)$$

for $k = 1, \ldots, K_0$ and

$$\sum_{k=1}^{K_q} w_{n_{q,k} m_{q,k}} = 0 \quad (12)$$

for $q = 1, \ldots, Q$ and all filter coefficients w_{nm} ($n = 0, \ldots, N-1$ and $m = 0, \ldots, M-1$) are used exactly once in (10).

We have in (10) partitioned the combinations of antenna elements n and PRIs m into Q groups, $q = 1, \ldots, Q$. There are K_q combinations, $k = 1, \ldots, K_q$, in group q. In (10)-(12) we have given subscripts to the subscripts m and n. For $n_{q,k}$ and $m_{q,k}$ the subscript q is the group index and the subscript k is index of the combination within the group. We give the name *q-group* to the antenna positions $\mathbf{r}_{n_{q,k}}$ and PRI indices $m_{q,k}$ for $k = 1, \ldots, K_q$ for a certain q.

We see that for each q-group belonging to $q = 1, \ldots, Q$ in (10), its sum over k is zero if the exponential function can be moved outside of the summation of k. It can be moved if it is independent of k. This is the case, if for each $q = 1, \ldots, Q$ for all $k = 1, \ldots, K_q$,

$$\mathbf{R}(m_{q,k})\mathbf{r}_{n_{q,k}} + 2m_{q,k}T\mathbf{v} = \mathbf{a}_q \quad (13)$$

where $\mathbf{a}_q$ is a constant vector. We may let $\mathbf{a}_q$ be dependent on the group q but it must not be dependent on the clutter cell i because we want the signal y_i to be zero for all clutter cells. Compare with equation (9) in [11] where $\mathbf{R}(m_{q,k})$ is missing.

Equations (11), (12) and (13) is our condition for clutter cancellation. Implicit in these equations is the partitions in q-groups.

III. Examples on possible antennas

In this section we show two examples on non-linear antennas which are solutions to the condition (11), (12) and (13). Figure 1 and 2 display a moving rigid antenna with three q-groups. Figure 3 and 4 depict a moving rotating antenna with two q-groups. Figure 2 and 4 try to explain the division of the filter weights into q-groups.

IV. The problem of optimizing the target signal

We see in (12) that despite the condition for total clutter cancellation there are still some freedom in how to choose the filter coefficients. This freedom could be used to optimize the target signal. Since the clutter is canceled we want to maximize the SNR (Signal to Noise Ratio) with receiver noise only [2]:

$$\max_{\tilde{\mathbf{w}}} \frac{\left|\mathbf{w}^H\mathbf{s}\right|^2}{\mathbf{w}^H\mathbf{K}\mathbf{w}} = \max_{\mathbf{w}} \frac{\left|\mathbf{w}^H\mathbf{s}\right|^2}{\sigma^2} = \max_{\mathbf{w}} \left|\mathbf{w}^H\mathbf{s}\right|^2 \tag{14}$$

where $\mathbf{w}$ is the filter weight vector, $\mathbf{s}$ is the received target signal and $\mathbf{K} = \sigma^2\mathbf{I}$ is the white receiver noise covariance matrix. The noise power is σ^2. We also choose $\|\mathbf{w}\|^2 = 1$ as in [2].

We assume that the q-groups, $q = 1, \ldots, Q$, are already selected, i.e. not part of our optimization problem. Then we can reduce the size of $\mathbf{w}$ and $\mathbf{s}$ by removing the rows where $\mathbf{w}$ has zeros according to (11). The optimization problem (14) will still be the same. Let the vector $\tilde{\mathbf{w}}$ be the reduced filter weight vector and $\tilde{\mathbf{s}}$ the reduced target signal.

The optimization problem is now

$$\max_{\tilde{\mathbf{w}}} \left|\tilde{\mathbf{w}}^H\tilde{\mathbf{s}}\right|^2 \tag{15}$$

subject to

$$\|\tilde{\mathbf{w}}\|^2 = 1 \tag{16}$$

and

$$\sum_{k=1}^{K_q} w_{n_{q,k}m_{q,k}} = 0 \tag{12}$$

$$\text{for } q = 1, \ldots, Q.$$

The subscripts $n_{q,k}$ and $m_{q,k}$ still refer to the original, unreduced, weight vector.

V. Discussion

In our previous paper [11] we had a discussion about antenna element positions, the constant vectors $\mathbf{a}_q$, the q-groups, the target signal, comparison with usual DPCA, effect of and handling of model errors, and restrictions on radar parameters. This discussion is valid also for our new paper. We refer our reader to [11].

The use of DPCA with a rotating antenna could be a mode for detection of moving targets with a moving surveillance radar which already has a rotating antenna. Even if the example with a rotating antenna in Figure 3 and 4 has the DPCA function when the antenna axis is close to perpendicular to the platform velocity vector, it is also possible with antennas which has the DPCA function when the antenna axis is close to the velocity vector.

Also a rotating antenna must follow the well-known principle of DPCA that antennas should take each others positions to cancel the clutter. This was also noted and discussed for the antennas in [11].

A rotating antenna faces additional difficulties compared to a fix antenna when used with DPCA: It is more difficult to achieve that the antenna elements take each others positions with a rotating antenna. Also the rotation frequency must be matched with the platform velocity vector and the PRF (Pulse Repetition Frequency). The reuse of the same antenna element will probably give a different antenna gain due to a different direction relative the element, giving channel mismatches. The DPCA condition is only valid for part of the rotation circle meaning that part of the time the clutter cancellation cannot be done.

The solution to the optimization problem (15), (16) and (12) is the weight vector $\tilde{\mathbf{w}} = \tilde{\mathbf{w}}_{\text{opt}}$ which is as parallel as possible to the target vector $\tilde{\mathbf{s}}$. The weight vector $\tilde{\mathbf{w}}$ can reside in a space Ω defined by (12). If $\tilde{\mathbf{s}}$ resides in Ω, then $\tilde{\mathbf{w}}_{\text{opt}} = \tilde{\mathbf{s}}/\|\tilde{\mathbf{s}}\|$. This gives the white-noise matched filter solution [2]. If $\tilde{\mathbf{s}}$ does not reside in Ω, then $\tilde{\mathbf{w}}_{\text{opt}}$ will be on the boundary of Ω as close as possible to be parallel with $\tilde{\mathbf{s}}$.

The q-groups can often be selected in different ways. This selection could also be included in the optimization problem.

VI. Conclusions

We have extended the condition for total cancellation of surface clutter in moving radar in [11] with a rotating array antenna. The condition is still based on an explicit model of the received clutter signal. We again arrive at the well-known principle that antenna elements should take each others positions at different points of time.

We also formulate an optimization problem for, besides the clutter cancellation, also maximizing the target signal.

Acknowledgment

This work has financially been supported by the Swedish Defence Research Agency.

References

[1] J. Ward, "Space-time adaptive processing for airborne radar," Lincoln Laboratory, Technical Report 1015, 1994.

[2] J. R. Guerci, *Space-Time Adaptive Processing for Radar*. Artech House, 2003.

[3] S. Goldstein and M. Picciolo, "STAP II - Advanced concepts. Tutorial," in *2008 IEEE Radar Conference*, 2008.

[4] M. Rangaswamy, "Modern CFAR techniques in heterogeneous radar clutter scenarios. Tutorial," in *2008 IEEE Radar Conference*, 2008.

[5] P. G. Richardson, "Analysis of the adaptive space time processing technique for airborne radar," *IEE Proc. Radar, Sonar, Navigation*, vol. 141, no. 4, pp. 187–195, August 1994.

[6] J. R. Guerci, J. S. Goldstein, and I. S. Reed, "Optimal and adaptive reduced-rank STAP," *IEEE Trans. Aerospace and Electronics Systems*, vol. 36, no. 2, pp. 647–663, April 2000.

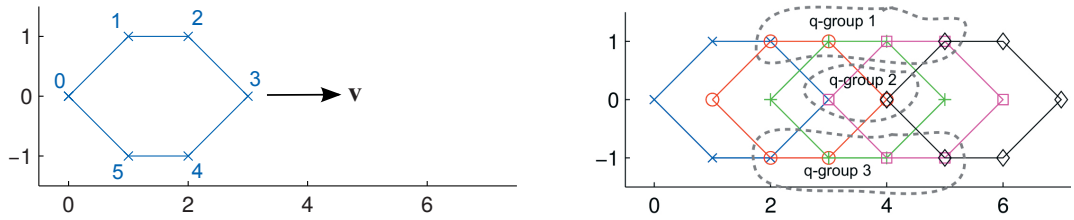

Figure 1. Example of a possible non-linear antenna. Left: The antenna with elements in the vertices. The antenna is moving to the right. The units of the axes is length in arbitrary units. Right: The antenna at different positions during the movement. Some elements will take each others positions. Different colors and markers for the different antenna positions: Time t=0 blue x, t=1 red o, t=2 green +, t=3 magenta squares, t=4 black diamonds. This antenna and its movement has three q-groups. Figure and caption partly from [11].

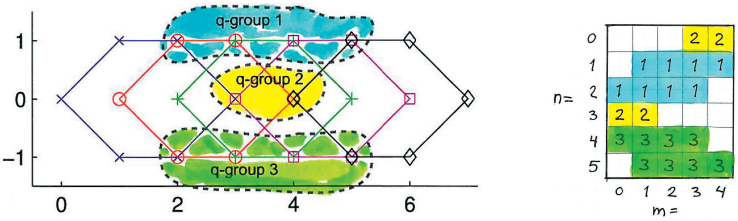

Figure 2. The same non-linear antenna as in Figure 1. Left: The antenna at different positions during the movement. Some elements will take each others positions. Different colors and markers for the different antenna positions: Time t=0 blue x, t=1 red o, t=2 green +, t=3 magenta squares, t=4 black diamonds. This antenna and its movement has three q-groups, denoted by blue, yellow and green background. Right: Matrix of membership of filter coefficients in q-groups. The numbers in the cells are the q-group numbers. The antenna element subscripts n are shown in the left image in Figure 1.

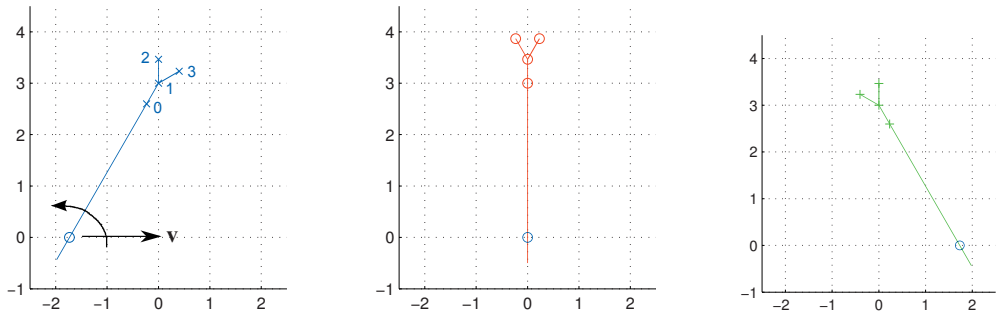

Figure 3. Example of a possible non-linear antenna, namely a rotating antenna. The antenna rotates anti-clockwise and moves to the right. The units of the axes is length in arbitrary units. Left to right: The antenna at time t=0 (blue x), t=1 red o, and t=2 (green +) in three images. In this example two antenna element positions are visited by several antenna elements during three radar pulses. This antenna and its movement and rotation as shown has two q-groups.

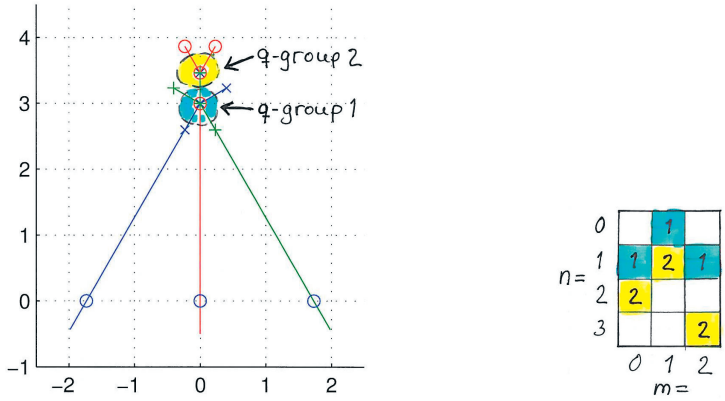

Figure 4. The same rotating antenna as in Figure 3. Left: The antenna at time t=0 (blue x), t=1 red o, and t=2 (green +) on top of each other in the same image. Two antenna element positions are visited by several antenna elements during three radar pulses. Right: Matrix of membership of filter coefficients in q-groups. There are two q-groups. The numbers in the cells are the q-group numbers. The antenna element subscripts n are shown in the left image in Figure 3.

[7] E. Kelly, "An adaptive detection algorithm," *IEEE Transactions on Aerospace and Electronic Systems*, vol. AES-22, no. 2, pp. 115–127, 1986.

[8] F. Robey, D. Fuhrmann, E. Kelly, and R. Nitzberg, "A CFAR adaptive matched filter detector," *IEEE Transactions on Aerospace and Electronic Systems*, vol. 28, no. 1, pp. 208–216, 1992.

[9] F. M. Staudaher, *Radar Handbook*, 2nd ed. McGrawHill, 1990, ch. 16. Airborne MTI, pp. 16.1–16.31, ISBN 0-07-057913-X.

[10] M. A. Richards, *Fundamentals of Radar Signal Processing*. McGrawHill, 2005, ch. 5.7 MTI for Moving Platforms: Adaptive Displaced Phase center Antenna Processing, pp. 287–293, ISBN 0-07-144474-2.

[11] S. Björklund and M. I. Pettersson, "A three-dimensional displaced phase center antenna condition for clutter cancellation," in *The Eighth IEEE Sensor Array and Multichannel Signal Processing Workshop (SAM 2014)*, A Coruña, Spain, June 22-25 2014.

[12] Rotation matrix. Read December 7, 2014. [Online]. Available: http://en.wikipedia.org/wiki/Rotation_matrix

Publication 8: Features for Micro-Doppler Based Activity Classification

Svante Björklund, Henrik Petersson, Gustaf Hendeby: "Features for Micro-Doppler Based Activity Classification", IET Radar, Sonar & Navigation, Special Issue: Micro-Doppler, Vol. 9, No 9, December 2015, pp. 1181-1187 [10].

IET Radar, Sonar & Navigation

Research Article

IET Journals
The Institution of Engineering and Technology

Features for micro-Doppler based activity classification

ISSN 1751-8784
Received on 9th February 2015
Revised on 24th July 2015
Accepted on 27th July 2015
doi: 10.1049/iet-rsn.2015.0084
www.ietdl.org

Svante Björklund[1,2] ✉, *Henrik Petersson*[1], *Gustaf Hendeby*[1,3]

[1]*Swedish Defence Research Agency (FOI), SE-581 11 Linköping, Sweden*
[2]*Blekinge Institute of Technology, SE-371 79 Karlskrona, Sweden*
[3]*Linköping University, SE-581 83 Linköping, Sweden*
✉ *E-mail: svabj@foi.se*

Abstract: Safety and security applications benefit from better situational awareness. Radar micro-Doppler signatures from an observed target carry information about the target's activity, and have potential to improve situational awareness. This article describes, compares, and discusses two methods to classify human activity based on radar micro-Doppler data. The first method extracts physically interpretable features from the time-velocity domain such as the main cycle time and properties of the envelope of the micro-Doppler spectra and use these in the classification. The second method derives its features based on the components with the most energy in the cadence-velocity domain (obtained as the Fourier transform of the time-velocity domain). Measurements from a field trial show that the two methods have similar activity classification performance. It is suggested that target base velocity and main limb cadence frequency are indirect features of both methods, and that they do often alone suffice to discriminate between the studied activities. This is corroborated by experiments with a reduced feature set. This opens up for designing new more compact feature sets. Moreover, weaknesses of the methods and the impact of non-radial motion are discussed.

1 Introduction

The world today has brought on a need to pay increased attention to safety and security issues, for example, search and rescue operations, surveillance, and protection of critical infrastructure. These tasks are often labour intensive and potentially dangerous. This provides an incentive to create systems that aid operators to gain situational awareness.

Part of gaining situational awareness is to know what people in an area are doing. This article addresses this problem by studying how to classify human activity using radar micro-Doppler measurements. The micro-Doppler measurements provide valuable information about the movements of different body parts, primarily the legs, arms, and torso. Compared with electro-optical sensors, radar offers better range and radial velocity information, as well as, insensitivity to light and weather conditions, at the cost of lower cross-range resolution. This motivates using a radar system.

The classification problem is often divided into two subproblems: *feature extraction* and *classification*. The latter is usually performed using standard methods. Feature extraction is very problem specific, and depends on factors such as the type of the radar used, the environment, and target characteristics. A wide variety of radar systems have been applied to the problem [1–6], contributing to a variety of different suggested features. Two main types of features are mostly pursued in literature: features derived directly from the received radar signal [7–10] and features computed from *time-velocity-diagrams* (TVDs) [1–3, 6, 11, 12]. The former features are often inspired by similar approaches used in speech processing.

In [9] human activities of a human standing still were classified. Fighting and/or if a target is carrying an object has also been studied in literature [1, 3, 11]; as well as, human activities including groups of people or vehicles [2]. The focus here is to study methods that distinguish between a number of different human activities; creeping, crawling, walking, jogging, and running, similar to [1].

TVDs can be used in several ways for classification: direct comparison with average class TVDs [11]; extraction of features using principal component analysis and linear discriminant analysis [3, 11]; or extraction of features with physical interpretation [1, 6]. Another approach is to derive *cadence velocity diagrams* (CVDs) from the TVDs and extract features directly from the CVD [4, 5]; or further process the CVDs to remove effects of the base velocity [2].

Several different classifiers have been used for micro-Doppler classification, for example, *support vector machines* (SVMs) [1, 2, 4, 6, 13], *Gaussian mixture models* [2], *Bayesian classifier* [14] and *k-nearest neighbour classifier* [13, 14]. Typically, a classification accuracy of approximately 90% is reported.

Here, a TVD based method with interpretable features [1] and a CVD based method [4, 5] will be described, compared, and discussed based on micro-Doppler datasets of people performing different activities. Based on this, two major information carriers in the dataset are pointed out, the target base velocity and the main limb cadence frequency, which together are enough to achieve classification performance comparable with the two other studied, and considerably more complex, methods. The two information carriers are present in both of the more complex methods. In this way we hope to highlight the question: How much information must a feature set contain to be useful. Neither of the two methods is new. Instead the novelty of this article is the comparison of the two methods; and based on the fact that they perform similarly, a discussion about what underlying properties are the most important for the classification.

The article is organised in the following way. In Section 2 the addressed problem and the available datasets are described, Section 3 deals with the classification problem with focus on the feature extraction step and the two studied methods. Section 4 describes how the experimental results are obtained. The results are then presented in Section 5 and discussed in Section 6 and the findings are summarised in Section 7.

2 Available data

2.1 Radar description

The radar system used is a frequency modulated continuous wave (FMCW) radar with linear FM sweeps (40 μs length and 160 MHz

Table 1 Available measurements in the experimental dataset (No. sequences/No. segments) distributed over the performed activities

	creep	crawl	walk	jog	run	Total
toward	4/11	3/9	6/22	2/8	2/4	17/54
away	2/5	1/2	6/23	2/7	2/4	13/41
Total	6/16	4/11	12/45	4/15	4/8	30/95

bandwidth), a PRF, i.e. the repetition frequency of the sweeps, of 17.6 KHz, a carrier frequency of 77 GHz and horizontal polarisation (called SIRS1600TD) by SAAB AB. Its designed target detection range is between 10 m and 200 m. The radar has a resolution of 1 m in range and 1° in azimuth. In our setup, the radar was pointing fairly horizontal. The sensor is a prototype of a general purpose mobile radar system. It is neither specifically optimised for obtaining micro-Doppler, nor for the specific classification task. The fact that the radar was not designed specifically for the studied classification task makes the results more applicable.

After acquisition, the signals were pulse compressed and velocity compensated, the latter in order to compensate for movements across range gates and shift each target into a single virtual gate. The signals were also filtered to remove stationary clutter using an ideal high-pass filter (in frequency domain) with a cut-off velocity of ±0.1 m/s.

2.2 Collected data

For this paper, data was collected from three test subjects (adult males of average height and build) crawling, creeping on their hands and knees, walking, jogging and running, directly toward or away from the radar at a distance of 20–60 m, on a clear day without rain and on fairly flat and dry ground covered with short grass. In total, 30 data sequences were collected (approximately 12 s each) and split into time segments of 2.5 – 3.5 s each, giving a total of 95 segments, see Table 1. Bookkeeping was done to keep record on which time segments that belong to the same sequence.

The available data only cover radial movements, which is a shortcoming. There are important security applications where non-radial motion occurs. However, in many security applications most interesting targets naturally approaches the radar radially or close to radially or the situation can be designed in such a way, for example, by placing two radars orthogonal to each other. Another argument for using radial data is that the features extracted stem from movements in the targets forward direction; hence, radial data makes a good candidate for evaluating the expressiveness of different features sets, whereas discussions about movements in non-radial angles become less well founded.

In [15] measured data for non-radial movement at 45° and 90° were also used. The TVDs of the movements at 45° are similar to the TVDs at 0° with some important differences, while the TVDs at 90° are totally different from the TVDs at 0° and 45°. These non-radial data could not be used in this article in the same classification experiment due to various reasons and new data are not possible to measure. However, the non-radial data have been used in Section 6.3 to discuss and predict the behaviour of the two features/parameters suggested as sufficient in this article, namely the base velocity and the cadence frequency.

2.3 Time-velocity diagram

The analysis in this article is based on target *micro-Doppler signatures*, represented as TVDs. A TVD is the absolute value of a *short time Fourier transform* (STFT) of the time domain radar

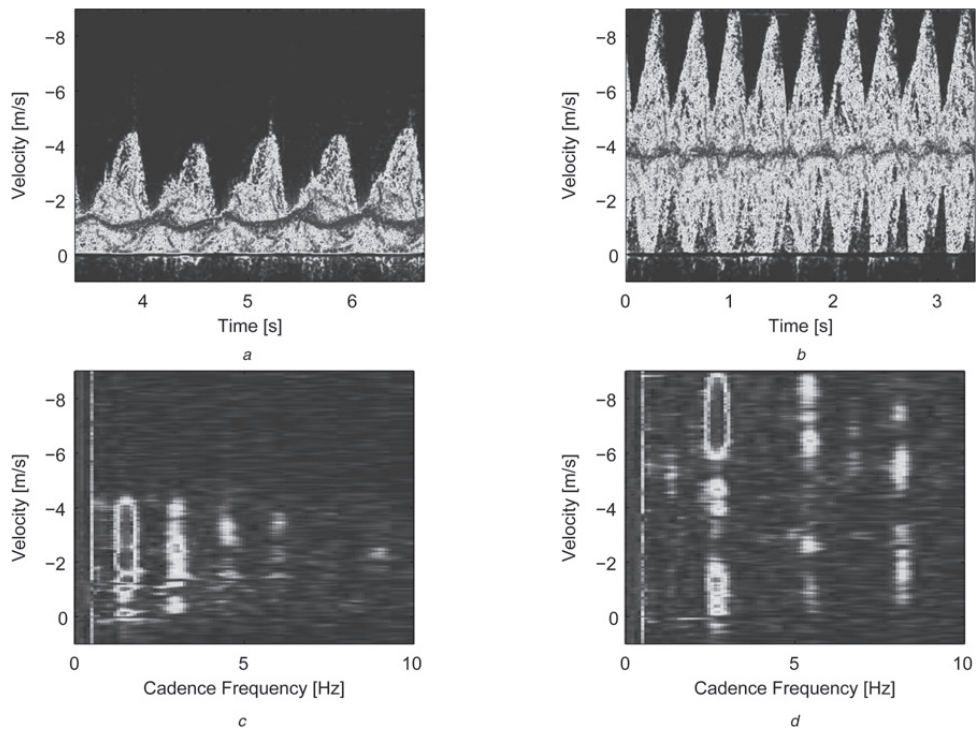

Fig. 1 *TVD and corresponding CVD for persons walking and running*

a TVD: walking person
b TVD: running person
c CVD: walking person
d CVD: running person

signal, see Fig. 1 for examples and [15] for an extensive set of TVDs. The time domain signal consists of different radar sweeps for the same radar range. The sampling frequency in the time domain is the PRF, thus 17.6 kHz.

The STFTs in this article were computed by overlapping FFTs with an integration time of 37.5 ms, a Hamming window and a time step of 5 ms. The integration time is a compromise between the velocity resolution for a constant radial movement (long integration time is good) and the smearing of the TVD caused by radial acceleration (short integration time is good). The chosen integration time is according to the experience of the authors suitable for this kind of target and movement. The chosen time step gives smooth TVDs in the time dimension. The window used is a standard window with low sidelobes. After the STFT the signal magnitude is converted to dB and this is the TVD used for the feature extraction.

2.4 Cadence-velocity diagram (CVD)

The article does also make use of CVDs, which are obtained as the absolute value of the Fourier transform of the TVDs with respect to time. Fig. 1 shows TVDs and corresponding CVDs. A CVD shows at which rate different velocities in a TVD repeat ('cadence frequencies'). The CVD characterises the shape, size, and frequency of the TVD components, which in turn relate to moving parts of the target. CVDs have previously been used to extract features, for example, [2, 16]. An interpretation of the CVD is given in [4, 5].

2.5 Ground truth

To create ground truth information, each data segment has been inspected and manually annotated with the target's *base velocity* (the velocity of the centre of the mass/main radar cross-section) and main *limb cadence/cycle frequency* (defined by the cycle time of the micro-Doppler effects produced by the limbs). Fig. 2 depicts the acquired values. These two properties will be used in Sections 4 and 5 to discuss about what are two important information carriers in the dataset.

3 Classification

Classification is often performed in two steps: *feature extraction* and *feature to class mapping* (or just *classification*).

In the first step, data, x, is mapped onto a set of features, z, using a *feature extractor*

$$z = F(x), \tag{1}$$

$x \in \mathbb{R}^n$ and $z \in \mathbb{R}^m$. In the second step, features, z, are mapped onto a discrete set of classes using a *classifier*

$$c = C(z), \quad c \in \{\mathcal{C}_1, \mathcal{C}_2, \ldots, \mathcal{C}_p\}. \tag{2}$$

This article applies both these steps, but focus lies on the feature extraction step which is further analysed.

The purpose of the feature extraction is to bring out the discriminating information contained in the data while at the same time suppressing natural variations. This is to simplify the classification task. In the context of this article, features should be robust to movements in the background, moving vegetation, etc., and thereto also be invariant to natural variations between human individuals, to persons carrying objects or not (unless this is of interest), to the direction of movements, and so on.

Two different feature extractors are considered: one by Kim and Ling [1], here denoted the *time-velocity* (TV) feature method, and one developed at FOI [4, 5], here denoted the *cadence-velocity* (CV) feature method. The method by Kim and Ling has been chosen for the comparison with the method developed at FOI because they have very similar problem formulations. Both the studied methods are outlined below.

3.1 TV features, [1]

The features considered in this section are extracted from the TV domain, using the method in [1]. The $z^{(\mathrm{TV})}$ comprises six features derived from the TVD representation of the radar signal: z_1, the torso Doppler frequency; z_2, the total Doppler bandwidth of the signal; z_3, the offset of the total Doppler; z_4, the Doppler bandwidth without micro-Doppler effects; z_5, the normalised standard deviation of Doppler signal strength; and z_6, the period of limb motion (i.e. the cadence/cycle frequency). See Fig. 3 and [1] for details.

How to implement these six features is not completely described in [1], hence here follows the interpretations used in this article:

- The upper and lower envelope in the TVD (needed for z_2, z_3, and, z_6), were computed as the top and lower 10%-percentile of the signal energy in each time slot. The noise below a threshold was first removed as in [1]. However, the threshold was selected in a different way than in [1] since the method used in [1] did not produce a good enough threshold to be useful in our case.
- The highest and lowest values of the upper and lower envelope (z_2 and z_3), have been implemented as the 5% highest/lowest values.
- z_5 was implemented as the standard deviation of all values in the TVD divided by the average of all the above-noise values in the TVD.
- The period of the limb motion (z_6), was computed by extracting the peaks of the upper envelope and averaging the time between them.

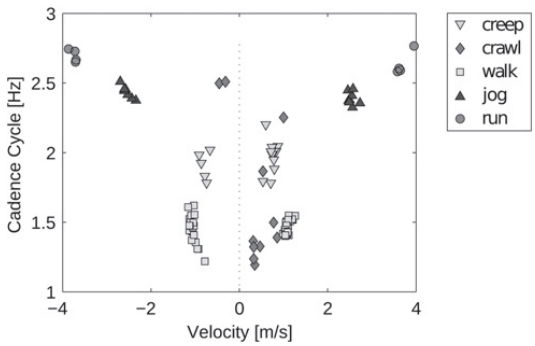

Fig. 2 *Distribution of base velocity and limb cadence frequency for all targets within the dataset*

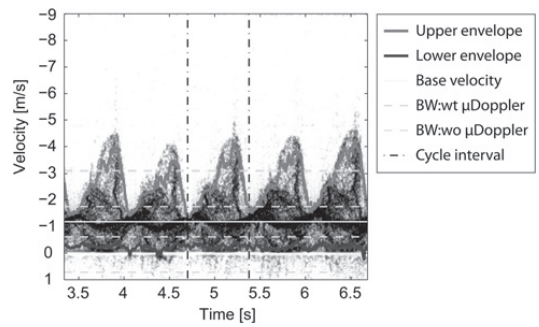

Fig. 3 *TV based feature extraction. A TVD with some of the features in the TV method illustrated*

Note that noise thresholding is needed in the TV method to remove the background noise prior to extraction. This tuning parameter is not needed in the CV method described next.

3.2 CV features, [4, 5]

The CV features, [4, 5], described in this section incorporates the strongest parts of the CVD in the feature vector as described below and illustrated in Fig. 4.

(i) Compute the total energy, $u(f^{\mathrm{c}})$, for each cadence frequency, f^{c}, in the CVD, that is, sum up the contribution of all velocities.
(ii) Choose the M (here $M=3$) strongest peaks (cadence frequencies) in $u(f^{\mathrm{c}})$, $\{f_i^{\mathrm{c}}\}_{i=1}^{M}$, and extract the matching velocity profiles (the energy content for the different velocities, f^{v}, for the cadence frequency, f^{c}), $\{v_i(f^{v})\}_{i=1}^{M}$, from the CVD. The choice $M=3$ is taken from [5], where this value gave good results.
(iii) Compute the base velocity v_0 as the peak velocity within the total velocity profile (sum the energy for all cadence frequencies).
(iv) Resample the velocity profiles with linear interpolation, in $L=100$ points, to obtain $\{v_i(f_i^{v})\}_{i=1}^{L}$. ($L$ is a tuning parameter, for which the value 100 seems to work well.)
(v) Normalise the velocity profiles, while maintaining relative magnitudes.

The final feature vector comprises in the given order: the chosen cadence frequencies, the sampled velocity profiles, and finally the base velocity, that is (see (3)).

An important difference to the feature vector in [4] is that in [4] the base velocity was not included in the feature vector. However in the current article we want to show the importance of the base velocity for different human activities and therefore it is included here. There were also differences regarding normalisation and reversion of the velocity profiles in the feature vector in [4]. Further, in [4] only two cadence frequencies were used. Although the feature selection method in principle was the same as in [4], the feature vector was not the same. It would be an interesting continuation of the presented work to also try to determine automatically how many cadence frequencies are needed.

3.3 Classification algorithm

In this article SVMs [17] are used for the classification task because they have a good reputation and nice properties and because they are frequently used in micro-Doppler classification literature. They have also given good results earlier [4, 5] with the CV features used in this article. A SVM is a maximum margin classifier, that aims to find hyperplanes that yields the largest possible margin of separation between clusters of data from each respective class. A SVM has some nice properties which makes it a suitable choice for this article, namely it can handle linearly non-separable classification problems, multi-class scenarios and multidimensional data. In the future it could be interesting to evaluate different classifiers.

4 Experimental details

In this section the experimental details behind the results presented in this article are given.

4.1 Feature extraction

For each TVD in the dataset, feature vectors were constructed using the two feature extraction methods. The fact that TVDs from the dataset originate from movements in both directions relative to the radar calls for post-processing of the feature vectors. The sign was hence removed from the base velocity, $z_{304}^{(\mathrm{CV})}=|v_0|$, leaving only the speed which avoids that the CV classification method is affected by the direction of movement. The TV features are changed accordingly to make the comparison fair, that is, the signs are removed from $z_1^{(\mathrm{TV})}$ and $z_3^{(\mathrm{TV})}$. This slightly improves the performance of the TV method on the considered data.

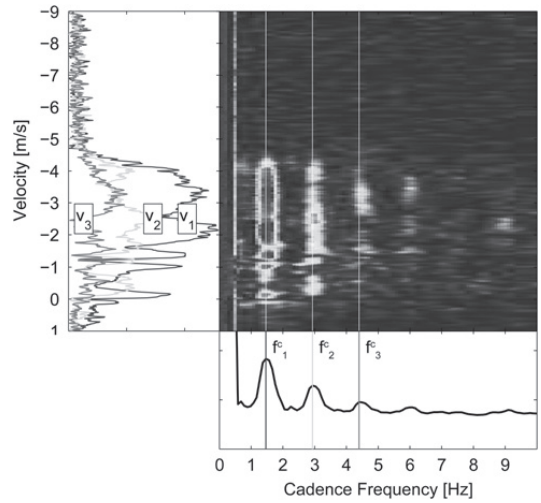

Fig. 4 *CV based feature extraction. A CVD with some of the features in the CV method illustrated (cadence frequencies and velocity profiles)*

Furthermore, to make the feature vectors suitable for the classifier, all features were normalised component-wise to achieve $|z_i|\leq 1$ for all i. This is important to avoid that features with larger numeric ranges will dominate over features with smaller ranges and to avoid numerical problems [18].

Finally, and for reasons to be discussed below, a reduced variation of the CV feature extractor, called the *reduced CV method* and denoted the CV^{-} method, was designed, which extracts only the M major cadence frequencies (here, $M=3$) from the CVD and the base velocity, that is

$$z^{(\mathrm{CV}^{-})}=\begin{bmatrix} f_1^{\mathrm{c}} & f_2^{\mathrm{c}} & \dots & f_M^{\mathrm{c}} & |v_0| \end{bmatrix} \tag{4}$$

4.2 Classification: set-up

The SVM classification was performed using LibSVM [19] and labelled time segments with five activities (disregarding the direction of movement)

$$c_i=\{\text{crawl, creep, walk, jog, run}\}. \tag{5}$$

In addition to the procedure of using a set of samples to train on, the SVM has a few extrinsic parameters that need to be set, namely a cost parameter and a kernel function [20]). For each feature extraction method, a grid-search based strategy was used to find an appropriate kernel (with parameters), and cost-parameter (C). The kernels in Table 2 were those being evaluated. To make efficient use of the limited set of data, leave-one-out cross validation was applied to evaluate each parameter setting within the grid. The best settings for each method are given in Table 3 together with the resulting classification accuracy. Accuracy is defined as the number of correctly classified samples divided by the total number of samples.

$$z^{(\mathrm{CV})}=\begin{bmatrix} f_1^{\mathrm{c}} & \dots & f_M^{\mathrm{c}} & v_1(f_1^{v}) & \dots & v_1(f_L^{v}) & \dots & v_M(f_1^{v}) & \dots & v_M(f_L^{v}) & v_0 \end{bmatrix}. \tag{3}$$

Table 2 Tested SVM kernel functions

Kernel	$K(u, v)$
Linear	$u^T v$
Polynomial	$(\gamma u^T v + c_0)^d$
RBF (radial basis function)	$\exp(-\gamma \lvert u - v \rvert^2)$
Sigmoid	$\tanh(\gamma u^T v + c_0)$

Table 3 Optimal SVM parameters as determined by leave one out cross validation and a multi-dimensional grid of candidate parameter settings

Features	Kernel	Parameters	Accuracy, %
$F_{CV}(x_k)$	Linear	$C = 2^7$	92
$F_{CV^-}(x_k)$	RBF	$C = 2^{-3}$, $\gamma = 2^{12}$	91
$F_{TV}(x_k)$	RBF	$C = 2^5$, $\gamma = 2^{-3}$	88

4.3 Classification: training and validation

For each set of feature vectors, a classifier was trained using the most appropriate setting as determined above. Due to the limited dataset, resampling was used to train and validate the classifiers. A 'leave-one-sequence-out' cross validation procedure was used, that is, one sequence at the time was removed from the training dataset and used for validation, and this procedure was repeated for each sequence. This approach was used to minimise the dependency between the training and validation phase.

5 Results

The results from applying the different feature extraction methods and then using an SVM are summarised in Fig. 5. In terms of overall accuracy, the results are comparable with what is reported in, for example, [1]. The results indicate that the TV and CV methods have comparable performance and that the base velocity and the major cadence frequencies capture the important differences between the activities. This is indicated by the separation between the classes in Fig. 2 and the performance of the reduced CV method, CV$^-$, in Fig. 5.

The most difficult activity to classify is crawling; a majority of miss-classified activities involve crawling. The same thing is indicated by Fig. 2, where crawling clusters poorly with instances close to several other activities. This makes it difficult to find a classifier that separates out crawling, at least using the base velocity and cadence frequency. The most common mis-classifications of the true class 'crawl' by the CV based methods (CV and CV^-) is with the class 'creep'. In addition, it was difficult in [4] to separate crawling and creeping with the CV based method used there.

6 Discussion

In this article we do not try to provide conclusive evidence that one feature extraction method is better than the other. Instead we provide a qualitative comparison of the two studied methods and what features which seem to provide most information about the human activity. The authors recognise the limited possibility to draw extensive conclusions about feature/classifier performance from the material presented here, partly due to the limited size of the dataset, the activities and the individuals studied. Trustworthy claims about a method's performance require a dataset with many repetitions, individuals, activities, conditions, scenes, directions of motion, etc. However, we think, that for the purpose of the article, the data we have used are sufficient. In this section we will discuss

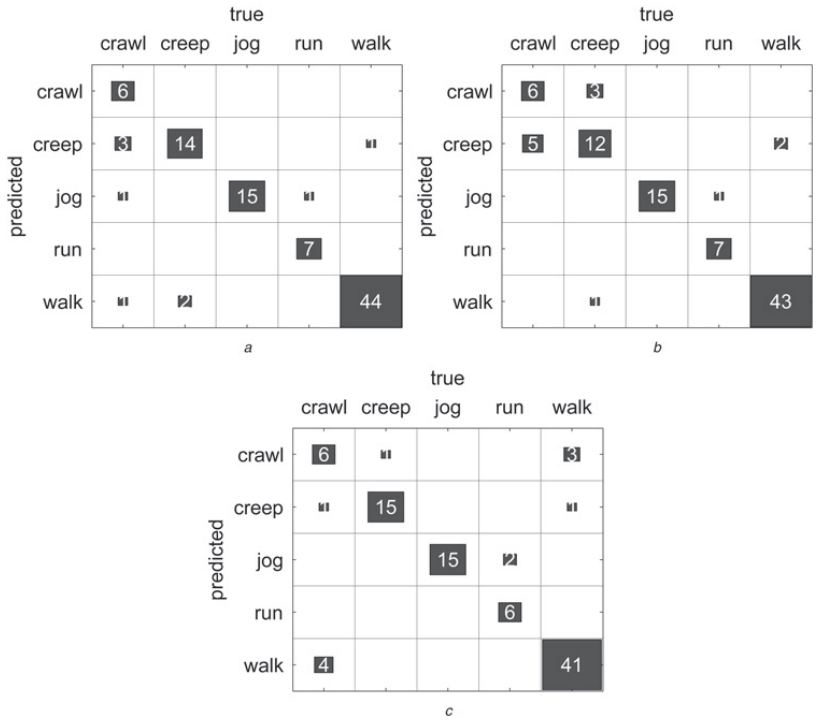

Fig. 5 *Classification results derived using 'leave-one-sequence-out' validation with 95 instances of data. The numbers in the boxes are the samples classified that way*

a Full CV method, $F_{CV}(x_k)$. Accuracy: 91%
b Reduced CV method, $F_{CV^-}(x_k)$. Accuracy: 87%
c TV method, $F_{TV}(x_k)$. Accuracy: 87%

more about sufficient features, weaknesses of the methods and non-radial movement.

6.1 Base velocity and cadence frequency are sufficient

It is interesting to discuss the feature extraction methods in light of the dataset being used. The data used in this article represent a quite 'normal' scenario with subjects moving with a fix aspect angle, and with 'normal' gaits (no excessive arm movements etc.). Under these conditions, the two features base velocity and cadence frequency can provide competitive classification results (see Fig. 2). This is interesting, especially as these properties are implicitly included in both the TV and CV methods. The TV features are mostly related to velocity information, but the period of the limb motion is closely related to the cadence frequency. On the contrary, CV features focus on cadence frequency information, but the feature vector also include the base velocity.

Thus, the base velocity and cadence frequency are two very descriptive parameters for human gait classification. Therefore, a feature vector containing derivatives of these parameters (such as the studied methods) are likely to perform well in 'normal scenarios'. A question is then how 'rich' a dataset must be to thoroughly evaluate feature extractors and classifiers? It is also interesting to determine in which situations a target's base velocity and main cadence frequency are sufficient to classify its activity. It may, in many situations, be advisable to focus on robust estimation of these two parameters instead of developing advanced feature extractors trying to mine-out every detail of a TVD. This aspect has just begun to get attention in the literature. In [21] a method for estimation of base velocity and main cadence frequency based on only the cadence frequency and mean velocity of the torso is suggested. A similar result to ours is found in [6], where the authors note that the cadence frequency and step length ('stride') are two very descriptive parameters for distinguishing between humans and small animals. The paper [22] applies mutual information to select features with a good discriminative quality and good feature estimation quality.

6.2 Problems with the TV and CV methods

The TV method relies heavily on the upper and lower envelope in the TVD of the target. Our experience is that it can be difficult to automatically estimate these envelopes, especially with low signal-to-noise ratio. This leaves us to believe that the CV method is more robust as the signal does not have to be separated from the noise (the TV method makes use of a user selected threshold for this, it affects the result, no such user input is needed in the CV method). The CV method can have a different problem, namely to robustly estimating the cadence frequencies from the CVD, point ii in Section 3.2. These conclusions should be further evaluated and tested with datasets including also non-radial data. Furthermore, the CV method uses a very high-dimensional feature space which, due to the 'curse of dimensionality', is not always wanted. Therefore, the reduced CV features set, CV^{-}, comprising only the base velocity and cadence frequencies, was evaluated. With the current dataset, reducing the feature set does not impair the classifier significantly, see Fig. 5.

6.3 Non-radial movement

We believe that the cadence frequencies of the CV method and the base cadence frequency of the TV method are robust up to at least 45° direction of movement. We motivate this by looking at the figures in [15] for a walking and a running person. The envelope of the TVD is clearly seen also for 45°, which would make it as easy to estimate as for 0° for the TV method and as easy to obtain the correct cadence frequencies for the CV method. See [4, 5] for how the CV method works.

The variation of radial velocity with direction of movement will make it more difficult to separate classes when using data from several directions of movements. This will affect the separation of 'crawl' from 'creep' and 'crawl' from 'walk' most, since the classes cannot be separated solely on cadence frequency information (see Fig. 2). Another complication with non-radial movement is that the trajectory of the torso becomes more unclear in the TVD, see figures for 'walk' and 'run' in [15]. This will probably lead to a more uncertain estimation of the base velocity and also making it more difficult for the 'crawl' class. Thus, there would be more misclassifications involving the 'crawl' class for non-radial movement. The classification of the other classes should be fairly robust up to at least 45°.

More extensive experimental data is needed to verify these hypotheses. To experimentally verify these we would need to measure on the same moving person simultaneously with several radars in different directions. The TVDs and CVDs of several subsequent measurements, as the ones that we have, vary also because of different human individuals and different movements of the same individual.

An idea for future work would be to replace the base velocity feature with features which are more independent of angle, such as the ratio of velocity bandwidth to base velocity, as suggested in [15].

7 Summary

In this article two different methods to extract features from micro-Doppler spectrograms, using features in the TV and CV domains, have been described and applied to a dataset containing measurements from different human activities. SVM was then used with these features to classify activities, with no significant differences in the classification results. Properties of the extracted features were discussed, and it was shown that comparable classification performance can be obtained using only two properties for the studied dataset, namely the target velocity and the main cadence frequency. This was demonstrated by reducing one of the feature sets. It was noted that these properties are present in both unreduced feature sets, that is, in both feature selection methods. This suggests that a feature vector with robust estimates of these two properties could be sufficient in many applications. The suggestion must be taken with some caution since the dataset was limited. An interesting direction for future research is to find more robust and efficient ways to construct feature vectors including the target velocity and the main cadence frequency. Moreover, weaknesses of the methods and the impact of non-radial motion have been discussed.

8 Acknowledgments

This work has been financially supported by Security Link and the Swedish Foundation for Strategic Research (SSF). We also gratefully thank SAAB AB and especially Mikael Hämäläinen, for cooperation with the measurements.

9 References

1 Kim, Y., Ling, H.: 'Human activity classification based on micro-Doppler signatures using a support vector machine', *IEEE Trans. Geosci. Remote Sens.*, 2009, **47**, (5), pp. 1328–1337
2 Molchanov, P., Astola, J., Egiazarian, K., *et al.*: 'Classification of ground moving radar targets by using joint time-frequency analysis'. IEEE Radar Conf., Atlanta, USA, 2012, pp. 366–371
3 Li, J., Phung, S.L., Tivive, F.H.C., *et al.*: 'Automatic classification of human motions using Doppler radar'. IEEE World Congress Computational Intelligence, Brisbane, Australia, 2012
4 Björklund, S., Johansson, T., Petersson, H.: 'Evaluation of a micro-Doppler classification method on mm-wave data'. IEEE Radar Conf., Atlanta, USA, 2012
5 Petersson, H., Björklund, S., Karlsson, M., *et al.*: 'Towards surveillance using micro-Doppler radar'. Int. Radar Symp., Hamburg, Germany, 2009
6 Kim, Y., Ha, S., Kwon, J.: 'Human detection using doppler radar based on physical characteristics of targets', *IEEE Geosci. Remote Sens. Lett.*, 2015, **12**, (2), pp. 289–293
7 Bilik, I., Khomchuk, P.: 'Minimum divergence approaches for robust classification of ground moving targets', *IEEE Trans. Aerosp. Electron. Syst.*, 2012, **48**, (1), pp. 581–603

8 Bryan, J., Kwon, J., Lee, N., *et al.*: 'Application of ultra-wide band radar for classification of human activities', *IET Radar Sonar Navig.*, 2012, **6**, (3), pp. 172–179
9 Fairchild, D., Narayanan, R.: 'Classification of human motions using empirical mode decomposition of human microdoppler signatures', *IET Radar Sonar Navig.*, 2014, **8**, (5), pp. 425–434
10 Bilik, I., Tabrikian, J.: 'Radar target classification using Doppler signatures of human locomotion models', *IEEE Trans. Aerosp. Electron. Syst.*, 2007, **43**, (4), pp. 1510–1522
11 Lyonnet, B., Ioana, C., Amin, M.G.: 'Human gait classification using microDoppler time-frequency signal representations'. IEEE Radar Conf., 2010, pp. 915–919
12 Tivive, F.H.C., Bouzerdoum, A., Amin, M.G.: 'A human gait classification method based on radar Doppler spectrograms', *EURASIP J. Adv. Sign. Proc.*, 2010, **2010**, doi:10.1155/2010/389716
13 Liu, L., Popescu, M., Skubic, M., *et al.*: 'Automatic fall detection based on doppler radar motion signature'. 2011 Fifth Int. Conf. on Pervasive Computing Technologies for Healthcare (PervasiveHealth), 2011, pp. 222–225
14 Balleri, A., Chetty, K., Woodbridge, K.: 'Classification of personnel targets by acoustic micro-doppler signatures', *IET Radar Sonar Navig.*, 2011, **5**, (9), pp. 943–951
15 Björklund, S., Petersson, H., Nezirovic, A., *et al.*: 'Millimeter-wave radar micro-Doppler signatures of human motion'. Int. Radar Symp., Leipzig, Germany, 2011
16 Ghaleb, A., Vignaud, L., Nicolas, J.M.: 'Micro-Doppler analysis of wheels and pedestrians in ISAR imaging', *IET Signal Proc.*, 2008, **2**, (3), pp. 301–311
17 Vapnik, V.: 'The nature of statistical learning theory' (Springer-Verlag Inc, 1999, 2nd edn.)
18 Hsu, C.-W., Chang, C.-C., Lin, C.-J.: 'A practical guide to support vector classification' (Department of Computer Science and Information Engineering, National Taiwan University, Taipei 106, Taiwan, 15 April 2010). Available at www.csie.ntu.edu.tw/_cjlin/libsvm
19 Chang, C.-C., Lin, C.-J.: 'LIBSVM: A library for support vector machines', *ACM Trans. Intel. Syst. Tech.*, 2011, **2**, pp. 27:1–27:27
20 Aizerman, M., Braverman, E., Rozonoer, L.: 'Theoretical foundations of the potential function method in pattern recognition learning', *Autom. Remote Contr.*, 1964, **25**, pp. 821–837
21 Sun, Z., Wang, J., Yuan, C., *et al.*: 'Parameter estimation of walking human based on micro-doppler'. 12th Int. Conf. on Signal Processing (ICSP2014), 2014, pp. 1934–1937
22 Gurbuz, S., Tekeli, B., Karabacak, C., *et al.*: 'Feature selection for classification of human micro-doppler'. 2013 IEEE Int. Conf. on Microwaves, Communications, Antennas and Electronics Systems (COMCAS), 2013, pp. 1–5

Publication 9: Target Classification in Perimeter Protection with a Micro-Doppler Radar

Target Classification in Perimeter Protection with a Micro-Doppler Radar

Svante Björklund[1], Tommy Johansson[2], Henrik Petersson[3]
[123]Swedish Defence Research Agency (FOI), SE-581 11 Linköping, Sweden
[1]Blekinge Institute of Technology, Karlskrona, Sweden
Email: [1]svabj@foi.se

***Abstract*—In security surveillance at the perimeter of critical infrastructure, such as airports and power plants, approaching objects have to be detected and classified. Especially important is to distinguish between humans, animals and vehicles. In this paper, micro-Doppler data (from movement of internal parts of the target) have been collected with a small radar of a low-complexity and cost-effective type. From time-velocity diagrams of the data, some physical features have been extracted and used in a support vector machine classifier to distinguish between the classes "human", "animal" and "man-made object". Both the type of radar and the classes are suitable for perimeter protection. The classification result are rather good, 77% correct classification. Particularly interesting is the surprisingly good ability to distinguish between humans and animals. This also indicates that we can choose to have limitations in the radar and still solve the classification task.**

I. Introduction

The application in this paper is security surveillance at the perimeter of critical infrastructure, such as airports and power plants. Approaching objects have to be detected and classified. Especially humans, animals and vehicles have to be separated.

In this paper we have used a small radar which is low-complexity and cost-effective in its micro-Doppler mode for the classification. We do not address the detection. We have collected micro-Doppler radar data of different target types, extracted features and classified the targets. By micro-Doppler we mean the Doppler shifts generated by the movements of internal parts of the target. We have used micro-Doppler data from humans, cars, a horse, a dog and from a consumer drone.

Advantages with a radar compared to electro-optical sensors is its ability of very accurate radial velocity measurements, its large surveillance area coverage, its ability of direct distance measurements and its ability to operate in all weather and all light conditions. A radar is also less affected of human clothing choices and is privacy preserving, which is to advantage for security surveillance.

The use of radar micro-Doppler is a relatively new area of research but has generated a large number of papers the last years. For example, classification of human activities has been performed in [1], [2], [3], distinguishing between humans and vehicles in [4], [5]. Birds and different kinds of consumer drones are classified in [6], [7]. Not much research results on automatic separation of humans from animals has been reported. In [8] TVDs (Time Velocity Diagrams) are shown for a human walking, power walking, jogging and running, for a horse (with rider) walking and trotting, for a lawn mower tractor (with driver), for a car and for a man riding a bicycle. The authors do not extract features or classify the targets but state that there is potential to classify the target type. In [9], which is the most similar work we have seen to our present paper, they classify the target types human, dog, bicycle and car using physical features from the TVD and a SVM (Support Vector Machine) classifier. They see as the main problem the separation between humans and animals. Two books, dedicated entirely to radar micro-Doppler, have appeared [10], [11].

II. Measurements

A. The radar

We have used an experimental radar from the company IMST in Germany. In the micro-Doppler mode it is a CW (continuous wave) radar without modulation. Only the carrier wave at 24 GHz is transmitted. The radar only measures Doppler and

without the sign of the Doppler. Internally the radar generates a TVD (Time Velocity Diagram) by non-overlapping FFTs. A TVD has time on one axis and velocity on the other. For each time instant it displays the velocity contents of the target. See Figure 1 for an example. The sampling frequency within the FFT was 12.8 kHz and the integration interval for a single FFT was 80 ms. The radar do not measure range nor direction to the target in the micro-Doppler mode. Its wide antenna beam and single "range bin" give a large coverage in direction and range (if the SNR is sufficient). Vertical polarization was used. The radar has low power requirements.

Two limitations of the radar are more important for us. First, the time resolution of the TVDs (approximately 90 ms) is too low to separate many internal target motions. Second, the SNR decreases quickly with range, probably because of low transmitted power and wide antenna beam.

The radar has other modes that we have not used in this paper.

B. Measurement campaign

On December 17, 2014, we conducted a measurement campaign at the backyard of FOI (Swedish Defence Research Agency) in Linköping, Sweden. The targets moved mostly radially towards or away from the radar.

C. Data pre-processing

We have performed manual detection of the targets and manual selection of the time intervals with target signal present. Such an interval we call a "target sequence". Then we have split the original target sequences into smaller ones, 2.5 – 3.5 s long with a nominal length of 3.0 s. We have manually assigned true classes to the target sequences. The total number of target sequences is 1136, of which 303 belong to the "human" class, 359 to "animal", 168 to "vehicle" and 306 to the "other" class. See below for the definition of the classes.

III. Feature extraction and micro-Doppler signatures

A. The Kim-Ling features

We have used the physical features defined by Kim & Ling [1]. They are extracted from the TVD. The features are:

- f(1) - Base velocity or torso/body radial velocity.
- f(2) - Total BW (Bandwidth) of Doppler signal.
- f(3) - Offset of total Doppler.
- f(4) - BW without micro-Doppler.
- f(5) - Normalized standard deviation of Doppler signal strength.
- f(6) - Cadence/cycle frequency (= period of limb motion for humans and animals).

See [1], [12] for details of the definitions. We estimate these features with the algorithms described in [12]. We have made some modifications of the noise thresholding since [12].

B. Micro-Doppler signatures and feature extraction

In this Section we will show TVDs of different target types and also illustrate the function of the Kim-Ling feature extraction. For different target types we have defined four classes to recognize, namely "human", "animal", "vehicle" and "other".

Figure 1-2 show the TVD of a single person walking radially relative the radar without carrying anything. The figures also illustrate the Kim-Ling feature extraction. There are three plots for each target sequence. The top plot depicts the original TVD before the feature extraction. The level in the TVDs is not normalized to the noise level. (The different background colors do not mean different background (i.e. noise) power. Look at the difference between the level of signal and background.) The middle plot shows the result after the noise thresholding. Ideally the target signal should be completely included and visible while the background should be clear from signal (a dark blue color).

The bottom plot illustrates the feature extraction. The feature f(1), torso radial velocity, is shown in the plots as a dashed white horizontal straight line. The features f(2), f(3) and f(6) need the estimation of the upper and lower envelopes. These envelopes are shown as solid red and blue lines. The total bandwidth without micro-Doppler, feature f(4), is shown as the band between two dotted black straight horizontal lines. The total bandwidth of Doppler signal, feature f(2), is shown as the band between two dashed green straight horizontal lines at f(1)± 0.5 f(2). Feature f(6), the period of limb motion, is shown as the distance between two red straight

vertical lines. The remaining feature, f(5), is not illustrated in the plot.

The estimation of the envelopes works well most times for humans. See Figure 1 for an example. The noise thresholding in the figure is perfect. A few times the noise thresholding fails for humans because of low SNR, see Figure 2.

Two different animals were included in the target class "animal", a dog and a horse. The dog performed two activities. First, the dog was running from and towards radar. Then, the dog was moving and looking for candy. See Figure 3, left plots. The horse had a rider but the rider will most likely not contribute significantly to the TVD. Compare with a human carrying an object in [13]. Figure 3, top right plot, displays the TVD of the horse "walking". Walking probably means slow-moving. The real gait is unknown. A TVD of the horse "running" (with rider) is depicted in Figure 3, bottom right plot. Running likely means fast-moving. The real gait is unknown.

We continue to Kim-Ling features for target class "vehicle". In Figure 4, top left plot, the radar target is a car driving with approximately constant speed radially relative the radar. We see that the estimation of an envelope fails because there is no micro-Doppler. Only the parts of the target sequences with pure radial movement of the car were included in this target class.

The target class "other" consists of two different types of target sequences. The first is a flying consumer drone, a quadrocopter with four horizontal rotors (Figure 4, right plots), and the second is the part of car target sequences with the car moving obliquely towards or from the radar (Figure 4, bottom left plot).

Figure 5 is a scatter plot showing the estimated values of three of the features, namely f(1), f(4) and f(5), in a 3D plot projected to 2D. Different classes have different marker symbols and colors. It seems like the classes cluster into groups. This is promising for the classification.

IV. Classification

We have employed a SVM (Support Vector Machine) [14] for the classification and used the software package LibSVM [15]. The SVM used a radial basis function kernel with the parameters $C = 2^{7.0}$

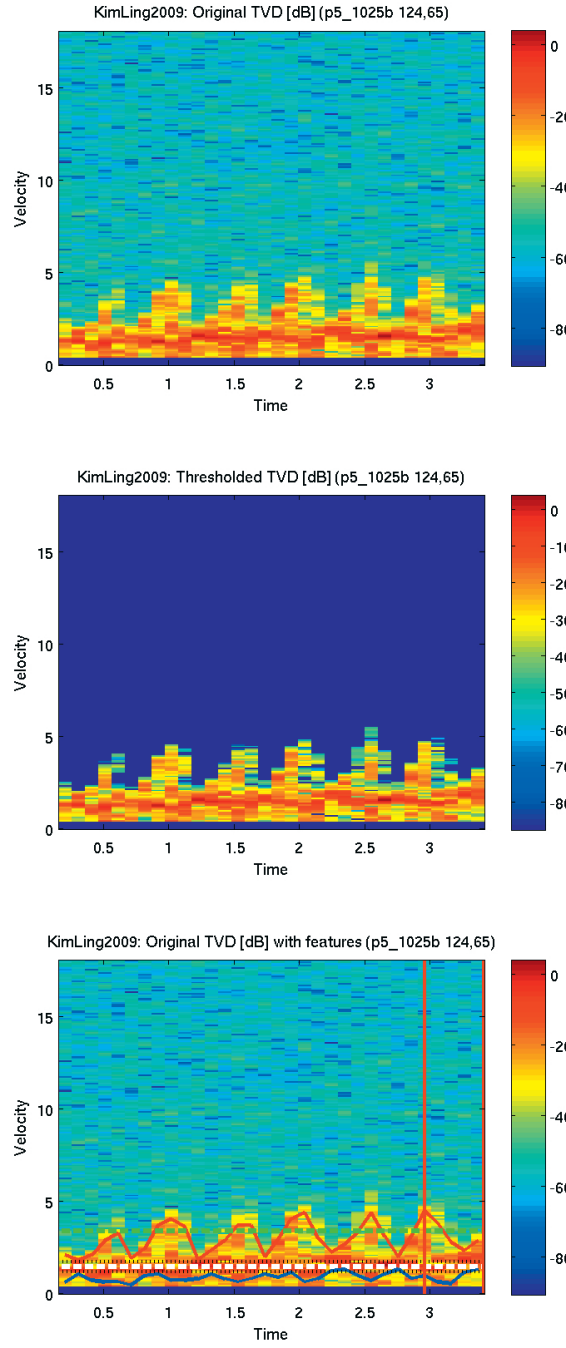

Figure 1. TVDs of a single human. High SNR. Top plots: Original TVD. Middle plots: TVD after noise thresholding. Bottom plots: TVD with illustration of the Kim-Ling feature extraction. See the text for an explanation.

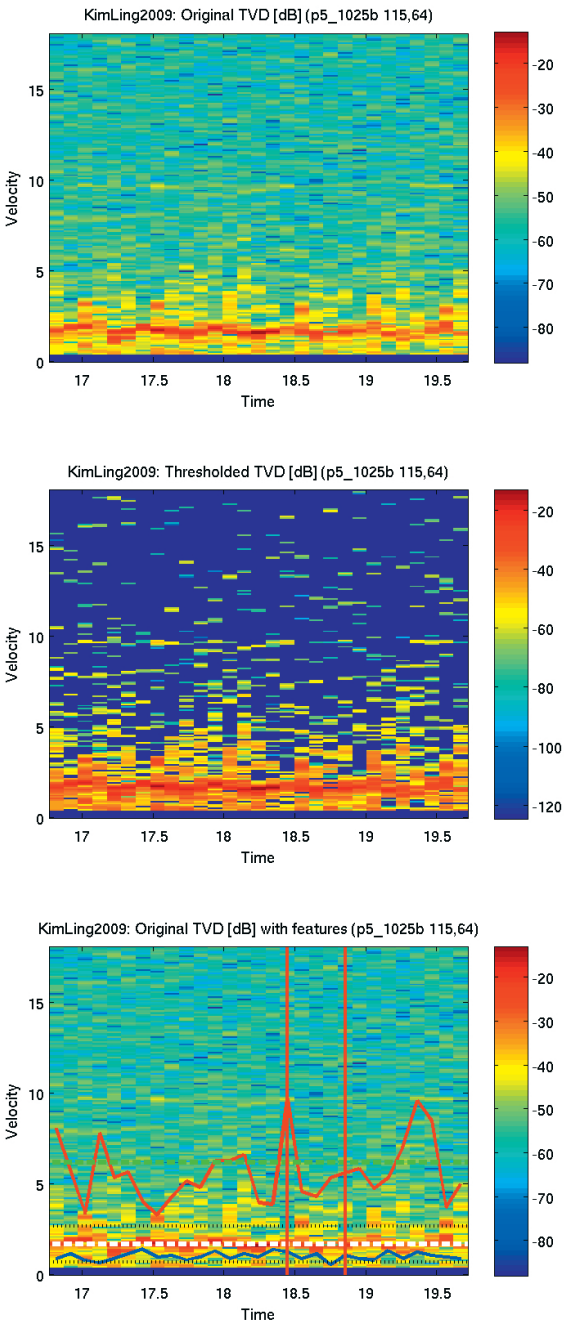

Figure 2. TVDs of a single human. Lower SNR. Top plots: Original TVD. Middle plots: TVD after noise thresholding. Bottom plots: TVD with illustration of the Kim-Ling feature extraction. See the text for an explanation.

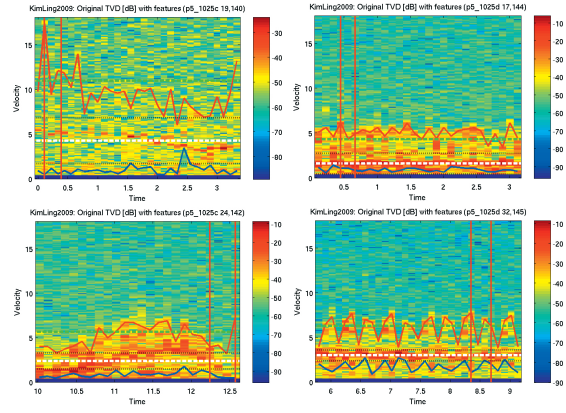

Figure 3. TVDs of a single animal. Left: The dog involved in two different activities. Top right: a horse "walking". Bottom right: A horse "running".

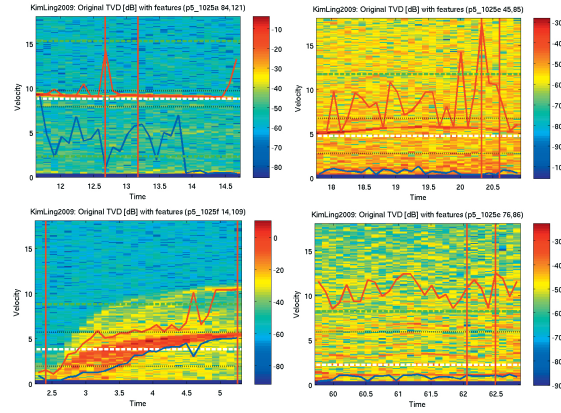

Figure 4. TVDs of man-made objects. Top left: A car moving radially relative the radar. Bottom left: A car moving at an oblique angle relative the radar. Right: A consumer drone, a quadrocopter.

and $\gamma = 2^{0.5}$ These parameters were found by a combination of a computer search with a 4-fold cross validation and a manual search. It was difficult to find good values of the parameters.

In the training and validation of the SVM classifier we performed a cross validation by leave one out, where "one" are the target sequences from the same measurement of the same target. The classification result is shown in Figure 6. With the original classes, i.e. "human", "animal", "vehicle" and "other", the accuracy (the percentage correct classification) is 64.0%. However, if we aggregate

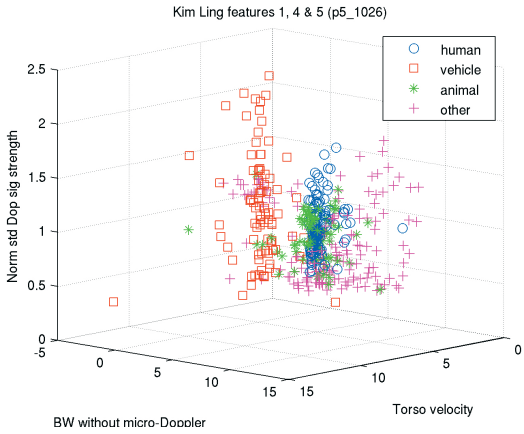

Figure 5. Scatter plot of three of the Kim-Ling features.

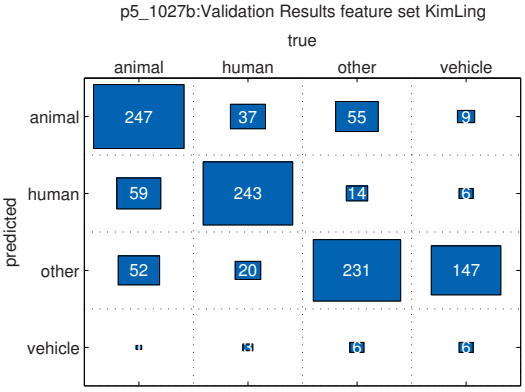

Figure 6. Classification result (a "confusion matrix") with the SVM. Percentage correct classification of classes "human", "animal", "vehicle" and "other": 64.0%. Percentage correct classification of classes "human", "animal", "vehicle" and "man-made object" ("vehicle" and "other"): 77.5%.

the classes "vehicle" and "other" into the new class "man-made object" the accuracy is 77%. The resulting classes "human", "animal" and "man-made object" are suitable for perimeter protection.

V. Discussion

In our present work the most difficult signal processing was the noise thresholding (middle plots in Figure 1 and 2). The noise thresholding is needed for estimation of features f(2), f(3) and f(6), see [12]. One reason for the difficulties is that the target signal and the noise signal (external clutter and internal noise) have varying characteristics due to varying target types, target ranges, target activities, backgrounds, weather, radar systems etc. The thresholding also needs high SNR. Also in [12] the noise thresholding was problematic. In [9] they seems to achieve a successful noise thresholding (see Fig. 4 in [9]). This indicates a high SNR.

There are clear differences in the MDSs (Micro-Doppler Signatures) of humans and animals on one side and man-made objects on the other side. The internal movements of man-made objects usually have much higher frequencies (motor vibrations, propeller revolutions, etc.) than for humans/animals. This means that for the integration time and observation time suitable for humans/animals there will be no envelope with antinodes (compare with [13]) for man-made objects.

A possibility to distinguish humans from four-legged animals could be to utilize that animals with quadrupedal motion has a higher cycle/cadence frequency than humans with bipedal motion for the same base velocity. This can be seen by comparing Figure 1 with Figure 3 (top right).

In the classification result in Figure 6 the class "vehicle" is most times incorrectly classified. There can be several reasons for that:

- The "vehicle" and "other" classes have similar micro-Doppler properties, which also are different from those of "human" and "animal". Our "other" class actually consists of some kinds of vehicles. They are all moving man-made objects.
- Some of the employed features, e.g. cycle frequency, are suitable only for humans and animals and not for man-made targets. The result of the estimation is presumably random values for these features for man-made objects. The SVM classifier should to some degree be able to disregard these random features but they cannot be used for separating the classes "vehicle" and "other".
- The data set was unbalanced. There were about half the number of target sequences for "vehicle" compared with the other classes.

There are several similarities between our present paper and the paper [9]. In [9] they also use physical features and most of them are estimated from the

TVD. They use a feature "stride" (step length) which we do not use but it can be derived from our features "cycle frequency" and "base velocity". The base velocity is not used in [9]. The paper [9] also uses noise thresholding and a SVM classifier. Unfortunately, in [9] the processing is only described on a high level and nearly no details are given.

The paper [9] presents better classification results than our paper but there are differences in the experimental conditions. In [9] they only try to distinguish humans from small animals (dogs). This is easier than with large animals, like horses in our paper, because the longer legs of the large animals make their MDSs more similar to humans. Horses resemble moose and roe deers, which are common in Sweden.

In [9] they have a higher time resolution in the TVD. This should make it easier to see discriminating details in the TVDs. In [9] they say that blurring of the TVD due to fast-changing micro-Doppler of a target "makes the algorithm processing difficult". We have blurring of two causes. First the low time resolution and second the fast movement of the dog and the wheels of the obliquely moving cars (in the class "other"). On the other hand, our carrier frequency is higher (24 GHz) than the one in [9] (7.25 GHz). This should make the velocity resolution of our radar higher and enhance the classification.

Figure 4 in [9] indicates a higher SNR than for us, which, of course, makes the classification task easier. The target types are not exactly the same in our paper and in [9] which makes the comparison uncertain.

VI. Conclusions

We draw these conclusions from our work:

- With the classes "human", "animal", and "man-made object", which are suitable for perimeter protection, the probability of correct classification on our data was 77%.
- Especially interesting in our results is the good ability of the classification to distinguish between humans and animals. Beforehand, we did not think this would be possible.
- Since it is not possible to see the identity of humans from the received radar signal, a radar is privacy preserving, something which often is desirable for perimeter protection.
- More investigations are necessary to confirm the classification results, to explain the results and to see their robustness under different circumstances (different target behaviors, target ranges, backgrounds, etc.).
- We have used a small radar of a low-complexity and cost-effective type, suitable for perimeter protection, with surprisingly good classification results. This indicates that we can choose to have limitations in the radar and still solve the classification task.

Acknowledgments

The research leading to these results has received funding from the European Union's Seventh Framework Programme under grant agreement n° 312784, P5 (Privacy Preserving Perimeter Protection Project) and from Security Link and the Swedish Foundation for Strategic Research (SSF). I would also like to thank IMST for kindly placing their experimental radar to our disposal and Gustaf Hendeby, Linköping University, for developing algorithms and software used in this paper.

References

[1] Y. Kim and H. Ling, "Human activity classification based on micro-doppler signatures using a support vector machine," *IEEE Transactions on Geoscience and Remote Sensing*, vol. 47, no. 5, pp. 1328–1337, May 2009.

[2] J. Li, S. L. Phung, F. H. C. Tivive, and A. Bouzerdoum, "Automatic classification of human motions using doppler radar," in *WCCI 2012 IEEE World Congress on Computational Intelligence*, Brisbane, Australia, June 10-15 2012.

[3] B. Lyonnet, C. Ioana, and M. Amin, "Human gait classification using microdoppler time-frequency signal representations," in *Radar Conference, 2010 IEEE*, may 2010, pp. 915 –919.

[4] P. Molchanov, J. Astola, K. Egiazarian, and A. Totsky, "Classification of ground moving radar targets by using joint time-frequency analysis," in *IEEE Radar Conference 2012*, Atlanta, USA, May 7-11 2012, pp. 366–371.

[5] I. Bilik and P. Khomchuk, "Minimum divergence approaches for robust classification of ground moving targets," *IEEE Transactions on Aerospace and Electronic Systems*, vol. 48, no. 1, pp. 581–603, January 2012.

[6] R. I. A. Harmanny, J. J. M. de Wit, and G. Premel-Cabic, "Radar micro-doppler mini-uav classification using spectrograms and cepstrograms," *International Journal of Microwave and Wireless Technologies*, vol. 7, no. Special Issue 3-4, pp. 469–477, June 2015. [Online]. Available: http://journals.cambridge.org/action/displayAbstract?fromPage=online&aid=9875227&fulltextType=RA&fileId=S1759078715001002

[7] P. Molchanov, K. Egiazarian, J. Astola, R. I. A. Harmanny, and J. J. M. de Wit, "Classification of small uavs and birds by micro-doppler signatures," in *EuRad*, Nuremberg, Germany, 9-11 October 2013, pp. 172–175.

[8] D. Tahmoush, J. Silvious, and J. Clark, "An UGS radar with micro-doppler capabilities for wide area persistent surveillance," in *Proc. SPIE 7669, Radar Sensor Technology XIV, 766904*, April 26 2010.

[9] Y. Kim, S. Ha, and J. Kwon, "Human detection using doppler radar based on physical characteristics of targets," *Geoscience and Remote Sensing Letters, IEEE*, vol. 12, no. 2, pp. 289–293, Feb 2015.

[10] V. C. Chen, *The Micro-Doppler Effect in Radar*. Artech House, 2011, ISBN-10: 1-60807-057-3.

[11] V. C. Chen, D. Tahmoush, and W. J. Miceli, Eds., *Radar Micro-Doppler Signatures, Processing and Applications*. The Institution of Engineering and Technology, www.theiet.org 2014, ISBN 978-1-84919-716-8.

[12] S. Björklund, H. Petersson, and G. Hendeby, "Features for micro-doppler based activity classification," *IET Radar, Sonar & Navigation*, vol. 9, no. 9, pp. 1181–1187, dec 2015.

[13] S. Björklund, H. Petersson, A. Nezirovic, M. B. Guldogan, and F. Gustafsson, "Millimeter-wave radar micro-doppler signatures of human motion," in *International Radar Symposium 2011*, Leipzig, Germany, September 7-9 2011, Available from IEEE Xplore.

[14] S. Haykin, *Neural Networks: A comprehensive foundation*, 2nd ed. Prentice-Hall Inc., 1999.

[15] C.-C. Chang and C.-J. Lin, "LIBSVM: A library for support vector machines," *ACM Transactions on Intelligent Systems and Technology*, vol. 2, pp. 27:1–27:27, 2011, software available at http://www.csie.ntu.edu.tw/∼cjlin/libsvm.

Publication 10: On Distinguishing between Human Individuals in Micro-Doppler Signatures

Svante Björklund, Henrik Petersson, Gustaf Hendeby: "On Distinguishing between Human Individuals in Micro-Doppler Signatures", International Radar Symposium (IRS 2013), Dresden, Germany, June 19-21, 2013. Reproduced with permission from DGON (German Institute of Navigation).

On Distinguishing between Human Individuals in Micro-Doppler Signatures

Svante Björklund[1], **Henrik Petersson**[1], **Gustaf Hendeby**[1,2]

[1]Swedish Defence Research Agency (FOI)
SE-581 81 Linköping, Sweden
email: {svabj, henpet}@foi.se

[2]Linköping University
Department of Electrical Engineering
SE-581 83 Linköping, Sweden
email: hendeby@isy.liu.se

Abstract: *Radar micro-Doppler signatures (MDS) of humans are created by movements of body parts, such as legs and arms. MDSs can be used in security applications to detect humans and classify their type and activity. Target association and tracking, which can facilitate the classification, become easier if it is possible to distinguish between human individuals by their MDSs. By this we mean to recognize the same individual in a short time frame but not to establish the identity of the individual. In this paper we perform a statistical experiment in which six test persons are able to distinguish between walking human individuals from their MDSs. From this we conclude that there is information in the MDSs of the humans to distinguish between different individuals, which also can be used by a machine. Based on the results of the best test persons we also discuss features in the MDSs that could be utilized to make this processing possible.*

1. Introduction

Technology for security applications has lately received much attention, for example as a means to detect and assess human activity at critical infrastructure such as airports and power plants. One approach to detect and classify the targets is to use radar and utilize Doppler information ("micro-Doppler") created by movements of parts of the human targets. In the literature, some results on automatic classification of target type and activity using Micro-Doppler Signatures (MDS) have been published, e.g. [1, 2, 3]. We have earlier, among others, classified different human gaits [4] and simultaneously estimated and tracked micro-Doppler and position parameters [5].

The problem we want to address in this paper is to distinguish between human individuals from their MDSs, or more specifically whether there is information in MDSs to distinguish between human individuals. By distinguishing between human individuals we mean to recognize the same individual in a short time frame but not to establish the identity of the individual. As far as we know, this problem has not been treated earlier for radar in the literature but in sonar it has [6, 7]. The ability to distinguish between human individuals can be utilized to enable target reacquisition and simplify association in multi-target tracking, allowing for longer consistent target tracks even if the target shortly leaves the field of view of the sensor or interacts with other targets. The tracking in its turn can facilitate classification of target type and activity and perhaps even foreseeing the intention of the target. An example is when different classifier models are used depending on the target direction of movement. Another is classification of target type and activity based on the target movement during a longer time interval.

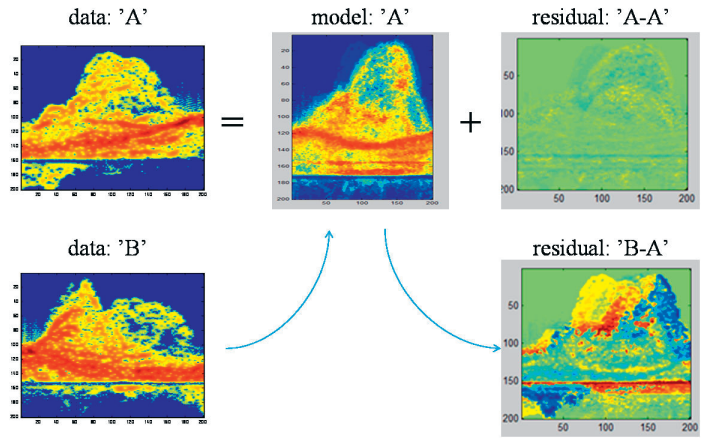

Figure 1: PCA analysis for distinguishing human individuals. The principal eigenvectors of the covariance matrix formed by the MDSs as images were used as the model of each individual. Then the residual image was formed for each model and MDS pair, where the residual image includes the parts of the MDS that cannot be explained by the model. The idea is that with the correct model the residual image (the right column) will be weak but with incorrect model it will be strong. In our tests we did not manage to obtain models stable enough over time to be useful. Fig. 9 in [9].

2. Problem description

It is possible for a human to visually discriminate different human gaits from MDSs and under easy conditions also a machine can do this, see e.g. [4, 8]. On the other hand, we have found it difficult to make a machine distinguish between human individuals from their MDSs. We have tested an approach for distinguishing human individuals using PCA (Principal Component Analysis), see Fig. 1. The result is so far not satisfying. It is not obvious that it is possible to distinguish between human individuals in MDSs. Therefore we want to investigate in this paper whether it is at all possible to do this.

3. Materials and methods

3.1. Choice of experiment

In order to answer the question of whether it is possible to distinguish between human individuals by their MDSs, we designed and conducted an experiment in which six test persons were given a number of MDSs from three different walking human individuals. The test persons were asked to put the MDS in three groups, one group for each of the individuals. The MDS in each group should thus be from the same individual, but not necessarily having a specific identity. Then we made a statistical hypothesis test so see if the test persons had distributed the MDSs better than randomly. The rationale behind this test is that if test persons are able to distinguish between human individuals from their MDSs, then the information is there for distinguishing by a machine as well.

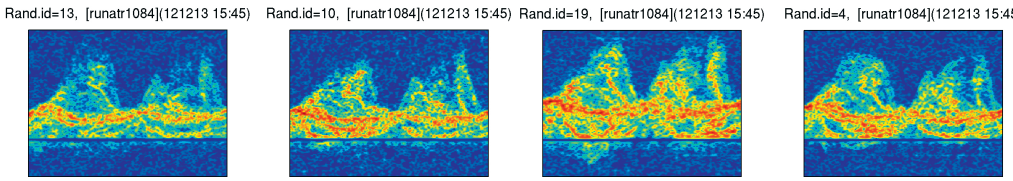

Figure 2: Four of the MDSs shown to the six test persons. The MDSs have a random number and were presented in random order. With four MDSs there must be at least one individual with at least two MDSs.

3.2. Measurement data

The data used in this paper came from an FMCW (Frequency Modulation Continuous Wave) radar (SIRS 1600 TD by SAAB AB) with linear FM sweeps, carrier frequency of 77 GHz and horizontal polarization. The range resolution is about 1 m. The Doppler filtering utilizes the phase shift between different sweeps, like in a pulsed radar. The measurements were a subset of the ones used in [10].

The measurements were conducted outdoors in Sweden in the summer 2010 on fairly plane ground covered with short grass. The weather was overcast and somewhat windy. It had rained earlier but now there was a pause in the rain. The radar targets were two adult men and one adult woman, which were all walking away obliquely from the radar in a similar way with an aspect angle of $45°$. The elevation angle was about $0°$.

3.3. Conducting the experiment

The test persons were given 29 MDSs with two gait cycles in each, see Fig. 2 for some examples. The test persons were given the same instructions. Since the individuals were walking obliquely, the gait cycles for left and right step probably were different. It was unknown whether the two-cycle MDSs started with a left or right step. The test persons were given a maximum of 30 min to accomplish the task.

3.4. Statistical analysis

We have used a hypothesis test to determine whether the test persons distributed the MDSs better than randomly. The null hypothesis $\mathcal{H}_0$ is that the test persons distributed the MDSs randomly and the alternative hypothesis $\mathcal{H}_1$ that they performed better than that. Let $f(i)$ be the probability density function (PDF) of the total correctly distributed MDS by six persons which are distributing randomly. Then $\alpha(k) = \sum_{i=k}^{K} f(i)$, with K being the total number of distributed MDSs, will be the *significance level* if we choose k as the threshold for the total correctly distributed MDS at or above which we reject $\mathcal{H}_0$. The significance level is the risk to state that the test persons distribute better than random when they do not do that. If the significance level is sufficiently low, e.g. $\leq 0.5\%$ we reject $\mathcal{H}_0$ and believe that the test persons distributed better than random. This PDF we have estimated by Monte Carlo simulations, see

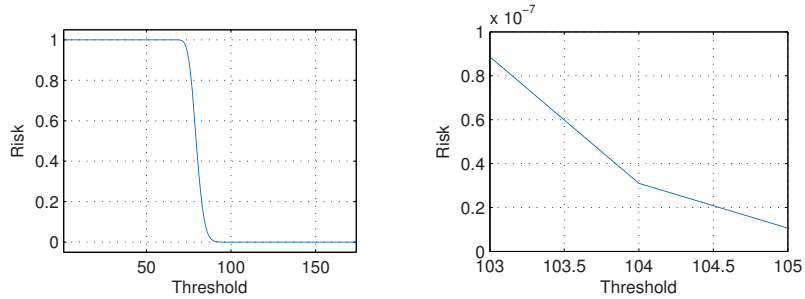

Figure 3: Significance level $\alpha(k)$ vs. threshold k of the total correctly distributed MDS by six persons which are distributing randomly. This is the same as $1 - F(k)$ where $F(k)$ is the cumulative distribution function. Shown is the mean value over 1000 repetitions of the significance level computed from the convolution of six copies of the PDF for a single test person estimated from 10^6 Monte Carlo simulations. Left: For all thresholds of the number of correctly distributed MDSs. Right: A zoom-in around 104.

Fig. 3. We chose a significance level $\alpha = 0.1\%$.

4. Results

The number of correctly distributed MDSs of the test persons were {14, 17, 22, 14, 15, 22}. The test persons together distributed 104 MDS correctly. By using the curve in Fig. 3 for 104 correctly distributed MDSs we get a significance level of $3.1 \cdot 10^{-8}$. We see that for our chosen significance level $\alpha = 0.1\%$, we can clearly reject the null hypothesis $\mathcal{H}_0$. Therefore we believe that the test persons extracted information from the MDSs that helped them distribute the human individuals better than randomly.

5. Discussion

5.1. The statistical test

Our test and statistical analysis indicate that there is information in the MDS to distinguish between human individuals. However, this might not be true for other human individuals, other scenarios, for longer time intervals between the MDSs, etc.

Unfortunately, even if the MDSs contain information to distinguish between human individuals, this says little about how to automatically extract the information.

5.2. Discriminating features

Having established that human test persons improve over randomly distributing MDSs in groups with the same human individual, the next interesting question is how this is done and whether it can be formulated in such a way that a machine can do it. Therefore, after having performed the

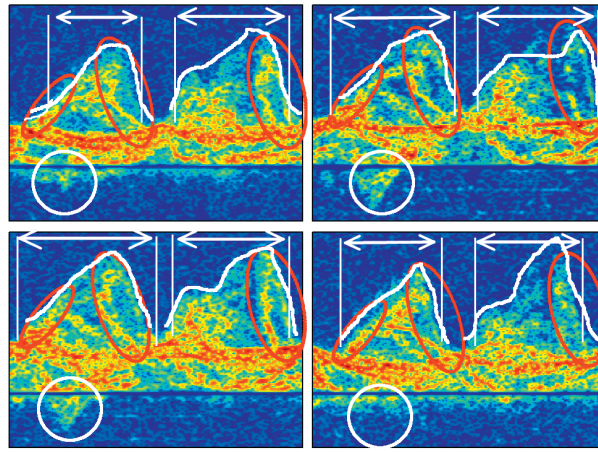

Figure 4: Illustration of the MDS features used by the most successful test persons. Ellipses (red=dark) are used to mark regions the first test person pointed out as important, whereas the circles, curves and arrows (white=bright) are used to illustrate the features the second person looked for.

experiments, the two test persons having the best test results were asked to describe how they reasoned when distributing the MDSs. The descriptions they provided were not very distinct, and focused on different aspects of the MDS.

The first test person focused on parts of the MDSs with distinctive energy lines; if they existed, their length and shape, and if they connected in loops. The test person also pointed out where he looked for the characteristic lines. The interesting regions are marked by the red ellipses in Fig. 4. The second test person focused on the shape of the envelope of the MDS; if it was wide or narrow, if an accentuated dip with negative speed was present, and if the envelope was concave or convex. Fig. 4 highlights these features in white. Both test persons did their grouping in steps, first considering what they regarded the strongest feature, and then refined the grouping using the more weak features.

5.3. Using MDSs to distinguish human individuals

Being able to follow targets throughout a scene is an important factor to gain scene understanding. Relying solely on kinematic information to keep consistent tracks of persons leaving and, shortly after, reappearing in the scene, or of people with poor spatial separation, is very challenging. Often the uncertainty in position makes conclusive association impossible. By introducing a measure on the probability that a target MDS can stem from a previously observed target, target association performance can be improved, yielding better tracks. To achieve this, a model of a target's MDS is learned when the target is well separated from other targets. This model is later used to recognize the target. Based on the recognition, and the confidence of the algorithm, the probability of a given MDS to be associated with a given track can be approximated. This can then be used as a factor in a probability based association method.

6. Conclusions

We have presented an experiment from which we conclude that radar micro-Doppler signatures of walking humans likely contain information to distinguish between different human individuals. We have also discussed features in the MDSs which could be utilized to make this possible. Finally we point out that this ability can be used to enhance target association and tracking in order to improve the classification of the target type and activity.

Acknowledgments

This work has financially been supported by Security Link and the Swedish Foundation for Strategic Research (SSF). We also gratefully thank SAAB AB and especially Mikael Hämäläinen for a fruitful cooperation with the measurements.

References

[1] I. Bilik and J. Tabrikian, "Radar target classification using doppler signatures of human locomotion models," *IEEE Transactions on Aerospace and Electronic Systems*, vol. 43, no. 4, October 2007.

[2] P. Molchanov, J. Astola, K. Egiazarian, and A. Totsky, "Classification of ground moving radar targets by using joint time-frequency analysis," in *IEEE Radar Conference 2012*, Atlanta, USA, May 7-11 2012, pp. 366–371.

[3] G. E. Smith, K. Woodbridge, and C. J. Baker, "Naïve Baysian radar micro-doppler recognition," in *2008 International Conference on Radar*, Adelaide, Australia, 2-5 September 2008.

[4] S. Björklund, T. Johansson, and H. Petersson, "Evaluation of a micro-doppler classification method on mm-wave data," in *IEEE Radar Conference 2012*, Atlanta, USA, May 7-11 2012.

[5] M. B. Guldogan, F. Gustafsson, U. Orguner, S. Björklund, H. Petersson, and A. Nezirovic, "Human gait parameter estimation based on micro-doppler signatures using particle filters," in *ICASSP 2011*, Prague, Czech Republic, May 22-27 2011.

[6] G. Garreau, C. M. Andreou, A. G. Andreou, J. Georgiou, S. Dura-Bernal, T. Wennekers, and S. Denham, "Gait-based person and gender recognition using micro-doppler signatures," in *2011 IEEE Biomedical Circuits and Systems Conference (BioCAS)*, November 10-12 2011, pp. 444–447.

[7] K. Kalgaonkar and B. Raj, "Acoustic doppler sonar for gait recogination," in *IEEE Conference on Advanced Video and Signal Based Surveillance, 2007. AVSS 2007*, September 5-7 2007, pp. 27–32.

[8] Y. Kim and H. Ling, "Human activity classification based on micro-doppler signatures using a support vector machine," *IEEE Trans. Geosc.&Remote Sens.*, vol. 47, no. 5, pp. 1328–1337, May 2009.

[9] H. Frennberg, S. Björklund, and N. Wadströmer, "FOI Centre for advanced sensors, multisensors and sensor networks, FOCUS - SSF ProInstitute Annual Report 2012," FOI, Tech. Rep. FOI Memo 4385, February 2013.

[10] S. Björklund, H. Petersson, A. Nezirovic, M. B. Guldogan, and F. Gustafsson, "Millimeter-wave radar micro-doppler signatures of human motion," in *IRS 2011*, Leipzig, Germany, Sept. 7-9 2011.

ABSTRACT

Radar (RAdio Detection And Ranging) uses radio waves to detect the presence of a target and measure its position and other properties. This sensor has found many civilian and military applications due to advantages such as possible large surveillance areas and operation day and night and in all weather. The contributions of this thesis are within applied signal processing for radar in two somewhat separate research areas: 1) radar with array antennas and 2) radar with micro-Doppler measurements.

Radar with array antennas: An array antenna consists of several small antennas in the same space as a single large antenna. Compared to a traditional single-antenna radar, an array antenna radar gives higher flexibility, higher capacity, several radar functions simultaneously and increased reliability, and makes new types of signal processing possible which give new functions and higher performance.

The contributions on array antenna radar in this thesis are in three different problem areas. The first is High Resolution DOA (Direction Of Arrival) Estimation (HRDE) as applied to radar and using real measurement data. HRDE is useful in several applications, including radar applications, to give new functions and improve the performance. The second problem area is suppression of interference (clutter, direct path jamming and scattered jamming) which often is necessary in order to detect and localize the target. The thesis presents various results on interference signal properties, antenna geometry and sub-array design, and on interference suppression methods. The third problem area is measurement techniques for which the thesis suggests two measurement designs, one for radar-like measurements and one for scattered signal measurements.

Radar with micro-Doppler measurements: There is an increasing interest and need for safety, security and military surveillance at short distances. Tasks include detecting targets, such as humans, animals, cars, boats, small aircraft and consumer drones; classifying the target type and target activity; distinguishing between target individuals; and also predicting target intention. An approach is to employ micro-Doppler radar to perform these tasks. Micro-Doppler is created by the movement of internal parts of the target, like arms and legs of humans and animals, wheels of cars and rotors of drones.

Using micro-Doppler, this thesis presents results on feature extraction for classification; on classification of targets types (humans, animals and man-made objects) and human gaits; and on information in micro-Doppler signatures for re-identification of the same human individual. It also demonstrates the ability to use different kinds of radars for micro-Doppler measurements. The main conclusion about micro-Doppler radar is that it should be possible to use for safety, security and military surveillance applications.

ISSN:1653-2090
ISBN: 978-91-7295-335-2

2017:02